Measurements of D^* Production in Deep Inelastic Scattering at HERA

William Michael Dunne

Department of Physics and Astronomy

University of Glasgow

Thesis submitted for the degree of

Doctor of Philosophy

March 2007

Abstract

In this thesis the first measurements of the differential cross sections for charm production have been made at ZEUS since both ZEUS and HERA were upgraded in 2000. The quantities $d\sigma/dx$, $d\sigma/dQ^2$, $d\sigma/dp_T(D^*)$, $d\sigma/d\eta(D^*)$, $d^2\sigma/dydQ^2$ and $F_2^{c\bar{c}}(x, Q^2)$ are presented. An integrated luminosity of 162 pb^{-1} of data were used and the kinematic range examined was $0.02 < y < 0.7$ and $5 < Q^2 < 1000$ GeV^2. The scaled momentum quantity $\log(1/x_p)$ has also been measured in the Breit frame using only charm data for the first time at ZEUS in a limited Q^2 range, giving a further handle on the hadronic final state of the event. The data are compared to next-to-leading-order calculations for $F_2^{c\bar{c}}(x, Q^2)$ related cross sections and to two leading order Monte Carlo simulations for $\log(1/x_p)$. These measurements will ultimately improve the precision to which the gluon content of the proton is understood and will further our understanding of the charm production mechanism in the proton.

For Mum

"It has been said that the whole of human endeavor is an effort to impress the opposite sex. If this is true than *Measurements of D^* production in Deep Inelastic Scattering at HERA* represents the biggest waste of time in the history of mankind."

The Author

Acknowledgments

I will start by thanking my supervisor Tony Doyle for his guidance in shaping the course of my PhD, even though what Tony said and what I actually did were rarely one and the same thing. You sir, are a scholar and a gentleman. A really big special thank you also has to go to James Ferrando and John Loizides whose support, advice and encouragement were invaluable in completing the massive challenge of a PhD Thesis. Your help was genuinely appreciated. I'd also like to thank PPARC for funding my PhD adventure and for Glasgow University for (bafflingly) employing me for the past three years.

In times of intellectual crisis the best place to be is at an international physics organisation. Luckily the ZEUS experiment was conveniently located at one of these and so I was never short of wise men to step in to offer support and advice, often from a different (and at times entirely contradictory) perspective. So I'll take the time to thank Matt Wing, Achim Geiser, Peter Bussey, David Saxon, Bruce Straub and Richard Hall-Wilton whose brain power never fails to impress.

Moving to a new country to study physics carries social as well as intellectual challenges. To this end I will take a moment to thank Elias Ron, John Carter, Pat Ryan, Tom Danielson and Jerome Whyte who all gave a much needed break at times of physics overload. A shout also goes out to Alessandro, Anna, the always smiling Umer, Gabriel, Eric, Homer, Marcos and of course Avraam with whom I shared many very special jokes. I'd also like to give a big special thank you to Dan and Naomi whose recipes helped me trick my girlfriend into thinking I'm a good cook and who were always at hand for everything from beer drinking, football playing to good old playstation fun. You have been great friends.

A thousand thanks go to Susan-Katrin Ketels who organised my bills, accommodation, health-care insurance and countless other things during my stay in Germany. Your tireless work behind the scenes made my transition to Hamburg deceptively easy. I won't include all one thousand thanks in the text here, instead you can exchange this piece of paper for those thanks at all participating Billys. Terms and conditions apply.

I had mixed feelings about moving back to Scotland after the completion of my LTA in Germany. On one hand it was sad to leave behind all my new Hamburg friends but on the other it was good to see all my old Glasgow mates again. I thank you for being there to drag me over the finish line: Scott, Dave, Claire, Helen, Davie, Birnie and all the guys at football; you helped keep me from going insane during the painful writing up process. I want to make a very special mention to my very good friends Gareth and Barry. You guys have always been there for me and I really appreciate it. Thank you. Also Chris was there.

My acknowledgments would not be complete with out recognising the ubiquitous ZEUS-UK group who were there for everything from social to intellectual support. A big thank you to Katherine, John (Morris), Mark, Philip, Cat, Alex, Tim, Matt (Forrest), Sarah, Claire, Andrew and Vincent. I'd also like to extend my thanks to Morgan Murray with whom I shared many meals at the now legendary Bloc House. I had a great time with all of you.

I will close with a great big thank you to my girlfriend Katie Oliver whom I met at ZEUS during my LTA. I appreciated your patience in reading the early drafts of my thesis (over and over again) and I look forward to outranking you until you finish your own PhD. I couldn't ask for a better companion and friend. I love you.

Author's Declaration

All the work presented here is my own, except where explicitly noted. Where it is based on other sources, they are referenced in the text. Since particle physics is by nature a collaborative discipline many of the analytical techniques used are based on the efforts of the ZEUS collaboration in its entirety.

The GTT algorithm was developed over many years by a working group of which I was a member. The development of the J/Ψ trigger using the GTT tracking algorithm is my own.

The HERA II measurements of the $d\sigma/dx$, $d\sigma/dQ^2$, $d\sigma/dp_T(D^*)$, $d\sigma/d\eta(D^*)$, $d^2\sigma/dydQ^2$, $F_2^{c\bar{c}}(x, Q^2)$ and $\log(1/x_p^{D^*})$ including any experimental systematic uncertainties, were performed by myself. The associated theoretical errors were taken from the corresponding HERA I measurement performed in the same kinematic range since no theoretical improvement has been made.

Contents

List of Figures

List of Tables

Chapter 1

Introduction to the Standard Model of Particle Physics

This chapter will briefly discuss the historical context of the Standard Model and introduce the particles it describes and postulates to be fundamental to all matter. The theory of Quantum Chromodynamics is presented, along with the tool of perturbation theory which allows predictions to be made. The chapter closes with a discussion of the importance of particle accelerators and why they are useful in fine tuning the Standard Model and exposing its flaws.

1.1 History

The origins of Particle Physics can be traced back to the 6th century BC in Ancient Greece. At this time, Greek philosophers Democritus and Leucippus taught the doctrine of *atomism* which states that all matter can be deconstructed into *atoms*. At the time these were considered to be the smallest objects in the universe. Little written account of this work remains, and it was not until 1802 that the ideas were formally stated by physicist John Dalton after his extensive study on the properties of gases.

In the late 1890s J.J. Thompson established that atoms themselves were not the smallest constituents of matter, rather that they themselves had an internal structure consisting of *electrons* and *protons*. By 1904 he (incorrectly) proposed that in the atom the electrons were evenly distributed, surrounded by a soup of positively charged protons. This model was short lived, for in 1911 Ernest Rutherford discovered that most of the atom was actually empty space; the protons were in fact concentrated in an incredibly densely packed core called the *nucleus* surrounded by a cloud of orbiting electrons. In 1932 the picture of the atom was complicated still further by the discovery of the neutron, found alongside the proton in the nucleus of the atom. In Particle physics experiments throughout the 1950s and 60s a bewildering array of new particles were discovered.

The discovery of such a large number of new particles brought with it an ugly and cumbersome picture of the universe. The scientific community endeavored to find an elegant and simple substructure to these particles; some architecture that would neatly explain their properties and that could be used to make further predictions. This formalism arose between 1970 and 1974 in the form of the *Standard Model* which soon became the accepted framework in which to talk about elementary particles and the interactions between them.

1.2 The Standard Model

The Standard Model is a gauge theory with the gauge group SU(3)×SU(2)×U(1). It describes the quantum field theories of electromagnetism, the weak force and the strong force through which the particles interact. It states that there are 12 fundamental particles from which matter is constructed, and 4 particles which mediate the forces between them. The masses and charges of these particles are given in table 1.1.

Matter is constructed from particles called fermions. Fermions have half-integer spin and so obey the Pauli exclusion principle. The fermion family is divided into two smaller classes of particles: quarks and leptons. There are 6 different types of quark from which more massive particles (hadrons) can be constructed; those containing 2 quarks are called mesons and those containing 3 quarks are called baryons. The leptons are generally speaking much lighter than their quark counterparts and do not form bound states.

If fermions are the building blocks of matter, then bosons are the mediators of force between them which allow fermions to interact; all particles fall into one of these two distinct categories. The complicated grouping of these particles is illustrated more clearly in figure

	Particle	Charge (e)	Approx. Mass (MeV)
Leptons	electron	-1	0.511
	electron neutrino (ν_e)	0	<2.2 eV (95% C.L.)
	muon	-1	106
	muon neutrino (ν_μ)	0	<190 keV (90% C.L.)
	tau	-1	1777
	tau neutrino (ν_τ)	0	<18.2 (90% C.L.)
Quarks	up	+2/3	1.5-5
	down	-1/3	3-9
	strange	-1/3	60-170
	charm	+2/3	1300
	bottom	-1/3	4200
	top	+2/3	174000
Bosons	photon (γ)	0	0
	8 gluons (g)	0	0
	$W^{\pm}$	$\pm$1	80410
	Z^0	0	91187

Table 1.1: The particles in the Standard Model with their approximate masses and electric charge [1].

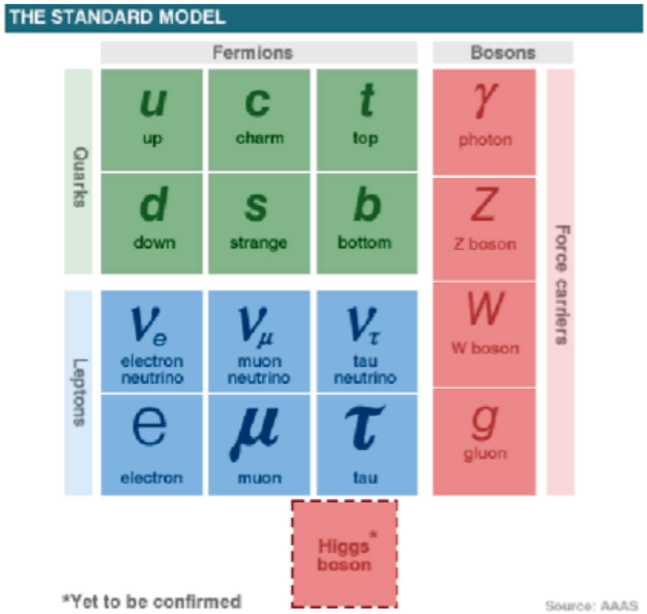

Figure 1.1: The elementary particles of the Standard Model.

1.1. The set of bosons is much smaller and includes exclusively: photons, W and Z bosons, gluons and, presumably, the Higgs whose existence has yet to be confirmed experimentally. Photons mediate the electromagnetic interaction, the W and Z mediate the weak nuclear force, the (8 species of) gluons mediate the strong nuclear force and the Higgs boson is said to give the other particles mass. By definition bosons have *integer* spin and therefore are not constrained by the Pauli exclusion principle.

1.3 Quantum Chromodynamics

The idea that hadrons could be constructed from quarks was a powerful tool in the early days of particle physics, giving structure and simplicity to the ever growing number of particles discovered at the time. However, the idea of quarks was still not developed enough to explain the existence of the Ω^- particle. The Ω^- is comprised of three strange quarks with parallel spins, a configuration that appeared to violate the Pauli exclusion principle and hence should not exist.

1n 1965 this problem was resolved by suggesting that quarks possess three additional degrees of freedom called *colour* charge. The three colour charges are analogous to the one electric charge used in the electroweak field theory. Under QCD, quarks would interact by the exchange of *gluons*. These new degrees of freedom are incorporated mathematically into the Standard Model as an additional SU(3) group describing the strong interaction. This new group sits on top of the SU(2)×U(1) groups which describe the unified electroweak interaction.

Quantum Chromodynamics (QCD) is then the theory of the strong interaction between quarks and gluons, as manifest by the colour charge. It is a non-abelian gauge theory with two important properties; *confinement* of quarks within hadrons and *asymptotic freedom* of quarks at high energies. Confinement is the idea that individual quarks cannot be observed, instead they are bound up inside hadrons at all times. Asymptotic freedom states that the interaction between quarks becomes weaker with decreasing distance. At distance scales of order of the width of a proton the interaction between quarks and gluons is small, so inside a proton quarks and gluons can be treated as non-interacting. Any theory which can be described as asymptotically free is amenable to perturbation theory calculation which will be discussed shortly.

The Heisenberg uncertainty principle states that the distance interaction scale is inversely proportional to the momentum scale:

$$\Delta x[\mathrm{fm}] \geq \frac{0.197[\mathrm{GeV\ fm}]}{\Delta p[\mathrm{GeV}]}.$$

Δx and Δp are distance and momentum scales respectively. Higher energy interactions therefore probe distance scales at which the partons may be considered free from the strong interaction. The interactions measured in this thesis are of this energy scale and so may be treated within the framework of perturbative QCD.

The probability of an interaction taking place, or *cross section* can be calculated using perturbation theory only if the strength of the interaction is small enough. If this is true then the cross section may be expressed as a sum of terms described by Feynman diagrams. Feynman diagrams represent mathematical terms associated with the probability of an interaction occurring.

1.3.1 Perturbation Theory

Perturbation theory is a mathematical device sometimes used to generate approximate solutions to unsolvable problems. Using perturbation theory, a full solution A (which may represent, for example, a scattering amplitude) may be expressed in terms of a small parameter ϵ as

$$A = A_0 + \epsilon A_1 + \epsilon^2 A_2 + \ldots$$

In this expression A_0 is the solution to the exactly solvable problem and A_1, A_2 etc are the perturbative corrections which solve the more complex problem. The perturbative approach only works if the problem can be expressed by the addition of a small term to an exactly solvable problem. Moreover the expansion parameter must be small enough for the series to be convergent. In perturbative Quantum Chromodynamics the expansion parameter is the colour coupling constant α_s whose value falls with increasing Q^2. $\alpha_s(Q^2)$ is expressible as a summation of smaller α_s^i components, and takes the leading order form

$$\frac{1}{\alpha_s} \approx \frac{1}{\alpha_s^0(Q^2)} = \frac{(33 - 2n_f)}{12\pi} \ln \frac{Q^2}{\Lambda_{\mathrm{QCD}}} = \beta_0 \ln \frac{Q^2}{\Lambda_{\mathrm{QCD}}}$$

where n_f is the number of active flavours at the scale Q^2, $\Lambda_{\mathrm{QCD}} \approx 200$ MeV is a fixed parameter of QCD, and β_0 is the beta function that is determined by the $\mathrm{SU}(3)_c$ gauge structure of QCD. Quark and gluon dynamics may therefore be calculated using perturbative QCD (pQCD) whenever the interaction scale (Q^2) is larger than this fundamental theoretical cut-off value, Λ_{QCD}. In this kinematic region $\alpha_s(Q^2)$ is small enough for perturbation theory to apply. The kinematic range treated in this thesis is amenable to perturbation theory.

Decades after the discovery of asymptotic freedom and the rise of perturbation theory as a predictive tool at short distances, there is still no precise tool for the prediction of long distance effects. It is for this reason that the discovery of asymptotic freedom was such a tremendous breakthrough for the theory of QCD. In 2004 David Gross, Frank Wilczek and David Politzer were awarded with the Nobel Prize in Physics for their discovery of asymptotic freedom 31 years previously.

Collaboration	Location	Collider
CERN	Geneva, France/Switzerland	LHC $p\bar{p}$ (formally LEP e^+e^-)
DESY	Hamburg, Germany	HERA II
Fermilab	Chicago, USA	Tevatron $p\bar{p}$
SLAC	Palo Alto, USA	PEP-II e^+e^-
Brookhaven	Brookhaven, USA	RHIC Aup

Table 1.2: Some of the major international collaborations in particle physics.

1.4 Particle Accelerators

Progress in high energy physics cannot be made without the aid of particle accelerators which are used to create the fundamental particles listed in the Standard Model. There is a strong dependence on funding from large international collaborations, some of which are listed in table 1.2, because of the incredible cost of constructing and running these devices. The work in this thesis is based on measurements made with the ZEUS detector at the DESY institute which houses the HERA accelerator; the largest electron proton collider in the world. Data collected from high energy particle collisions has led to unprecedented advances in the understanding of the quantum world. It is only under these unusual energy conditions that the strong interaction of the Standard Model (as mediated by the gluon) can be measured and used to increase our understanding of the sub-atomic realm. ZEUS and its sister experiment H1 have played a pivotal role in furthering the development of QCD.

Chapter 2

Theoretical Background

This chapter will give a brief introduction to the basic theory of Deep Inelastic Scattering with emphasis on the Lorentz invariant variables used to characterise these events and the relationship between cross sections and structure functions. The chapter moves on to discuss the evolution of the Quark Parton Model and the impact this has made on the theory of structure functions. A discussion of DGLAP evolution, parton density functions and the nature of heavy quark production at ZEUS is then presented, followed by an explanation of Monte Carlo event generation and the different implementations of the hadronisation and fragmentation stages of quark jet production. The chapter closes with a discussion of scaled momenta distributions and their measurement in the Breit frame.

2.1 Deep Inelastic Scattering

Neutral current Deep Inelastic Scattering (DIS) is the process by which a proton fragments after the absorption of a virtual photon (or Z-boson) emitted by a lepton. In doing so the constituent quarks are released and information is revealed about the underlying structure of the proton. DIS is a productive environment in which to study heavy quark production. In the kinematic region considered for this analysis the contribution from the Z boson is negligible and so only the case of photon exchange is considered.

Figure 2.1 shows a leading order DIS event where the incoming lepton 4-momentum is $\mathbf{k}$ and the outgoing 4-momentum is $\mathbf{k}'$. During the scatter this lepton emits a virtual photon

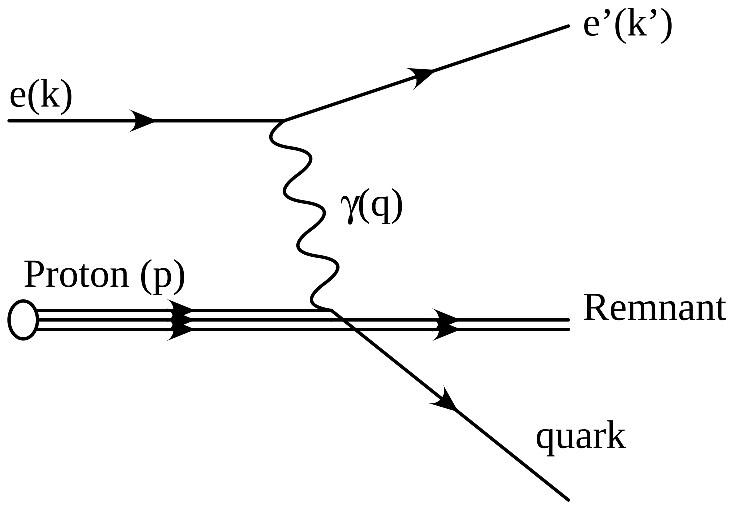

Figure 2.1: A DIS event at lowest order in the Quark Parton Model.

with 4-momentum $\mathbf{q}$ which strikes a proton of 4-momentum $\mathbf{P}$, knocking out a quark which fragments into hadrons. The proton remnant is poorly understood since it is lost down the beampipe of the ZEUS detector.

A DIS scatter is formally represented by the equation

$$e(\mathbf{k}) + p(\mathbf{P}) \rightarrow e'(\mathbf{k}') + X(\mathbf{P}' = \mathbf{P} + \mathbf{q})$$

where X is the final state of the interaction and includes the proton remnant. The interaction does not occur with the proton as a whole, rather between a single quark carrying a fraction x of the total momentum of the proton. x is sometimes called the Bjorken scaling variable and is one of a number of important Lorentz scalars used to describe DIS events. Four variables typically used (of which only any two are independent) are:

$$Q^2 = -\mathbf{q}^2 = (\mathbf{k} - \mathbf{k}')^2$$

$$x = \frac{-\mathbf{q}^2}{2\mathbf{P} \cdot \mathbf{q}}$$

$$y = \frac{\mathbf{P} \cdot \mathbf{q}}{\mathbf{P} \cdot \mathbf{k}}$$

$$W^2 = (\mathbf{P} + \mathbf{q})^2$$

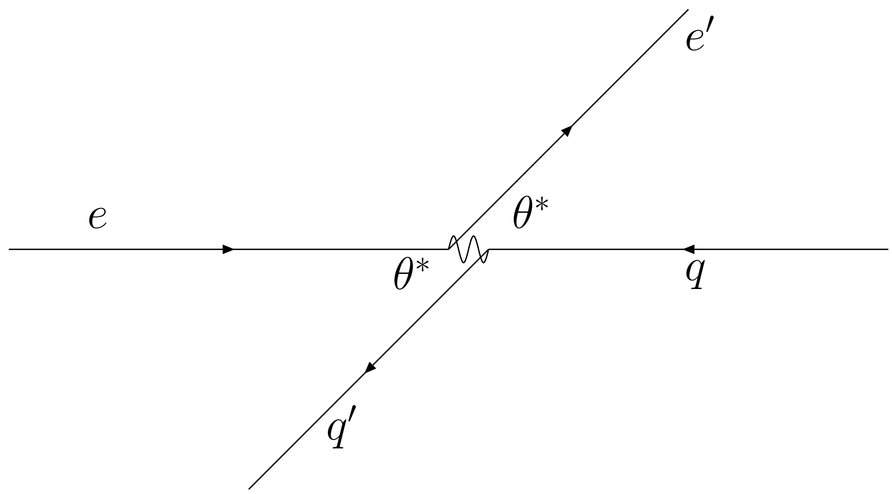

Figure 2.2: An quark-electron scatter in its center of mass frame. The electron e scatters off a quark q with angle θ^*.

Any DIS event may be characterised by using any two of these four parameters. x, y and Q^2 are connected by the relationship

$$Q^2 = sxy,$$

assuming that $\sqrt{s}$ is much larger than the mass of the proton. Here, $s = (\mathbf{k} + \mathbf{p})^2$ is the square of the centre of mass energy of the ep collision. At HERA, s has a value of 318 GeV^2. The Q^2 (or *virtuality*) of the event gauges how deeply the proton has been probed. Q^2 represents the resolving power of the exchange photon; a high energy exchange photon would have a shorter wavelength and would so probe a smaller distance scale. In this way high Q^2 events resolve the proton at the quark level, rather than interacting with the proton as a whole.

The quantity y can be interpreted as the *inelasticity* of the event. Consider the quark-lepton center of mass frame where, as illustrated in figure 2.2, the scattered electron (and quark) are deflected by angle θ^*. In this frame y is a measure of this deflection angle according to the relation $y = \frac{1}{2}(1 - \cos\theta^*)$. An event with $y = 1$ corresponds to one in which the electron has completely doubled back on itself with $\theta^* = \pi$. In the proton rest frame however, y is a measure of how much energy is lost by the scattered electron after its interaction with the proton. A process is said to be elastic if the proton remains intact afterwards.

Finally, W^2 may be interpreted as the squared centre of mass of the hadronic system after the collision. W is related to x and Q^2 by the relationship

$$\frac{W^2}{Q^2} = \frac{1}{x} - 1,$$

with $W^2/Q^2 \approx 1/x$ at low x. A number of experimental techniques exist for measuring the eP scattering kinematics, these rely on the angle and energy reconstruction of the scattered electron as well as the measurements of the hadronic system. Such techniques are discussed in more detail in the reconstruction section in chapter 6.

Events for which 1 GeV$^2 < Q^2 <$ 100 GeV^2 are sufficient to probe the internal structure of the proton and are called DIS events at moderate Q^2 events. At higher Q^2 the Standard Model contribution becomes small and the limits of existing theories may be tested. At the time of writing HERA is the only device capable of producing such events.

2.1.1 Structure Functions

When DIS is described purely by the exchange of one virtual gauge boson, the unpolarised neutral current $e^{\pm}p \rightarrow e^{\pm}X$ cross-section may be written in its most general form as:

$$\frac{d^2\sigma(e^{\pm}p)}{dxdQ^2} = \frac{2\pi\alpha^2}{xQ^2}[Y_+F_2(x,Q^2) - y^2F_L(x,Q^2) \mp Y_-xF_3(x,Q^2)]$$

where $Y_{\pm} = 1 \pm (1-y)^2$, α is the electromagnetic coupling constant, F_L is the coupling to longitudinally polarised virtual photons and xF_3 is a parity violating term which arises from Z^0 exchange. The xF_3 contribution is neglected completely in this thesis because low Q^2 ($Q^2 < M_z^2$) events are completely dominated by the virtual photon exchange process. The $-y^2F_L$ term is only significant at $y \approx 1$ and because the measurements made in this thesis are for $y < 0.7$ the contribution is small and therefore neglected.

If the partons in the proton are thought of as non-interacting the structure functions can be expressed in terms of quark momentum distributions, $q_i(x)$,

$$F_2(x) = x\sum_q e_i^2(q_i(x) + \bar{q}_i(x)) \tag{2.1}$$

where $q_i(x)$ are the quark momentum densities of the various quark flavours in the proton, over which the summation runs. $q_i(x)$ is also known as a Parton Density Function (PDF) and describes the probability of finding a particle of species i with any given x. PDFs are not calculable from first principles due to non-perturbative effects that exist in a QCD binding state, so instead they must be obtained from fits to data. One should be aware that this interpretation of structure functions fails for higher order QCD.

PDFs and structure functions are often confused because of their close relationship at leading order, they are however very different concepts: PDFs are theoretical constructs which can only be determined indirectly; structure functions on the other hand are physical observables which can be measured in DIS. Measurement of structure functions enable us to infer information about PDF shapes [2].

2.2 The Quark-Parton Model

The Quark-Parton Model (QPM) was inspired by early SLAC structure function measurements which indicated that $F_2(x, Q^2) \to F_2(x)$ as $Q^2 \to \infty$. This is known as scaling and its observation implies that the photon is scattering off *point like* constituents [3] in the proton. The reasoning for this is that as the virtuality of the photon increases it will be unable to resolve any further architecture within the proton and so no changes in F_2 are observed. Moreover the scattering of the lepton is now considered to be an elastic scatter from one of these point-like constituent quark particles. No gluon emission is accounted for in the QPM.

In parton models the lepton-hadron cross section is intuitively linked to the cross section for lepton-parton scattering by

$$\frac{d\sigma^{lh}}{dxdQ^2} = \sum_i \int_0^1 d\xi q_i(\xi) \frac{d\sigma^{li}}{dxdQ^2}$$

where $d\sigma^{lh}$ is the cross section for a lepton-hadron scatter and $d\sigma^{li}$ is for lepton-parton scattering. The momentum carried by the parton is given by ξP where P is the total momentum carried by the hadron. q_i are parton distribution functions (PDFs) in which $q_i(\xi)d\xi$ give the probability of finding a parton of flavour i in the hadron. PDFs are independent of the particular hard scattering process.

Measurement of $q_i(\xi)$ for the three valence quarks found that the momentum sum rule,

$$\int_0^1 x \sum_i q_i(x) dx = 1$$

was violated. This value was found to be ≈ 0.5 which indicates that only 50% of the total proton momentum is carried by these quarks. From this result it must be concluded the extra momentum is carried by additional neutral particles and that the QPM is not a complete description of the proton. The extra momentum is carried by gluons, and their assimilation into the QPM theoretical framework leads to the QCD improved Quark Parton Model.

2.2.1 The QCD Improved Quark Parton Model

The QCD improved Quark Parton Model may be summarised as follows:

- All hadrons consist of particles called *quarks* and *gluons* (identified as such by QCD)
- In electron proton scattering the electron scatters off of a parton constituent of the proton
- This parton is considered to be point-like
- Scattering between the partons in the proton is incoherent
- Interactions between the scattered parton and the non-interacted partons are negligible.

This final point is justified by application of time dilation effects and the Lorentz contraction of the proton system as seen by the exchange photon in the infinite momentum frame. Effectively the photon sees the partons frozen during the interaction which can therefore be approximated as non-interacting during a DIS scatter.

The hard scattering process may be factorised from the long range parton-parton hadronisation since once the collision has occurred hadronisation takes place much too late to affect the initial photon interaction. An important consequence of this separation is that any PDF extracted from DIS are universal and can be applied to all hadronic interactions provided the same order of perturbation theory is maintained and *renormalisation schemes* are consistent. A renormalisation scheme is a mathematical tool to remove the singularities that arise in calculations of higher order cross sections. Selection of a renormalisation scheme

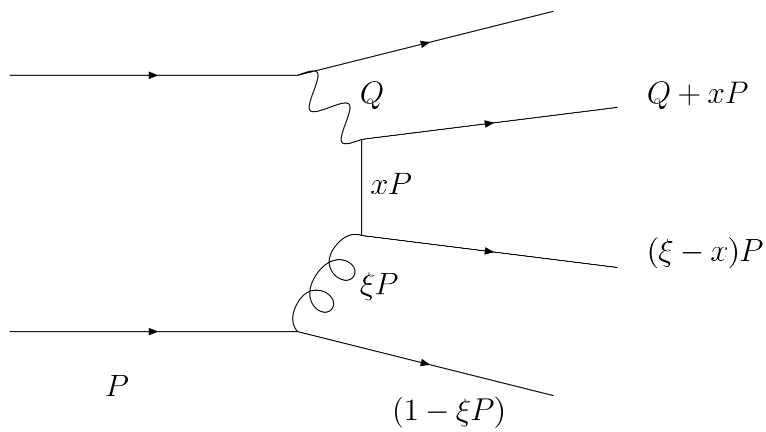

Figure 2.3: Distribution of the total proton momentum P during Boson-Gluon fusion.

amounts to choosing a particular set of quantities that avoids divergences in the calculation and gives a finite and physical solution.

In QCD F_2 is dependent on both x and Q^2 which breaks the scaling predicted by the QPM. Scaling violation arises because quarks can now acquire large p_T by the emission of gluons, leading to $\alpha_s \ln Q^2$ terms in the expression for F_2. The scaling violations predicted by QCD have been experimentally observed at ZEUS in low x measurements of F_2 [5]. Moreover the summation in equation 2.1 now extends to include heavier quarks which are formed by gluon splitting and exist in a "sea" around the proton. Contributions from the heaviest quarks are neglected from this sum since at HERA energies their contribution is vanishingly small.

2.2.2 DGLAP Evolution of the Parton Densities

A consequence of the QCD improved Quark Parton Model is that the measured proton quark and gluon densities evolve with increasing Q^2. This evolution is caused by the emission of gluon radiation from quarks and by gluons splitting into $q\bar{q}$ pairs. Figure 2.3 illustrates the boson-gluon fusion process in which a proton with momentum P emits a gluon with momentum ξP. This gluon then emits a pair of quarks, one with momentum xP which interacts with a virtual photon and one with momentum $(\xi - x)P$. The final quark pair have momentum $Q + xP$ and $(\xi - x)P$. The subprocess $\xi P \rightarrow xP + (\xi - x)P$ is equivalent to

$P \to z_{AP}P + (1 - z_{AP})P$ where $z_{AP} = x/\xi$.

The evolution of parton distributions can be evaluated using the Dokshitzer-Gribov-Lipatov-Altarelli-Parisi (DGLAP) equation. The evolution of quark distributions is described by

$$\frac{\partial q_i(x,Q^2)}{\partial \mathrm{ln}Q^2} = \frac{\alpha_s(Q^2)}{2\pi}\int_x^1 \frac{d\xi}{\xi}\left[\sum_j q_j(\xi,Q^2)Pq_iq_j\left(\frac{x}{\xi}\right) + g(\xi,Q^2)Pq_ig\left(\frac{x}{\xi}\right)\right]$$

and for evolution of gluon distribution it is given by

$$\frac{\partial g_i(x,Q^2)}{\partial \mathrm{ln}Q^2} = \frac{\alpha_s(Q^2)}{2\pi}\int_x^1 \frac{d\xi}{\xi}\left[\sum_j q_j(\xi,Q^2)Pgq_j\left(\frac{x}{\xi}\right) + g(\xi,Q^2)Pgg\left(\frac{x}{\xi}\right)\right].$$

Where the Pij terms are the so-called "splitting" functions. The splitting functions $P_{ij}(x/\xi = z_{AP})$ may be interpreted physically as the probability of parton i being emitted by parton j with a fraction z_{AP} of parton j's momentum. This is a manifestation of the idea that the particle undergoing interaction may not have originally been a constituent of the proton and may have been radiated in a higher order process [4]. $P_{ij}(z_{AP})$ is calculated using a pertubative expansion in α_s, which given a particular factorisation and renormalisation scheme looks like,

$$\frac{\alpha_s}{2\pi}P_{ij}(z_{AP}) = \frac{\alpha_s}{2\pi}P_{ij}^{(1)}(z_{AP}) + \frac{\alpha_s}{2\pi}^2 P_{ij}^{(2)}(z_{AP}) + \ldots$$

where the termination after the first two terms defines the next-to-leading Order (NLO) DGLAP evolution. Higher $P_{ij}^{(l)}$ terms for successive values of l represent an increase in the number of allowed splittings in the approximation. To leading order these terms have been calculated explicitly as:

$$P_{qq}^1(z_{AP}) = \frac{4}{3}\left(\frac{1+z_{AP}^2}{1-z_{AP}}\right)_+$$

$$P_{gq}^1(z_{AP}) = \frac{1}{2}(z_{AP}^2 + (1-z_{AP})^2)$$

$$P_{qg}^1(z_{AP}) = \frac{4}{3}\left(\frac{1+(1-z_{AP})^2}{z_{AP}}\right)$$

$$P_{gg}^1(z_{AP}) = 6\left(\frac{z_{AP}}{1-z_{AP}} + \frac{1-z_{AP}}{z_{AP}} + z_{AP}(1-z_{AP})\right) + \left(11 - \frac{n_f}{3}\delta(1-z_{AP})\right)$$

where $\delta(1-z)$ is the delta function and the + subscript in P_{qq}^1 indicates that the expression is not defined for $Z_{AP} = 1$. The Feynman diagrams corresponding to these splitting functions

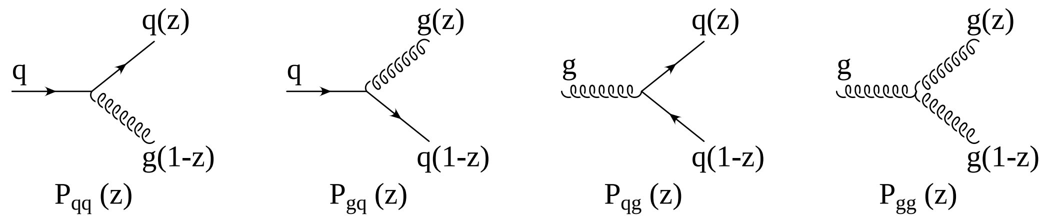

Figure 2.4: Feynman representation of the Altarelli-Parisi splitting functions.

are shown in figure 2.4. Progress is currently being made in numerically calculating the next-to-next-to-leading order contribution P^3 and higher orders of P^l [4].

An important prediction arising from the DGLAP equation is violation of scaling whereby there will be an observed increase in parton density at low x as Q^2 increases. This arises at the cost of initially high x partons which split and contribute to the lower x region. Scaling violations can be thought of as a consequence of the increase of resolution obtained by increasing Q^2; this increases the probability of finding a quark at small z_{AP} because high-momentum quarks lose momentum by radiating gluons [4]. ZEUS has measured these scaling violations which indirectly give a handle on the proton's gluon density. The DGLAP equation is arguably the most important equation in perturbative QCD. Using DGLAP it is possible to relate PDFs measured at one scale to other scales and to make predictions for very high Q^2 processes in searches for new physics.

2.3 Measurement of Parton Density Functions

The QCD factorisation theorem allows separation of long range effects from the short range interactions. The visible cross section for a hadronic final state is then a distinct combination of a PDF contribution, PDF, the cross section for a QCD scattering process, $\hat{\sigma}$, and a quark→hadron fragmentation, $\mathrm{F}(q \to H)$

$$\sigma = PDF \otimes \hat{\sigma} \otimes \mathrm{F}(q \to H).$$

This makes it possible to predict the Q^2 dependence of partons using perturbative QCD. However there is no purely theoretical framework with which to predict parton density functions. The only way to obtain them is to perform fits to data at some fixed scale Q_0^2 and rely on DGLAP to evolve these fits to higher scales. In this process postulations are made to justify some functional form which is then fitted to structure function measurements from a number of world experiments. Measurements of structure functions may be performed by direct observation of hadronic final states and measurements of scaling violation to indirectly observe gluon density.

The fits from ZEUS [6], CTEQ [7] and MRST [8] are examples of PDFs which have been used in previous measurements of the $F_2^{c\bar{c}}$ contribution to F_2. PDFs are expected to be universal and independent of the scatting process involved. This justifies the decision by CTEQ and MRST to combine data from every collider experiment in their fits.

2.4 Monte Carlo Simulation

Monte Carlo (MC) simulations of QCD processes fall naturally into two distinct categories: leading order (LO) and next-to-leading-order (NLO) packages. LO programs such as RAPGAP[9] and HERWIG[10] are used to determine acceptances, resolution and efficiency effects of the detector as well as gauging the backgrounds that arise in an event sample. NLO simulations such as HVQDIS[11] generate cross-section predictions which are used for comparison with measurements of data.

The leading order MC programs used in this analysis were RAPGAP 2.08/18 and HERWIG 6.3/01 from which a total of 494 pb^{-1} of simulated data were generated. The output from these physics simulations was passed through the GEANT 3.13[12] package which provides a complete simulation of the ZEUS detector. The output from GEANT is directly analogous to the output produced by a real physics event. This sample of MC can then be processed in exactly the same way as the data with identical selection cuts.

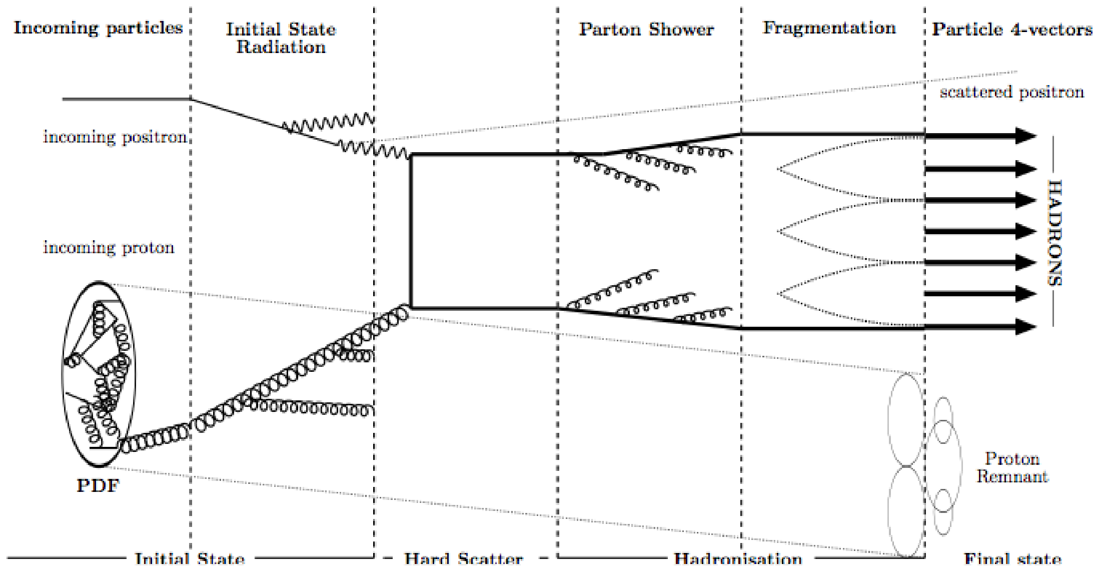

Figure 2.5: A representation of an algorithm for physics event generation. The initial state is shown to undergo a hard scattering process, followed by a distinct parton shower stage and concluding in a fragmentation algorithm. Fragmentation produces a final state of colourless hadrons.

2.4.1 Construction of a MC event

The Fragmentation Theorem permits the deconstruction of any event into a number of distinct stages:

1. The initial state: comprised of an electron and a proton described by PDFs.

2. The scattering process: described by the interactions of quarks and gluons.

3. Fragmentation and hadronisation into the final state: the process of creating colourless hadrons from the isolated quarks produced in stage 2.

This concept is utilised by both RAPGAP and HERWIG, both of which engineer events according to the prescription outlined in the following list and illustrated in figure 2.5. The differences between the two implementations are summarised in table 2.1.

- *Initiation of colliding particles.* In the ZEUS experiment the colliding particles always consist of a single lepton and a proton. The MC simulation is equipped with the 4-

vectors of both beams and a PDF to describe the parton constituents of the proton, one of which is selected for interaction with the lepton.

- *Initial state radiation (ISR).* There is a non-negligible probability that the incoming lepton will emit a photon before interaction with the proton. This must be accounted for in the MC simulation since this phenomenon is known to disturb the event kinematics to a measurable degree.

- *Hard Scatter.* After ISR has been accounted for the hard scatter is calculated using LO matrix elements. This reduces the scatter to a single interaction between photon and parton.

- *Parton Showering.* The production of quarks and gluons after the hard scatter. Typically secondary partons are produced according to the probabilities given by the Altarelli-Parisi splitting functions (figure 2.4). The showering process generates a vast cascade of new particles of decreasing energy until a lower energy scale, μ_F, ≈ 1 GeV is reached.

  The parton showering process differs between MC models; HERWIG uses the colour dipole method and RAPGAP uses the parton shower model. In the colour dipole method the secondary gluons are emitted from an extended expanding colour dipole. This arises because two colour charges accelerating away from each other produce a gluon radiation field. If the wavelength of the emitted radiation is longer than the distance between the charges then the system can be treated as a dipole. In this way the individual charges are not themselves resolved but instead are seen as an "aerial" consisting of two charges that emit radiation as a dipole field.

  In the parton shower model the gluons are produced in two ways; hard gluon radiation is calculated using QCD matrix elements, soft gluon radiation is calculated using the leading log method. Regardless of the model used, once the lower limit is reached the environment consists of a number of partons all existing in a state of isolated colour.

- *Fragmentation.* The final stage of MC simulation is fragmentation. This is the process by which the colourless final state hadrons are formed from the swarm of coloured

MC	RAPGAP	HERWIG
Charm Production	BGF	BGF
Proton PDF	GRV94	GRV94
Parton Shower	Parton Shower	Colour Dipole
Fragmentation	Lund String (+ Peterson)	Cluster Fragmentation (+ Peterson)

Table 2.1: Table outlining the principal differences and similarities between the RAPGAP and HERWIG MC simulations. Both produce charm using the BGF mechanism and the proton PDF used was GRV94. The MC models differ in their implementation of the parton shower and fragmentation processes.

partons generated by the parton shower. As with the parton shower, the exact implementation of the fragmentation process differs according to the choice of MC. RAPGAP uses the Lund string model (discussed below) and HERWIG uses the clustering algorithm.

2.4.2 Leading Order MCs

RAPGAP

The principal MC program used in this analysis is RAPGAP [9] which specialises in the simulated production of heavy quarks. In this simulation charm is produced only by the Boson Gluon Fusion (BGF) process which is discussed in more detail in section 2.6. The PDF GRV94 [13] was used to describe the proton and QCD parton cascades are described using the colour dipole model [14] performed according to the Peterson function. The Peterson function is described in section 2.5.2. In this analysis, events were generated for which $Q^2 > 0.6$ GeV^2.

HERWIG

The physics results produced in this analysis were cross checked using the HERWIG [10] MC program, which uses the same proton PDF but simulates the QCD parton cascades using the colour dipole model. Charm fragmentation is evaluated using cluster fragmentation [15] whereby the nearest neighbour of each quark is identified and combined to form colour singlet clusters. Once a cluster has been established, fragmentation will proceed in one of two ways; if the cluster is not massive enough to decay into two smaller hadrons it will become a final state hadron. If it is massive enough it will decay into pairs of hadrons which are fragmented until the conditions for first step are met. HERWIG does not include radiative corrections and so will produce incorrect electron energies.

2.4.3 Next-to-Leading order MC

HVQDIS

HVQDIS [16] is a package used to predict NLO (specifically $c\bar{c}$) cross-sections. The total charm cross-section and differential cross-sections in Q^2, x, y, W are generated in a given kinematic range, along with differential cross-sections in quark properties such as $p_T(D^*)$ and $\eta(D^*)$.

HVQDIS operates within the fixed-flavour-number scheme (FFNS) whereby the initial state proton is assumed to consist only of up, down and strange quarks. In this way there are only ever three active quarks in the proton regardless of the Q^2 of the event. Indeed the only mechanism by which charm is produced is BGF.

In HVQDIS there is no process analogous to the parton shower stage seen in the LO programs and so no information on quark jets is produced. Instead the four-vectors of the BGF initial quark pair are transformed directly into a heavy meson by the Peterson fragmentation function, discussed in section 2.5.2.

The following parameters were used as input to the HVQDIS package:

- The proton PDF: ZEUS-S
- Mass of the charm: $m_c = 1.35$ GeV
- Epsilon parameter in the Peterson fragmentation function: $\epsilon_{\mathrm{Peterson}} = 0.035$
- Renormalisation and factorisation scales: $\mu = \sqrt{Q^2 + 4m_c^2}$

ZEUS-S [19] is the latest ZEUS NLO QCD fitted to structure function data using the FFNS. In this fit the QCD cut off scale $\Lambda_{QCD} = 0.363$ was applied with the charm mass $m_c = 1.35$.

2.5 Fragmentation

Unlike quark production in the parton shower, the hadronisation of isolated quarks into particle jets is not calculable in perturbative QCD. Phenomenological models must instead be constructed and fit to data to describe the transition from quark to hadron. Some of the most common parameterisations are given below

2.5.1 Lund String Fragmentation

The method favoured by RAPGAP to turn shower partons into hadrons is that proposed by the Lund group in 1983 [17]. Pairs of coloured quarks which could combine to form a colourless hadron are connected together by a "colour-string". This string is allowed to stretch and eventually snap at any point, producing quark-antiquark $q_i\bar{q}_i$ pairs at this location. This model attempts to replicate the phenomenon of colour confinement. Such pairs are connected to nearby $q_j\bar{q}_j$ quarks to form bound $q_i\bar{q}_j$ (and occasionally $q_iq_jq_k$) states. Once a bound state has been produced it is propelled transverse to the string according to:

$$P(p_\perp) \propto e^{-\frac{\pi m_\perp^2}{k}}$$

where $m_\perp^2 = m^2 + p_\perp^2$ and k is a parameter called the string tension. The transverse momentum supplied is compensated locally within the $q_i\bar{q}_j$ hadron which carries a momentum fraction z of the total energy available to it. The creation process ends when the pairs of coloured partons do not have sufficient invariant mass to break the string.

The hadron formed from $q_i\bar{q}_j$ quarks carries with it only a fraction of the total available momentum to it. This fraction is z_L which in the Lund string model is given by

$$(E + p_z)_{\text{hadron}} = z_L(E + p_z)_{\text{quark}}$$

The probability density function of z_L is called the fragmentation function and for light

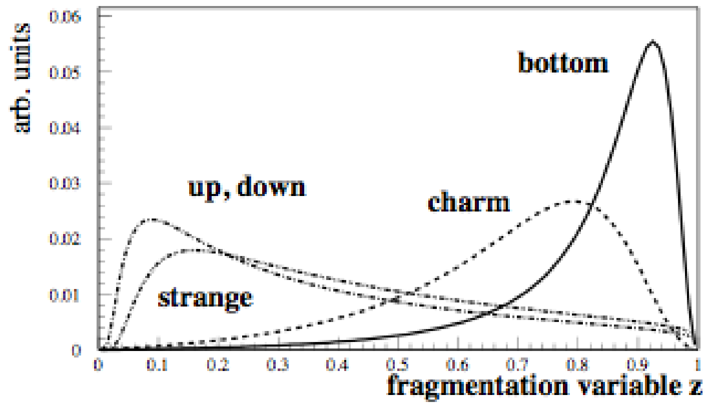

Figure 2.6: Fragmentation function as a function of z for a selection of quark flavours. z is the fraction of the total energy available carried by the produced hadron. Heavier quarks peak at larger z.

quarks is given by

$$D(z_L) \propto \frac{(1-z_L)^a}{z_L} e^{-\frac{b m_{h,\perp}^2}{z_L}}$$

which contains parameters a and b. These are evaluated by fitting to data and are typically taken to be $a = 0.11$ and $b = 0.52$ GeV^{-2}. Whilst this gives a reasonable description of light quarks, it was shown experimentally to be inadequate for the description of the heavier partons [18]. In these instances the Peterson Fragmentation is used.

2.5.2 Peterson Fragmentation

The shape of the fragmentation function is strongly dependent on the mass flavour of the quark. Figure 2.6 illustrates that lighter quarks peak at lower values of z whereas charm and beauty quarks are produced much more favorably at high z. An accurate description of fragmentation functions is necessary to transform a QCD prediction of a cross-section into a quantity which may be detected. This is important because a non-negligible fraction of the charm production cross-section is excluded by cuts placed on the final charmed state.

The most commonly used fragmentation function for heavy quarks (and the one used in this analysis) is the Peterson fragmentation function [20]. In line with observation, the Peterson fragmentation function ensures that the majority of energy contained in the heavy quark will be transferred onto the hadron formed from it. The functional form of the Peterson fragmentation function is:

$$D_c^{\text{peterson}}(z_P) \propto \frac{1}{z_P}\frac{1}{(1-\frac{1}{z_P}-\frac{\epsilon}{1-z_P})^2}$$

Where $z_P = \frac{p_L}{p_L^{\max}}$ in which p_L is the longitudinal momentum of the heavy quark meson (in this analysis the D^*) and $p_L^{\max}$ is the longitudinal momentum of the heavy quark (in this analysis the charm quark). The Peterson fragmentation function has only one free parameter, ϵ, which is determined by fitting to data. The world average measured value of $\epsilon = 0.035$ which is the value used in this thesis. In practice when measuring the effects of Peterson fragmentation, z_L is ratio of D^* momentum to the momentum of the charm jet. This approach is valid in the high energy, small θ limit where θ is the deviation the D^* makes from the charm momentum (as shown in figure 2.7).

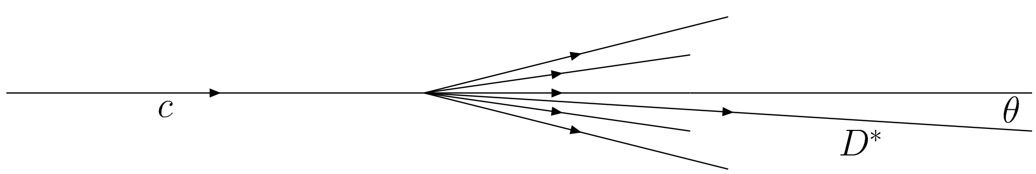

Figure 2.7: The fragmentation of a charm quark into a jet containing a D^* which deviates from the direction of the charm quark by small angle θ.

2.5.3 Other Fragmentation Functions

There exist many other fragmentation functions such as Collins [21] and Spiller [22] which are not considered in this thesis. Collins belongs to a class of time-reversal odd fragmentation functions. Spiller demands that the fragmentation function should be related to the hadronic structure function and so is consistent with reciprocity. However Peterson remains the most consistently used fragmentation function in heavy flavour physics and describes the data well enough to be implemented as the principal model here.

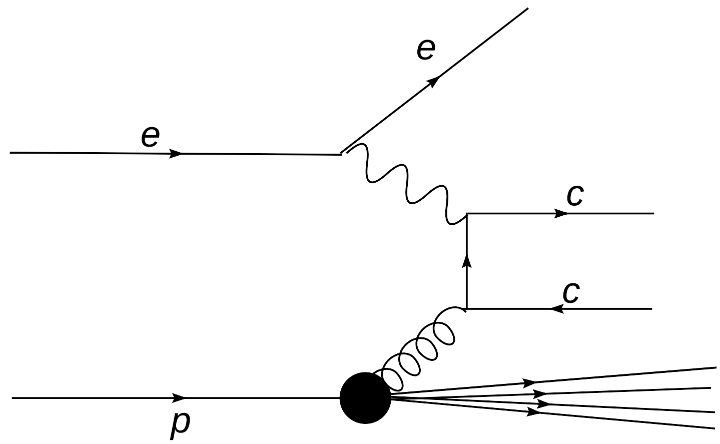

Figure 2.8: Illustration of the Boson Gluon Fusion production mechanism for charm. A gluon within the proton splits into a pair of gluons, one of which is absorbed by the virtual exchange boson.

2.6 Production of Charm at High Energies

During a deep inelastic scatter a gluon will sometimes split into a pair of quarks with large transverse momenta, one of which is absorbed by the virtual exchange boson as illustrated in figure 2.8. This process, which causes two jets to be observed in the final state, is called Boson Gluon Fusion (BGF) [4]. BGF is by far the dominant source of charm production at high energies.

This corresponds to the subprocess

$$\gamma^*(\mathbf{q}) + g(\mathbf{k}_2) \to \bar{q}(\mathbf{p}_3) + q(\mathbf{p}_4) + X$$

The lepton differential cross section for charm production via BGF is written

$$\sigma^{(e)} = \frac{\alpha}{\pi}\frac{dQ^2}{Q^2}\frac{dy}{y}\Theta(Q^2 - \frac{y^2m^2}{1-y})\left[(1-y)\sigma_2\left(\frac{\rho}{y}, \frac{Q^2}{M_c^2}; \frac{M_c^2}{Q_0^2}\right) + \frac{1}{2}y^2\sigma_1\left(\frac{\rho}{y}, \frac{Q^2}{M_c^2}; \frac{M_c^2}{Q_0^2}\right)\right]$$

where m is the lepton mass, M_c is the mass of the charm quark and σ_1 and σ_2 are related (in the limit of $M_c \to 0$) to the DIS structure functions by the relations;

$$\sigma_1 = \frac{4\pi\alpha}{Q^2}2x_B F_1, \quad \sigma_2 = \frac{4\pi^2\alpha}{Q^2}F_2$$

where Q^2, s, y and x are as defined in section 2.1 and

$$\rho = \frac{4M_c^2}{s}$$

The lepton differential cross section is dominated by σ_2 in the y range considered in this thesis. At leading order it has the explicit form:

$$4M_c^2\sigma_2(\rho, Q^2/M_c^2) = 2\pi\alpha e_q^2\Theta(\tfrac{1}{\rho} - 1 - \tfrac{Q^2}{4M_c^2})\rho\beta' \cdot$$
$$\left|\left[(1+\rho-\tfrac{1}{2}\rho^2)\mathcal{L}(\beta') - 1 - \rho\right] + [8+\rho-(2+3\rho)\mathcal{L}(\beta')]\tfrac{\rho Q^2}{4M_c^2} + [-8+2\mathcal{L}(\beta')]\left(\tfrac{\rho Q^2}{4M_c^2}\right)^2\right|$$

consisting of a second order polynomial in $\frac{\rho Q^2}{4M_c^2}$, the bremsstrahlung function $\mathcal{L}(\beta') = \frac{1}{\beta'}\ln\frac{1+\beta'}{1-\beta'}$ and a step function Θ for which

$$\Theta(x) = \begin{cases} 1 & (x > 0) \\ 0 & (x < 0) \end{cases}$$

which reduces the expression to 0 at $Q^2 = s - (2M_c)^2$ corresponding to the upper kinematic limit of the interaction [23]. σ_2 here is strongly suppressed by the mass of the created quark. Given that previous measurements of $\log(1/x_p)$ were made using an inclusive quark sample dominated by light flavours we expect the $\log(1/x_p)$ measurement in this analysis to be statistically poor. In addition we expect the lower Q^2 bound for heavy quark production to be raised since more energy must exist in the photon to first create a $c\bar{c}$ pair.

2.7 Scaled Momentum

One of the most important predictions of QCD was the phenomenon of scaling violations in structure functions which helped establish it as the theory of strong interactions. Scaling violations are also predicted in the fragmentation functions of quarks and gluons[24] which represents the likelihood that a quark or gluon parton fragments to form a hadron carrying a fraction x_p of the total parton momentum.

Studies of the scaled momentum spectra, $x_p = 2p/\sqrt{s}$, of final state hadrons have been made at experiments at LEP[25, 26] where p is the momentum of the final state hadron momentum and $\sqrt{s}$ is the centre of mass energy of the e^+e^- system. At LEP the two outgoing quarks also carry momentum $Q/2 \equiv \sqrt{s}/2$. In these measurements scaling violations were observed in the single parton density distribution, $\frac{1}{\sigma_{tot}}\frac{d\sigma}{dx_p}$.

Inclusive DIS measurements at HERA I have successfully confirmed the scaling results seen at LEP [27]. The HERA I measurements were made in the current region of the Breit frame where, in the QPM model interpretation, the outgoing struck quark carries momentum $Q/2$. The HERA I sample was statistically rich and was dominated by light flavoured quarks. This thesis will use the D^* decay channel to isolate and measure the charm contribution to the scaled momenta spectrum.

2.7.1 Scaled Momenta in the Breit Frame

The Breit frame [28] attempts to isolate the struck quark from the proton remnant so that the clearest separation can be made in the study of single particle distributions. This frame is obtained by transforming the exchange boson into a completely space-like 4-vector $\mathbf{q} = (0, 0, 0, -Q)$ that is aligned along the negative z axis. In this way if an electron of 4-momentum $(q_0, \overrightarrow{q})$ scatters off of a proton of 4-momentum $(P_0, \overrightarrow{P})$ in the lab frame, the Breit frame of this interaction will move with relative velocity $\overrightarrow{\beta} = (\overrightarrow{q} + 2x\overrightarrow{P})/(q_0 + 2xP_0)$.

The exchange boson provides a natural axis to this frame which is analogous to an e^+e^- collision in the center of mass (CMS) frame. All particles for which $p_z > 0$ fall by definition into the "target" region. This region is poorly understood and contains the proton remnant which evolves with $p_z = (1 - x)Q/2x$. The "current" region is populated with particles of $p_z < 0$; if the kinematics are suitable and the struck quark evolves in this region it does so with $p_z = Q/2$. There is a strong resemblance between the hemisphere of an e^+e^- interaction and the current region of a DIS scatter in the Breit frame; this normally allows for comparisons to be drawn between LEP measurements and those made at HERA although there is residual interference between current and target regions which will always remain [29]. However, in this analysis the dominant source of charm production is BGF which is not present in e^+e^- collisions and so no direct comparison of measurements will be drawn.

Final state quarks are produced either through Boson Gluon Fusion (BGF) or via QCD Compton (QCDC) as illustrated in figure 2.9. BGF is the process by which a gluon splits into two quarks with large transverse momenta, one of which is absorbed by the virtual exchange boson. QCDC is the other possibility whereby the quark emits a hard gluon before the virtual photon is absorbed. Charm production is completely dominated by the BGF process. These production subprocesses can be described in terms of a number of parameters analogous to the Lorentz invariant parameters used to describe a DIS scatter. One of these is the jet

LO scatter (Lab)	Production sub-process
$x = \frac{Q^2}{W^2+Q^2-m_p^2}$	$x/\xi = \frac{Q^2}{Q^2+\hat{s}}$
$y = \frac{1}{2}(1-\cos\theta^*_{eq})$	$z_p = \frac{1}{2}(1-\cos\theta^*_{\gamma g})$

Table 2.2: The analogous variables in a leading order scatter and the quark production subprocess. $\cos\theta^*_{\gamma g}$ is the angle between the gluon and the struck quark in the gluon quark centre of mass system. θ^*_{eq} is the angle between the initial and scattered electron in the eq centre of mass frame. $\sqrt{\hat{s}}$ is the invariant mass of the two jet system.

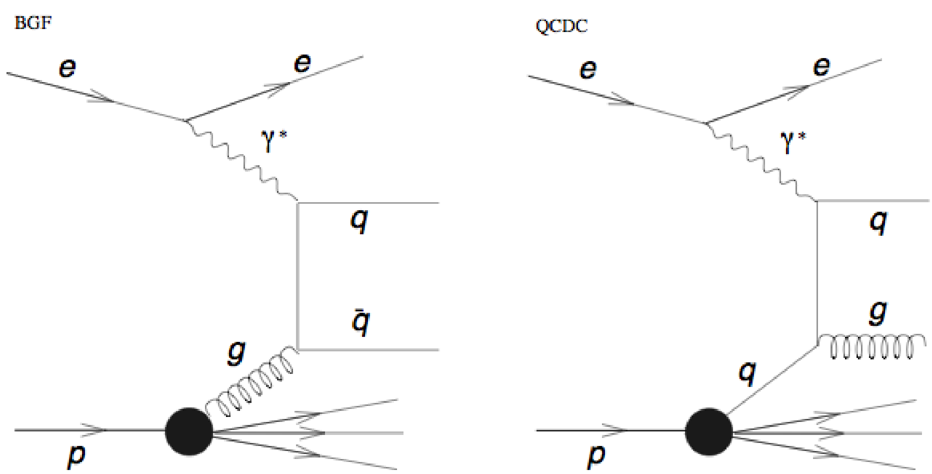

Figure 2.9: Feynman diagrams for BGF (left) and QCDC scattering (right).

scaling variable

$$z_p = \frac{\mathbf{P}\cdot\mathbf{p}_{\text{jet}}}{\mathbf{P}\cdot\mathbf{q}} = \frac{1}{2}(1-\cos\theta^*_{\text{jet}})$$

in the $\gamma^* g$ centre of mass system where θ^*_{jet} is the polar angle of the jet. The other is the event variable

$$x/\xi = \frac{Q^2}{2\mathbf{p}\cdot\mathbf{q}} \approx \frac{Q^2}{Q^2+\hat{s}}$$

where $\sqrt{\hat{s}}$ is the invariant mass of the dual jet system. Table 2.2 details the analogous terms used to describe DIS scattering and the quark production sub process.

The cross sections for both of these subprocesses are of the form

$$d\sigma^{BGF} \propto \frac{1}{z_p(1-z_p)} \quad \text{and} \quad d\sigma^{QCDC} \propto \frac{1}{(1-x/\xi)(1-z_p)}$$

where the singularities at $z_p = 0$ and $z_p = 1$ correspond to the emission of collinear partons. The QCDC $1/(1-x/\xi)$ singularity arises because this production mechanism favours a small jet-jet invariant mass as illustrated in figure 2.10 which gives the most probable topology. These events favour a topology where both jets are found in the current region of the Breit frame. This is not the dominant source of charm production and plays little role in the physics studied in this thesis.

The heavier final state partons are produced via BGF and may possess large transverse momentum. This gives rise to probable event topologies whereby neither of the final quarks populate the current region at relatively low Q^2 (figure 2.11). At moderate Q^2 the generated quarks tend to populate both regions equally whereas at higher Q^2 the tendency is for both heavy quarks to evolve in the current region. This is shown in figure 2.12 which illustrates the probable evolution for a range of Q^2. Because charm production is suppressed by the mass of the charm quark, and because the likely event topology favours production outwith the current region of the Breit frame it is expected that the measurement of $1/x_p$ for charm particles will be statistically limited.

2.8 Summary

This chapter gave a brief introduction to the basics of Deep Inelastic Scattering with emphasis on the Lorentz invariant variables used to characterise these events and the relationship between cross sections of quark production and structure functions. A discussion was then made on the evolution of the Quark Parton Model and the impact this had on the theory of structure functions. The basic principles of of DGLAP evolution, parton density functions and the nature of heavy quark production at ZEUS were then presented. An outline was given of Monte Carlo event generation and the different implementations of the hadronisation and fragmentation stages of quark jet production. The chapter concluded with a discussion of the feasibility of the measurement of scaled momenta distributions and their measurement in the Breit frame for charm production.

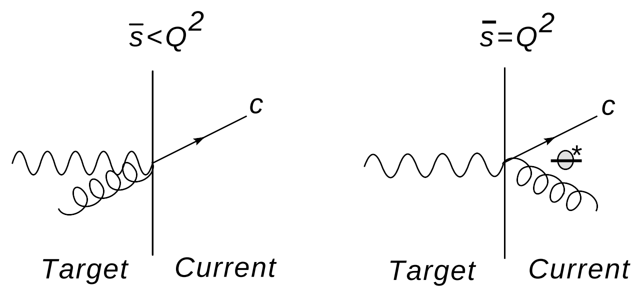

Figure 2.10: Possible event topologies for the QCD Compton production subprocess in the Breit frame.

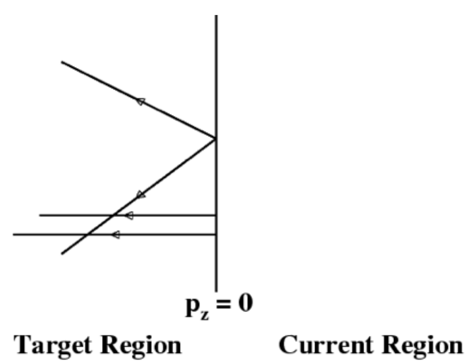

Figure 2.11: Typical low Q^2 topology for heavy quarks produced by BGF.

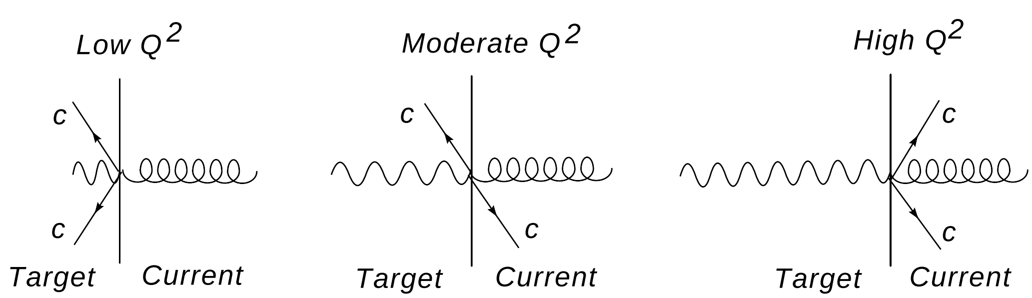

Figure 2.12: Probable BGF $c\bar{c}$ production subprocess in the Breit frame.

Chapter 3

HERA and ZEUS

In this chapter the design and operation of the ZEUS detector and associated Hadron-Electron Ring Accelerator (HERA) electron-proton accelerator is described.

HERA operation began in 1991 with significant data taking in May 1992. Operation ran until 2000 delivering a total of 120pb^{-1} of data to the ZEUS and H1 experiments located around the HERA ring. At this time HERA was closed for one year so that upgrades could be performed to increase the luminosity and proton beam energy. To exploit the higher luminosities and maximise the physics gain ZEUS itself was also upgraded. This upgrade took the form of the installation of a silicon microvertex detector and a straw tube tracker.

HERA II operation began in summer 2001 and has now delivered twice as much luminosity as HERA I of which 162 pb^{-1} is used in this analysis. Operation is expected to continue until summer 2007 when the experiment will be shut down and the pre-accelerator the Positron-Electron Tandem Ring Accelerator (PETRA) will be used as a source of synchrotron radiation.

This chapter will outline the operation of the HERA machine and describe the components of the ZEUS detector most relevant to this thesis.

3.1 The HERA Machine

The construction of the HERA machine was a significant landmark in the field of high energy physics; it was the first and only electron-proton colliding-beam accelerator in the world.

Figure 3.1: Aerial view of the area surrounding the DESY lab showing the path of the HERA ring.

It was constructed in a tunnel of circumference 6.3 km 20 meters below the earth on the grounds of the research center Deutches Electronen Synchrotron (DESY) in Hamburg and the surrounding area, tracing the path mapped out in figure 3.1. The project began in May 1984 and was completed after 79 months in November 1990. The entire construction cost 516 million Euro and was the result of a collaboration between eleven countries.

The protons used in the eP collisions are derived from hydrogen gas (H_2 molecules) which are split into single hydrogen atoms and supplied with an additional electron to produce H^- ions. These ions are accelerated to an energy of 0.75 GeV and are injected into the proton LINAC whose position in the HERA scheme is shown in figure 3.2. The LINAC raises the ion energy to 50 MeV. At the end of LINAC the ions are fired through a thin aluminum foil which strips off the outer electrons to leave only protons. The protons are then fed into DESY III which ramps their energy up to 7.5 GeV. Upon reaching this energy the protons are transferred to PETRA II where they are accelerated to 40 GeV and stored for injection

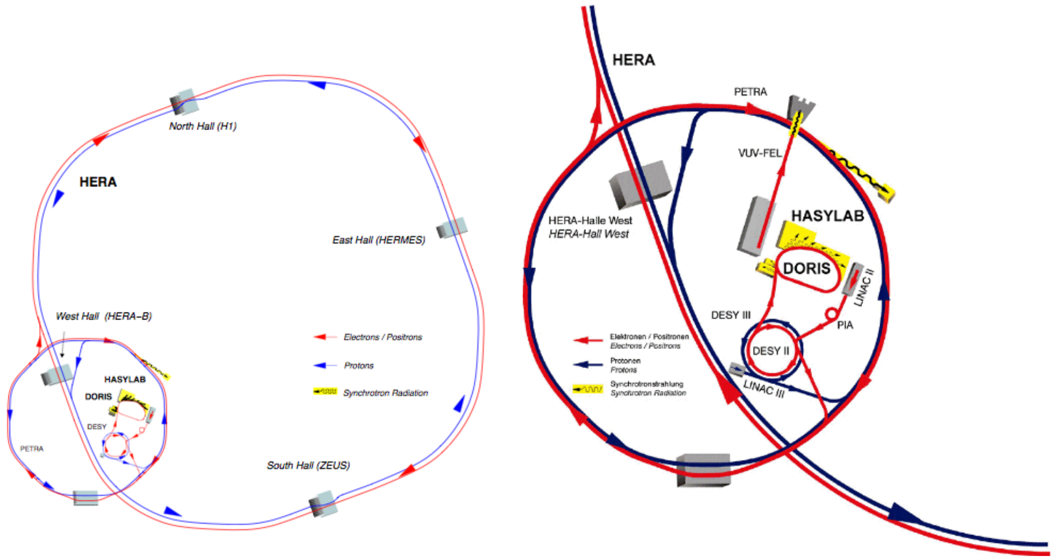

Figure 3.2: HERA (left) and a close up of the associated pre-accelerators (right).

into HERA. Finally they are directed into HERA where they reach a final energy of 920 GeV. An overview of the pre-accelerator stages and their position in the HERA ring is given in figure 3.2.

In the first stages of electron acceleration they are ramped up to 200 MeV in the LINAC and moved into DESY II where they are further accelerated to 7.5 GeV. Following this they are transferred to the PETRA ring and their energy is ramped up to 14 GeV before the ultimate injection into HERA where they reach a final energy of 27.5 GeV.

Once inside the HERA ring the proton's path is guided by superconducting dipole and quadrupole magnets and accelerated using non-superconducting radio frequency cavities. By contrast the electrons are guided using non-superconducting magnets and accelerated using superconducting radio frequency cavities.

During a normal orbit of the HERA ring the electrons and protons are kept separate in their own vacuum pipes. However they are required to meet once they arrive at each of the detectors. At this stage guiding magnets are used to lower the proton into the electrons' vacuum pipe such that they collide with zero crossing angle. This interaction does not occur in one continuous stream, rather each beam contains bunches of electrons and protons which are separated by a distance of 29m. There can be a maximum of 220 bunches stored in

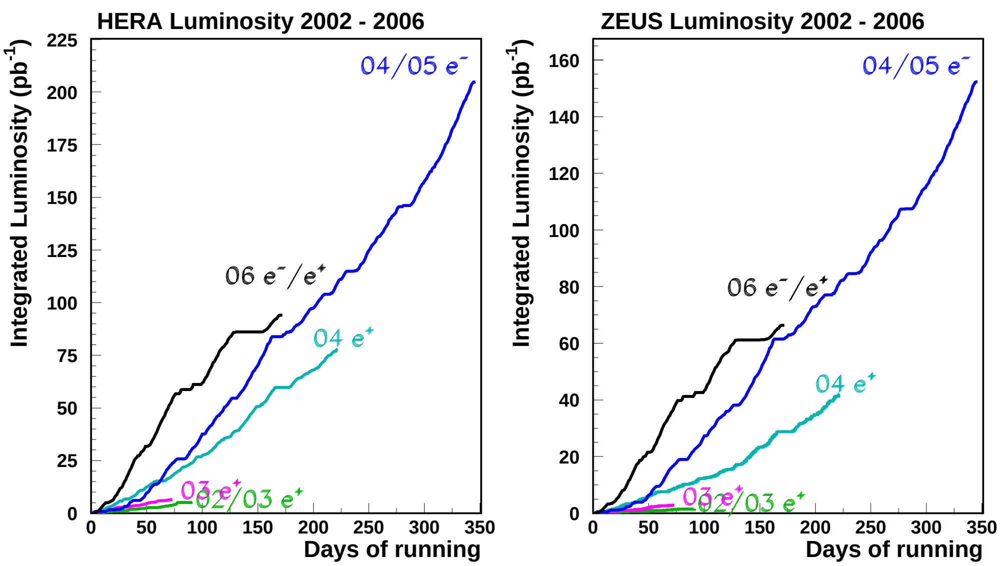

Figure 3.3: HERA luminosity delivered (left) and the luminosity gated by ZEUS (right).

HERA, with each crossing occurring once every 96ns. After passing through the interaction point the proton beam is raised out of the path of the electron beam and the orbit around the ring continues as before.

Such stable orbits may typically be preserved for between 8 hours for electrons and 1 day for protons. Throughout this time many collisions occur and a great deal of data may be collected by the ZEUS and H1 detectors. At the time of writing around 250 pb^{-1} of data has been gated by ZEUS as shown by figure 3.3, of which 162 pb^{-1} had been used in this analysis.

3.2 ZEUS

The ZEUS detector, one of two eP collision detectors positioned along the HERA ring, is located 30 meters underground and weighs approximately 3600 tons. The primary components of ZEUS include a tracking detector close to the interaction point surrounded by a calorimeter which is itself encased in a muon chamber. The ZEUS detector is shown in figure 3.4 with the upgraded parts highlighted; an invitation is given to study its design in greater detail than will be given here [31]. This section of the detector chapter will outline the principle features of the ZEUS components most relevant to this thesis.

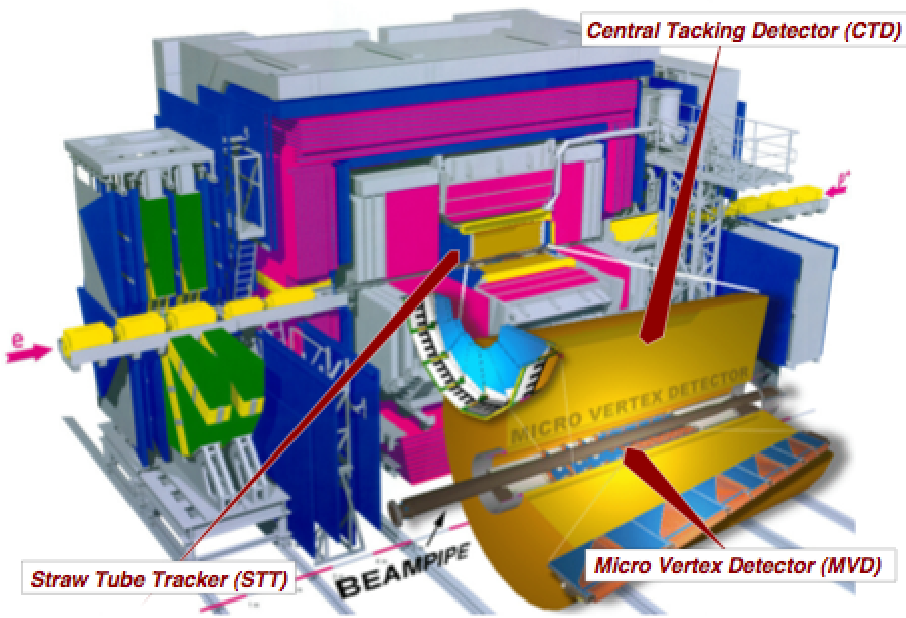

Figure 3.4: The ZEUS detector with the CTD, MVD and STT tracking components shown in expanded views.

3.2.1 The Central Tracking Detector

The ZEUS detector reconstructs the final state of particles by identifying tracks and vertices, and by measuring momentum and the loss of energy per unit distance (dE/dx). It is important therefore that any tracking detector has good spatial and momentum resolution with a wide angular acceptance and short drift time. The ZEUS Central Tracking Detector (CTD) meets these specifications by using small individual cells which separate close tracks.

The CTD is a cylindrical drift chamber with 72 layers of sense wires organised in 9 superlayers operating in a magnetic field of 1.43 T [32, 33]. The chamber itself is filled with a mixture of argon (to provide good gain at low voltages), CO_2 (to reduce electron drift velocity and provide better spatial resolution) and ethane (a quencher to enable the CTD to operate at a higher voltage). Its angular coverage is very broad, spanning the polar-angle region $15^0 < \theta < 164^0$. The transverse-momentum resolution for a track extending the full length of the CTD is $\sigma(p_T)/p_T = 0.0058p_T \oplus 0.0065 \oplus 0.0014/p_t$.

In total the CTD consists of 600 drift cells, 5000 sense wires and 20000 field wires. The

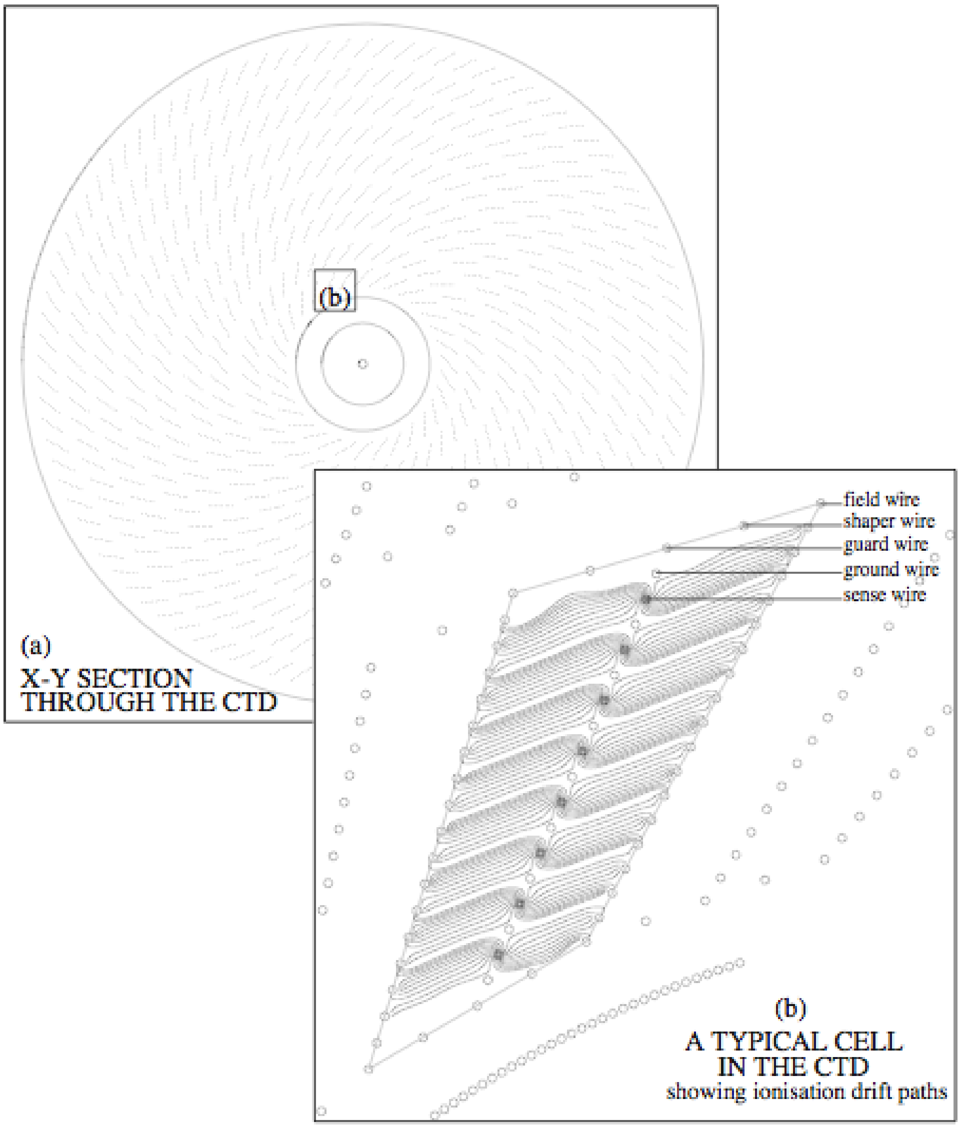

Figure 3.5: The $x - y$ section view through the CTD (background) with an exploded view of a typical drift cell (foreground). Field lines are drawn.

wires in the CTD are organised into 576 drift cells as shown in figure 3.5. Each cell contains 8 sense wires and 34 field wires. The field, ground and shaper wires combine to provide a uniform field leading towards the sense wires.

Charged particles which traverse the chamber ionise the gas atoms and create electrons which drift towards these sense wires and generate a pulse. This pulse is proportional to the lost energy of the initial ionising particle and in this way the average energy loss per unit length (dE/dx) can be measured. Care must be taken to ensure that dE/dx has been calibrated to account for variations in gas pressure and gain as well as the track angle. To maintain an accurate calibration CTD data quality management is undertaken on a run by run basis. Particle identification is not used in this analysis.

The calibrated dE/dx value when plotted against the momentum of the track forms a band corresponding to the Bethe-Bloch prediction in figure 3.6 for a sample of negative tracks. This figure shows excellent agreement between the Bethe-Bloch prediction and the measured bands for the π^-, K^- and $\bar{p}$ particles. In this way it is possible to identify particles using the dE/dx measurement for certain momentum ranges.

An octant of the CTD can be seen in figure 3.7 in which the 9 superlayers are identified. The wires in odd numbered super layers extend parallel to the beampipe and are called axial superlayers. The first three axial layers are equipped with an additional z-by-timing readout which transmits an approximate z position of the hit using the difference in pulse arrival time at the ends of the wire. Some parameters of the CTD are given in table 3.1. Wires in even numbered superlayers are inclined at a stereo angle of 5^0 and are used to reconstruct the z position of the track more precisely than the z-by-timing method. This enables a better track fit at the event reconstruction stage. The segments used to reconstruct a complete track are also identified in this figure along with their corresponding ghost segments. These ghost segments are rejected at a reconstruction level by identifying which of the two points away from the interaction point. The even numbered tracks which correspond to layers inclined at an angle are clearly offset.

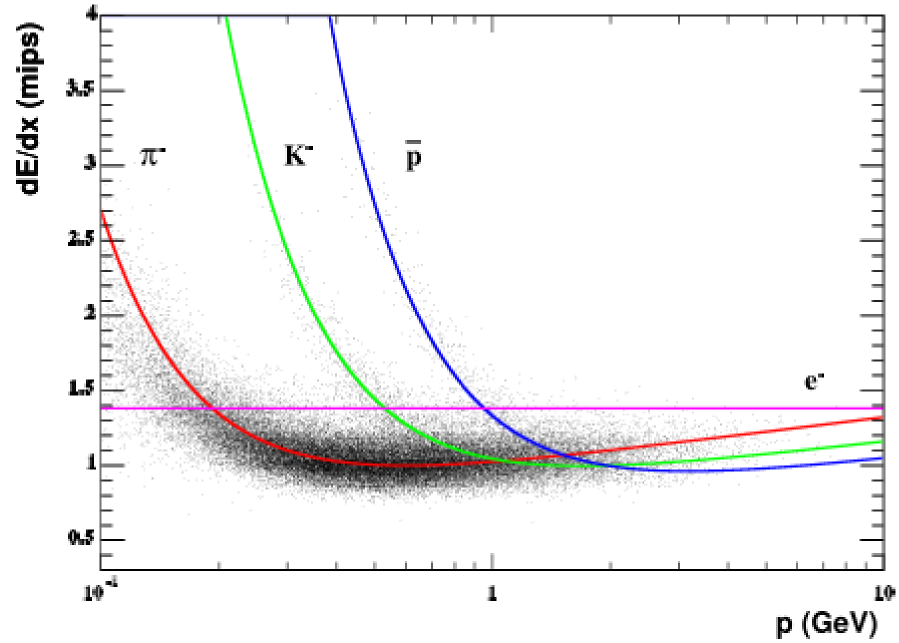

Figure 3.6: The measured dE/dx against momentum for negatively charged CTD tracks. The predictions for various particles are shown in coloured lines.

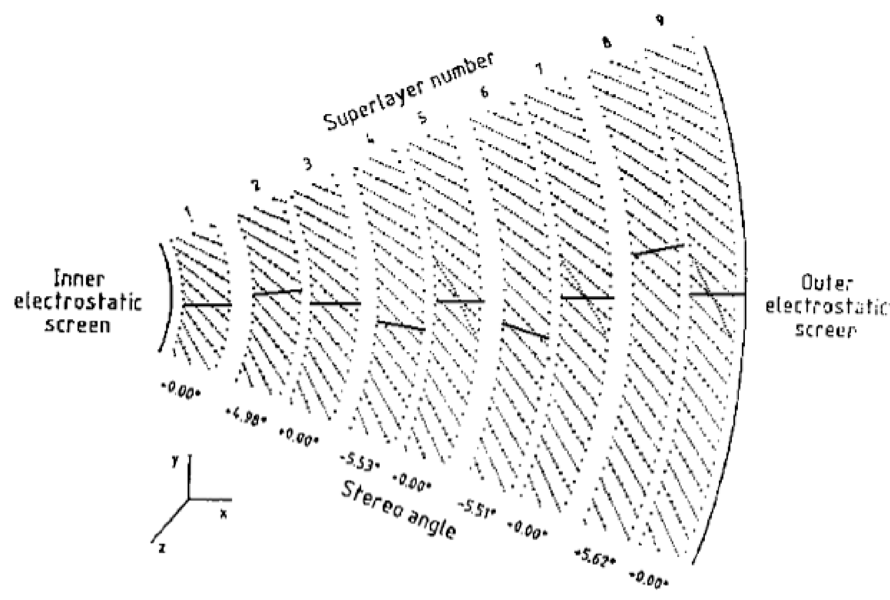

Figure 3.7: A CTD octant indicating the structure of the superlayers. Segments of reconstructed tracks are shown in bold lines.

Quantity	Resolution
$r - \phi$ hit resolution	180 μm
z resolution (stereo)	2 mm
z resolution (timing)	< 4 cm

Table 3.1: CTD tracking resolutions in $r-\phi$ and z. Resolutions in z are given for the stereo and z-by-timing methods.

3.2.2 The Uranium Calorimeter

Over 99.6% of the solid angle around the interaction region is enclosed by the ZEUS uranium calorimeter (CAL). The CAL uses interleaved plates of depleted uranium as absorber and plastic scintillator as active material to halt all entering particles (bar the muon and neutrino) and measure their energy. It consists of the forward (FCAL), barrel (BCAL) and rear (RCAL) parts each of which is divided into an electromagnetic and hadronic calorimeter as indicated by the cross section in figure 3.8.

Each part of the CAL is divided transversely into towers and longitudinally into one electromagnetic section and either one or two hadronic sections for the RCAL or BCAL and FCAL pair respectively. Any energy leakage is absorbed by and measured with the Backing Calorimeter (BAC) which is constructed from iron plates and aluminum rods and is not directly relevant to this thesis.

Particles may be identified in the CAL by analysis of their energy signature as they traverse the calorimeter and interact with the uranium. During this process a cascade of secondary particles (often called a shower) is generated whose shape is dependent on the physics origins of the cascade process. Leptons interact using typically QED interactions like bremsstrahlung whereas the hadronic interaction is dominated by nuclear effects. As electrons traverse the CAL they radiate photons which split into e^+e^- pairs and cause a shower of particles in the detector. Hadronic particles have greater mass and their interaction is dominated by the nuclear force and so interact with the nuclei of the absorbing material.

It follows therefore that the shower shape and size is a characteristic of electrons (immediate shower), hadrons (later, broader shower) and muons (minimal interaction) and in this

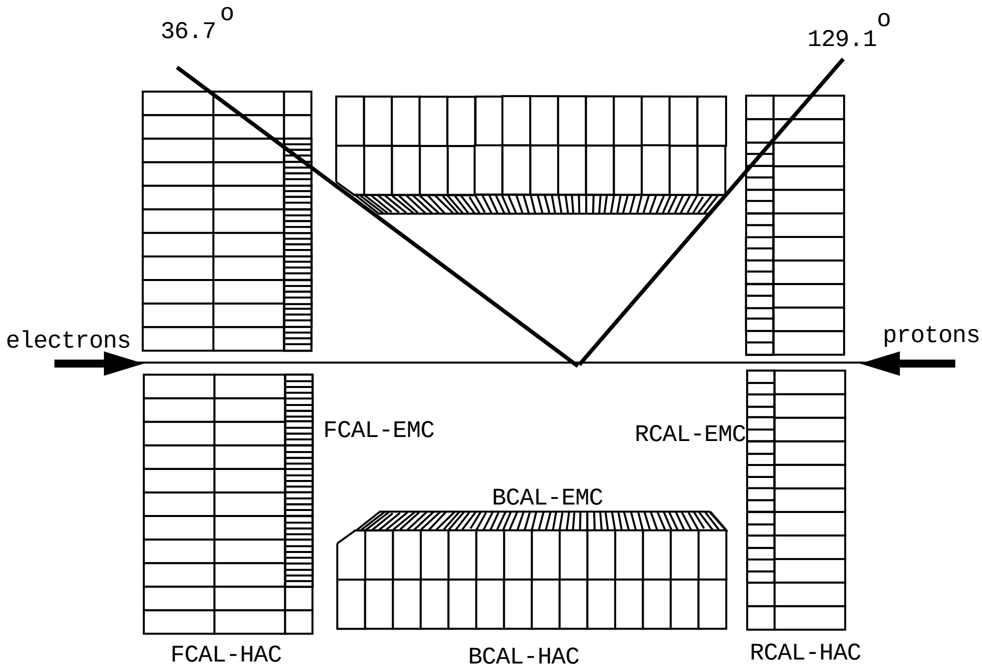

Figure 3.8: The components of the uranium calorimeter showing the barrel, forward and rear detectors.

way each type of particle can be easily identified at ZEUS. Typical shower profiles are shown in figure 3.9. Calibration is performed by measuring the uniform natural radioactivity of the depleted uranium in an extensive process [34] which will not be discussed here.

The smallest subdivision of the CAL is a cell. The electro-magnetic (EM) cells measure 5x20cm^2 in the FCAL and BCAL and are slightly larger in the RCAL measuring 10×20cm^2. Hadronic cells are always 20×20cm^2 regardless of which CAL part they are located in. FCAL and BCAL towers contain four EM and two hadronic cells whereas the RCAL contains only one larger EM and one hadronic cell. When particles are detected in a CAL cell the scintillation material produces light which is then read out from each cell and fed into a photomultiplier tube.

The dimensions of the scintillation and uranium layers were chosen such that the response (i.e. measured light output) of the CAL is equal for both hadrons and electrons. In other words a hadron and electron of equal energy will generate the same light output from the scintillators, in this way ZEUS is said to be a *compensating* calorimeter. Whilst the

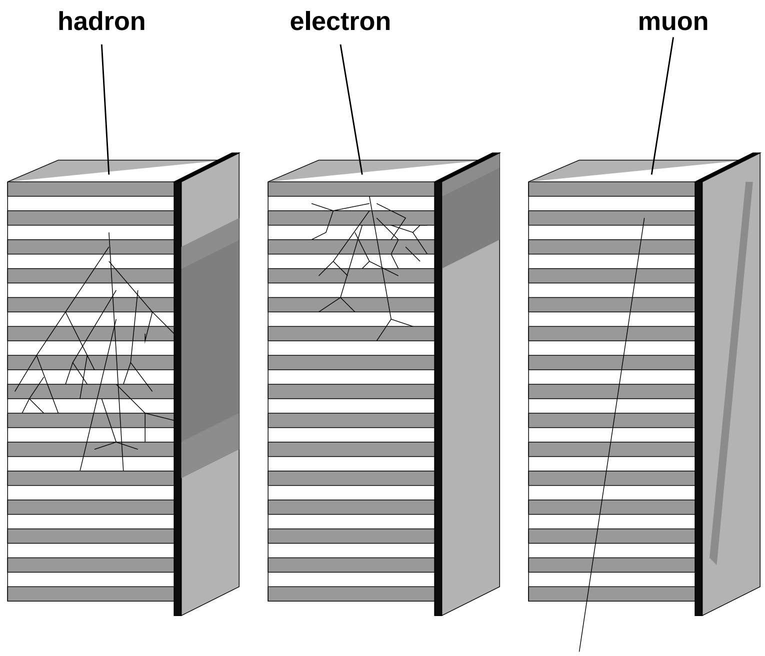

Figure 3.9: Typical shower profiles for hadrons, electrons and muons. Electrons shower earlier than hadrons in the CAL, and muons do not shower at all.

response is the same for electrons and hadrons the energy resolutions are known to differ by some degree. Under test beam conditions an energy resolution of $\sigma(E)/E = 0.18/\sqrt{E}$ was measured for electrons and $\sigma(E)/E = 0.35/\sqrt{E}$ for hadrons where the energy E is measured in GeV.

3.2.3 The Hadron Electron Separator

Accurate identification of leptons at HERA is crucial when attempting to differentiate between neutral and charged current events. When the electron is isolated the EM and Hadronic components of the CAL are sufficient in this identification process, however this is a much more troublesome feat when the electron is in the presence of hadronic jets. In such cases the hadronic background is many orders of magnitude above the signal from the lepton, and measurements from the CAL and CTD are insufficient and an additional device is required. The Hadron Electron Separator (HES) is a few layers of silicon diodes employed a few radiation lengths inside the EM sections of the CAL, one layer in the barrel and rear CAL, two layers in the forward. Hadrons and Electrons have very different shower signatures

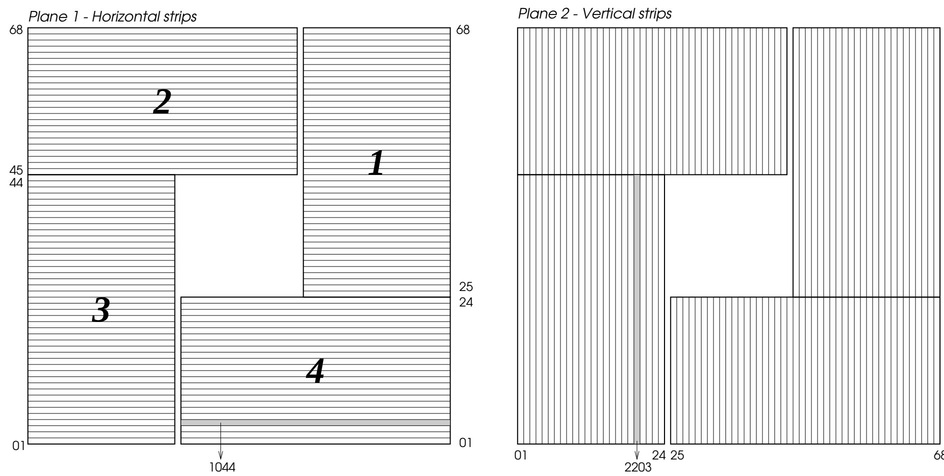

Figure 3.10: View of SRTD strips from the interaction point. The numbers of the horizontal strips are marked on the side of the diagram and the four quadrants are labeled 1 to 4.

in the CAL and generally speaking leptonic showers will start much earlier and will be less broad, as indicated in figure 3.9. The HES is installed at an optimal position to differentiate between these showers and identify electron candidates with the necessary efficiency [31].

3.2.4 The SRTD

The Small Rear Tracking Detector (SRTD) is a system of 2 orthogonal planes of scintillator strips attached to the face of the RCAL at $z = -148$ cm. Its strips are 1 cm wide by 0.5 cm thick spanning an area of 68×68 cm^2 from which information is extracted using a network of photo-multipliers and optical fibers. The SRTD boasts a resolution of around 3 mm, superior to that of the CAL (3 cm) and HES which were constructed with a much coarser segmentation.

This detector is often used to understand and correct for the dead material present in ZEUS which causes premature showering of the scattered electron. This may be accounted for by interaction with the beampipe, screws, cables and now in HERA II, the MVD. Corrections to the CAL energy for this effect must be made using the SRTD pre-showering information which is related to the energy loss of the particle. This energy loss is related to the number of interactions made, and hence the multiplicity of the emerging shower around the original particle as it traverses the dead material. It follows then that dense regions in the SRTD hit maps correspond to more dead material in the detector. The corrected energy is calculated in the following way:

$$E_{\mathrm{corr}} = E_{\mathrm{CAL}} + \alpha E_{\mathrm{SRTD}}$$

where E_{cal} and E_{SRTD} are the CAL and SRTD energies respectively and $\alpha = 0.039$ is a parameter extracted from MC studies.

The procedure for clustering the strips and reconstructing the energy, position and time of the hits is a 3 stage process. A cluster is defined to be a group of active strips separated by no more than 2 empty strips (a strip is empty if it has a noise below a defined background threshold). Since dead channels affect the estimate of the reconstructed energy, their activity is assumed to be the average of its neighbours (although this information is not stored in any data table). The horizontal and vertical strips must now be paired in what is a trivial procedure for quadrants with a single hit but increasingly complex for high multiplicity events. If several particles enter simultaneously the algorithm constructs a number of ghost hits which may only be resolved by matching total energy deposits. This ambiguity breaking is sensitive to low ($<$ 5 Minimum Ionising Particles) shower multiplicity due to fluctuations in photostatistics which swamp the signal. In these cases all combinations are stored and the points are flagged as 'ambiguous'. Once the showers have been identified, the position is extracted by first locating the strip corresponding to the shower maximum and then extracting the center of gravity position. The strip which contains the shower maximum is the one which maximises

$$\alpha E(N-1) + E(N) + \alpha E(N+1)$$

where $\alpha = 0.5$ and N is the number of the strip candidate. An energy weighted sum of 3 neighbouring strips is used because this procedure diminishes the effect of photostatistic fluctuations [35]. Chapter 4 in this thesis covers work done to align the CAL, HES and SRTD to improve track reconstruction.

3.2.5 The Micro Vertex Detector

The Micro Vertex Detector (MVD) is a very precise silicon tracking detector close to the interaction point. Its installation in 2001 during the upgrade shutdown was motivated by a desire to improve tracking and secondary vertex resolution. These upgrades were necessary to perform secondary vertex tagging of long lived particles and so select a pure charm sample.

Before the upgrade there was a separation of 16.2 cm between the beampipe and the innermost surface of the CTD. This made it very difficult to resolve track positions near the interaction point and a track separation of around 1 cm was required to make the distinction. Given that a typical decay length of a charmed particle is of the order 100-300μm this resolution is not sufficient. The separation between beampipe and detector was reduced to 6.2 cm by the introduction of the MVD.

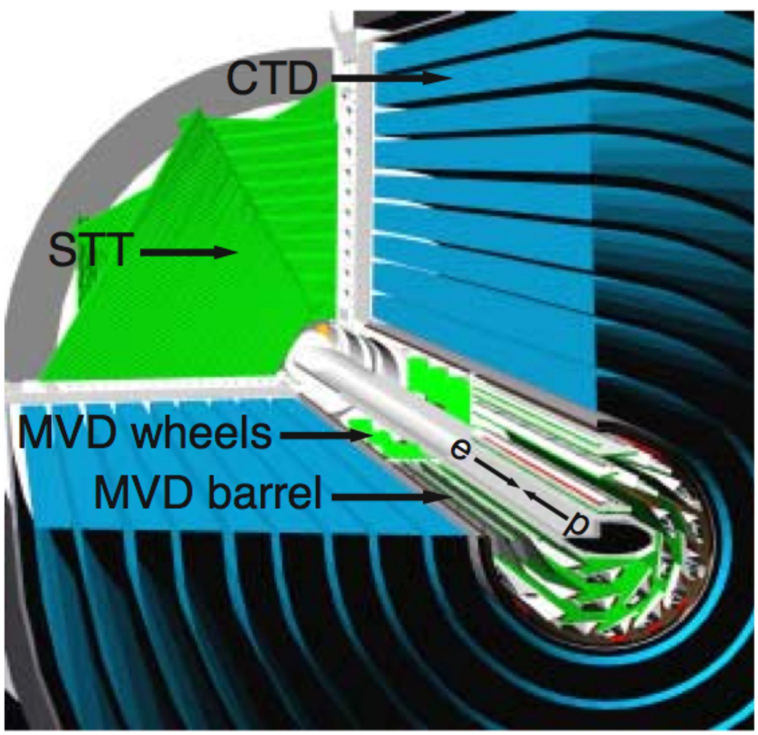

Figure 3.11: Cutaway of the ZEUS experiment showing the MVD, CTD and STT detectors.

The position of the MVD with respect to the CTD and STT is given in figure 3.11. This figure shows how the ladders in the barrel are oriented so that tracks will always pass through a minimum of 3 silicon layers. The elliptical shape of the beampipe had to be accommodated leading to a design which is anisotropic. In total the MVD contains 712 silicon strip sensors although these are distributed between the forward and barrel regions, covering a polar angle of $7^0 - 170^0$.

The intrinsic hit resolution of the MVD is between $20-30\mu$m whilst the spatial resolution of primary and secondary vertices is between $100 - 200\mu$m. In 2006 much work was done to precisely align the MVD to improve the tracking near the interaction point and improve on the previous alignment which was performed using cosmic ray muon events. The new alignment study used eP events to provide coverage in all regions of the MVD and not just the central region populated by cosmic tracks. These studies reduced the alignment accuracy from 50μm to 25μm using an approach based on the measurement of residuals; a residual in this case being the distance between the real MVD hit measurement and the expected measurement from the track parameters.

3.3 Summary

In this chapter the HERA accelerator and important components of the ZEUS detector have been described. Although the HES and the SRTD are not used explicitly in the measurements work was done to align both of these components together and so their description was included. The MVD, CTD and CAL are all used in the measurements of hadronic charm which will be described in this thesis. Whilst the MVD is not *fully* exploited in this analysis it is however used in the tracking algorithm upon which all measurements rely. In the future the MVD will be used to measure impact parameters and improve the precision to which heavy quarks may be measured.

Chapter 4

Component Alignment

This chapter details the alignment of the CAL, CTD, SRTD and the HES. The basic alignment procedure of any two components is stated and the data and MC required for the alignment procedure are defined. The dead channels in (x, y) maps of scattered electron position for CAL, HES and SRTD are compared between both samples to ensure that they agree and are therefore suitable for this study. The alignment procedure will first be applied to the HES and all 4 quadrants of the SRTD and conclude they require corrections of 0.25 ± 0.05 cm in x and 0.10 ± 0.05 cm in y. The effect of these corrections on some DIS control plots will be studied and found to be negligible. The alignment of the CTD, HES and CAL will then be conducted and found to be unnecessary since the required shifts are below measurement errors.

4.1 Introduction

To produce a reliable simulation of the ZEUS detector it is imperative to know precise spatial information on all of its components relative to each other. If a component is found to be misaligned, or offset from the design position, corrections must be made in order for any event reconstruction to proceed in a meaningful way. When the data has been corrected the purity of the sample increases, as does the reliability of all measured quantities. Alignment studies are therefore the foundation of any successful measurement. Moreover in HERA I the hadronic energy was scaled by 0.97 and the scattered electron energy was scaled by 0.98

in MC to improve agreement with data. If it can be shown that any realignment affects neither the hadronic nor electron energies then the reapplication of these same scalings can be justified.

4.2 Method

The method outlined here broadly follows that used in the ZEUS 96-97 analysis [37], the basic premise of which is as follows; the HES and the four quadrants of the SRTD are aligned before the alignment of the HES to the CTD, the CAL is then aligned to the CTD and the alignment process is complete. This chain of alignments ensures that all components are aligned to the CTD upon which the ZEUS co-ordinate system is defined.

4.2.1 Basic Procedure

The components of a perfectly aligned detector would exist in the same spatial co-ordinates as those input into the MC simulator. One would expect therefore the physical separation between components to be the same in both MC and data. If this separation is found to be different then corrections are made to account for this. Given that high energy electrons may be easily reconstructed and follow a linear path they are a powerful tool in the alignment process. The energy deposits left by the electron are stored in (x, y) co-ordinates denoted in this chapter by $(x^{\mathrm{e}}_{\mathrm{SRTD}}, y^{\mathrm{e}}_{\mathrm{SRTD}})$ and $(x^{\mathrm{e}}_{\mathrm{HES}}, y^{\mathrm{e}}_{\mathrm{HES}})$ for the SRTD and HES positions respectively.

A well aligned detector would show good agreement between MC and data when $x^{\mathrm{e}}_{\mathrm{HES}} - x^{\mathrm{e}}_{\mathrm{SRTD}}$ and $y^{\mathrm{e}}_{\mathrm{HES}} - y^{\mathrm{e}}_{\mathrm{SRTD}}$ are histogrammed. Any discrepancy may be attributed to misalignment.

Before the subtraction may be carried out the physical distance between the HES and SRTD must be accounted for along with the initial vertex position. Figure 4.1 shows the (z, x) plane of an electron leaving a vertex at position $C = (z_v, x_v)$. The electron travels in a straight line, hits the SRTD at position $B = (-z_s, x_s)$ and proceeds to the HES, striking at $A = (-z_h, x_h)$. The subtraction in x-coordinates will not center around $x = 0$ because of the additional x distance traveled. To account for this effect a correction factor δ is added to the SRTD x position. δ is derived using similar triangles on ACD and ABE in figure 4.1

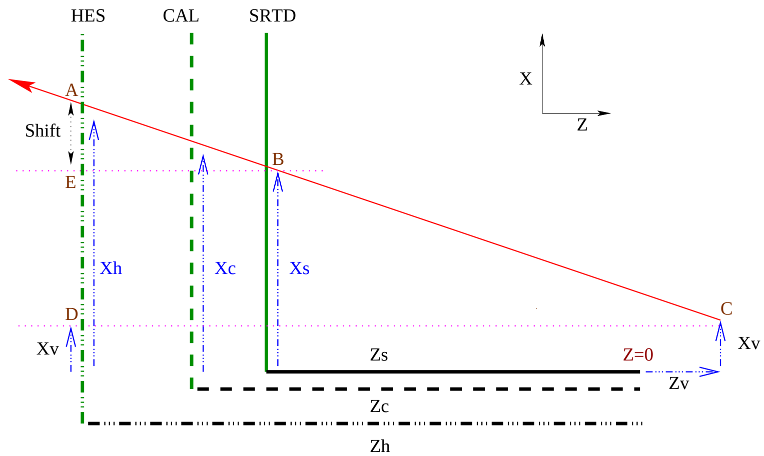

Figure 4.1: Illustration of the relative position of the CAL, HES and SRTD in the $z-x$ plane. An electron leaves from the vertex at C, passes through the SRTD at position B and hits the HES at A. The separation in z between the HES and the SRTD results in the quantity $x^{\mathrm{e}}_{\mathrm{HES}} - x^{\mathrm{e}}_{\mathrm{SRTD}}$ peaking at a non-zero value. To correct for this a quantity δ must be added to the HES electron position (A) which shifts it to a modified position (E) which is input into the subtraction. This quantity is calculated using similar triangles on (ACB) and (ADC).

to obtain (in x),

$$\delta = \frac{(x_h - x_v) \times (|z_h| - |z_s|)}{|z_h| + z_v}$$

such that $x^{\mathrm{e}}_{\mathrm{SRTD}} \to x^{\mathrm{e}}_{\mathrm{SRTD}} + \delta$ and subtractions between corresponding points on the SRTD and HES are now correctly centered about 0. The values used in the correction were $Z_{\mathrm{CAL}} = 153.03$ cm, $Z_{\mathrm{HES}} = 154.93$ cm and $Z_{\mathrm{SRTD}} = 148$ cm.

Figure 4.2 shows the $x_{\mathrm{HES}} - x_{\mathrm{SRTD}}$ and $y_{\mathrm{HES}} - y_{\mathrm{SRTD}}$ before the spatial difference has been corrected for. The peak of the distributions are offset from 0 by differing but significant degrees; in particular the X component of SRTD quadrant four is off by 1 cm. This is dramatically corrected as shown in figure 4.3 in which all distributions are very clearly shifted towards the center. The discrepancy between MC and data is minimal in the Y axis and is significant in X only in quadrants one and two.

Fits are applied to the MC and data samples as shown in figure 4.3 and the position of the peak is extracted and compared to the extracted peak position of the MC. The difference between the two is the correction factor to be applied. Both data and MC are extremely well described by their associated fits.

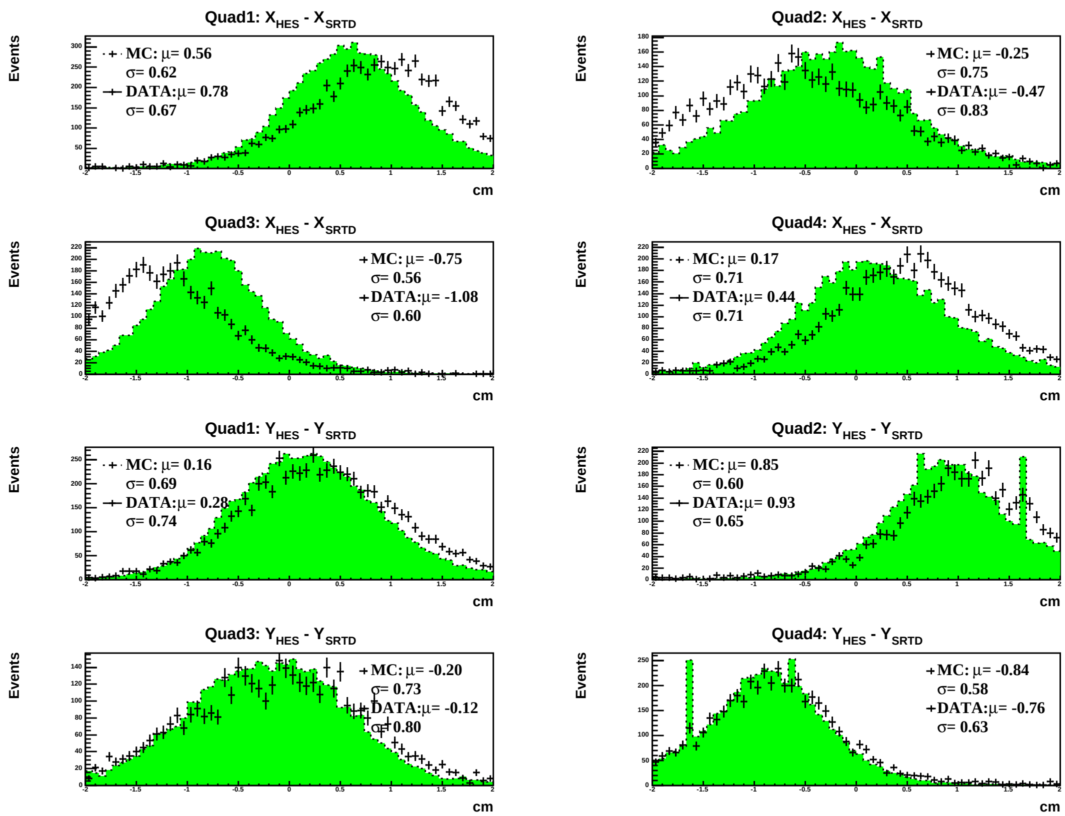

Figure 4.2: Difference between x (and y) co-ordinates of the scattered electron between the HES and the SRTD. The plots are not centered about zero since no correction has been made for the spatial difference between the two components. MC is shown in green and data is shown in points.

4.2.2 Brief investigation of structures in Δx distributions

Inspection of the Quad 2: $y_{\text{HES}} - y_{\text{SRTD}}$ distribution in figure 4.3 yields identification of a peak structure at about 0.8 cm. Similar structures also appear at regular intervals when the difference between y co-ordinates of the CAL and SRTD electron position is histogrammed as shown in figure 4.4. To investigate their origin, (x, y) maps of the electron hits on the SRTD and CAL components were filled only for events which contribute to these structures.

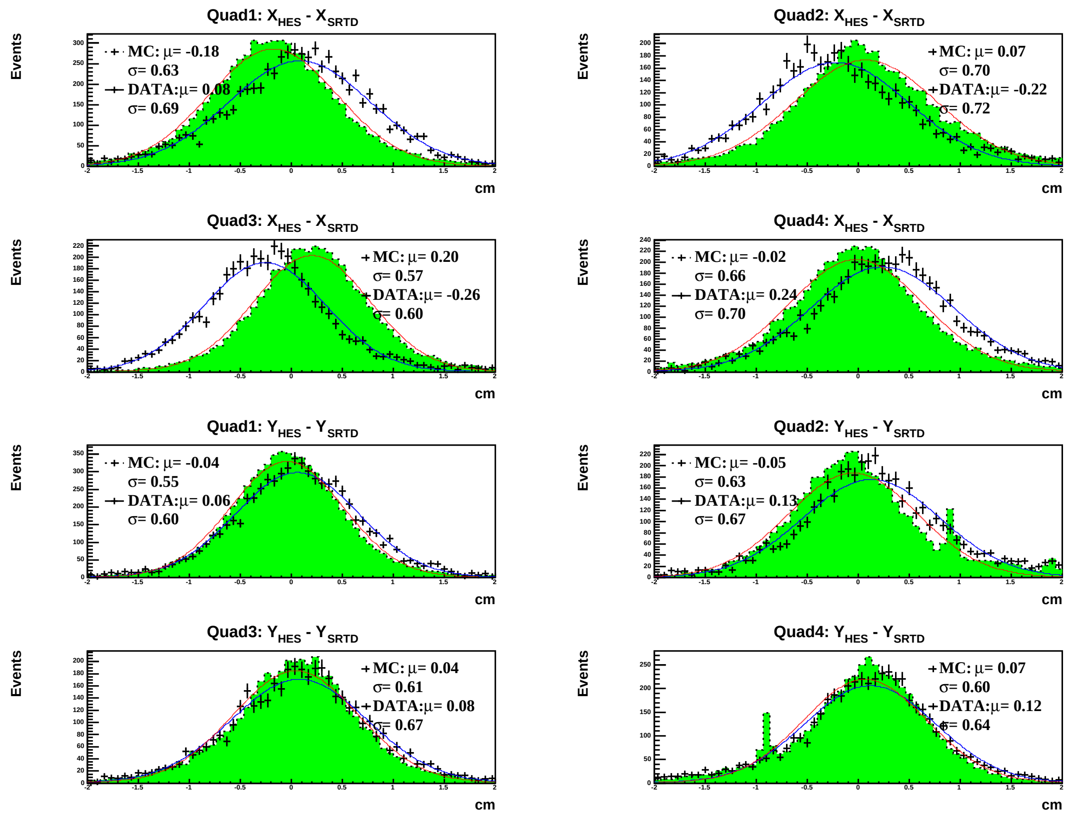

Figure 4.3: Difference between x (and y) co-ordinates of the scattered electron between the HES and the SRTD. Corrections for the separation between components and the vertex of the electron have been made. The fit on the data points is shown in blue and the fit on the green MC is shown in red. The width and mean extracted from the fits are also shown.

As shown in figures 4.5 and 4.6, the peaks are a result of hits near the beampipe. In this region the electron is detected correctly by the SRTD but not by the CAL which instead assigns the same y position repeatedly. This is an artifact of the CAL position algorithm which attempts to generate a center of energy position using neighbouring cells. For hits on the cells neighbouring the beampipe, the algorithm incorrectly models the distribution since no energy information exists on the side facing the beampipe. This has the effect of biasing the measurement but is understood and does not affect the procedure by which the alignment corrections are evaluated.

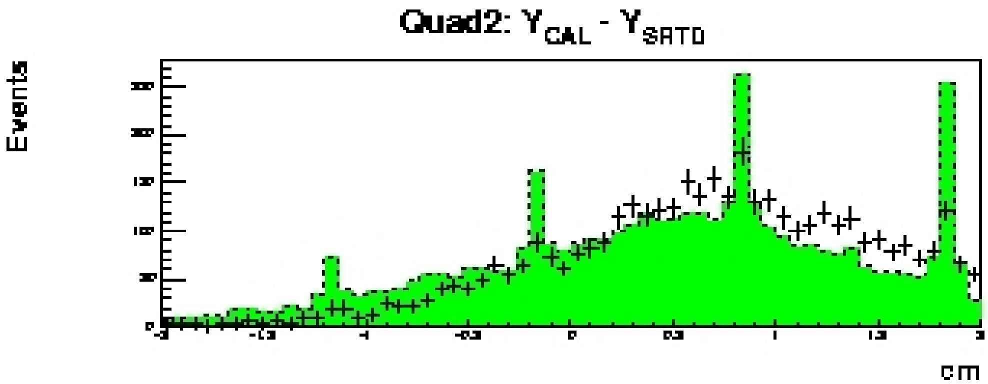

Figure 4.4: Difference in the y coordinate of the electron position as measured by the CAL and SRTD in quadrant 2 of the SRTD. The Data is shown in crosses and MC is shown in solid green. Structures appear at 1 cm intervals in both MC and data.

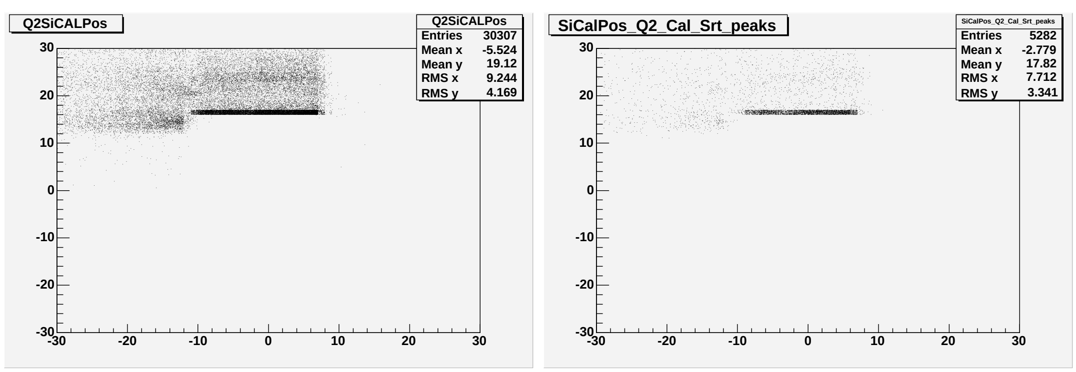

Figure 4.5: (x, y) map of the electrons which pass through quadrant 2 of the SRTD as measured by the CAL (left) and the same (x, y) map filled only for events contributing to the structures seen in figure 4.4. The x and y axes are measured in cm.

4.2.3 Data Selection

A 0.702 pb^{-1} subset of the June $'04$ - August $'04$ e^-P running period was used for this analysis alongside a 5.28pb^{-1} inclusive DIS Monte Carlo sample. This data range exhibits excellent trigger agreement with the MC in addition to dead channel agreement on the SRTD (figure 4.7), HES (figure 4.8) and CAL (figure 4.8) on maps of electron signals. The following standard DIS selection cuts were required:

- $5 < Q^2_{elec} < 1000$ GeV^2
- $0.02 < y_{JB}$
- $y_e < 0.95$
- $|z_{vtx}| < 30$ cm
- Electron Energy > 10 GeV.

where Q^2_{elec}, y_e and y_{JB} are DIS event kinematics as defined in Chapter 2. The e subscript denotes that the parameter has been reconstructed using the electron method whilst JB denotes a 'Jacquet-Blondel' reconstruction. Details of both methods are given in the same chapter. These selection cuts are designed to reduce background and to ensure that the scattered electron is easily identified and reconstructed.

4.3 Results

The fits shown in figure 4.3 are used to determine the correction factor that must be applied to data to ensure a consistent description of the detector in both event samples. The difference between this extracted peak is the correction factor to be applied to the data. The event reconstruction process draws on information stored in "gafs" which can be thought of as databases containing a list of calibration constants, including the spatial position of detector components. In MC everything is perfectly aligned already by design, therefore during reconstruction if the data is not in the position as assumed by the gafs incorrect conclusions may be drawn. Given that we know the SRTD measures the position incorrectly in data we

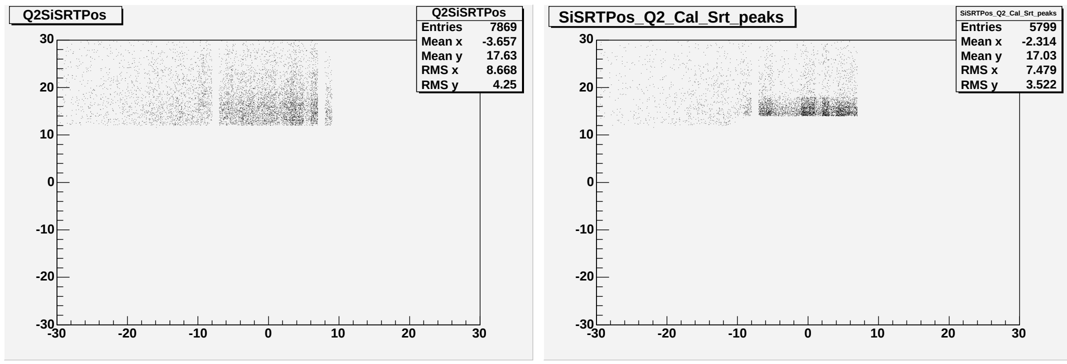

Figure 4.6: (x, y) map of the electrons which pass through quadrant 2 of the SRTD as measured by the SRTD (left) and the same (x, y) map filled only for events contributing to the structures seen in figure 4.4. The x and y axes are measured in cm.

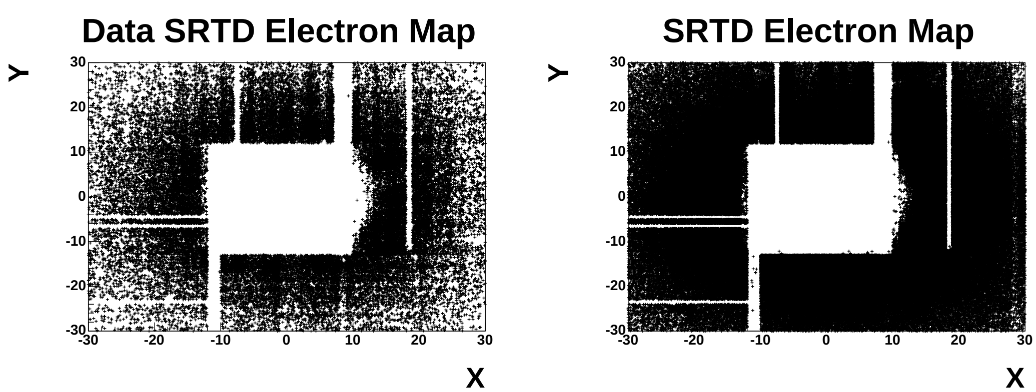

Figure 4.7: (x, y) map of all electron hits on the SRTD in the data (left) and MC (right) sample. The x and y axes are measured in cm.

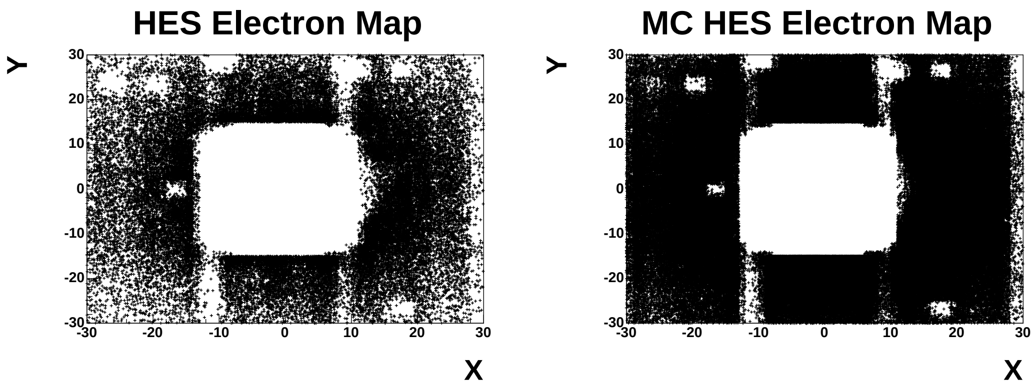

Figure 4.8: (x, y) map of all electron hits on the HES in the data (left) and MC (right) samples. The x and y axes are measured in cm.

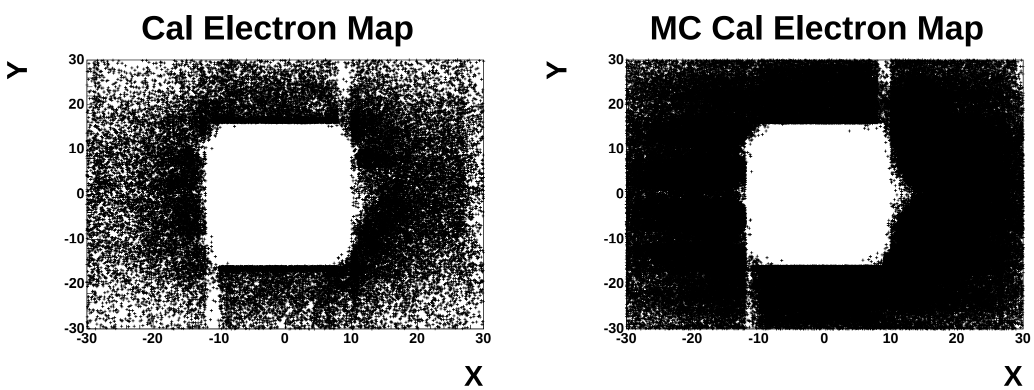

Figure 4.9: (x, y) map of all electron hits on the CAL in the data (left) and MC (right) sample. The x and y axes are measured in cm.

shift the measured position so that its correlation with the HES and CAL impact points is equivalent to that in MC. The shifts that have been evaluated and listed in the following sections are therefore applied to data rather than to the MC.

4.3.1 SRTD-HES Alignment

The gaussian distribution fit to the corrected $x^{\mathrm{e}}_{\mathrm{HES}} - x^{\mathrm{e}}_{\mathrm{SRTD}}$ and $y^{\mathrm{e}}_{\mathrm{HES}} - y^{\mathrm{e}}_{\mathrm{SRTD}}$ distributions in figure 4.3 peak at x_{MCPeak} and x_{dataPeak} (and the corresponding y value). The quantity $x_{\mathrm{dataPeak}} - x_{\mathrm{MCPeak}}$ is given in table 4.1. The systematic error of ± 0.05 cm comes from the biggest shift in the distributions.

Component	Quadrant 1	Quadrant 2	Quadrant 3	Quadrant 4
SRTD X	0.25 ± 0.05 cm	-0.29 ± 0.05 cm	-0.46 ± 0.05 cm	0.25 ± 0.05 cm
SRTD Y	0.10 ± 0.05 cm	0.18 ± 0.05 cm	-0.04 ± 0.05 cm	0.05 ± 0.05 cm

Table 4.1: Required SRTD shifts in x and y for each quadrant.

The $x^{\mathrm{e}}_{\mathrm{HES}} - x^{\mathrm{e}}_{\mathrm{SRTD}}$ and $y^{\mathrm{e}}_{\mathrm{HES}} - y^{\mathrm{e}}_{\mathrm{SRTD}}$ distributions in figure 4.3 are re-evaluated and the new distributions are shown in figure 4.10. The agreement between data and MC in this figure is now much more satisfactory since any difference is now negligible within the systematic measurement error of ± 0.05 cm.

To gauge the effect of the alignment the corrections to a number of DIS kinematic variables; y, Q^2, x and $\theta_{\mathrm{electron}}$ using the electron, double angle and JB reconstruction methods was measured. Control plots for these variables are shown before the alignment process in figure 4.11, the difference between data and MC after the alignment is given in figure 4.12.

The alignment procedure has had minimal effect on the agreement and by inspection of figure 4.12 it is seen that any shift in measurement is much smaller than any original discrepancy. In general corrections are not obvious to the naked eye.

The fractional shift of the MC control plot variables is shown in figure 4.13. The histogrammed parameter is

$$\frac{\mathrm{data}_{\mathrm{pre-alignment}} - \mathrm{data}_{\mathrm{post-alignment}} + \mathrm{MC}_{\mathrm{pre-alignment}}}{\mathrm{MC}_{\mathrm{pre-alignment}}}$$

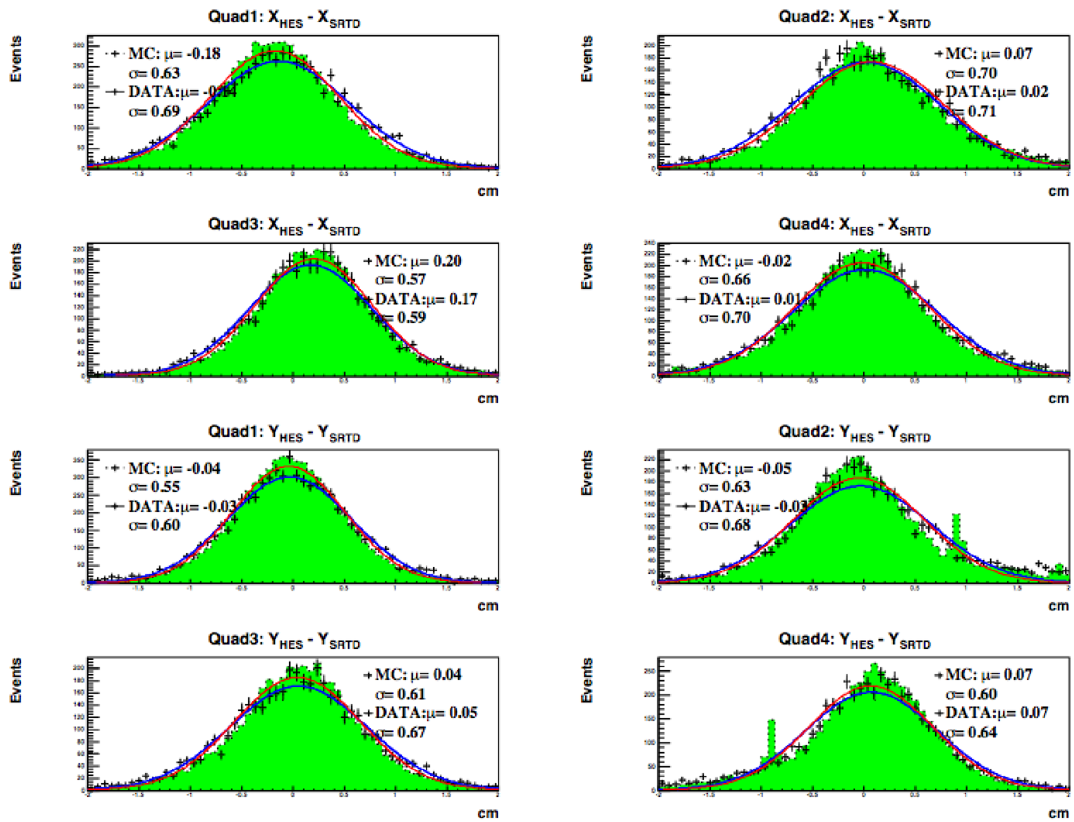

Figure 4.10: Difference in x (and y) co-ordinates of the scattered electron between the HES and the SRTD after alignment. Corrections for the separation between components and the vertex of the electron have been made. The fit on the data points is shown in blue and the fit on the green MC is shown in red. The width and mean extracted from the fits are also shown.

which gives an indication of the fractional correction made to the MC kinematic variables after the SRTD-HES alignment. All fractional shifts lie within the measurement errors and are therefore negligible. There exist a handful of exceptional points which suggest a non-negligible correction (the 7$^{\text{th}}$ bin of y_{DA} indicates a 1% shift and corrections as large of 4% in measurements of x_{electron} are observed in select bins regions) but in general any improvement in data reconstruction is not measurable in these control plots.

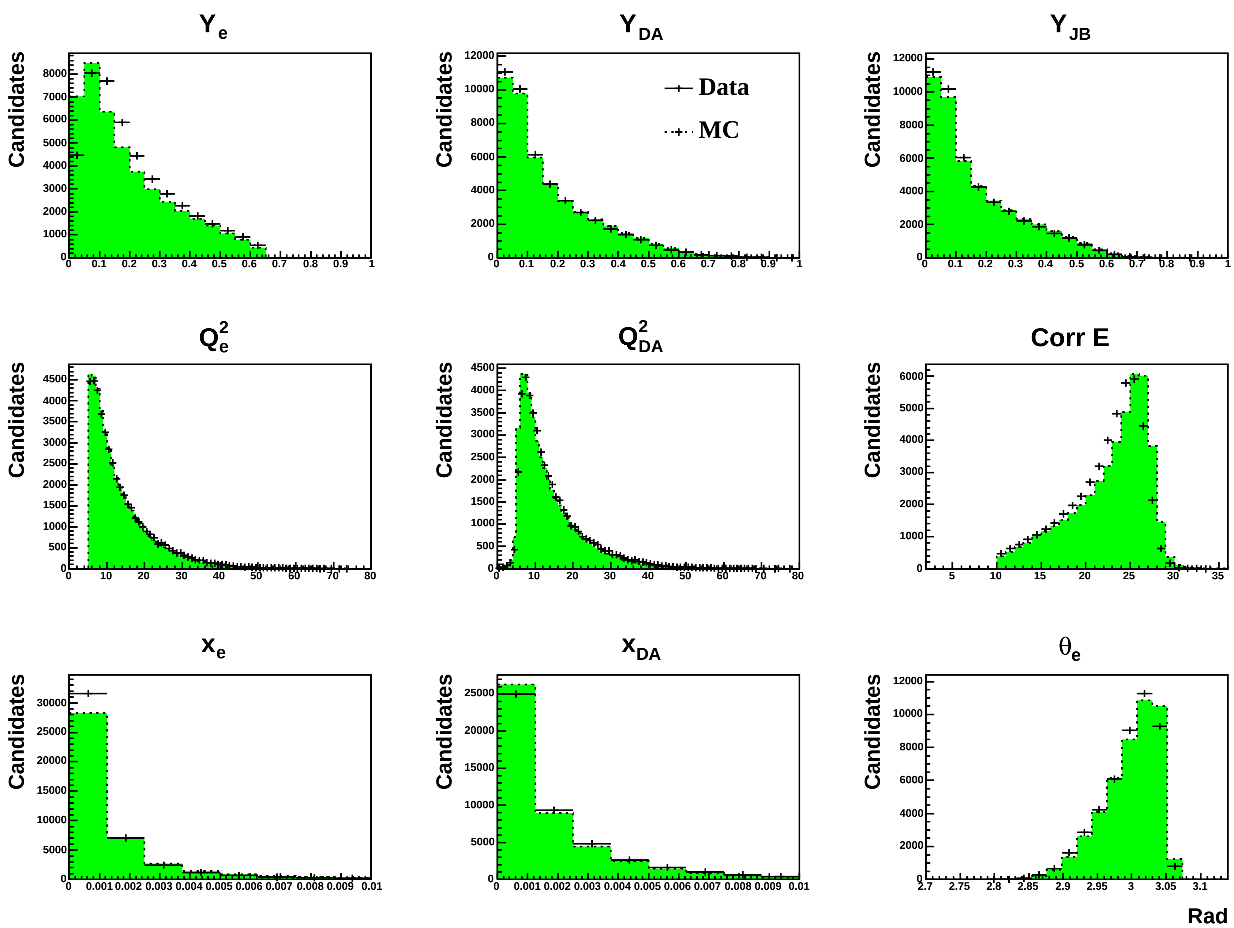

Figure 4.11: Control plots for kinematic variables prior to the SRTD HES alignment. Q^2 is measured in GeV^2 and E is measured in GeV. Data is indicated by points and MC by the filled green area. Alterations after the alignment are generally not visible by eye.

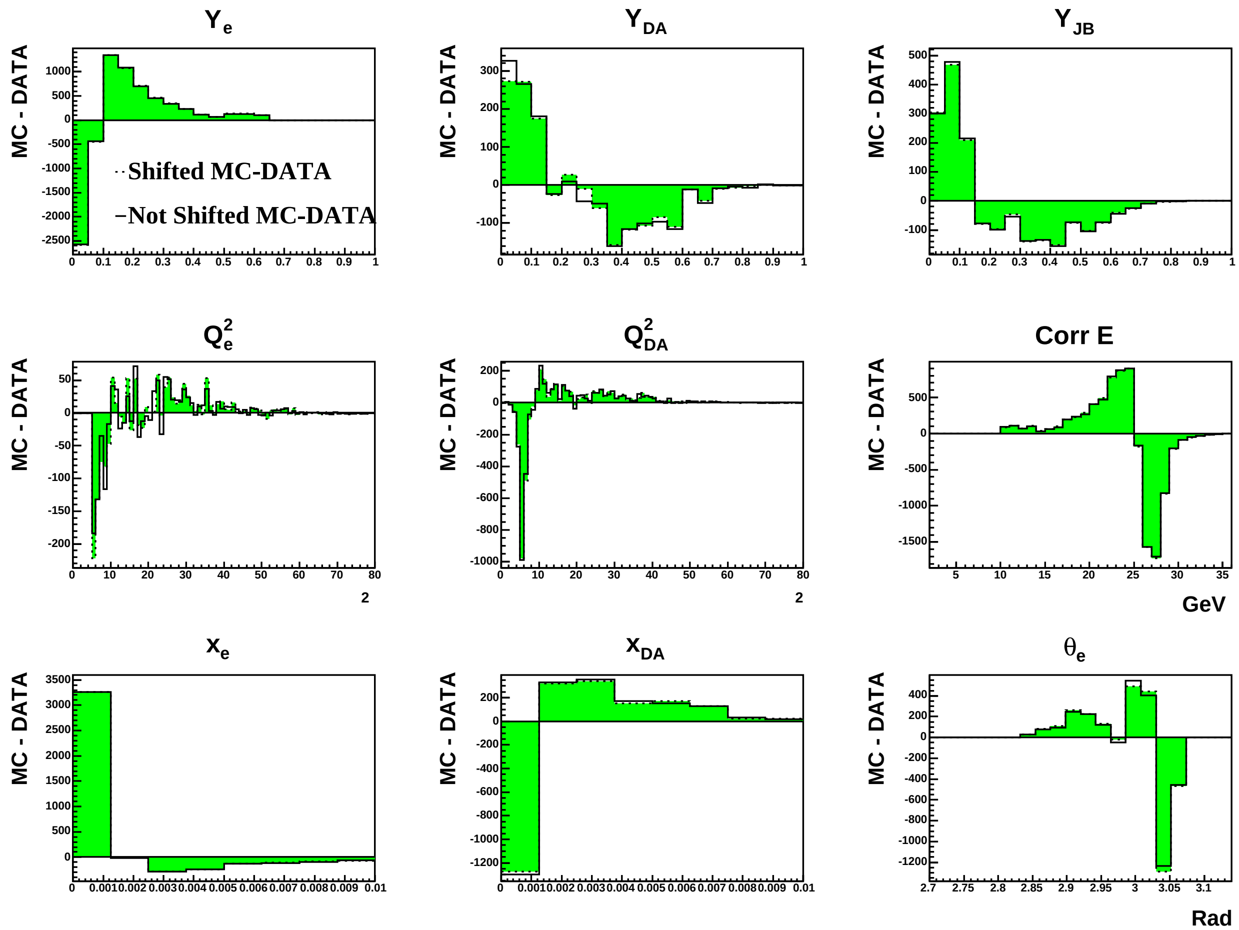

Figure 4.12: The difference between data and MC before (green) and after (dotted line) the SRTD-HES alignment correction in control plots of kinematic variables. Q^2 is measured in GeV^2 and E is measured in GeV.

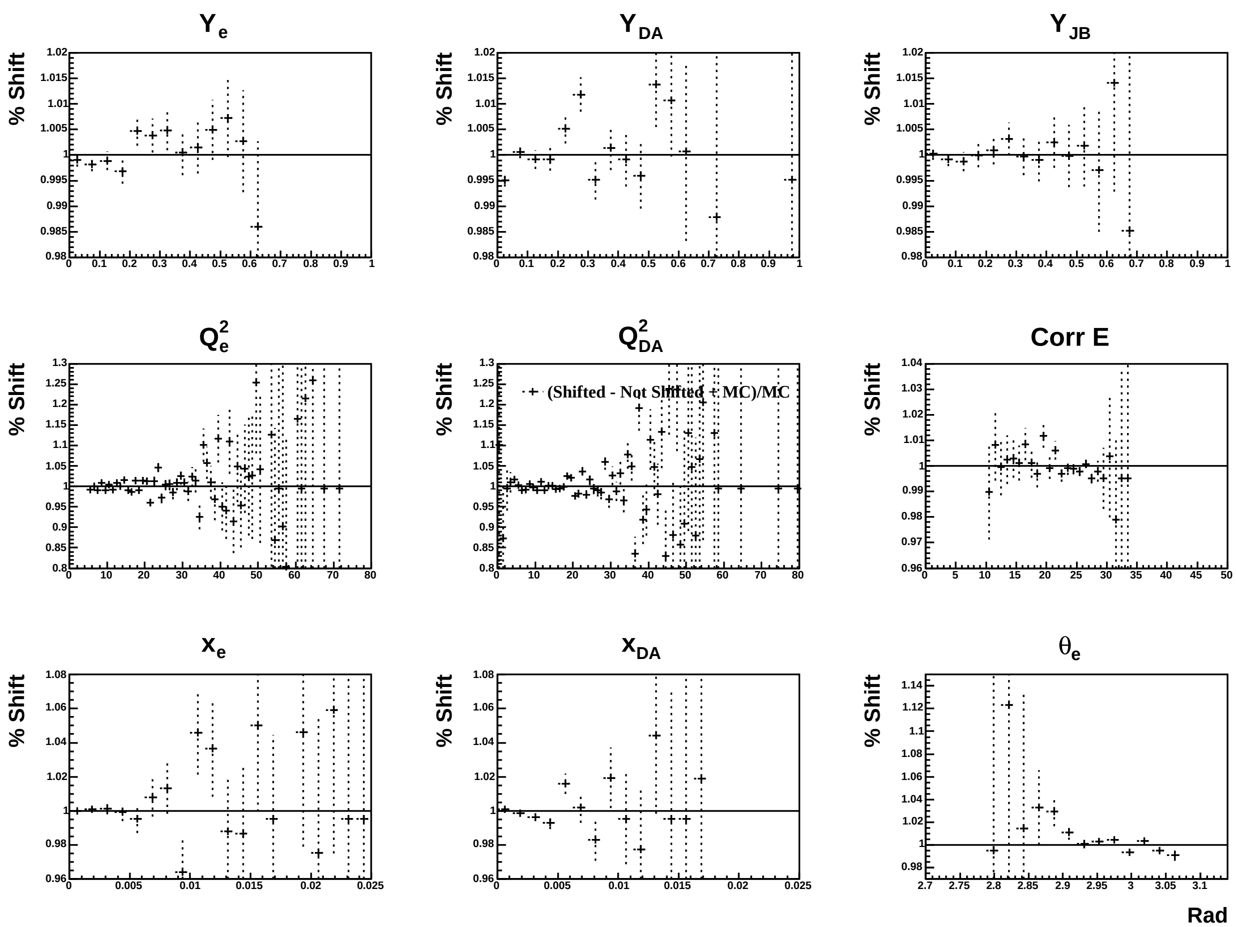

Figure 4.13: The difference in data between the pre and post alignment control plots divided by the total MC value +1. Q^2 is measured in GeV^2 and E is measured in GeV.

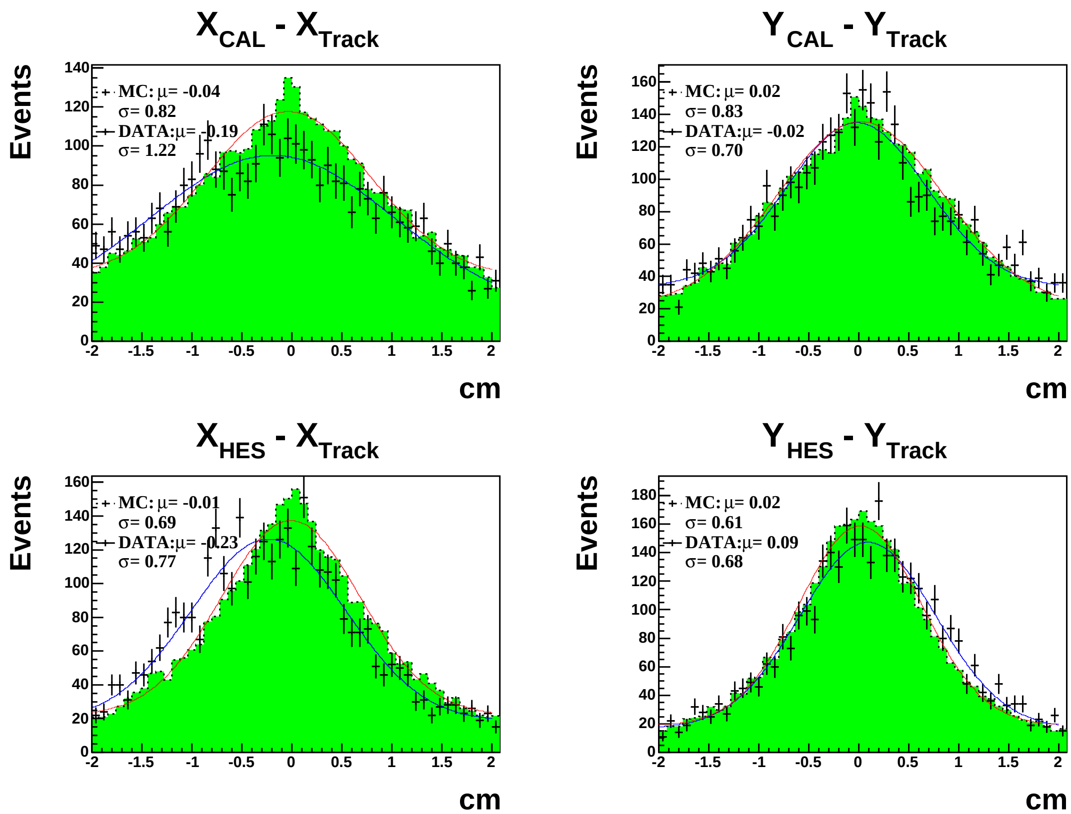

Figure 4.14: The difference between the electron position as measured firstly by the CAL and extrapolated CTD position and secondly by the HES and extrapolated CTD position. The differences in X position and Y position are given separately. The difference in the MC sample is shown in green with the fit shown in red and the difference in the data sample is shown in points with the fit indicated in blue. The gaussian fit parameters are also given.

4.3.2 CAL-CTD and HES-CTD Alignment

The final step of the alignment procedure was to align the CAL and HES components to the CTD. For this alignment a further cut on the electron momentum is required to improve track matching and reduce background effects. A momentum cut of $P_{\text{electron}} > 8$ GeV was used in the previous study and so was applied here. In this procedure the CTD track identified as the electron was extrapolated to the face of the CAL and HES before subtractions between the two are made. The differences are shown in figure 4.14 for both MC and data samples. A gaussian fit is also performed and the extracted parameters are found to be very similar.

Component	Shift (cm)
CAL:Track X	-0.16 ± 0.25
Cal:Track Y	-0.04 ± 0.25
HES:Track X	-0.22 ± 0.25
HES:Track Y	$+0.08 \pm 0.25$

Table 4.2: X and Y shifts of CAL and HES required for alignment with CTD.

A resolution of ± 0.25 cm is appropriate for these measurements and is greater than or equal to the shift required to align these detectors as shown in table 4.2. The conclusion is that these components of ZEUS are already aligned to a level that may not be improved upon by this method.

4.4 Summary

In this chapter the procedure for aligning the CAL, CTD, SRTD and the HES was detailed. The dead channels in (x, y) maps of scattered electron position for CAL, HES and SRTD were in agreement between MC and data, ensuring their suitability for alignment studies. The HES and SRTD were first aligned, requiring minor corrections of the order 0.25 ± 0.05 cm to be applied to the SRTD in the x direction and 0.10 ± 0.05 cm in the y. Application of these shifts has a negligible affect on a number of DIS kinematic variable control plots. The alignment of CTD, HES and CAL was then completed but could not be improved upon using the above methods. This was because the required shifts were less than the resolution of the histograms (typically 0.1 ± 0.25 cm). In addition, since only minor corrections with respect to HERA I are required we are justified in using the HERA I systematic energy corrections in later chapters.

Chapter 5

A GTT J/Ψ Trigger

This chapter is a feasibility study of the Global Tracking Trigger's (GTT) ability to trigger on events containing the J/Ψ meson. It begins with an overview of the ZEUS trigger system and a discussion of how tracking is implemented by the GTT. This is followed by a discussion of how the GTT may be used to trigger on J/Ψ events and then a demonstration that the J/Ψ mass peak can indeed be resolved at the Second Level Trigger (SLT). An investigation is then carried out using Monte Carlo to determine how strongly cuts on track variables and invariant mass affect reconstruction efficiency and signal-to-noise ratios. This information is used to optimise cuts in the online version of the trigger such that the rate may be kept reasonable without compromising too harshly on efficiency. The performance of the trigger is found to be equivalent in rate to existing triggers but frequently identifies J/Ψ candidates missed by them. The work on this project contributed to the GTT NIM paper *The Design and Performance of the ZEUS Global Tracking Trigger* [38].

5.1 Introduction

Prior to the HERA upgrade tracking at the Second Level Trigger (SLT) was performed with only CTD axial and z-by-timing information with a z vertex resolution of 9 cm. Advances in computing power enabled execution of faster, better tracking drawing on the CTD, STT and MVD at this stage of the three tier trigger process. Previously the reconstruction was performed on obsolete transputer technology. The increase in computer power makes it feasible for the first time to perform detailed tracking at the SLT. When this capability is combined with the improved hit resolution of the MVD the event reconstruction capabilities of the SLT might be sufficient to use an invariant mass spectrum to flag heavy vector mesons. This chapter is a feasibility study of constructing a J/Ψ trigger based entirely on the improved SLT tracking package the GTT, concluding that it is possible to construct such a trigger and that the trigger is capable of identifying unique J/Ψ events that are not flagged with existing triggers.

5.2 The ZEUS Trigger System

The ZEUS trigger system[39] is a three stage process designed to reduce the bunch crossing event rate from 10^7 Hz to 500 Hz, 500 Hz to 80Hz and 80Hz to 8 Hz after passing through the First, Second and Third level triggers respectively. As an event progresses through each trigger the available computational time increases along with the precision to which event kinematics are evaluated. It follows then that the earlier levels typically have to sacrifice precision for speed of computation.

5.2.1 The First Level Trigger

The First Level Trigger (FLT) is activated at each bunch crossing, i.e. every $96ns$, and will arrive at a decision after 44 bunch crossings ($4.4\mu s$). This corresponds to a typical rate of 10^7 Hz. Events are selected in such a way that a rate of 500Hz is passed to the SLT. Such a high input rate requires a selection process based on dead-time-free hardware and forces the FLT to perform at a rudimentary level, hence global component decisions are impossible at this stage. Calorimeter cells for instance may not be individually resolved so only broad energy estimates may be made, whilst tracks are required only to originate from the nominal interaction region ($Z_{vtx} \pm 50$ cm) using simple CTD FLT tracking. The FLT is used primarily for rejecting uninteresting data such as beam gas background events. Each detector component has its own logic which is combined in the Global First Level trigger. Events which pass the first level trigger are buffered for processing by the second level trigger (SLT).

5.2.2 The Second Level Trigger

A series of parallel transputers process the event in greater detail than the FLT, providing access to a larger fraction of the full event data so that evaluation may be made between detector components. Access is given to individual CAL cells and one may now determine if a track originates from the event vertex by reconstructing CTD hits. Post-upgrade ZEUS boasts a state-of-the-art PC farm which enables faster and more efficient tracking. A direct consequence of this was the development and implementation of the Global Tracking Trigger (GTT) algorithm which permits high level event reconstruction at the SLT for the first time, the details of which are discussed later. The data from events passing the SLT are sent to the event builder (EVB) which builds and stores complete events until the Third Level Trigger (TLT) is ready to accept and process them. Overall this process is designed to reduce the data rate to 80 Hz arriving at a decision within 10 ms. Events passing the SLT are passed onto the third level trigger.

5.2.3 The Third Level Trigger

Events passed from the SLT to the TLT are reconstructed with a simplified version of the final ZEUS analysis package on an Intel processor based computer farm. At this level it is possible for instance to fully reconstruct ZEUS CTD tracks and resolve individual calorimeter cells. The TLT decision making process reduces the event rate to around 8 Hz.

5.2.4 Reconstruction

All events passing the TLT are processed again a few days after the data has been taken. Calibration constants available only after data quality management analysis are implemented at this stage and CPU intensive reconstruction code are implemented here. Different physics filters are applied to the data to select common event types and corresponding *DST* bits are allocated. DST 9 for instance is used to detect a scattered electron with an energy greater than 4 GeV.

5.3 The Global Tracking Trigger Algorithm

With the MVD's superior hit resolution it is possible to improve SLT tracking and to more accurately reconstruct important event properties such as the primary vertex position. However due to the limited number of MVD hits per track it does not offer sufficient tracking information in isolation from other tracking components. To resolve this issue the GTT incorporates MVD, CTD and STT tracking information into the SLT tracking architecture.

A tracking algorithm in operation at the SLT must be able to operate in a harsh environment with limited algorithm time, breaking all track ambiguities quickly and efficiently [40]. Such limitations prevent a detailed event reconstruction since many approximations and assumptions must be made which sacrifice time and resolution for speed; necessity dictates therefore that the GTT use an extremely fast algorithm.

Only 10 ms are available for the event to be both transfered to and processed by the GSLT. 3 ms are required to read data from the CTD and STT using transputer electronics and 1 ms for MVD readout and data transfer for all three components to the GTT interface. This interface is run on a 1 GHz PC farm and events are reconstructed in a further 3 ms. The results of this are sent to the SLT which determines whether or not to pass the event to the TLT.

Broadly speaking the approach adopted identifies segments of *linear tracks* found in the CTD, combines them into a large curved track (figure 5.1) and matches this track to MVD hits. The track is then assigned a weight, w_{track}, which is in part dependent on the number of MVD hits upon which it lies. This implementation is motivated by the excellent resolving power of the MVD. The vertex for each track, Z_{track}, is binned with weight w^n_{track}. The value $n = 2$ was used in this implementation of the GTT since it gives more weight to high quality tracks which improves the reconstruction in busy events.

It is assumed that each track originates from the same initial vertex, Z_{initial}, a position evaluated using

$$Z_{\text{initial}} = \frac{\sum_{\text{track}} Z_{\text{track}} w^n_{\text{track}}}{\sum_{\text{track}} w^n_{\text{track}}}.$$

Only tracks with Z_{track} within ± 9 cm of Z_{initial} are considered and re-evaluated with $Z_{\text{track}} = Z_{\text{initial}}$. Overall the GTT Barrel Algorithm operates in 4 distinct logical stages:

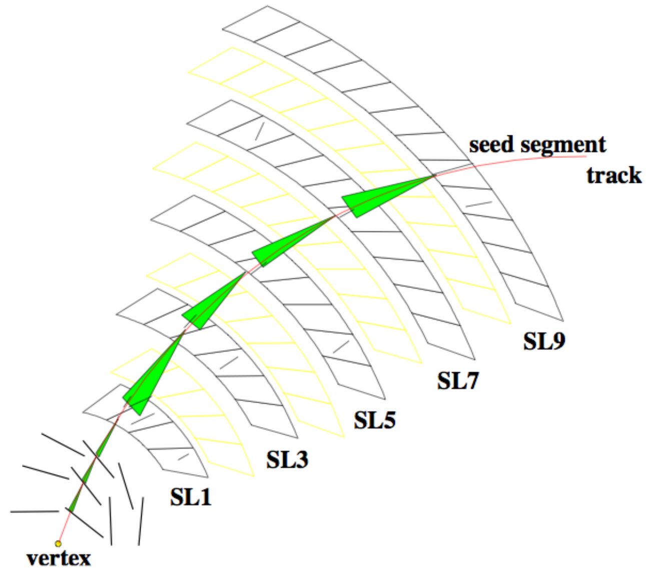

Figure 5.1: GTT axial track finding. The shaded green band indicates the attempted linear segments in each Super Layer.

- Axial track finding:
  - CTD axial segments are found and $r - \phi$ tracks fitted.
- Vertex identification and z tracking:
  - Matching of z-by-timing hits to axial tracks found in step 1. These are assumed to be locally linear in the fit.
  - Tracks are improved using stereo segments.
  - An initial primary vertex is found and then used to constrain the $z-$tracks in a refit.
- MVD matching and vertex refinement:
  - Axial MVD hits are matched and used to refit axial tracks.
  - z MVD hits are matched and used to refit z tracks.
  - Recalculation of the primary vertex.

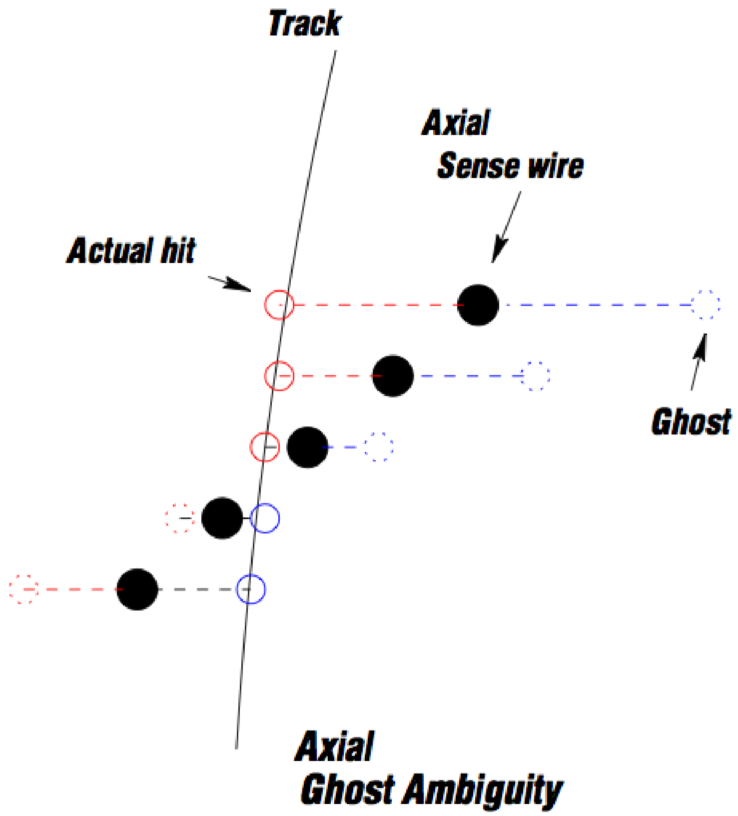

Figure 5.2: Representation of CTD left-right hit ambiguity. Red denotes the actual track position, blue denotes the ghost track position; a *possible* (albeit false) hit based on unsigned drift time information.

Each linear segment used in step 1 corresponds to a straight line fit to hits on a CTD cell. Because the drift time information recorded by the cell is unsigned there is no immediate way to identify the direction from which the signal arose. Indeed there are two potential contributions from each hit, the actual signal and a ghost signal as indicated in figure 5.2. To break this ambiguity the cell geometry was designed so that the sense wires lie at an angle of 45^0 to the r-plane. In this way a series of ghost hits can be immediately rejected as those whose track points furthest away from the beam pipe. By this method the number of considered candidates is halved which avoids an unacceptably high computational time. This however leads to greater efficiency for higher p_T tracks and a charge asymmetry for lower p_T tracks. A modification of this approach is used in the stereo super-layers since the wires are inclined here.

5.4 Reconstruction of the J/Ψ in MC at the SLT

The GTT J/Ψ trigger identifies events containing J/Ψs by calculating the invariant mass of track pairs using only GTT variables. Using offline tracking there is a very clear resonance at $M_{J/\Psi}$, although there was some initial doubt as to whether the inferior GTT tracking will be able to resolve a J/Ψ signal at all. This brief section investigates the cleaning cuts that will help resolve a J/Ψ mass peak in data using the GTT. MC distributions are used to justify reasonable cuts which will later be applied to a data sample to help resolve the signal. These cuts will not be applied to the trigger.

5.4.1 The J/Ψ

The J/Ψ is a vector meson comprised of a $c\bar{c}$ pair with a rest mass of 3096.916 ± 0.011 MeV. Of the J/Ψ's many decays modes two can be most easily recognized in ZEUS:

$$J/\psi \to \mu^+\mu^-$$

$$J/\psi \to e^+e^-.$$

The branching ratio for each of these process is equal at $5.94 \pm 0.06\%$. To reduce the computational time the GTT J/Ψ trigger will operate under the assumption that the J/Ψ has decayed into one of these two body channels and will therefore only consider pairs of tracks. The lepton mass does not significantly contribute to the invariant mass calculation since $M_J/\psi \approx 3.1$ GeV $>> m_\mu \approx 0.1$ GeV $>> m_e \approx 0.0005$ GeV and is therefore set to zero.

5.4.2 Monte Carlo

A small $J/\Psi \to \mu^+\mu^-$ photo-production sample of around $100,000$ events was generated using the DIPSI [43] MC package for use in determining suitable SLT track cuts. Figure 5.3 is a histogram of invariant mass track pairs using reconstructed tracks (green) and the MC true decay tracks (blue). As expected the true tracks peak at the J/Ψ mass precisely and with a width of 91 keV. The smearing of the true measurement by the GTT demonstrates how inefficiencies and approximations hide the natural distribution.

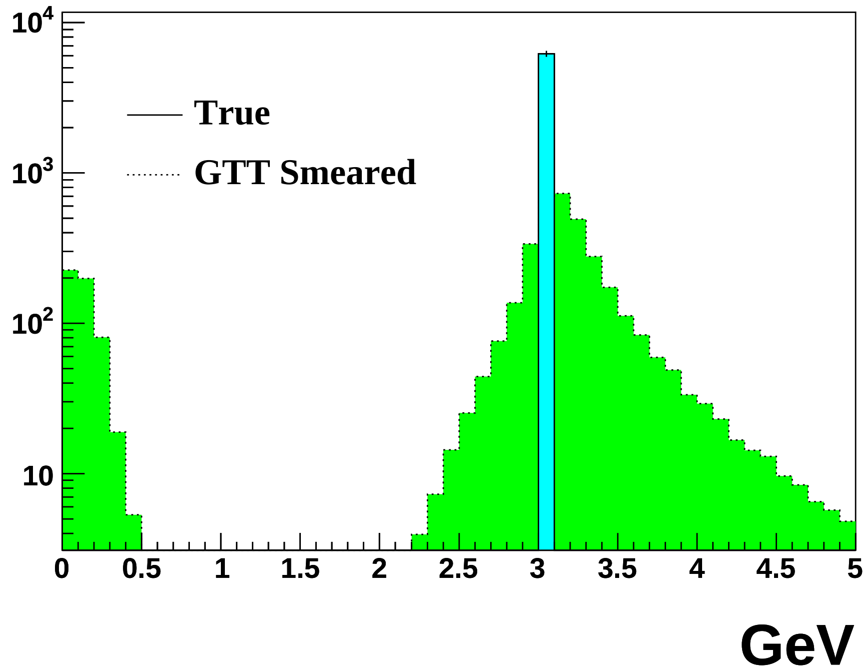

Figure 5.3: Smearing of true J/Ψ invariant mass in reconstruction by the GTT. MC true is shown in blue, GTT reconstruction in green.

The peak at zero is a byproduct of the GTT reconstruction which sometimes splits one track into two similar tracks of the same charge. This effect may be removed by evaluating only oppositely charged pairs of tracks as shown in figure 5.4. There is also an observed left-right asymmetry in the mass distribution about $M_{J/\Psi}$ arising from multiple scattering within the MVD. This effect is markedly reduced when cuts of $p_T > 1$ GeV and $|\eta| < 1.75$ are applied, rejecting the low p_T tracks prone to this behaviour. The early version of the ZEUS MC used in this section does not have accurate dead material maps describing the MVD, and so this asymmetry is seen to a much lesser degree in data.

Selection of cleaning cuts using MC distributions

Distributions of track p_T, η and event multiplicity in the MC sample can be seen in figure 5.5, inspection of which suggests that cuts of $p_T > 1$ GeV and $|\eta| < 1.75$ will minimise J/Ψ

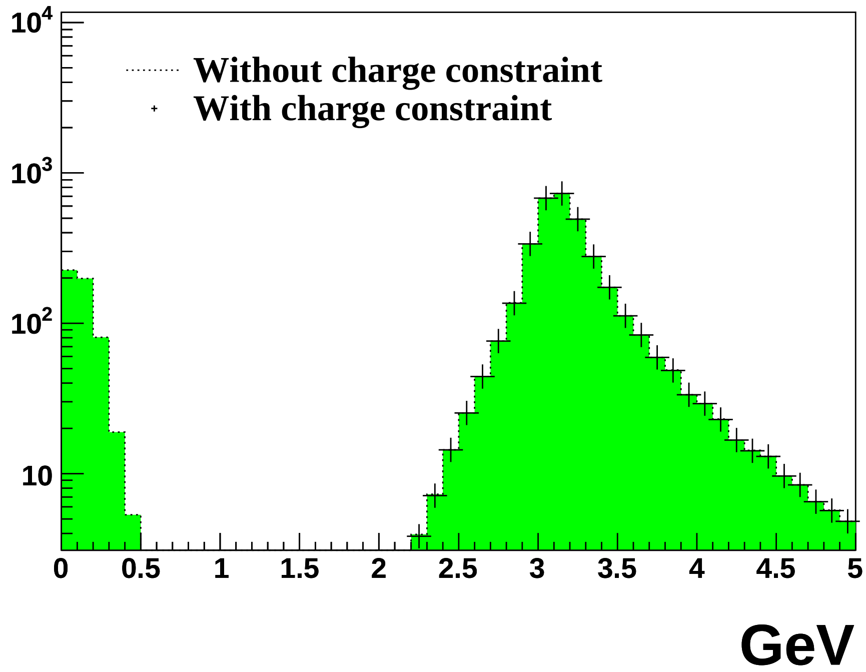

Figure 5.4: MC J/Ψ mass spectrum evaluated with GTT tracking variables. The shaded green region denotes the algorithm where all track pairs are considered, the points represent the same spectrum when like-charged tracks are excluded.

loss and reject candidates that are certainly not J/Ψ. Tracks are also required to originate from within 5 cm (the vertex resolution of the GTT) of each other. The effect of these cuts on data are shown in figure 5.6 and discussed in section 5.5 which also provides justification of these cuts in terms of efficiency conservation and signal to noise reduction. This study follows immediately after the following section, which is an investigation of how efficiently true tracks are reconstructed in a number of kinematic regions.

5.4.3 Efficiency of true J/Ψ GTT reconstruction

In this section the trigger efficiency is defined by

$$\text{Efficiency} = \frac{\int_{m_{\mathrm{b}}}^{m_{\mathrm{a}}} S_{\mathrm{GTT}}}{\int_{m_{\mathrm{b}}}^{m_{\mathrm{a}}} S_{\mathrm{true}}} \tag{5.1}$$

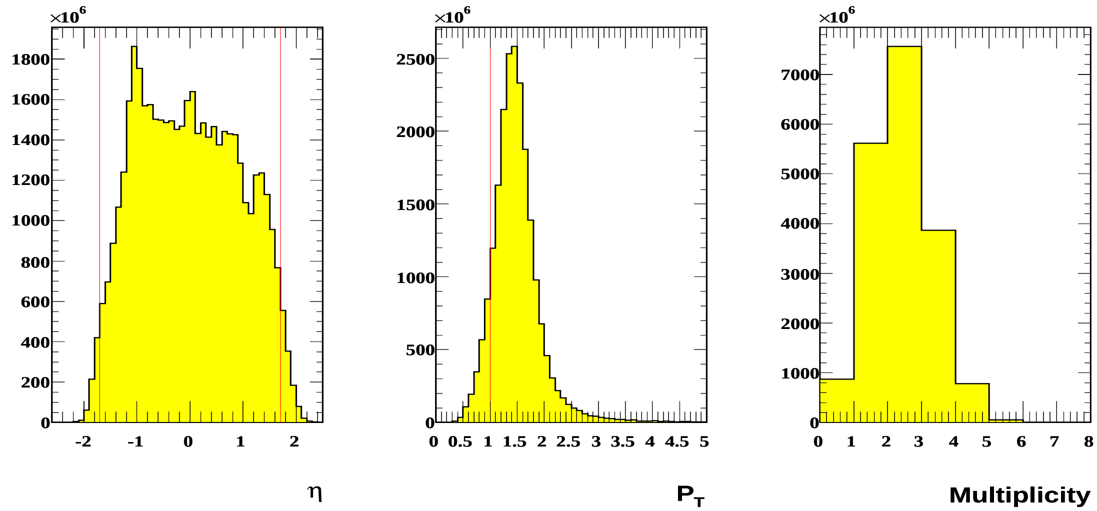

Figure 5.5: η, p_T and multiplicity distributions for γP MC J/Ψ daughter decay leptons as measured with GTT tracking parameters in the MC sample. p_T is given in GeV. The red lines indicate the positions of the cuts placed to reduce combinatorial background in an inclusive data sample and minimise signal loss.

where $S_{\rm true}$ denotes the invariant mass plot containing MC true information and $S_{\rm GTT}$ is the invariant mass plot of the same true information as seen after passing through the detector simulator and evaluated by the GTT. $m_{\rm a}$ and $m_{\rm b}$ denote the upper and lower limits of the mass window.

For each event $|\eta_{\rm True}|$ for both *true leptons* is evaluated, the higher $|\eta_{\rm True}|$ is called $|\eta^{\rm Max}_{\rm True}|$. Events are then divided into 5 bins of $|\eta^{\rm Max}_{\rm True}|$ with $\Delta\eta = 0.5$. The efficiencies for each of these bins are given in table 5.1. The events are similarly binned according to the lower $p_{\rm T,True}$ value, denoted $p^{\rm Min}_{\rm T,True}$, in bins of $\Delta p_T = 0.5$. The efficiency for these bins is also given in this table.

Table 5.1 shows that the efficiency falls with decreasing $p_{\rm T,True}$, and is highest when both true μs are generated within the central CTD range of $|\eta| < 1.7$. Tracks with the greatest p_T are more successfully resolved by the GTT with an efficiency in the order of 60%, falling rapidly for $p_T < 1.5$ to 36%. This feature arises because of the difficulty the GTT has in identifying ghost hits for low p_T tracks. A generated particle that traverses the central region

$p_{\mathrm{TTrue}}^{\mathrm{Min}}$ range (GeV)	Efficiency	$\lvert\eta_{\mathrm{True}}^{\mathrm{Max}}\rvert$ range	Efficiency
$0.0 \rightarrow 0.5$	0 %	$0.0 \rightarrow 0.5$	67.5%
$0.5 \rightarrow 1.0$	8.3 %	$0.5 \rightarrow 1.0$	66.7%
$1.0 \rightarrow 1.5$	36 %	$1.0 \rightarrow 1.5$	51.5%
$1.5 \rightarrow 2.0$	60 %	$1.5 \rightarrow 2.0$	16.0%
2.0+	60 %	2.0+	0%

Table 5.1: GTT efficiencies in different decay particle kinematic regions. P_T refers to the *lowest* P_T true track, $|\eta|$ refers to the highest $|\eta|$ true track in the event. A mass window of 3.1 ± 2 GeV was used.

of the CTD ($|\eta| < 0.5$) is reconstructed 67% of the time. The reconstruction efficiency falls to 16% when $|\eta| > 1.5$ as the boundaries of the CTD are probed. Overall we expect central, high $p_T > 1.5$ GeV true particles to be reconstructed most efficiently.

5.5 Resolving J/Ψ in data at the SLT

A 17.66pb^{-1} sample of inclusive ZEUS eP data was used to determine whether the J/Ψ mass could be resolved at the SLT. No specific trigger configuration was required in this data set, all that was demanded was that GTT track information was present. This data was analysed using a prototype GTT J/Ψ trigger algorithm which cycles through pairs of tracks and evaluates the invariant mass if the tracks share a vertex and pass the cleaning cuts outlined above, returning the mass in the event closest to $M_{J/\Psi}$. The cleaning cuts consisted of the opposite charge requirement, $p_T > 1$ GeV for at least one track and $|\eta| < 1.75$ for both tracks. Setting the mass of both contributing tracks to zero has little effect on the distributions in the J/Ψ region due to the comparatively high J/Ψ mass. For this reason we detect a large number of J/Ψs from both lepton decay channels simultaneously. The GTT J/Ψ trigger is therefore decay channel independent.

5.5.1 Reduction of background in data

Figure 5.6 shows the effect of applying cuts on multiplicity, charge and transverse momentum both in turn and together. When no cuts are applied the scale of the background problem is apparent, the signal is completely swamped by noise and no J/Ψ mass signature can be extracted. Progressing from left to right through figure 5.6 it can be seen first that a large amount of background is reduced by simply cutting on $N_{\text{tracks}} < 4$. This reduction also significantly reduces the time required to process each event, and biases the selection towards elastic J/Ψs. The introduction of the $p_T > 1$ GeV cut for one track greatly reduces the background, however it is still impossible to resolve any clear J/Ψ signal. The ρ spectrum at around 0.6 GeV can now be resolved. Similarly by rejecting tracks with matching charge the background is reduced but not to the extent that a J/Ψ peak is visible. Combining $p_T > 1$ GeV and $N_{\text{tracks}} < 4$ appears to be sensible as now a J/Ψ peak is clear, an effect more obvious when tracks of the same charge are additionally rejected as shown in the 6th plot.

The final plot comprising the $p_T > 1$ GeV, $N_{\text{tracks}} < 4$ and oppositely charged tracks was fitted locally around the J/Ψ mass in figure 5.7. For the purposes of this fit the background was assumed to be (locally) linear and the peak itself assumed to be Gaussian. Also shown is the expected peak distribution using a luminosity weighed MC sample, and the fit of the Gaussian only region. The two compare well, although the MC sample displays a slight asymmetry, with the higher mass half of the peak favoured somewhat. The fitting parameters in figure 5.7 were computed using a χ^2 fitting algorithm value where $\chi^2/NDF = 1.097$. Here χ^2 is defined as

$$\chi^2 = \sum_{\mathrm{i}} \frac{(\mathrm{O_i} - \mathrm{E_i})^2}{\sigma_i^2}.$$

where O = observed value, E = expected value, σ_i is the corresponding error and the summation is performed over the bins. A good fit would yield a value around the order of

$$\frac{\chi^2}{NDF} = \frac{\chi^2}{\text{nbins} - \text{N parameters}} = 1.$$

The width of the distribution is in good agreement with the MC prediction, a promising result since this was the first version of ZEUS MC for HERA II data. The log scale however reveals a slight discrepancy between the fit and MC at higher $M_{J/\Psi}$, a known feature of this particular MC version. The J/Ψ amplitude of 609 ± 40 very reasonably confirms that this peak is not a statistical effect. There is a slight shift in measured J/Ψ mass which after fitting was 3.129 ± 0.012 GeV, a small deviation from the accepted mass 3.09 GeV due to the inadequacies of the linear background assumption. Regardless this clearly demonstrates that it is possible to extract a J/Ψ signal using only GTT tracking variables which lends support to the feasibility of a GTT J/Ψ trigger.

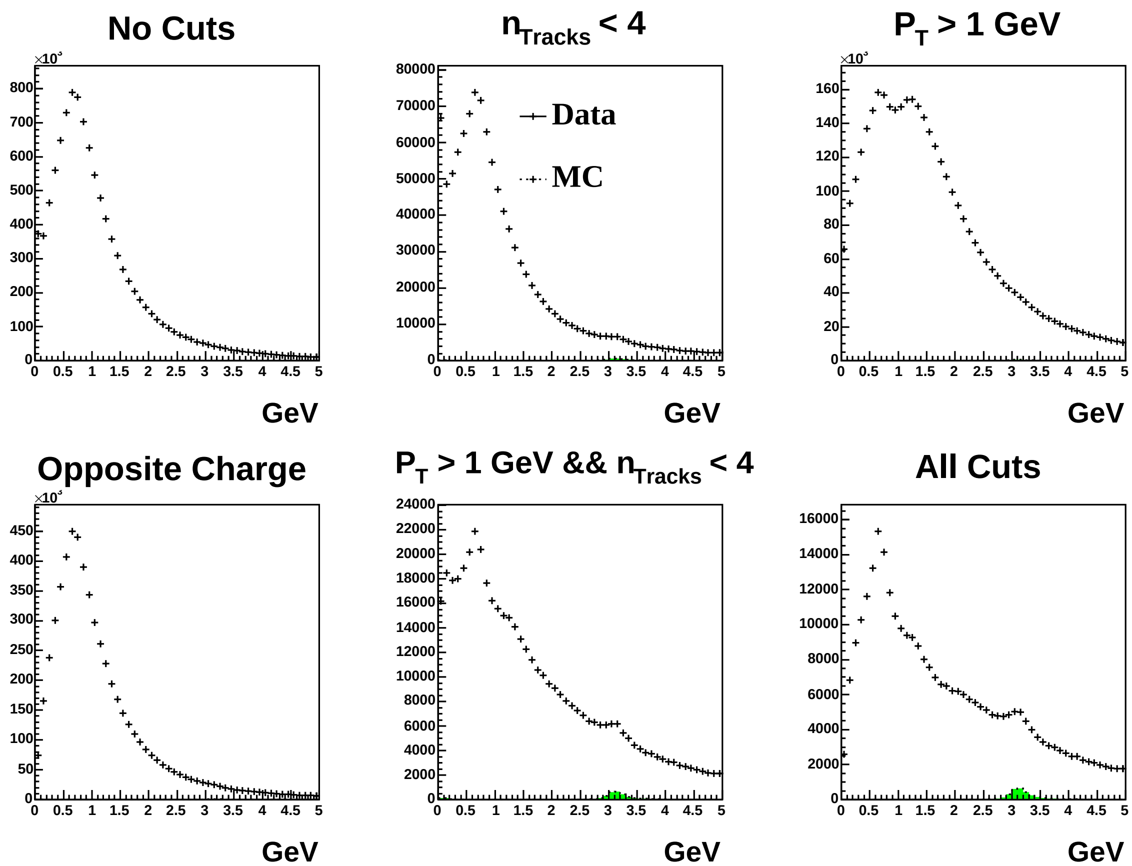

Figure 5.6: GTT mass distributions for 17.66pb^{-1} of data (points) and MC (green) computed for the indicated GTT tracking cuts.

5.5.2 Optimisation of Efficiency and Signal to Noise

The results of section 5.5.1 show that it is possible to resolve the J/Ψ at the SLT and so a J/Ψ SLT trigger is indeed feasible. This section contains a study of the efficiency with

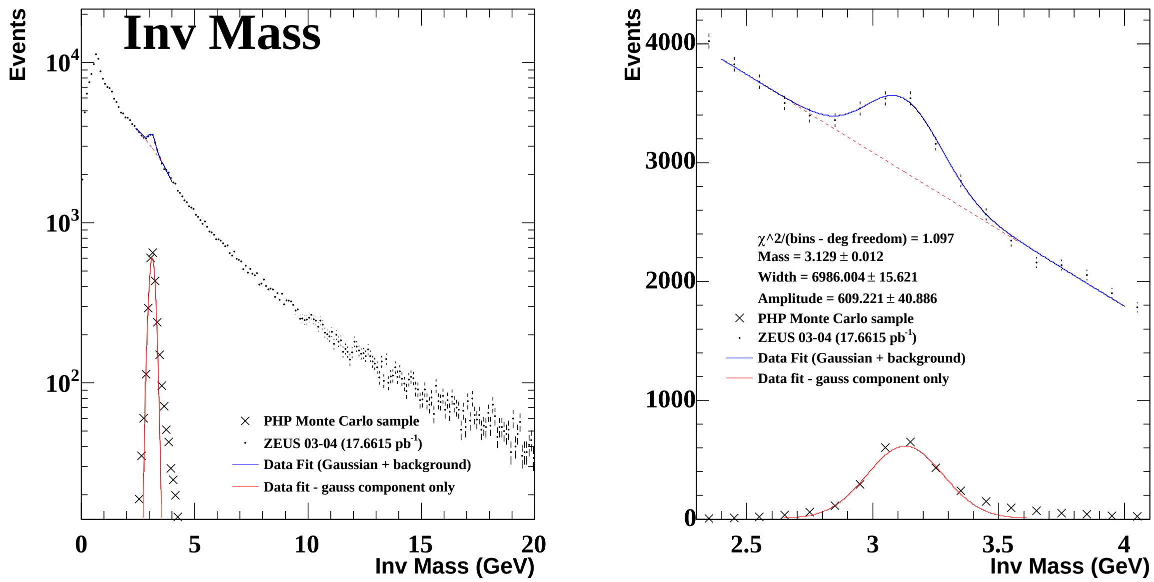

Figure 5.7: Local and global J/Ψ mass spectrums for a tracking enriched data sample, fitted locally to a Gaussian + linear function (blue). The fit is performed on the data (points) before the Gaussian component (solid red) is extracted and drawn over the MC prediction (crosses).

which MC true J/Ψs are resolved and the signal to background ratio of the trigger. This study will be important if the trigger rate is too high and must be reduced with cuts that maximise efficiency and signal to noise ratio.

The data sample used is the same as in section 5.5 and the MC sample is that used in section 5.4.2. The efficiency of J/Ψ reconstruction and the signal to noise ratio are given as functions of the track cuts determined in section 5.5.1. The data and reconstructed MC sample used in this section do not require any trigger configuration, and an invariant mass is calculated whenever there exists GTT information in the event. This will not bias the efficiency measurement since no true J/Ψ events are discarded, and efficiency here is a measurement of their reconstruction. In section 5.6.1 a sample of pass-through data will be used to determine the trigger rate and efficiency of finding $J/\Psi \rightarrow \mu\mu$ events that have been well reconstructed offline. The studies in 5.6.1 will be necessary to determine how the trigger will behave when implemented online, and will rely on the results of this section.

Efficiency study

The efficiencies computed in table 5.2 are defined by equation 5.1. As well as evaluating the efficiency for all events, table 5.2 also indicates which types of events are easiest to detect. To quantify this effect a number of true μ decay scenarios were chosen and the amount detected by the GTT measured. The four columns describe, in order; a MC set for which no true cuts are applied, one true μ has $p_T > 1$ GeV, both μs are fully enclosed in the CTD, and both μs are fully enclosed, one with $p_T > 1$ GeV. The rows indicate the data cuts placed on these increasingly restrained true samples. These data cuts proceed row-wise as; no cuts, $p_T > 1$ GeV for at least one track pair, less than 4 GTT tracks per event, a combination of the $p_T > 1$ GeV and multiplicity cuts, $|\eta| < 1.75$ for both tracks (a fully enclosed pair), and a combination of all p_T, $|\eta|$ and multiplicity cuts. For our purposes, a GTT measurement is defined as a pair of tracks with an invariant mass between m$_a$ and m$_b$, where $m_a = M_{J/\Psi} - w$ and $m_b = M_{J/\Psi} + w$. w is half the measurement window and takes the values $0.3, 0.5$ and 1 GeV successively. Widening the counting window increases the efficiency but will affect the signal to noise ratio considerably. The presence of a matching charge cut changes efficiency by no more than 1% and so for clarity is not included in this table.

Consultation of table 5.2 reveals that 46.0% of all MC true events pass the combination of p_T, multiplicity and $|\eta|$ detector cuts with a large mass window. In other words the ZEUS detector is capable of detecting 46.0% of all simulated $J/\Psi \to \mu\mu$ decays with detector cuts of $p_T > 1$, $|\eta| < 1.75$ and less than 4 tracks detected. Under favourable μ true conditions (high p_T, within CTD acceptance range) the trigger scenario with all cuts will record 66.9% of the *existing* J/Ψs. Under these optimal conditions only 12.5% of these J/Ψs are excluded by our cuts at the true level. The remainder are lost through detector inefficiencies. Under normal conditions only 8.5% of J/Ψ which register in some way at detector level are excluded. Shortening the bin width from ± 1 to ± 0.3 the excluded-by-data-cuts-but-potentially-detectable J/Ψs fall to 9.5% and 6.5% for both ideal and standard true conditions respectively. Overall it appears that efficiency is most sensitive to restrictions on invariant mass.

		No true cuts	1 true μ has Pt > 1	2 μ tracks have $\|\eta\| < 1.75$	Both true cuts
M range (GeV)	Detector Cut	Efficiency	Efficiency	Efficiency	Efficiency
3.1±0.3	no cuts	44.9%	52.3%	59.0%	65.4%
	Pt > 1	43.9%	51.2%	57.8%	64.0%
	Track < 4	40.2%	46.8%	52.9%	58.5%
	Pt and Track	39.3%	45.8%	51.7%	57.2%
	2 PS < 1.75	43.8%	51.1%	57.5%	63.7%
	All cuts	38.4%	44.8%	50.4%	55.9%
3.1±0.5	no cuts	50.0%	58.2%	65.6%	72.7%
	Pt > 1	48.8%	56.9%	64.2%	71.1%
	Track < 4	44.6%	52.0%	58.7%	65.0%
	Pt and Track	43.6%	50.8%	57.3%	63.5%
	2 PS < 1.75	48.6%	56.6%	63.7%	70.6%
	All cuts	42.5%	49.5%	55.6%	61.7%
3.1±1	no cuts	54.5%	63.5%	71.1%	79.4%
	Pt > 1	53.3%	62.1%	70.1%	77.7%
	Track < 4	48.6%	56.7%	63.9%	70.8%
	Pt and Track	47.5%	55.4%	62.4%	69.2%
	2 PS < 1.75	52.8%	61.5%	69.2 %	76.7%
	All cuts	46.0%	53.7%	60.3 %	66.9%

Table 5.2: GTT J/Ψ detection efficiency for the true level (columns) and detector level (rows) cuts prescribed above.

Signal to noise study

A method to quantify the size of the peak relative to the background is evaluation of the signal to noise ratio. Signal to noise is defined as

$$S:N = \frac{\int_{\mathrm{m}_b}^{\mathrm{m}_a} S_{mcGTT}}{\int_{\mathrm{m}_b}^{\mathrm{m}_a} S_{dataGTT} - \int_{\mathrm{m}_b}^{\mathrm{m}_a} S_{mcGTT}}.$$

and is effectively the ratio of J/Ψ track pairs to background track pairs. The true kinematic scenarios and detector cuts investigated are the same as in the efficiency study in section 5.5.2. As noted in table 5.2 increasing the bin width improved efficiency but at the cost of a considerable increase in S:N (table 5.3), a result of a number of “false positives” infiltrating the detection range. As before, a GTT measurement is defined as a pair of tracks with an invariant mass between limits m_a and m_b. A combination of all cuts and a small mass window yields a satisfactory S:N of 20.49%, falling to as low as 0.5% when no cuts are applied and a large mass window is considered. Changing the true scenario has little effect on the S:N. As with efficiency, the signal to noise ratio is most sensitive to invariant mass cuts.

When all detector level cuts are applied a peak is clearly visible despite the large background. Indeed J/Ψ signal parameters such as height and width may be easily evaluated as demonstrated by the fit. The removal of these cuts restores the entire background noise and swamps the signal, illustrating how difficult it is to extract a signal when presented with uncut data.

If one wishes to find a compromise between efficiency and the signal to noise ratio, it is desirable to maximise the quantity A, where A = efficiency $\times$ S:N. This is largest for the mass range $2.8 < M_{J/\Psi} < 3.4$ with $p_T > 1$ GeV, multiplicity < 5, $|\eta| < 1.7$ and an opposite charge constraint. Therefore if the trigger rate is too large these cuts may be suitably applied to reduce the rate but preserve the usefulness of the trigger and allow a clear reconstruction at SLT. However because the GTT will not be used to resolve the J/Ψ it is not necessary to maximise the signal to noise ratio at this level. It is therefore acceptable to widen the mass window to $2.6 < M_{J/\Psi} < 3.6$ which yields the second highest A but will increase statistics. This study also concludes that efficiency and S:N are most sensitive to invariant mass restrictions, typically by a factor 4 more so than the other investigated cuts. Therefore if one wished to apply a rate restriction by restraining only one parameter, it is recommended invariant mass is used. This is the preferred option since it will reduce rate significantly and will not bias any final measurement by excluding a kinematic region. The following section will determine whether it is necessary to reduce the rate using one of these recommended proposals.

5.6 Final Implementation of the GTT J/Ψ Trigger

The final implementation of the J/Ψ Trigger is as follows: The algorithm considers all events with at least 2 and fewer than 100 GTT tracks; The invariant mass for all pairs of tracks is calculated, provided that the tracks have opposite charge and intersect the z-axis within 5 cm of each other; The highest invariant mass per event is returned by the code and stored online. Returning the highest invariant mass enables the same trigger system to be used as an Υ and J/Ψ trigger. The computational time for this process is negligible when compared to the overall GTT track finding algorithm in figure 5.8, therefore the J/Ψ trigger will not use unacceptably high computational resources.

M range (GeV)	Reconstruction Cut	No truth cuts	$Pt_{\text{true}} > 1$ (1 track)	$\lvert\eta\rvert_{\text{true}} < 1.75$ (2 tracks)	Both cuts
		Signal:Noise	Signal:Noise	Signal:Noise	Signal:Noise
3.1±0.3	no cuts	1.3%	1.3%	1.3%	1.3 %
	Pt > 1	1.6%	1.6%	1.6%	1.6 %
	Multi .<. 4	12.0%	11.7%	11.7%	11.5%
	Matching Ch	2.5%	2.4%	2.4%	2.4%
	$\lvert\eta\rvert < 1.75$	1.5%	1.5%	1.5 %	1.48 %
	Pt and multi	16.3%	15.9%	15.9%	15.5%
	Pt, multi, ch	19.0%	18.6%	18.5 %	18.1 %
	Pt, multi, ch, $\lvert\eta\rvert$	20.4%	19.6 %	19.5 %	19.1 %
3.1±0.5	no cuts	1.1%	1.0%	1.1 %	1.1 %
	Pt > 1	1.3%	1.3%	1.3 %	1.3 %
	Multi .<. 4	9.9%	9.7%	9.7 %	12.7 %
	Matching Ch	2.0%	2.0%	2.0 %	1.9 %
	$\lvert\eta\rvert < 1.75$	1.2%	1.2 %	1.2 %	1.21 %
	Pt and multi	13.4%	13.1%	13.0 %	12.7%
	Pt, multi, ch	15.6%	15.2%	15.2 %	14.8 %
	Pt, multi, ch, $\lvert\eta\rvert$	16.3%	15.9 %	15.8 %	15.5%
3.1±1	no cuts	0.5%	0.5%	0.5 %	0.5 %
	Pt > 1	0.7%	0.69%	0.6 %	0.7 %
	Multi .<. 4	5.0%	4.8%	4.8 %	6.7 %
	Matching Ch	1.0%	1.0%	1.0 %	1.0 %
	$\lvert\eta\rvert < 1.75$	0.6%	0.58 %	0.6 %	0.5 %
	Pt and multi	7.1%	6.9%	6.9 %	6.7 %
	Pt, multi, ch	8.3%	8.1%	8.0 %	7.8 %
	Pt, multi, ch, $\lvert\eta\rvert$	8.7 %	8.5 %	8.4%	8.3%

Table 5.3: GTT J/Ψ S:N for the true level (columns) and detector level (rows) cuts prescribed above.

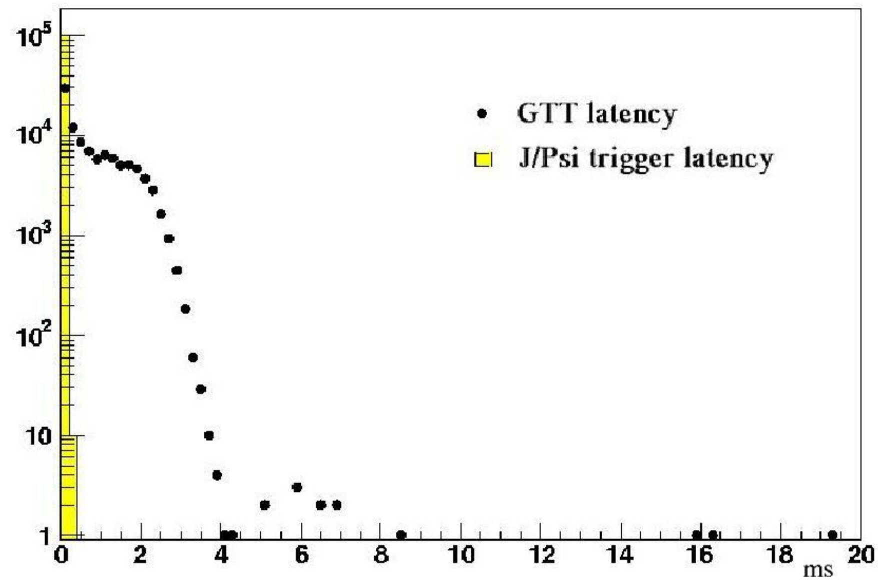

Figure 5.8: Latency of the J/Ψ algorithm (yellow) and whole GTT algorithm (points).

5.6.1 Passthrough Data Samples

In this section the efficiency and rate of the final implementation of the trigger system is evaluated using a passthrough data sample (described below). A new definition of efficiency different to that defined in equation 5.1 is used in this section,

$$\text{Efficency} = \frac{\text{No. Triggered Events in Clean Sample}}{\text{Total No. of Events in Clean Sample}}$$

where "clean sample" in this case is a data sample of J/Ψ events selected with constraints demanding that 2 well resolved muons were detected with opposite charge, at least one of which had $p_T > 1$ GeV. The invariant mass of the track pair, as determined with the standard ZEUS offline tracking package VCTRAK, must be such that $3.0 < M_{\mu\mu} < 3.2$ GeV. This ensures a clean sample of $J/\Psi \rightarrow \mu\mu$ events is selected. Figure 5.9 shows an invariant mass spectrum of this sample as seen by both the GTT and offline tracking packages. It was necessary to compromise the GTT resolution in favour of faster track finding given the time constraints present at the SLT level.

An unbiased selection of passthrough events is required to determine a trigger rate. In this thesis, rate is given in arbitrary units and is simply the total number of passthrough events flagged by a trigger. There are 2 types of passthrough events: FLT and SLT passthroughs.

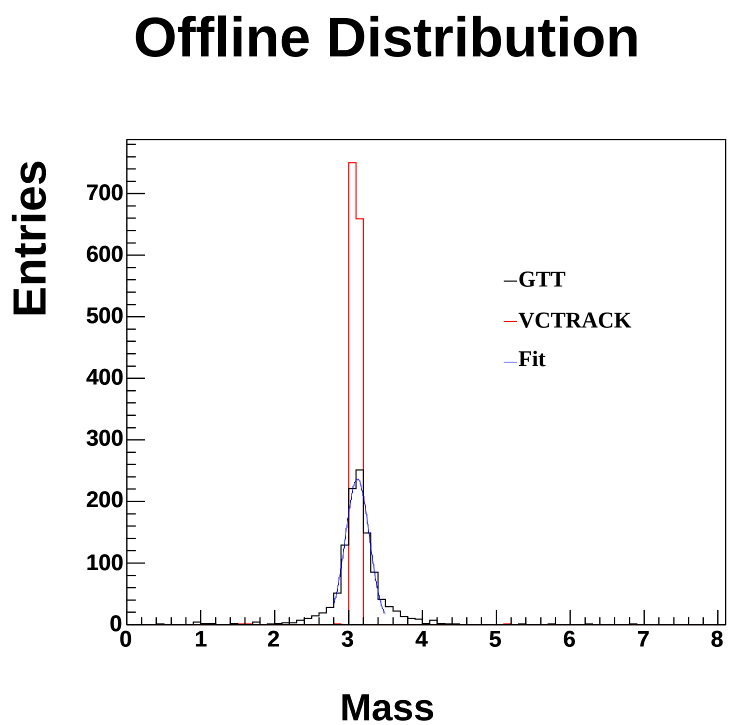

Figure 5.9: GTT (black) and VCTRACK (red) mass spectrum of offline J/Ψ sample with fit shown in blue.

A FLT passthrough is a selection of events as seen by the FLT, or more precisely a selection of events on which no cuts at all are placed. A SLT passthrough is a selection of events whose only requirement is that they passed the FLT. Passthrough events are given special passage through the trigger system in that they are not required to be accepted by any other trigger. This is a useful property when conducting studies into the trigger rates since they provide insight into what the trigger will encounter online. A total of 84082 passthrough events were selected for this analysis. The invariant mass spectrum for these events is given in figure 5.10.

Prior to the implementation of our J/Ψ trigger, J/Ψs were detected at the SLT by triggers drawing on a series of energy cleaning cuts and requiring detection of a lepton. A more detailed outline of the operation of the triggers (specifically GTT05, HFL19, MU02 and SPP04) may be found in appendix A. It is against these existing triggers that the

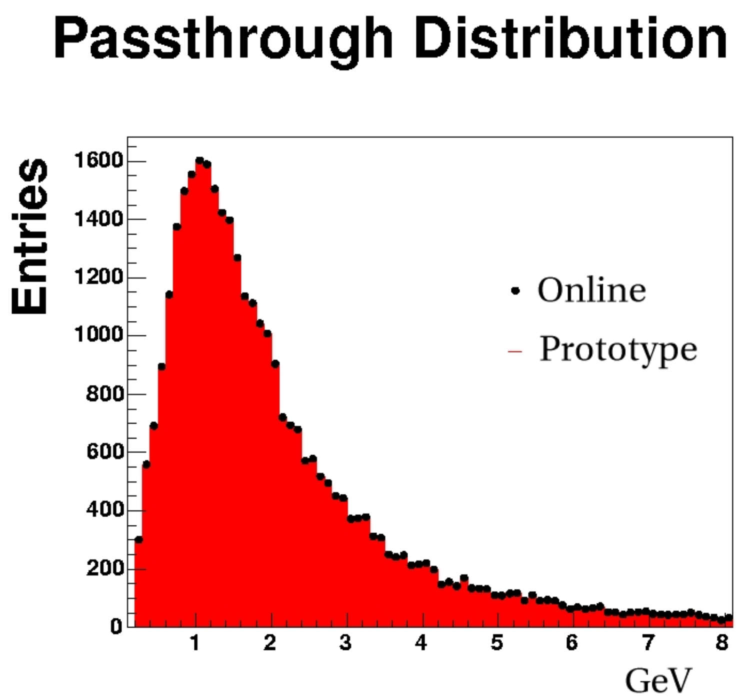

Figure 5.10: GTT mass spectrum of SLT Passthrough events. Online implemented code (black) and the offline prototype (red) are shown and match perfectly.

performance in terms of rate and efficiency on which the GTT μ trigger is compared.

5.6.2 GTT J/Ψ online trigger rates and efficiencies

The GTT J/Ψ algorithm if left unconstrained will trigger events at a rate 10 times higher than the existing SLT trigger slots. It is clear therefore that some additional constraint must be placed upon the trigger which will reduce the rate and yet preserve efficiency, as measured by the clean J/Ψ data sample defined above.

The results of section 5.5.2 indicate that efficiency is most sensitive to an invariant mass cut. Therefore in this section two methods of rate constraint are proposed; both of which define a region in which the returned mass from the GTT J/Ψ algorithm is accepted. A lower limit is first defined below which events are rejected. The effect of raising this limit from zero is seen in figure 5.11. It can be seen that when the lower limit is zeroed the measured rate is far from acceptable at 6 times higher than the high-rate GTT05. Increasing the lower limit rapidly reduces the rate, however at $M_{\text{lower}} = 4$ where $\text{Rate}_{\text{GTT J/}\Psi} = \text{Rate}_{\text{GTT05}}$ an efficiency of around 5% is measured. Study of figure 5.11 indicates that the GTT J/Ψ algorithm operates with the highest efficiency (85%) until the lower limit approaches $M_{\text{J/}\Psi}$ when understandably it falls rapidly. Prior to this drop however the rate is still unacceptably high at roughly twice that of GTT05. This method of restraint is therefore considered not suitable for a J/Ψ trigger, more suitable instead for the high mass Υ trigger.

In the second method a mass window is defined centered about $M_{J/\Psi} = 3.1$ GeV such that accepted events satisfy

$$3.1 - M_{\text{Dev}} < M_{GTT\ J/\Psi} < 3.1 + M_{\text{Dev}}.$$

In this instance $M_{GTT\ J/\Psi}$ is the mass returned by the GTT J/Ψ trigger algorithm. The effect on rate and efficiency of expanding the parameter M_{Dev} is shown in figure 5.12. At even the lowest tested deviation of 0.1 GeV the efficiency is superior to MU02 and HFL19 at 40%, 30% and 20% respectively. At this mass there is still room for manoeuvre in that only a third of the budget for rate is harnessed. A mass window of 3.1 ± 0.8 GeV provides the lowest rate that preserves the existing efficiency levels, however the rate overshoots that of the existing triggers by 50%. The most reasonable balance is struck with a range of 3.1 ± 0.5 GeV at which point the rate is equal to that of a typical trigger system and an efficiency of around 65% is recorded, a drop of only 10% from the maximum available. This corresponds to the findings of section 5.5.2.

The real benefits do not come from matching rates and efficiencies, but rather from exclusive selection of J/Ψ events. That is to say that the J/Ψs detected by the GTT are often different from those detected by the existing triggers. A combination of triggers would therefore noticeably improve statistics when figure 5.13 is considered. To quantify this increase we first define the form of the GTT J/Ψ trigger to be used. The decision was taken to implement the mass range which struck the most reasonable balance between rate and efficiency, passing only events for which the evaluated trigger mass fell in the range of 3.1 ± 0.5. The Venn diagram in 5.13 indicates that 18.7% of the J/Ψ sample consists of events which activate both the GTT and HFL19 triggers, 46.3% are triggered *exclusively* by

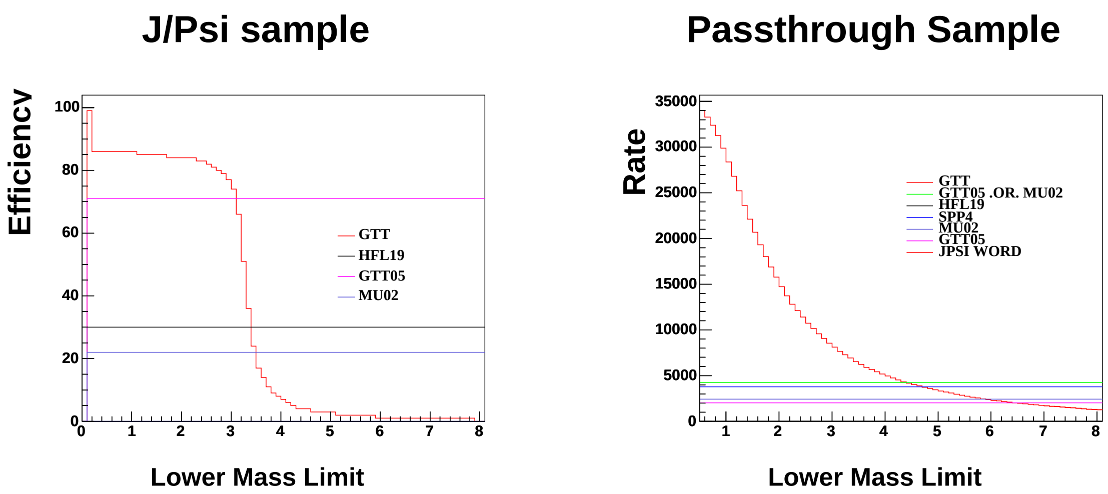

Figure 5.11: Efficiencies and rates of standard SLT triggers (indicated by coloured lines) compared to the GTT J/Ψ trigger (red) as a function of lower mass limit. Rates were tested on a sample of SLT passthroughs and efficiencies on an offline selection of J/Ψ events.

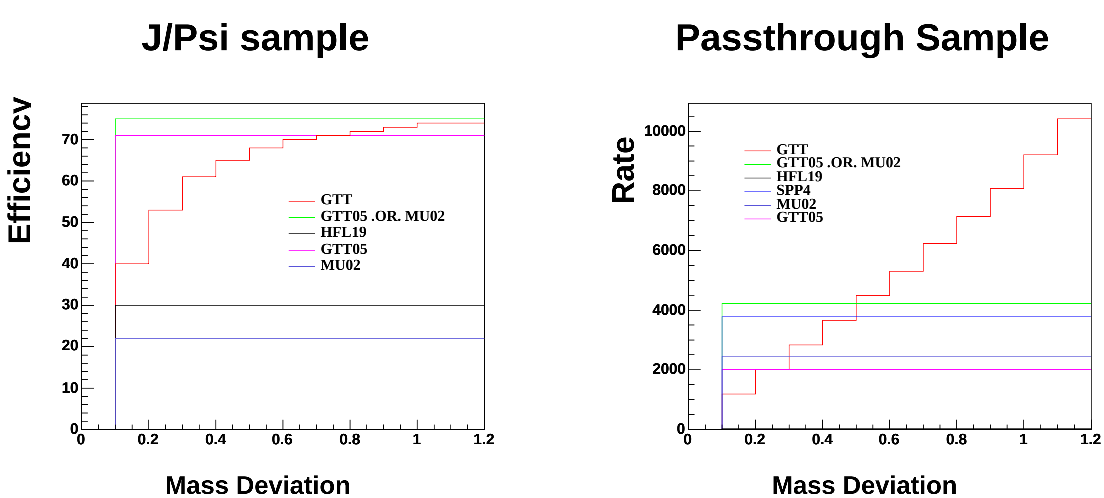

Figure 5.12: Efficiencies and rates of standard SLT triggers (indicated by coloured lines) compared to the GTT J/Ψ trigger (red) as a function of mass window. Rates were tested on a sample of SLT passthroughs and efficiencies on an offline selection of J/Ψ events.

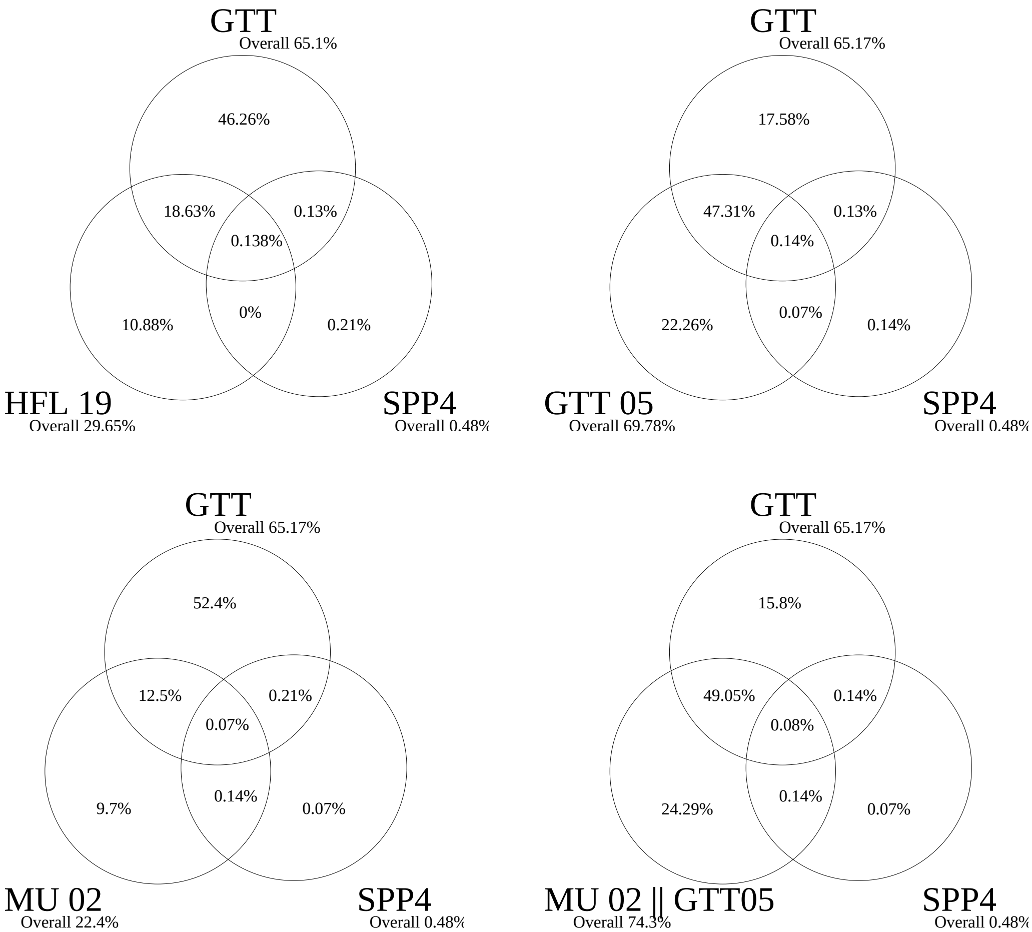

Figure 5.13: Venn diagrams showing the efficiencies of different trigger combinations for tagging clean J/Ψ events.

the GTT trigger and only 10.8% are triggered *only* by HFL19. This means that for every 100 J/Ψs present HFL19 only detects $10.8 + 18.7$. Introduction of the new GTT trigger detects an *additional* 46.3 J/Ψ events. Similarly the GTT detects an *additional* 52.6 and 17.7 J/Ψs for every $12.5 + 9.8$ and $47.5 + 22.3$ detected by MU02 and GTT05 respectively. The statistical advantage gained by using the GTT extends therefore from an increase of 17.7% to 52.6% additional J/Ψ events.

The number of events in the passthrough sample (figure 5.14) flagged by the GTT J/Ψ trigger comprise a selection missed by the standard triggers. Indeed between 15% and 52% of J/Ψs are found by the GTT *exclusively*, and between 0.2% and 25% are found *exclusively* by the other triggers. The overlap region ranges from 12.5% to 49.1%, and occasionally no

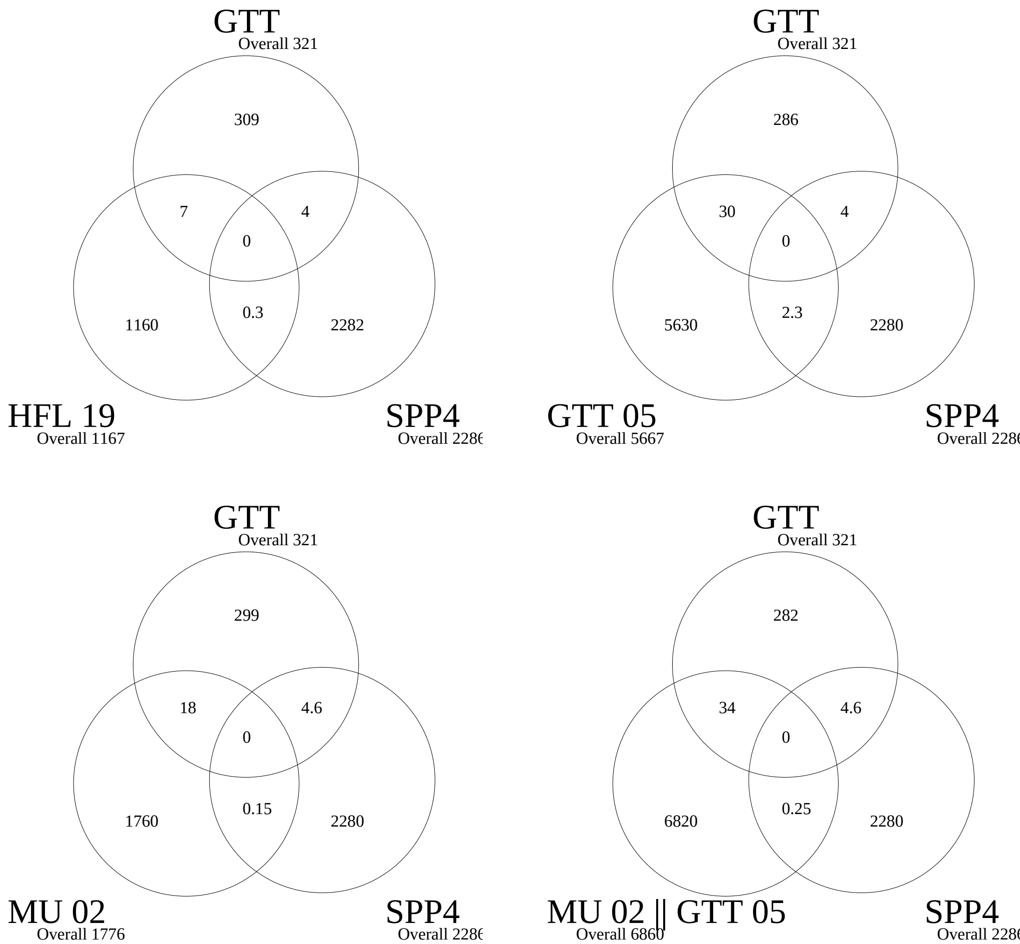

Figure 5.14: Venn diagrams showing the relative rates of trigger combinations for ≈ 700000 SLT Passthrough Events.

SLT trigger detects the event.

This clearly demonstrates that statistical advantages may be gained by using this trigger system and at rates and efficiencies compatible with those already in operation at ZEUS. Indeed as many as 52.6% of the events triggered with this algorithm are unique and so when used in tandem with other triggers statistics could be increased by just over 50% in favorable conditions. This benefit was reduced to an increase of 15.9 when compared to an 'OR' of GTT05 and MU02, although a significant gain is still achieved. Overall at a cost of a 5% increase in rate there is a 50% increase in efficiency when the GTT J/Ψ trigger is used.

5.6.3 Upsilon Proposal

The same system may in principle be used as an Υ trigger. It is clear that no adjustments are needed to the GTT J/Ψ algorithm, only to the prescribed mass window in which the trigger will fire. For the Υ trigger it is recommended that the *lower mass limit* method is implemented as indicated in figure 5.15, above 7 GeV so as not to cut into the signal at $M_\Upsilon = 9.46$ GeV. At this level the rate is comparable with the GTT05 trigger, which is the trigger considered here with the lowest rate. A rate two thirds that of GTT05 may be obtained by raising this limit to 8 GeV although any further restriction will result in a loss of signal and efficiency as seen in the J/Ψ study. A limit has yet to be placed online, giving physics groups the freedom to determine their own cut off value for implementation.

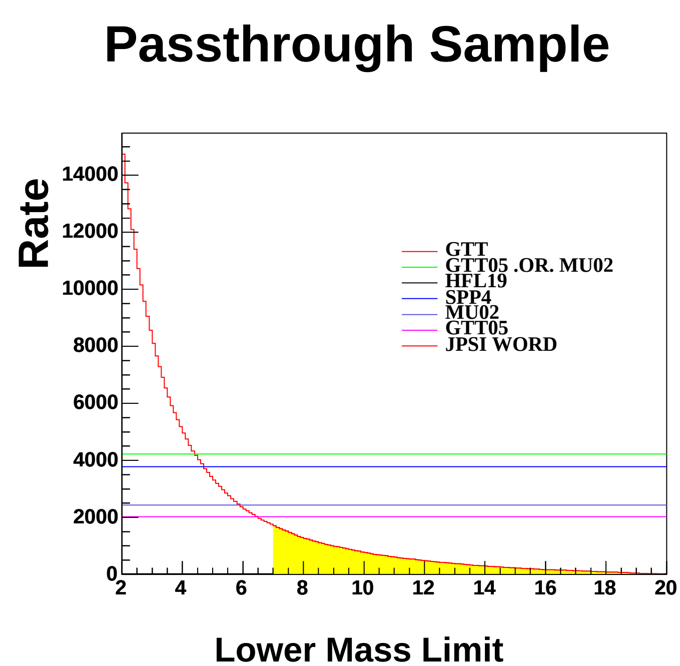

Figure 5.15: Region recommended for Υ flagging highlighted in yellow. The GTT Υ trigger rate (red) is measured in arbitrary units relative to existing triggers shown in the remaining coloured lines. A SLT passthrough sample was used to determine the rate.

5.7 Summary

In this chapter a feasibility study concerning the use of the Global Tracking Trigger (GTT) to select J/Ψ events was conducted. After an overview of the ZEUS tracking system and a discussion of the operation of the GTT the principles of the proposed invariant mass trigger were selected. After an efficiency, signal to noise and trigger rate study it was recommended that events should be selected if the computed invariant mass falls within $2.6 < M_{J/\Psi} < 3.6$. This J/Ψ trigger developed in this chapter can be used to flag unique J/Ψ events that would not have been found using existing triggers. Statistics may be improved by as much as 50% if this trigger is used in conjunction with them. This invariant mass trigger quantity has been installed online and is ready for use by the physics groups.

Chapter 6

Event Reconstruction

This chapter describes how a selection of important event kinematics are reconstructed at ZEUS and quantifies the extent to which MC faithfully replicates how these quantities appear in data. It opens with a brief study of the MC description of the trigger chain to determine whether a trigger-based systematic error is required. This is followed by definitions of the Double Angle, Electron and Jacquet-Blondel methods of reconstructing x, y and Q^2 and measurements of their resolution, purity and efficiency. The hadronic and electron energy scales necessary to improve MC description of the data are then defined and justified, followed by an explicit statement of the event selection cuts. The chapter concludes with a comparison of control plots between RAPGAP and HERWIG to determine which shall be the principal MC for extracting cross-sections.

6.1 Trigger study

The DIS event sample used in this analysis was selected using triggers at the first and third level of the ZEUS trigger system. The event was required to fire any one of FLT triggers 30, 34, 36, 44 or 46 and either of the TLT triggers SPP02 or HFL02. If the event passed both of these trigger levels it was included in the data sample. The definitions of these triggers are given in appendix A.2.1, although broadly speaking the FLT triggers require an energy deposit somewhere in the detector (with the exception of FLT 46 which also has a tracking requirement), and the TLT triggers require either the presence of a D meson or for the event to have passed a number of standard DIS selection cuts.

The FLT trigger configuration used in this analysis is therefore simply an OR of each of the FLT triggers listed above. To measure the degree to which the MC models the trigger response seen in data one trigger was removed from the FLT chain and the amount of events lost was recorded. This measurement is made in the $(Q^2 - y)$ bins from which $F_2^{c\bar{c}}$ will be extracted in this thesis. The results are shown in figures 6.1 to 6.5 using a scale in which a value of 0.95 corresponds to a loss of 5% of the total events that fired the standard trigger configuration. In every bin and for every trigger there is excellent agreement between MC and DATA, with typical disagreement of the order of a few %. The largest disagreement is never greater than 5% although such figures are rare and occur only in isolated bins. The same measurements are repeated for the TLT triggers and the results are given in figures 6.6 and 6.7 showing excellent agreement between MC and DATA in all bins.

In conclusion the removal of one trigger is carefully balanced by the presence of other triggers and the response to its removal is well described by Monte Carlo; in almost every bin the relative rate stays between 95% and 100% for both MC and data. Because the MC and data are in good agreement it is therefore not necessary to include a systematic error based on trigger effects in this analysis and the matter is not considered further.

6.2 Reconstruction of Event Kinematics

The kinematics of a DIS event may be specified with any two of the Lorentz invariant variables specified in section 2.1. To reconstruct these variables the ZEUS detector measures the scattered electron energy, E'_e, its polar angle, θ_e and the transverse and longitudinal momentum of the hadronic final state. This information may be arranged in a number of configurations to reconstruct the kinematic variables. The method of reconstruction chosen depends on resolution and migration issues in the measured kinematic region. This section will review the definitions of the electron, double angle and Jacquet-Blondel methods of reconstruction used in this analysis.

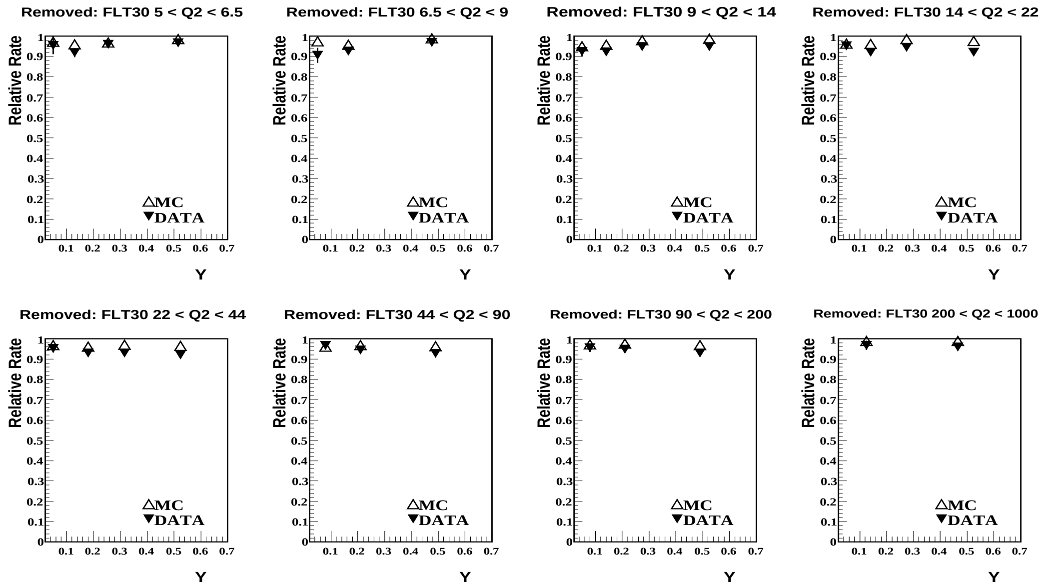

Figure 6.1: The fraction of total FLT events passed when FLT 30 is removed from the FLT trigger chain in $Q^2 - y$ bins. The MC rates are represented by open triangles and the DATA rates are represented by solid triangles.

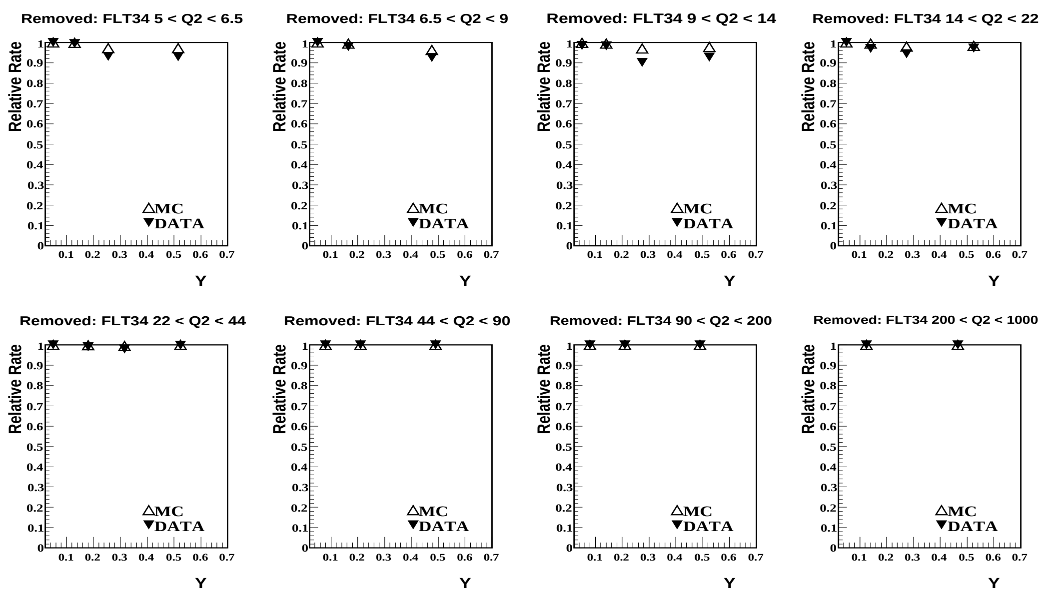

Figure 6.2: The fraction of total FLT events passed when FLT 34 is removed from the FLT trigger chain in $Q^2 - y$ bins. The MC rates are represented by open triangles and the DATA rates are represented by solid triangles.

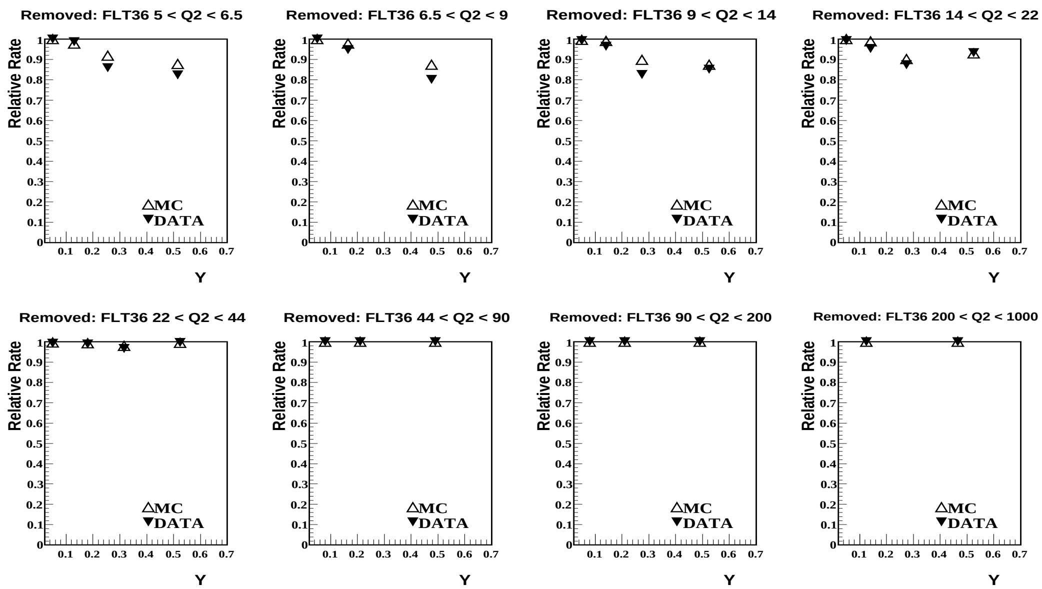

Figure 6.3: The fraction of total FLT events passed when FLT 36 is removed from the FLT trigger chain in $Q^2 - y$ bins. The MC rates are represented by open triangles and the DATA rates are represented by solid triangles.

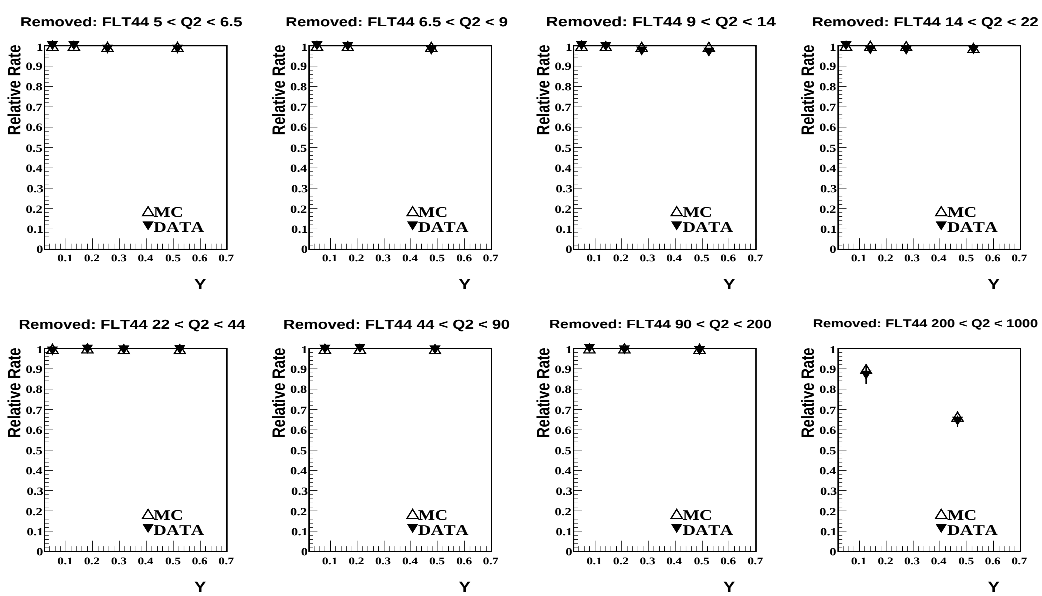

Figure 6.4: The fraction of total FLT events passed when FLT 44 is removed from the FLT trigger chain in $Q^2 - y$ bins. The MC rates are represented by open triangles and the DATA rates are represented by solid triangles.

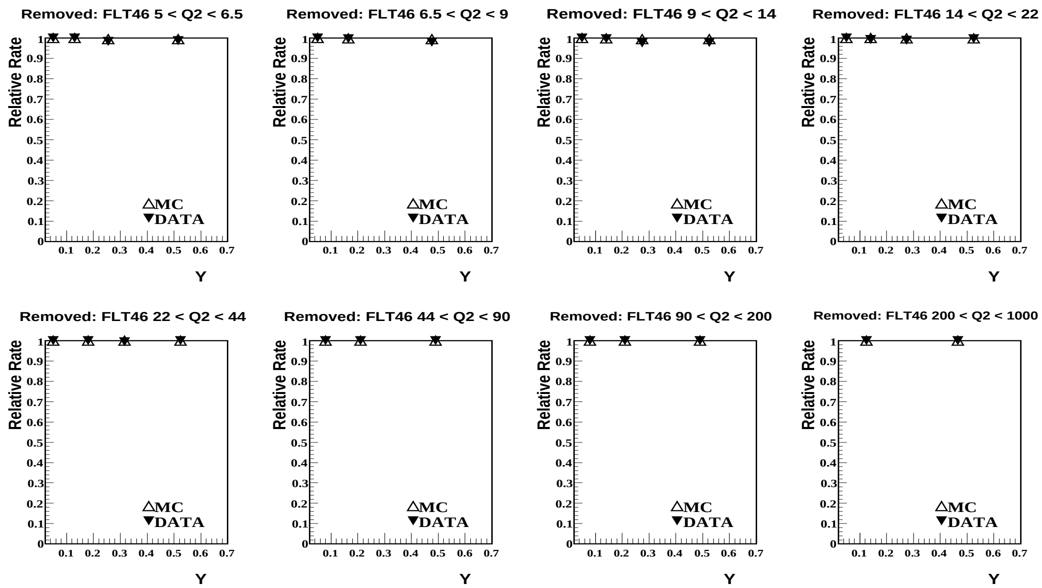

Figure 6.5: The fraction of total FLT events passed when FLT 46 is removed from the FLT trigger chain in $Q^2 - y$ bins. The MC rates are represented by open triangles and the DATA rates are represented by solid triangles.

6.2.1 The Electron Method

The Electron method reconstructs the event variables using only information about the scattered electron. It is therefore important when using this method to ensure that the electron is well identified and reconstructed. The electron method is sensitive to initial and final state radiation since it assumes that the incoming energy is that of the beam. The required quantities are the scattered electron energy ($E_{e'}$) and the angle of scatter (θ_e)

$$x_e = E_e E_{e'} \left(\frac{1 - \cos\theta_e}{2E_p E_e - E_p E_{e'}(1 - \cos\theta_e)} \right)$$

$$y_e = 1 - E_{e'} \left(\frac{1 - \cos\theta_e}{2E_e} \right)$$

$$Q_e^2 = 2E_e E_{e'}(1 + \cos\theta_e)$$

θ_e is defined as the angle between the scattered electron and the z-axis as illustrated in figure 6.8 and E_p, E_e are the positron and electron beam energies respectively. Fake electron deposits are caused by hadronic activity in photoproduction events and contribute to a high y_{el} value. These can be rejected with a cut on y_{el} which helps select a purely DIS sample.

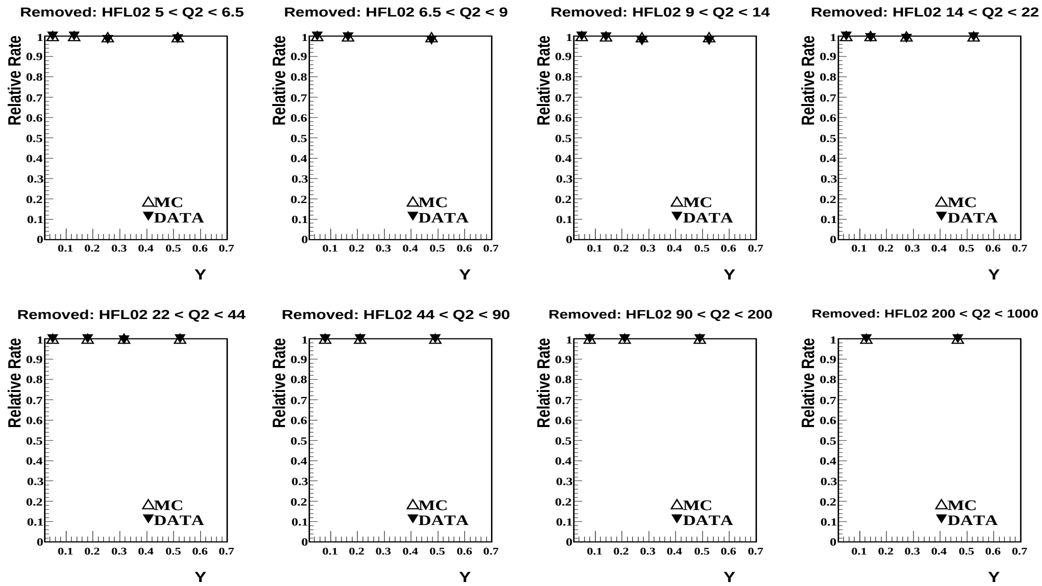

Figure 6.6: The fraction of total TLT events passed when HFL 02 is removed from the TLT trigger chain in $Q^2 - y$ bins. The MC rates are represented by open triangles and the DATA rates are represented by solid triangles.

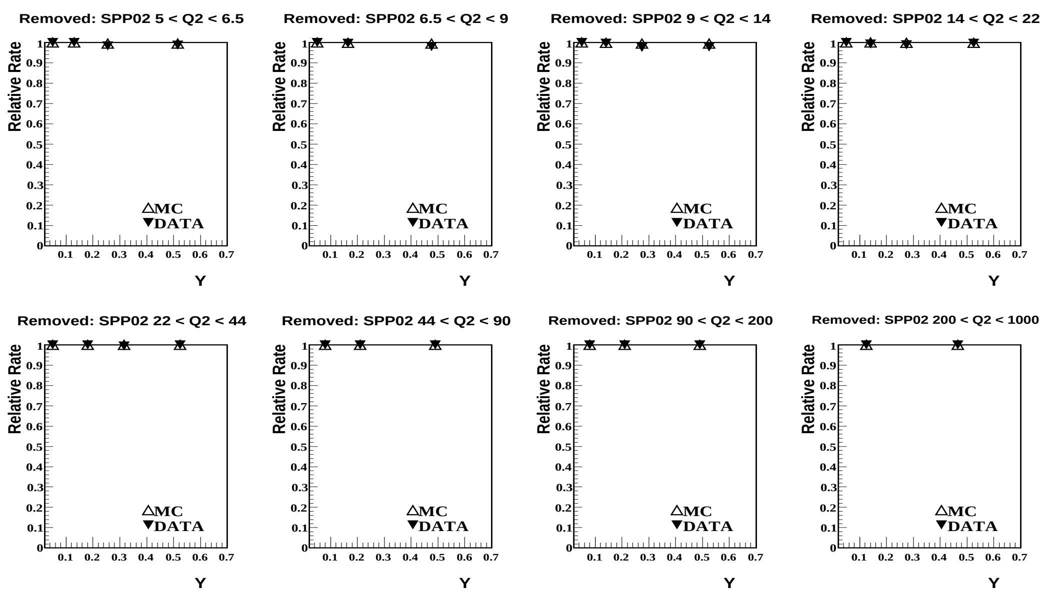

Figure 6.7: The fraction of total TLT events passed when SPP 02 is removed from the TLT trigger chain in $Q^2 - y$ bins. The MC rates are represented by open triangles and the DATA rates are represented by solid triangles.

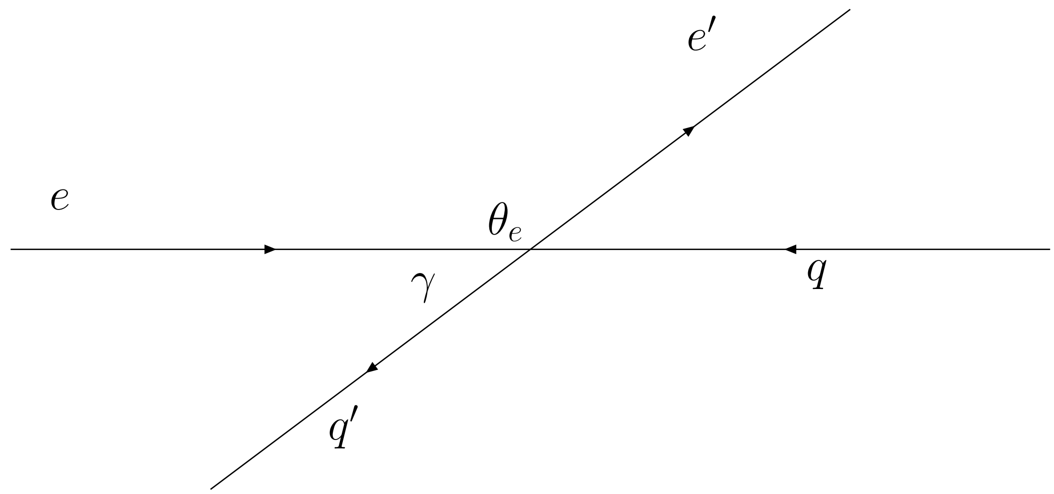

Figure 6.8: Diagram illustrating the scattering angle θ_e of an electron interacting with quark q. The hadronic scattering angle γ is also shown.

6.2.2 The Jacquet-Blondel Method

The Jacquet-Blondel (JB) method [46] is similar in principle to the electron method although it relies only on measurements of the hadronic system. Where in the electron method a measurement was made of the lepton scattering angle and energy, the JB method measures the scattered quarks' angle and energy. Since this may not be measured directly it is naively assumed that the quark originally followed the same path as the jet of particles it inspired. In this thesis JB is only used to reconstruct y by

$$y_{JB} = \frac{\delta_h}{2E_e}$$

where δ_h is the hadronic $E - P_z$ contribution

$$\delta_h = \sum_h (E - p_z)$$

whose sum runs over the energy deposits of all final state hadrons in the CAL.

This method is sensitive to the hadronic energy scale and so requires that the entire hadronic system is contained. It is often used in photoproduction selections where information on the lepton is typically lost since energy losses down the forward beampipe do not contribute much to y. y_{JB} is an excellent measure of hadronic activity and since D^* events will have a hadronic signal of at least $M_{D*} = 2$ GeV, a cut of $y_{JB} \approx 0.04$ will reject a significant amount of background activity. In this thesis a cut of $y_{JB} > 0.02$ is applied to reject events that would have insufficient hadronic activity to be amenable to the Double Angle method.

6.2.3 The Double Angle Method

The double angle (DA) method provides a good reconstruction over a wide kinematic range. The DA method measures the electron polar angle and the hadronic angle γ which in LO DIS approximates to the scattering angle of the struck quark (as illustrated in figure 6.8) and where

$$\cos\gamma = \frac{(\sum_h P_{x,h})^2 + (\sum_h P_{y,h})^2 - (\sum_h (E - p_z))^2}{(\sum_h P_{x,h})^2 + (\sum_h P_{y,h})^2 + (\sum_h (E - p_z))^2} = \frac{P_{\perp,h}^2 - \delta_h^2}{P_{\perp,h}^2 + \delta_h^2}$$

for which $\sum_h$ runs over the hadronic energy deposits in the CAL. To ensure that sufficient hadronic activity exists in the event for γ to be well reconstructed a cut of $y_{JB} > 0.02$ is imposed as a detector cut. x, y and Q^2 are expressed in terms of γ in the following relations:

$$x_{DA} = \frac{E_e}{E_p} \frac{\sin\gamma + \sin\theta_e + \sin(\theta_e + \gamma)}{\sin\gamma + \sin\theta_e - \sin(\theta_e + \gamma)}$$

$$y_{DA} = \sin\theta_e \frac{1 - \cos\gamma}{\sin\gamma + \sin\theta_e - \sin(\theta_e + \gamma)}$$

$$Q^2_{DA} = 4E_e^2 \sin\gamma \frac{1 + \cos\gamma}{\sin\gamma + \sin\theta_e - \sin(\theta_e + \gamma)}$$

The double angle method has the advantage of being relatively insensitive to the electron energy scales and is only slightly affected by radiative corrections.

6.3 Resolution of Electron, Jacquet-Blondel and Double Angle reconstructions

To select the most appropriate method of reconstructing Q^2 and y their resolutions were measured in a number of (Q^2, y) bins. The resolution in (Q^2, y) bin i, σ_i, is a measure of the spread of difference between the true and reconstructed values. It is defined as

$$\sigma_i = \sigma\left(\frac{\text{True} - \text{Rec}}{\text{True}}\right)$$

and is identified as the width of a gaussian fit to the (True $-$ Rec)/True distribution in each bin i. In this thesis the resolution was measured using the same 484 pb^{-1} of RAPGAP MC as used in chapter 8 to measure $F_2^{c\bar{c}}$. The resolution is evaluated for measurements of Q^2, x and y for all three reconstruction techniques listed in the previous section, although only Q^2 and y resolutions are shown here since the others are not directly relevant to this thesis.

The resolutions are evaluated in (y, Q^2) bins identical to those used in the extraction of $F_2^{c\bar{c}}$. The position of these bins in the (Q^2, x) kinematic plane is given in figure 6.9, the resolutions given in this thesis are shown as a grid of gaussian distributions arranged as shown by the lower half of this figure. This figure indicates how the position of the resolution plots in the format used in this thesis correspond to the kinematic regions measured. Generally speaking Q^2 increases along the y axis and y increases along the x axis, although the bin sizes themselves are variable.

Figure 6.10 is the resolution of Q^2 as measured by the double angle method. The resolution improves with increasing Q^2, falling from 10% in the lowest y, lowest Q^2 bin to 3% in the lowest y, highest Q^2 bin. Resolution decreases with increasing y and becomes as poor as 20% in the lowest Q^2 highest y region. The double angle method outperforms the electron method in the lower y region but is poorer at higher y, generally producing resolutions of around 9% in most bins.

Measuring y using the electron method shows poor (63%) resolution in the lowest Q^2 and y bin (figure 6.13). This increases with rising Q^2 to a maximum of 40%, and also improves with rising y to resolutions of the order of 10%. The double angle method (figure 6.12) follows similar trends but is superior in most low y bins, particularly in the low Q^2 low y region where it has a resolution of 31%. At high Q^2 we see a resolution as low as 8% and at low Q^2 as low as 25%. The electron method gives a better resolution in the highest y region and so to improve overall resolution a composite system of the two methods could be introduced. This would however introduce complications in the overlap region of the two methods and so is not considered in this analysis. The Jacquet Blondel method is useful for reconstructing the y parameter as indicated by the distributions in figure 6.14. Unlike JB reconstructions of x and Q^2 the y distributions are gaussian in every bin. In particular the JB reconstruction of y is the best out of all three methods for reconstructing in the lowest y

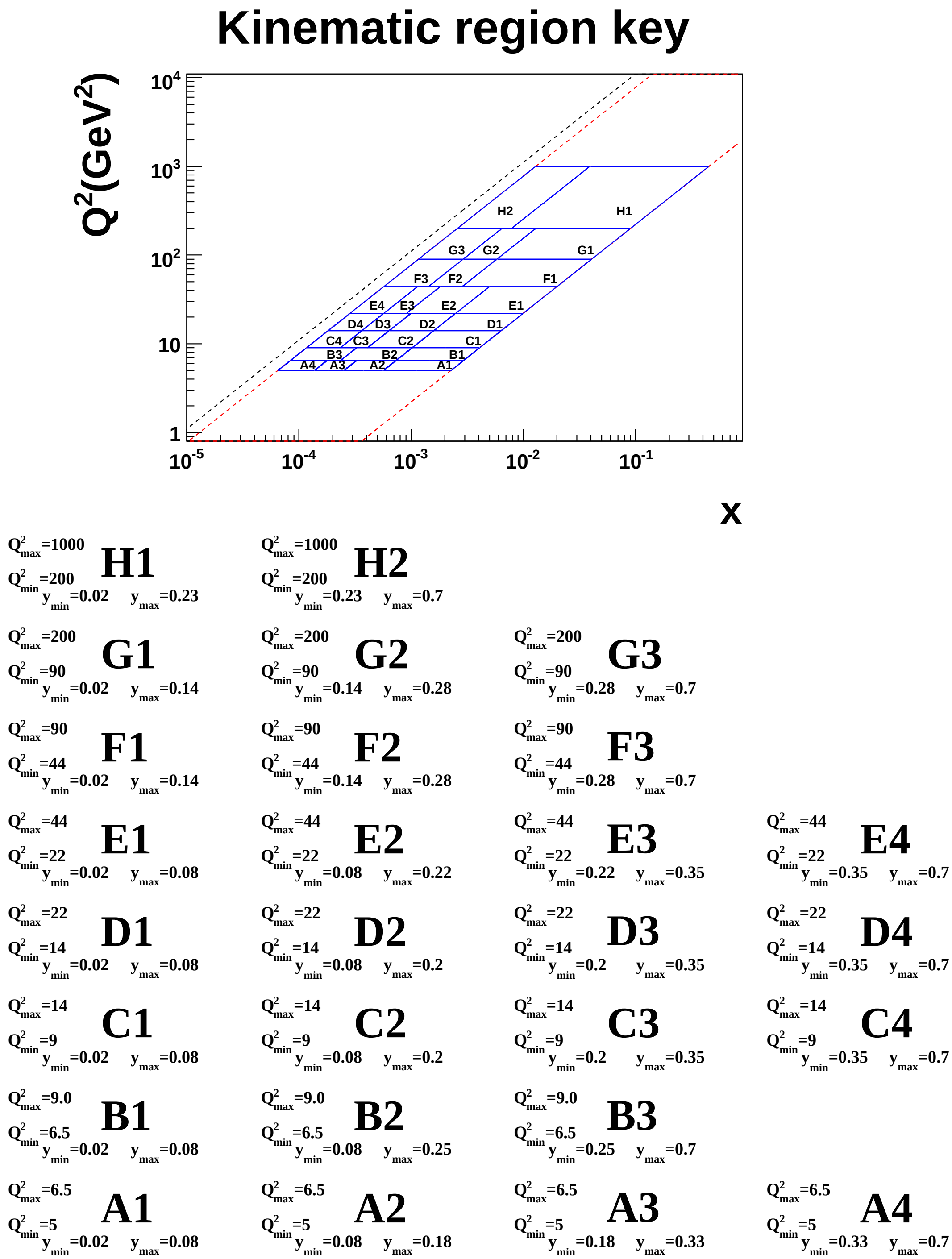

Figure 6.9: The (Q^2, x) kinematic plane identifying the bins in which $\sigma(D^*)$ is extracted (above) and the corresponding position of these bins in the format in which the resolution plots are given in this thesis (below).

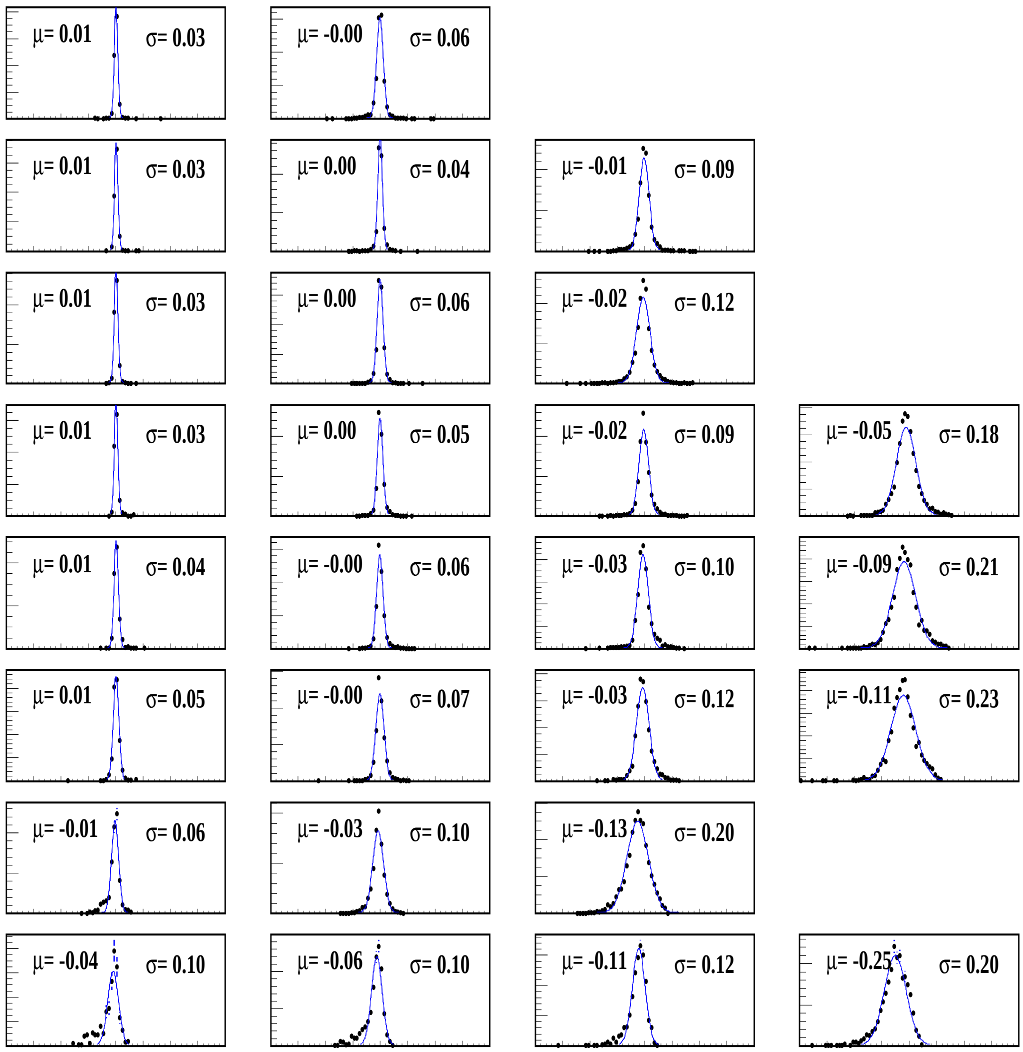

Figure 6.10: Q^2 resolution using the double angle method in bins of Q^2 and y. Q^2 increases vertically and y increases horizontally. The x-axis (not shown) runs from -2 to $+2$.

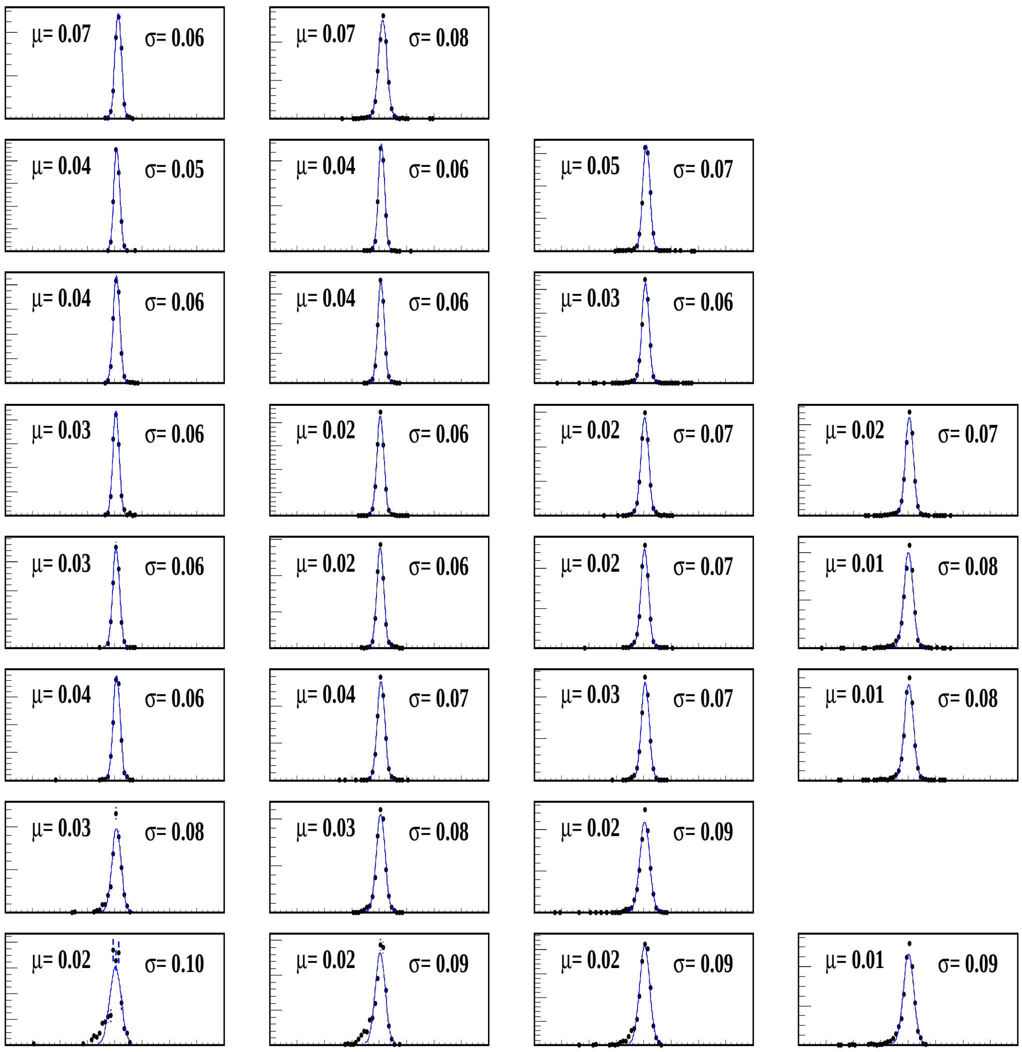

Figure 6.11: Q^2 resolution using the electron method in bins of Q^2 and y. Q^2 increases vertically and y increases horizontally. The x-axis (not shown) runs from -2 to $+2$.

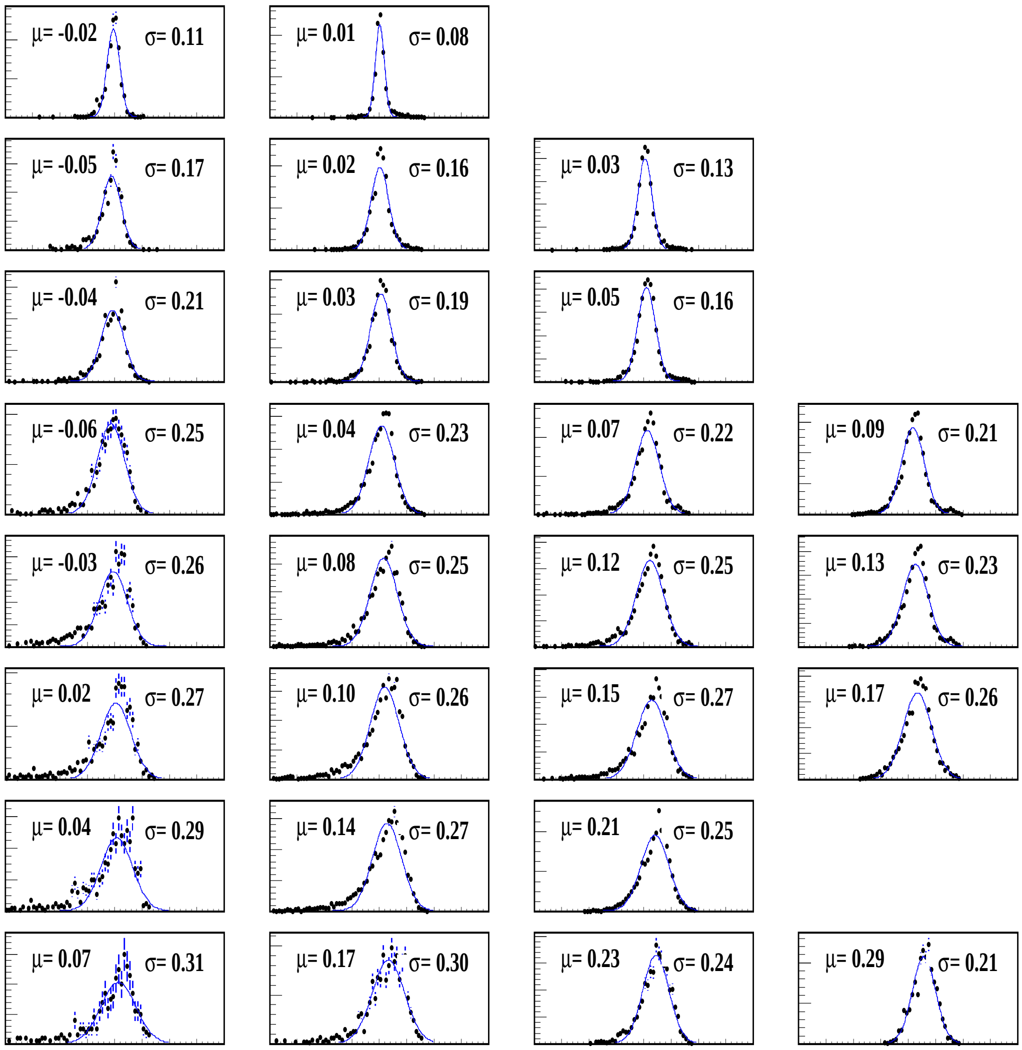

Figure 6.12: y resolution using the double angle method in bins of Q^2 and y. Q^2 increases vertically and y increases horizontally. The x-axis (not shown) runs from -2 to $+2$.

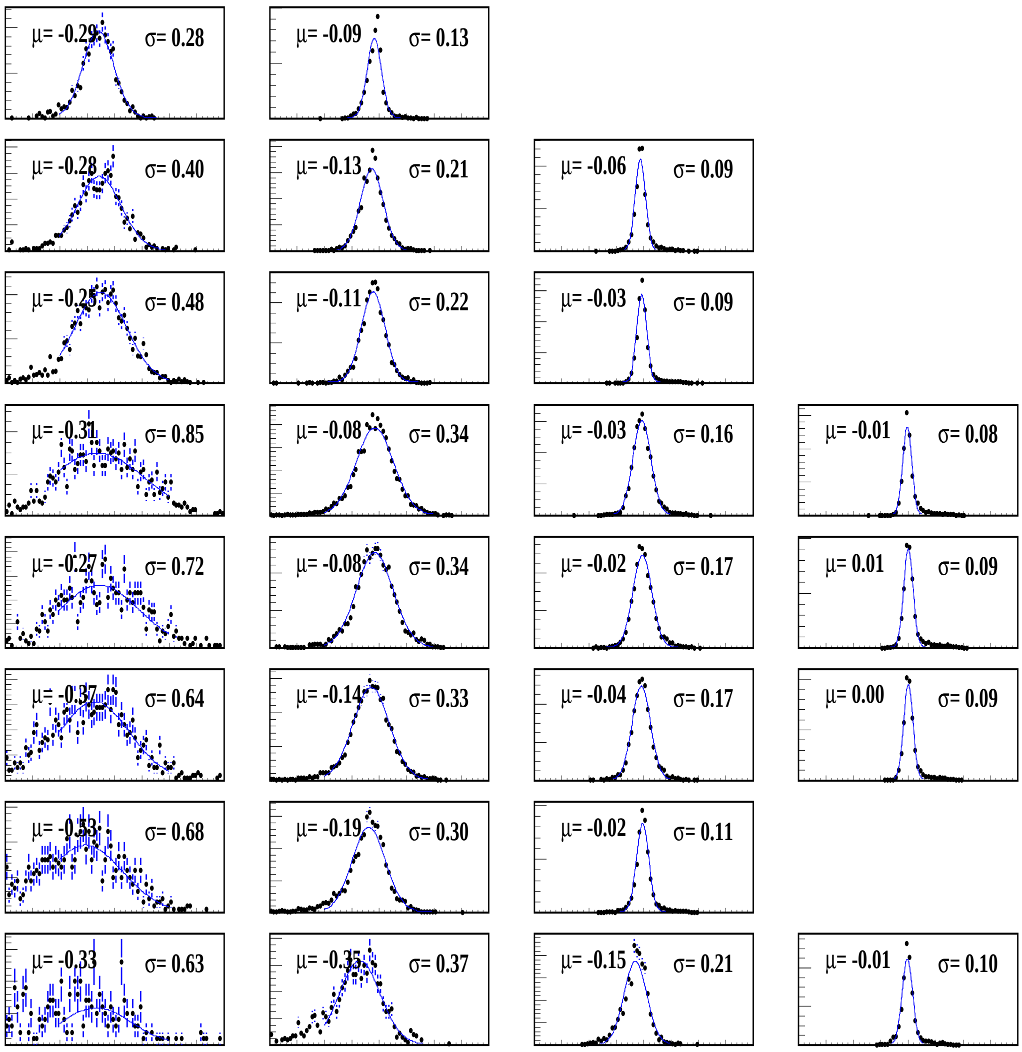

Figure 6.13: y resolution using the electron method in bins of Q^2 and y. Q^2 increases vertically and y increases horizontally. The x-axis (not shown) runs from -2 to $+2$.

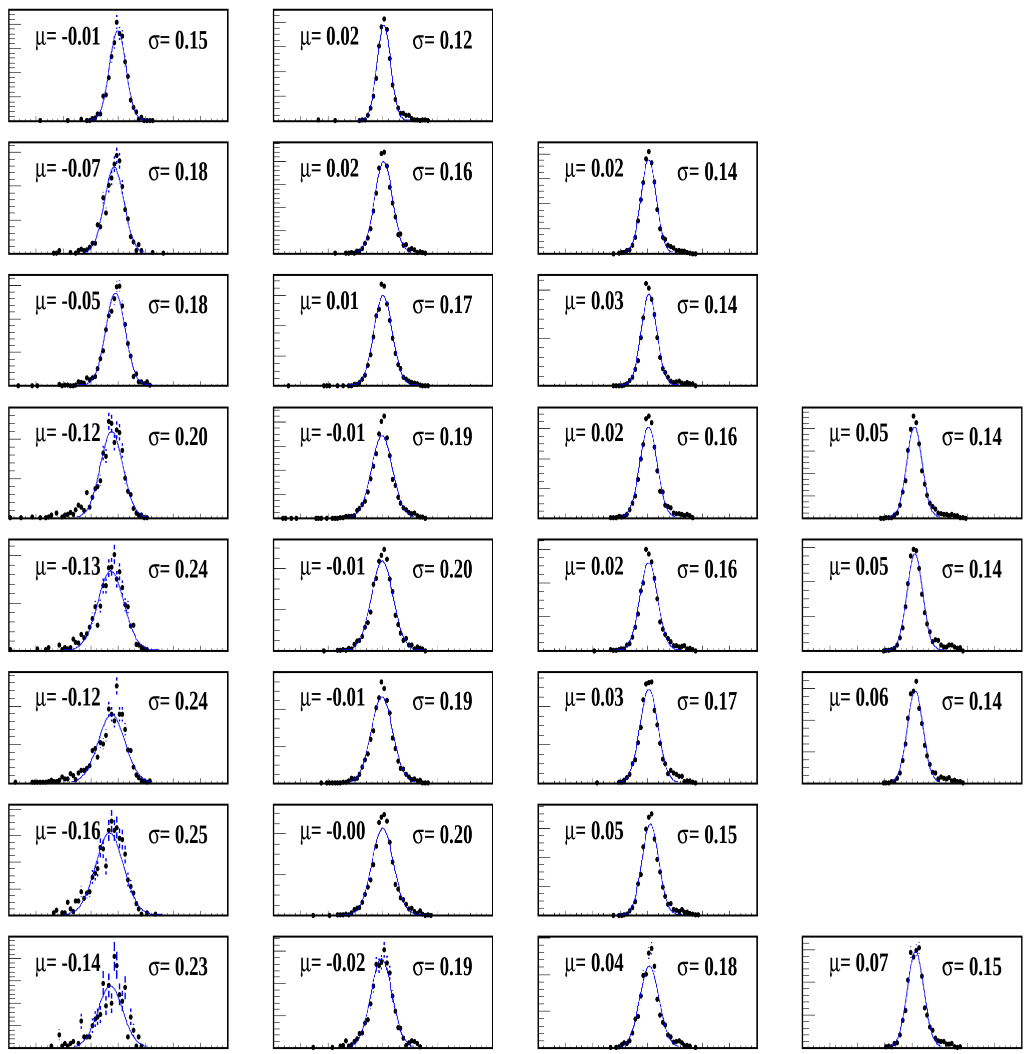

Figure 6.14: y resolution using the Jacquet-Blondel method in bins of Q^2 and y. Q^2 increases vertically and y increases horizontally. The x-axis (not shown) runs from -2 to $+2$.

bins. For low Q^2 low y where the electron method struggles, the JB method has a resolution of 23%, sufficient to enable a default cut at $y_{JB} > 0.02$. In conclusion the double angle method typically gives a superior resolution to the electron and JB method. Therefore in the data selection the double angle method is used with $5 < Q^2 < 1000$ GeV^2 and $y < 0.7$ cuts. The JB method has good resolution at low y and so is utilised in the $y > 0.02$ cut to ensure that there is a minimum hadronic activity in the event. An additional $y_{el} < 0.95$ DIS cleaning cut is also placed using the electron method.

6.4 Efficiency, purity and acceptances of reconstruction methods

The purity of a sample in any given bin is defined as the fraction of events generated *and* reconstructed in a particular bin over those reconstructed in that bin. For any bin i purity P_i is therefore given by

$$P_i = \frac{N_i^{Gen} \cap N_i^{Rec}}{N_i^{Rec}}$$

where N_i^{Rec} is the number of events reconstructed in the bin and N_i^{Gen} is the number generated in that bin. Similarly efficiency is defined as

$$E_i = \frac{N_i^{Gen} \cap N_i^{Rec}}{N_i^{Gen}}$$

where N_i^{Rec} and N_i^{Gen} are defined as before and $\cap$ represents the overlap of events generated *and* reconstructed in the i^{th} bin. Measurements of purity and efficiency are useful indicators of whether the chosen bin sizes are suitable and gauge the level of migration of true level events between bins. Events which are reconstructed with low efficiencies will rely more heavily on the MC simulation to accurately describe the event; this situation is undesirable if one wishes to produce a reliable measurement independent of the choice of MC package used. Detector inefficiencies in cross section measurements are corrected using the $1/A_i$ factor where A_i is the acceptance and is related to purity and efficiency by

$$\frac{1}{A_i} = \frac{P_i}{E_i} \tag{6.1}$$

The acceptances used in the measurement of $F_2^{c\bar{c}}$ are discussed in more detail in chapter 8.

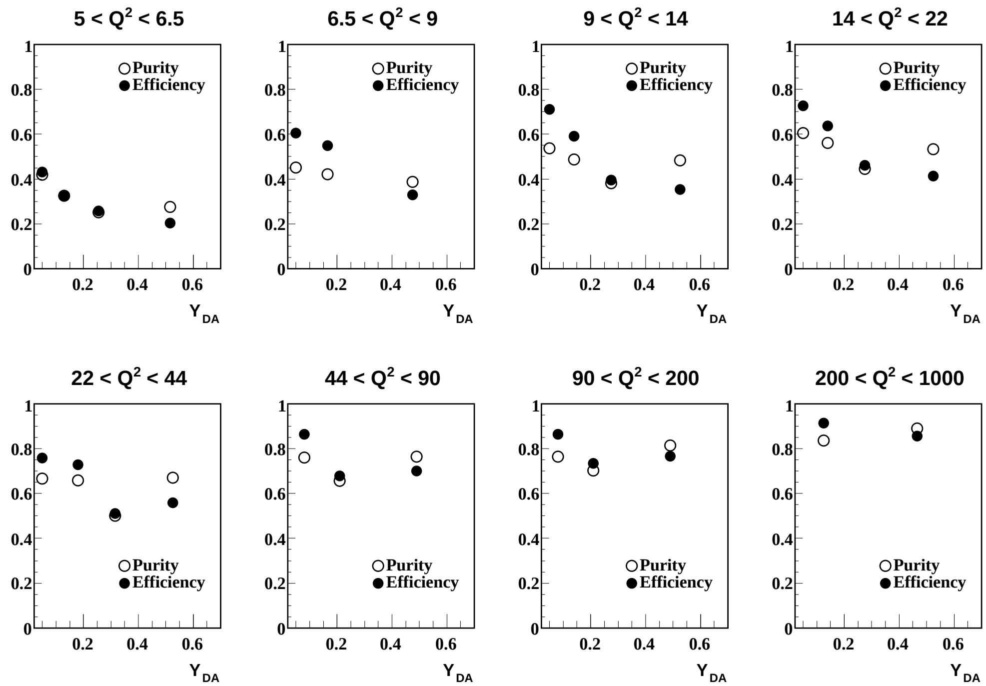

Figure 6.15: Purity (open circles) and Efficiency (closed circles) values in bins of y and Q^2 as measured using the double angle method.

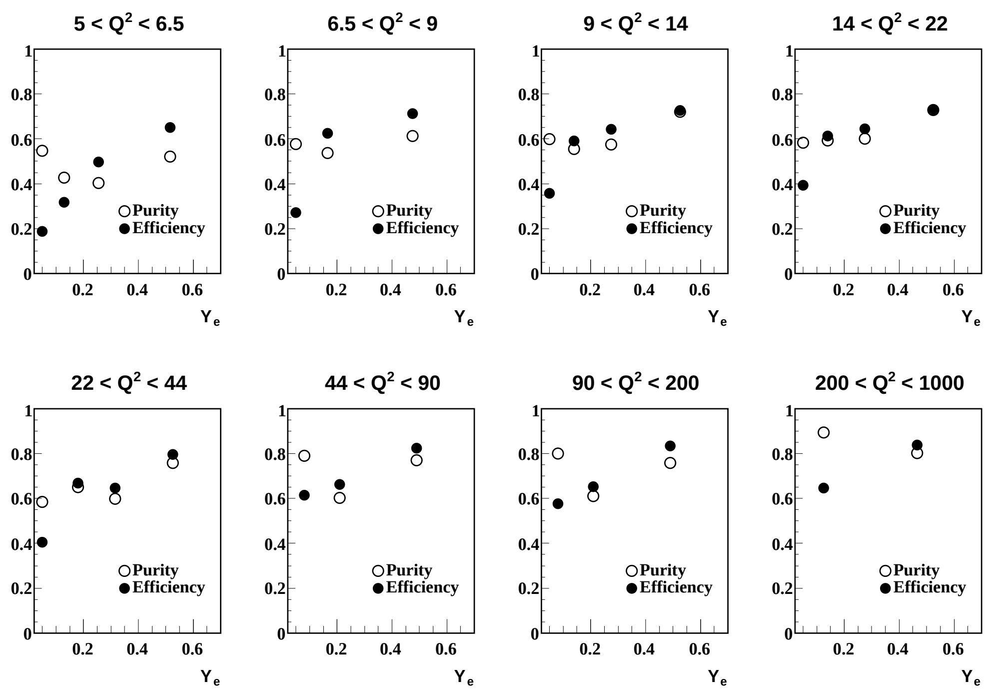

Figure 6.16: Purity (open circles) and Efficiency (closed circles) values in bins of y and Q^2 as measured using the electron method.

Figure 6.15 shows the purities in open circles and efficiencies in closed circles for the Monte Carlo sample used in section 6.3. In the lowest Q^2 bin the purity falls from 40% to 30% with increasing y and efficiency follows the same trend but falls from 40% to 20%. The low purities and efficiencies are expected because of the poor resolution in this kinematic region. Both purity and efficiency improve with Q^2 reaching 90% in the $200 < Q^2 < 1000$ GeV^2 region. Generally speaking both quantities improve with increasing y at lower Q^2 although for $Q^2 > 44$ GeV^2 the distributions are relatively flat with varying y. High y events are broadly susceptible to migrations between bins leading to lower purities in these regions. Both quantities follow the same broad pattern and so the migrations into and out of the bins are the same in all bins and therefore the corrections are close to one.

Figure 6.16 shows purity and efficiencies in the same format as measured by the electron method. As with the double angle method these quantities increase with rising Q^2, although the improvement is not as marked; in the highest Q^2 bin the efficiency is between 65% and 85%, and the purity between 80% and 90%. Unlike the double angle method, the purity rises with increasing y, typically increasing by about 40%. Efficiency is less sensitive to y and varies by no more than 20% at most, and in some Q^2 bins by as little as 5%. As with the double angle method both quantities exhibit the same trends and so the migrations in and out of bins balance.

Overall the double angle method displays higher purity and efficiencies at larger Q^2 and the electron method is better at lower Q^2. As expected a general rise in purity corresponds to an improvement in resolution and so purity and efficiency are functions of y. It would be possible to improve the measurement by using a combination of the electron and double angle methods, although this would lead to complications in the threshold region and so is not considered in this thesis.

This thesis will in part attempt to improve upon the HERA I $F_2^{c\bar{c}}$ measurement by improving the accuracy in the statistically limited high Q^2 bins. Therefore it is important to minimise the acceptance corrections in this region and to have a high efficiency of event reconstruction. The measurements in chapter 8 will therefore be made primarily with the double angle method, although the electron method is also used as a systematic cross check. The decision to primarily use the double angle method is also based on the results of the resolution study earlier in this chapter.

The results of this study indicate that there will be significant drift between bins in lower Q^2 events and that the agreement between true and reconstructed tracks is superior at high Q^2. We therefore expect the D^* scaled momentum distributions as measured in chapter 9 to be worse at lower Q^2 and y. Transformation into the Breit frame requires accurate reconstruction of the electron 4-momentum and of x in construction of the boost vector. If these quantities cannot be measured with high purity and efficiency then the accuracy of the final measurement will be compromised.

6.5 $E - P_z$ corrections

The difference between the total event energy and longitudinal momentum is calculated by summing over the energy (E_i) and longitudinal momentum (P_{zi}) of the calorimeter cells using

$$\delta = E - P_z = \sum_i (E_i - P_{zi}).$$

A cut on this quantity is used as an alternative to one based on energy conservation, a principle which cannot be used at ZEUS due to energy losses down the beampipe. δ is exactly conserved when the scattered lepton is detected in the main detector and peaks at $2E_e$, arising because the incoming proton has $E = P_z$ before and after the scattering it will provide no contribution to δ. In contrast the electron will contribute double since in the ZEUS co-ordinate frame it is traveling in a negative z direction and so $\delta = 2E_e \approx 55$GeV before the scattering process.

δ is very sensitive to losses in the rear region and generally insensitive to forward losses typically only seen in photoproduction and beam-gas events. These events have low values of δ and peak well below $\delta = 30$ GeV. In contrast DIS events do not exhibit electron energy loss down the beampipe and so δ will be conserved after the collision. Therefore demanding a cut of $30 < \delta < 60$ will ensure that a clean sample of DIS events has been selected. However the MC description of δ does not correspond well to that seen in data. Indeed the discrepancy between δ distributions in data and MC is significant and peaks in data at approximately 5 GeV lower than in MC (figure 6.18). This section will describe the corrections to the hadronic and leptonic energy scales necessary to improve the description and which will be used in all measurements in this thesis.

6.5.1 Correction of hadronic and electron energies

The discrepancy between data and MC is significant and must be corrected for to reduce the systematic errors associated with the measurement. Because δ may be broken down into contributions from the electron (δ_e) and hadronic (δ_{had}) system (so that $\delta = \delta_{had} + \delta_e$) it is possible to improve agreement by adjusting separately the hadronic and electron energy scales. In a 2006 ZEUS NC DIS publication [45] the corrections applied were scales of $S_H = 0.97$ to the hadronic system and $S_E = 0.98$ to the electron energy in MC only. In this paper the electron energy was also smeared by 3%. These corrections are used to improve description of the CAL energy loss due to inactive material [47].

Such corrections are used in conjunction with the standard adjustments to the energies already made at ZEUS. In this procedure the electron energy is adjusted using HES and SRTD information to account for any energy loss and to correct for hits that occur at the edge of cells. The hadronic energy is also normally corrected using an algorithm named *corandcut* [48], which removes any electron contribution and evaluates a corrected energy assuming the system is now entirely hadronic. Corandcut also corrects for back-splash, where the hadrons bounce off of the FCAL and contribute twice, and for any energy loss down cracks between cells and dead material [48].

To confirm that the $S_E = 0.98$ is a reasonable correction this quantity was adjusted and its effect on a number of standard DIS control plots was measured. The agreement between MC and data was parameterised using a χ^2 quantity

$$\chi^2 = \sum_{\mathrm{i}} \frac{(\mathrm{MC_i} - \mathrm{DATA_i})^2}{\sigma_i^2}.$$

where i runs over the bins in which the MC and DATA measurements of the various DIS quantities are made. Figure 6.17 shows how this quantity varies for: y, as measured using the electron, double angle and JB method; Q^2 as measured using the electron and double angle method; the corrected electron energy; x as measured using the electron and double angle method; and δ. χ^2 is shown as a function of S_E which is varied from 0.9 to 1.05, the

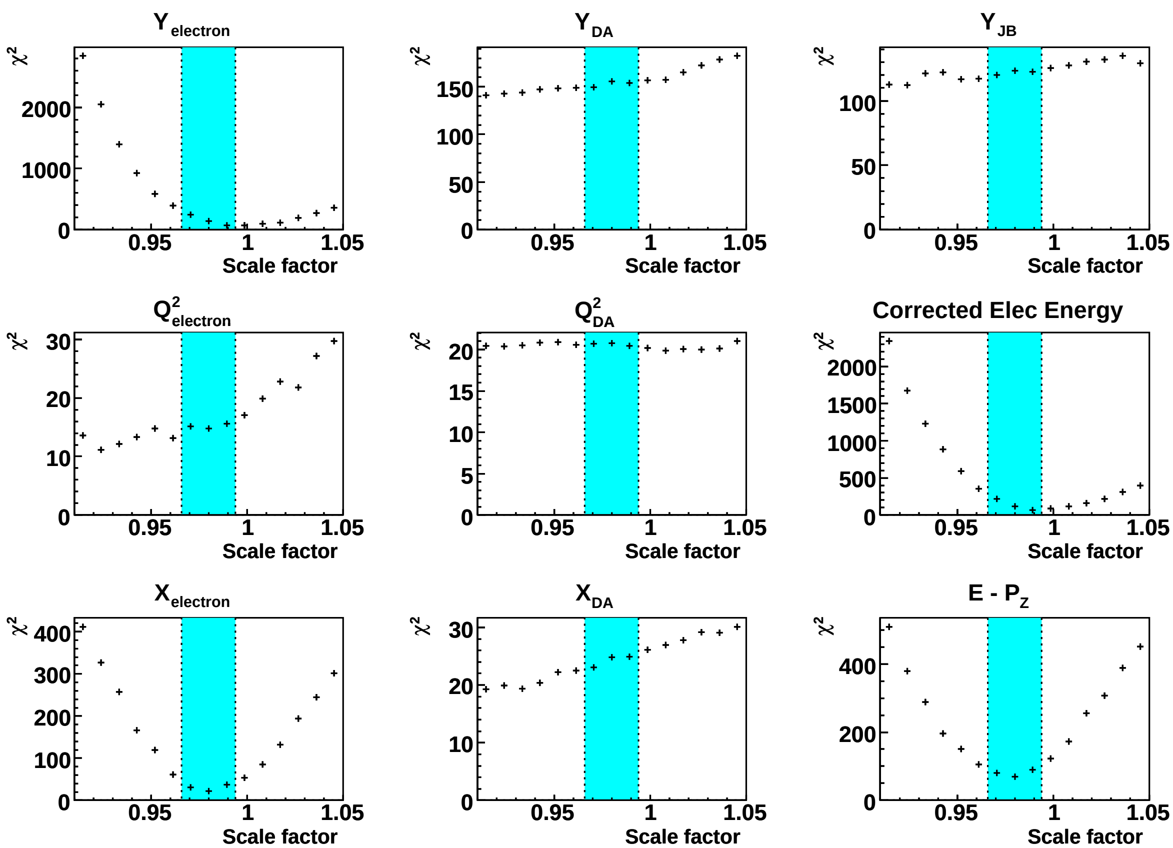

Figure 6.17: χ^2 as a function of energy scale for DIS kinematic control plots. The blue region represents the range over which the energy scale is altered to determine the systematic uncertainty associated with the Electron energy.

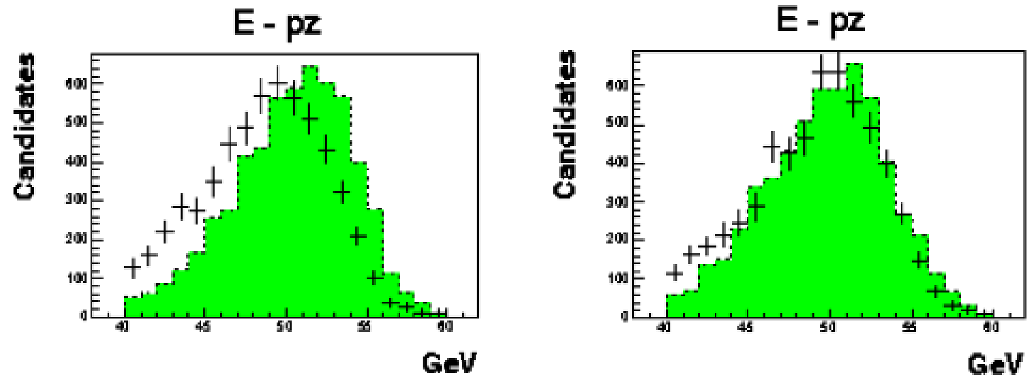

Figure 6.18: δ distributions before (left) and after (right) scaling and smearing of hadronic and electromagnetic components. Data is shown in points and MC is shown in green blocks. Before correction δ peaks at lower energies in data.

blue band indicates the range over which the electron energy scale is adjusted in calculation of the associated systematic error. As expected the electron method is most sensitive to S_E, the double angle and JB reconstructions of Q^2, y and x are generally unaffected by varying S_E. y_e agrees with MC best when a scale of $S_E \approx 0.99$ is applied, x is clearly minimised with a scale of $S_E \approx 0.98$ and Q^2 seems to be insensitive for $S_E < 0.99$ after which the agreement worsens rapidly. The corrected electron energy itself follows the same trend as y_e and is best described with $S_E \approx 0.99$. The best description of δ, the quantity these corrections are intended to improve, is achieved with $S_E = 0.98$ which gives a clear and graphically obvious minimisation.

The effect of this correction on δ is shown in figure 6.18 showing the MC distribution in green blocks and the data distribution in points. Prior to the corrections the MC peaks 3 GeV higher than the data, afterwards the agreement is much more satisfactory. These corrections are applied in all future measurements in this thesis.

6.6 Event Selection Cuts

This section summarises the cuts used to select the DIS events in this analysis. These cuts were based on the resolution results in this chapter and motivated by a desire to mirror the cuts used in the HERA I measurement of $F_2^{c\bar{c}}$ [49]. The event selection cuts are as follows:

- Triggers
  - $\mathrm{FLT}_{30} \cup \mathrm{FLT}_{34} \cup \mathrm{FLT}_{36} \cup \mathrm{FLT}_{44} \cup \mathrm{FLT}_{46}$
  - $\mathrm{HFL}_{02} \cup \mathrm{SPP}_{02}$
- Detector Cuts
  - $5 < Q^2_{DA} < 1000$ GeV^2
  - $y_{JB} > 0.02$
  - $y_{DA} < 0.7$
  - $y_e < 0.95$
  - $40 < \delta < 60$ GeV
  - $|Z_{vtx}| < 30$ cm
  - $E_{\mathrm{corrected}} > 10$ GeV

The FLT and TLTs are defined explicitly in section 6.1. In general the FLTs require deposits of energy consistent with a DIS event and to reject beam-gas background. At the TLT (where it is possible to fully reconstruct the event) at least one charmed hadron candidate must be found. An event was required to pass at least one first and one third level trigger.

The kinematic region was defined by cuts of $5 < Q^2_{DA} < 1000$ GeV^2, $y_{JB} > 0.02$ and $y_{DA} < 0.7$, where the double angle method was used as the primary reconstruction tool. This kinematic region is similar to the HERA I measurement except that HERA I extended from $3.5 < Q^2 < 1000$ GeV^2. This is because the movement of the CAL to accommodate the installation of the MVD altered the smallest angle at which the scattered electron could be measured, in turn raising the lowest possible Q^2 measurement.

The $40 < \delta < 60$ GeV cut is used to reject photoproduction events or DIS events with high energy Initial-State-Radiation (ISR). To reduce the background arising from beam-gas interactions events were required to have a reconstructed vertex within 30 cm of the nominal interaction point in z. Finally, to ensure that the electron was well reconstructed it was demanded that it's energy was > 10 GeV.

6.7 DIS Control Plots

To have confidence in the ability of the MC packages to unfold cross sections it is imperative that the event variables used in the measurement are similar in both MC and data. At ZEUS there are two principle MC packages; RAPGAP[9] and HERWIG[10]. In this section the accuracy with which these two MC packages can reproduce distributions seen in data is compared to determine which should be the principle measurement tool. As a systematic check the cross-sections will also be unfolded using the inferior package.

The upper half of figure 6.19 shows a selection of DIS kinematic variables as measured in data (points) and modeled by HERWIG (yellow). The lower half of this figure shows the same parameters but this time as modeled by RAPGAP. On each plot the parameter χ^2 is shown which gauges the agreement between MC and data. In these plots χ^2 is defined as

$$\chi^2 = \sum_{\text{bins}} \frac{(A_i^{MC} - A_i^{Data})^2}{(\sigma_{A_i^{Data}})^2}. \tag{6.2}$$

where A_i^{MC} and A_i^{Data} represent the entry in the i^{th} bin of observable A's distribution in MC and data respectively, and finally $\sigma_{A_i^{Data}}$ is the error associated with A_i^{Data}. Each A_i point has been background subtracted using the wrong charge method. A lower χ^2 value corresponds to better agreement between MC and data.

HERWIG does a poor job of reconstructing y in using all three reconstruction methods. Whilst the reconstruction is better at large y, at lower values the MC dramatically underestimates the measured value. Such discrepancy will cause a large systematic error at these values of y when switching between packages. HERWIG also struggles to model the Q^2 distribution of the data using both the electron and double angle reconstruction methods. As with y the description is reasonable at larger values but much poorer at the lowest bins

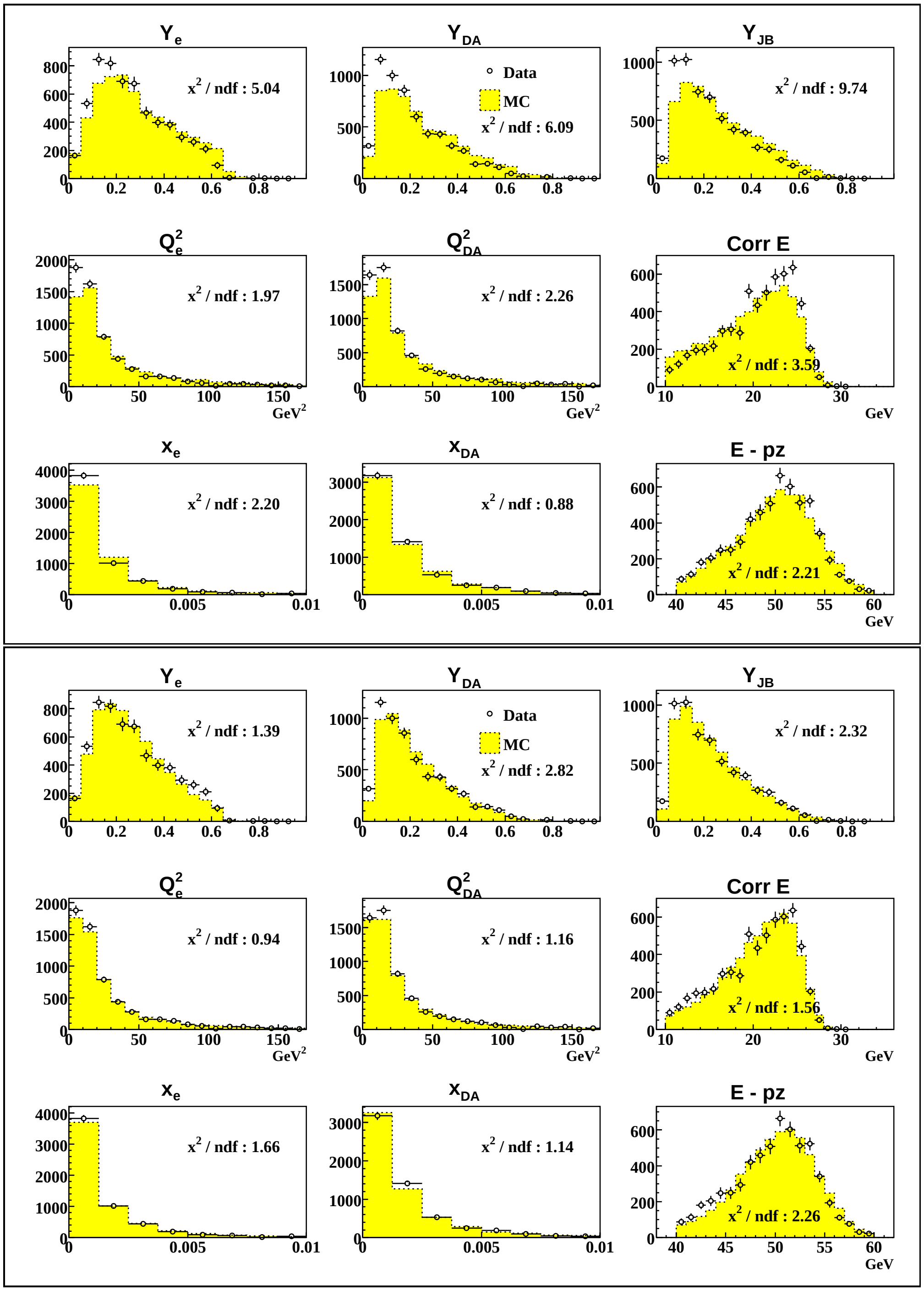

Figure 6.19: DIS kinematics control plots. Distributions of y, Q^2 and x are shown measured using different methods. Electron energy and $E - p_Z$ distributions are also shown. The upper plot shows the agreement between data (points) and HERWIG (yellow) for these parameters, the lower plot shows data and RAPGAP (yellow). A measurement of χ^2 is also shown which quantifies the agreement between MC and data. Background subtraction has been performed in each bin.

where the data bins are more populated. The HERWIG description of corrected energy, x_e, x_{DA} and $E - p_Z$ are reasonable and are comparable with the RAPGAP reconstruction.

In contrast RAPGAP does a much better job of reconstructing y although there is still a slight discrepancy in the earliest bins. Q^2 is well described using both reconstruction methods and the reconstruction of the corrected energy, x_e, x_{DA} and $E-p_Z$ are all reasonable. Because RAPGAP offers a superior representation of the data it is chosen as the primary tool for calculating acceptances. However the representation is not perfect and work is ongoing at HERA II to improve the MC. This work is outwith the scope of this thesis and at present MC remains a large source of systematic error.

6.8 Summary

In this chapter we learned that the trigger system is well simulated in MC and that it is not necessary to include a trigger-based systematic in the measurement. The resolution of the double angle method of event reconstruction was found to be superior to that of the JB and electron methods and so will be the principle reconstruction tool in this thesis. To improve the MC description of $E - p_Z$ it was found necessary to scale the hadronic system by 0.97 and to scale and smear the electron energy by 0.98 and 3% respectively. The event selection cuts were then explicitly stated and the chapter concluded a comparison of two MC packages, finding that RAPGAP most faithfully reproduces what is seen in data.

Chapter 7

D^* Reconstruction

In this chapter the tracking capabilities of HERA II are compared with those of HERA I, and D^* reconstruction from tracks is described. Whilst HERA II tracking is superior at high p_T the resolution is inferior at lower momenta owing to the increased multiple scattering in the MVD. D^* reconstruction is then described and a discussion is made of how its reliance on tracks makes it more difficult at HERA II. The chapter then moves on to describe how D^*s are counted using ΔM distributions and we learn how the error associated with it is calculated. As with the previous chapter on event reconstruction, this chapter concludes with a comparison of control plots between RAPGAP and HERWIG to identify where we expect to find large systematic errors associated with D^* measurements.

7.1 Reconstruction of D^*

The D^* mesons are identified using the decay channel $D^* \to D^0\pi_s^+$ with the subsequent decay $D^0 \to K^-\pi^+$, where π_s^+ refers to a low momentum ("slow") pion. Charge conjugation is implied. Reconstructed detector tracks are used to reconstructed D^* candidates using the following process.

D^0 candidates are formed by combining oppositely charged tracks with $p_T > 0.4$ GeV and $|\eta| < 1.75$ which are alternately assigned the mass of the K and π and the invariant mass of the track pair, $M_{K\pi}$, is calculated. This D^0 meson candidate is combined with a final third track with a charge opposite to that of the track assigned the kaon mass. This third track is assigned the mass of the pion and the combination of all three tracks forms a D^* candidate. The combinatorial background is determined by assembling wrong-charge D^* candidates for which the kaon and pion tracks have the same charge and the slow pion track has the opposite charge. The spectrum of combinations for which $1.80 < M(D^0) < 1.92$ GeV and $0.143 < \Delta M < 0.148$ GeV is used where $M(D^0)$ is the reconstructed mass of the D^0 and $\Delta M = M_{K\pi\pi_s} - M_{K\pi}$.

Once the D^* candidates have been reconstructed the cuts which determine the kinematic region for D^* production may be applied; $1.5 < p_T(D^*) < 15$ GeV and $|\eta(D^*)| < 1.5$. Once these cuts have been made the D^* ΔM distribution is histogrammed and fit to a modified gaussian of the form:

$$MG = p_1 \mathrm{exp}\left(-\frac{1}{2}x^{1+\frac{1}{1+0.5x}}\right) + p_4(\Delta M - m_\pi)^{p_5}$$

where $x = |(\Delta M - p_2)/p_3|$, the p_i are free parameter and m_π is the pion mass. This distribution is shown in figure 7.1 with the corresponding fit to a modified gaussian given shown in blue. The fit is only used to extract $N(D^*)$ as a systematic cross check in the evaluation of cross sections and $F_2^{c\bar{c}}$.

The following list summarises the track cuts that are used in the reconstruction of D^* candidates:

- $1.5 < p_T(D^*) < 15$ GeV
- $-1.5 < \eta(D^*) < 1.5$
- $p_T(K, \pi) > 0.4$ GeV
- $p_T(\pi_s) > 0.12$ GeV
- $-1.75 < \eta(K, \pi, \pi_s) < 1.75$
- $1.80 < M(D^0) < 1.92$ GeV
- $0.143 < \Delta M < 1.48$ GeV

The kinematic region of the final measurement is given by the D^* cuts in the first two points and the rest of the cuts reject very low resolution tracks and those that fall outside of the CTD central region.

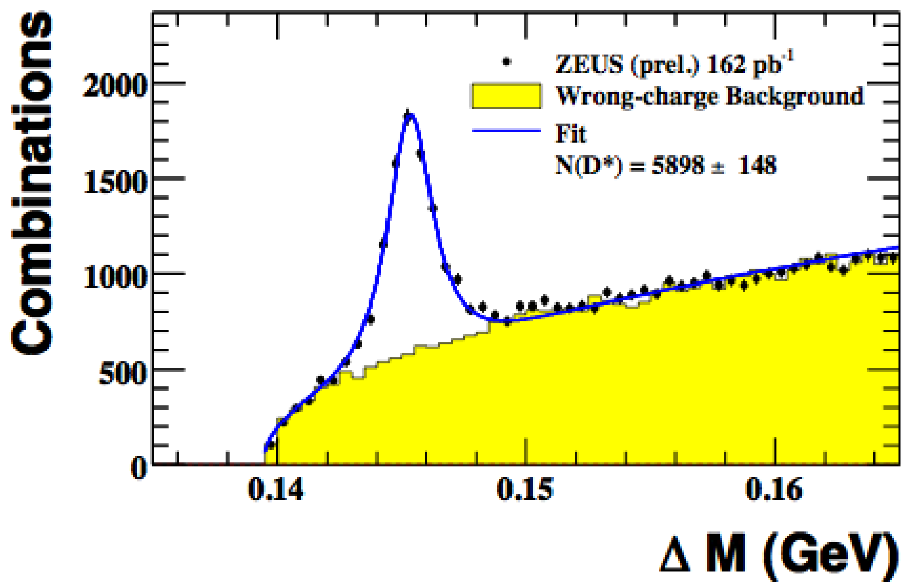

Figure 7.1: The HERA II ΔM distribution for D^* candidates (points) is shown with the corresponding wrong charge distribution (yellow). The solid line is a modified gaussian fit to the distribution.

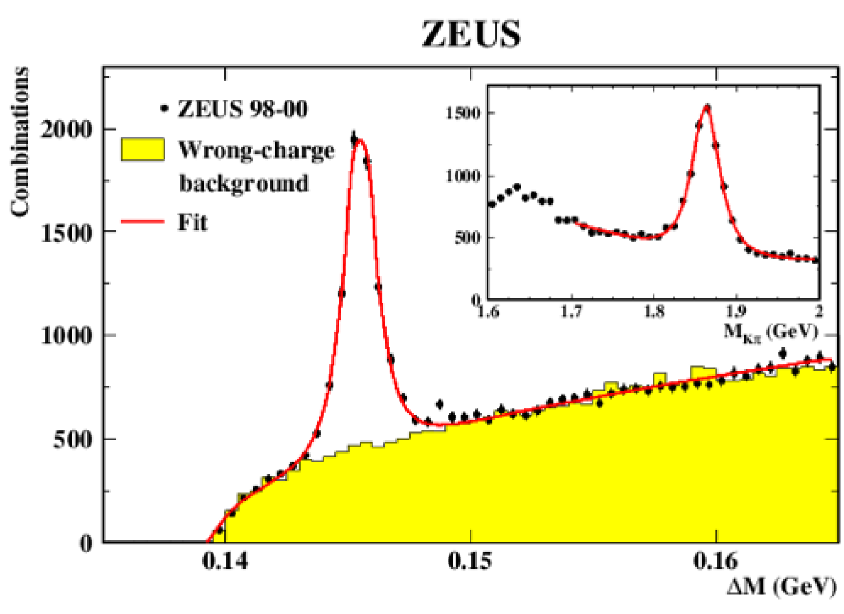

Figure 7.2: The HERA I ΔM distribution for D^* candidates (points) is shown with the corresponding wrong charge distribution (yellow) [52]. The solid line is a modified gaussian fit to the distribution.

7.2 Extraction of $\Delta M(D^*)$ distribution

D^* reconstruction relies entirely on combining all possible track configurations from tracks that conform to the requirements listed in the previous section. This procedure creates a large number of meaningless background combinations that arise from random track configurations that must be accounted for and removed. Combinatorial background is significant and accounts for around half of the total candidates in the signal region.

Background is estimated by storing D^* candidates constructed from wrong charge track combinations (defined in section 7.1) corresponding to unphysical particles and which have a mathematically identical shape to the background in the $\Delta M(D^*)$ distributions. To count the number of reconstructed D^*'s the wrong-charge background must be subtracted from the right-charge candidates in the region $0.143 < \Delta M < 0.148$. The ΔM plots are divided into a number of regions; The signal region spans $0.143 < \Delta M < 0.148$ GeV and the background normalisation region covers $0.150 < \Delta M < 0.170$ GeV.

Figure 7.3 [54] identifies the signal and background regions of ΔM and assigns relevant labels. The number of D^*'s in the signal region for the right charge combination candidates is A and the number in the background normalisation region is B. The corresponding labels for the wrong charge candidates are C and D for the signal and background regions respectively.

The wrong charge distribution is background normalised to the right charge region and the two signal regions are subtracted [55]. The number of D^* candidates is therefore

$$N(D^*) = N(A) - \frac{N(B)}{N(D)} \cdot N(C)$$

where N(A), N(B), N(C) and N(D) are the numbers in each of these regions.

The error associated with this number has a contribution from the background normalisation which is given by propagation of errors[1] as

$$\delta N(D^*) = \sqrt{N(A) + \left[(N(C) \cdot N(B)) \cdot \left(\frac{N(C) + N(B) + N(C) \cdot \frac{N(B)}{N(D)}}{N(D)^2} \right) \right]}$$

[1]The formula for propagation of errors

$$(\Delta f)^2 = \sum_{i=1}^{n} \left(\frac{\partial f}{\partial x_i} \Delta x_i \right)^2$$

is used to calculate the uncertainty Δf of f where x_i are independent variables with uncertainty Δx_i.

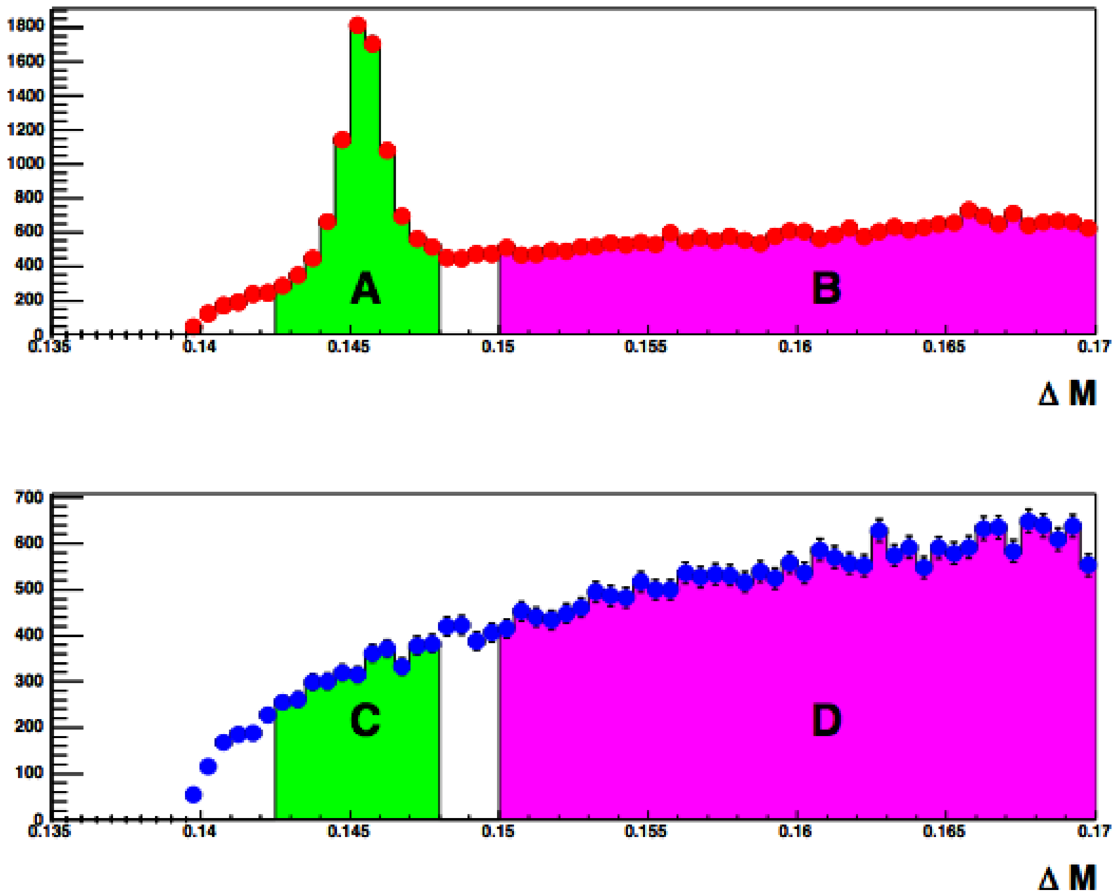

Figure 7.3: Illustration of the signal and background regions of the right (above) and wrong (below) charge combinations of D^* candidates. The signal region is coloured green and the background normalisation region is coloured purple [54].

As shown in figure 7.1 the number of D^* mesons reconstructed using this method was 5898 ± 148.

To gauge the systematic uncertainty associated with the signal extraction procedure the cuts defining the signal and background region are varied. Moreover the signal is also extracted using a fitting procedure whereby the signal is described by a modified gaussian (eq 7.1) and the background is assumed to be exponential (eq 7.2)

$$G_{mod}(x; d, p_1, p_2, p_3) = \frac{d \cdot p_t}{\sqrt{2\pi} \cdot p_3} exp\left(-\frac{1}{2}T^{1+\frac{1}{1+0.5T}}\right) \tag{7.1}$$

where

$$T = |\frac{x - p_2}{p_3}|$$

$$BG = p_4(x - m_\pi)^{p_5} \tag{7.2}$$

where $x = \Delta M$, d is the bin width, m_π is the pion mass and p_1, p_2, p_3, p_4 and p_5 are free parameters [54]. Using this parameterisation the number of D^*'s is given by

$$N(D^*) = p_1 \cdot G_0$$

where G_0 is the normalisation factor. This factor is evaluated numerically

$$\int_{-\infty}^{+\infty} G_{mod}(x; d, p_1, p_2, p_3)dx = 1.218.$$

The principal method of D^* extraction is the background subtraction method which gives the best stability over the whole kinematic region and does not rely on an accurate model of the background distribution. As an overall check a second measurement is made using fits and the change is found to be 3% in the lowest y bins and rising to 9% at high y, in every case the shift is within statistical errors.

7.3 Impact of MVD on tracking resolution

In this thesis D^*s are reconstructed using tracks fitted to MVD and CTD hits. Whilst the MVD has a superior intrinsic hit resolution it also placed a significant additional amount of dead material between the CTD and the beam interaction point. This material, in addition to the beampipe and CTD outer casing already present, causes charged particles to experience increased multiple scattering as they traverse the detector. Multiple scattering has the effect of smearing the resolution of reconstructed tracks and therefore increases the error on any tracking measurement. Because D^* reconstruction relies entirely on tracking there is expected to be a large systematic error associated with it at HERA II compared with HERA I. This arises largely from the reconstruction of the slow pion π_s, whose low momentum is highly predisposed to the multiple scattering effect and so has a low tracking resolution for reasons described in the following section.

7.3.1 Derivation of resolution parameterisation

The tracking resolution of ZEUS when expressed as a function of transverse track momentum (P_T) takes the following form:

$$\sigma(P_T)/P_T = a_0 P_T \oplus a_1 \oplus a_2/P_T \tag{7.3}$$

where $\oplus$ indicates that the terms are added in quadrature. This form arises from consideration of both scattering effects and inaccuracies in measuring the position of hits along the fitted track [51]. The $a_0 P_T$ term is justified by consideration of errors in hit measurement, the a_1 term is ascribed to multiple scattering of the particle as it traverses the CTD, and the a_2/P_T term arises from multiple scattering effects prior to reaching the CTD. The coefficients are determined from fits to data, and will be reduced by careful detector calibration and precise alignment of the MVD. Given that these effects are uncorrelated they may be safely added in quadrature to give the form presented above. A more detailed justification of this formalism is given in appendix B.1.

7.3.2 Measurement of tracking resolution

The latest ZEUS measurement of tracking resolution [50] used Monte Carlo to determine the new CTD + MVD tracking resolution and compared it to the 1996 HERA I values. In this method a Monte Carlo generator was used to prepare a selection of true level events which were passed through a simulation of the ZEUS detector. A series of cuts were then made on a selection of random tracks ensuring that they emerged from a primary vertex, passed through three super layers of the CTD, had $|\eta| < 1.75$, struck at least 50 CTD hits and finally could actually be matched to a true level track. The generated tracks were then matched to their true counterparts in a number of P_T bins. In each of these bins the resolution was evaluated by extracting the width of a gaussian fit as a function of p_T. CTD+MVD tracking resolutions were obtained as a function of P_T for CTD and CTD+MVD. A fit was performed on this resolution curve assuming the form of equation 7.3 to extract the following values for a_0, a_1 and a_2.

$$\text{CTD Tracking} : \sigma(P_T)/P_T = 0.0063 P_T \oplus 0.0083 \oplus 0.0032/P_T$$

$$\text{REG Tracking} : \sigma(P_T)/P_T = 0.0038P_T \oplus 0.0134 \oplus 0.0033/P_T$$

where $\oplus$ indicates that the terms are added in quadrature. The corresponding HERA I result is

$$\text{HERA I} : \sigma(P_T)/P_T = 0.0063P_T \oplus 0.0070 \oplus 0.0016/P_T.$$

The CTD only resolution is the same as in HERA I except with additional multiple scattering as expected. The REG tracking package includes MVD information and so possesses superior hit resolution. This manifests itself in an extracted value of a_0 which is half that of the CTD tracking in HERA I and HERA II, improving the resolution at high P_T by a factor of two. However the presence of the MVD also increases the multiple scattering effect which doubles the a_1 and a_2 coefficients. In short whilst higher momentum tracks are measured with greater accuracy at HERA II, lower momentum tracks are measured more poorly. The effect may be reduced by careful calibration of the MVD and alignment studies, although a great deal of work is required and is still ongoing to improve the tracking to match the HERA I level. This has great implications for the reconstruction of D^* since it requires accurate measurement of a low momentum slow pion. In this analysis the REG tracking mode was used since it is reasonably well understood.

The HERA I ΔM distribution is shown in figure 7.2 below figure 7.1 which shows the HERA II distribution. The resolution in HERA I is approximately twice as good as HERA II which exhibits a ΔM width twice as wide. The background is also higher in HERA II which will increase the statistical error associated with the measurement. These changes arise as a result of the poorer tracking resolution for low p_T π_s at HERA II leading to a less efficient reconstruction. Therefore there will be a large systematic error associated with reconstruction of D^* until the tools for reconstructing the D^* can be refined. When the MVD is properly aligned and ZTT tracking is fully refined it will be possible to improve upon the measurements.

7.4 D^* kinematics control plots

In section 6.7 RAPGAP and HERWIG control plots for a selection of DIS variables were compared and RAPGAP was identified as the model that best agrees with data. In this chapter a similar comparison is made between these MC packages, although this time control plots for D^* kinematics are compared. The upper half of figure 7.4 shows a selection of D^* parameters as measured in data (points) and modeled by HERWIG (yellow). The lower half of this figure shows the same parameters but this time as modeled by RAPGAP. On each plot the parameter χ^2 is shown which gauges the agreement between MC and data and is defined in equation 6.2.

Whilst the p_T of K, π, π_s and D^* distributions have the same broad shape in both MC and data and are well described at high p_T, there is a stark departure at low values where MC peaks at lower p_T. This discrepancy is a large source of systematic error and arises in part because ZEUS measurements at HERA II do not yet fully account for multiple scattering effects. This potential detector effect cannot however be disentangled from the possibility that the discrepancy is physics based, which can be quantified by manipulating the shape of the distribution by reweighting the events with a function based on MC information. With this weighting applied, the measurements were repeated and any shift in the final answer recorded and added in quadrature to the other systematic shifts. This procedure is described in more detail in section 8.4.2 and was a dominant source of systematic error.

η distributions for the K, π, π_s and D^* are in better agreement between MC and data although both RAPGAP and HERWIG predict a less forward distribution than is measured in data. A similar systematic to that calculated for the $p_T(D^*)$ is calculated for $\eta(D^*)$

The $\phi(D^*)$ distribution is flatter in MC although the description has the same shape and is reasonably well described. Overall, whilst HERWIG is marginally better than RAPGAP at modelling D^* kinematics RAPGAP's far superior description of the event kinematics justifies its use as the primary MC. Moreover RAPGAP is known to better model the background distribution of the D^* event sample which is important when performing background subtraction.

The impact of the MVD on HERA II tracking is well documented [50, 56] and is discussed briefly in section 7.3 and in greater detail in appendix B.1. Until the MVD is optimally aligned and ZEUS finalises a tracking package capable of better modelling multiple scattering it is not possible to improve D^* reconstruction. D^* reconstruction will also be improved by developing the underlying physics modelling in the MC packages, although it not possible

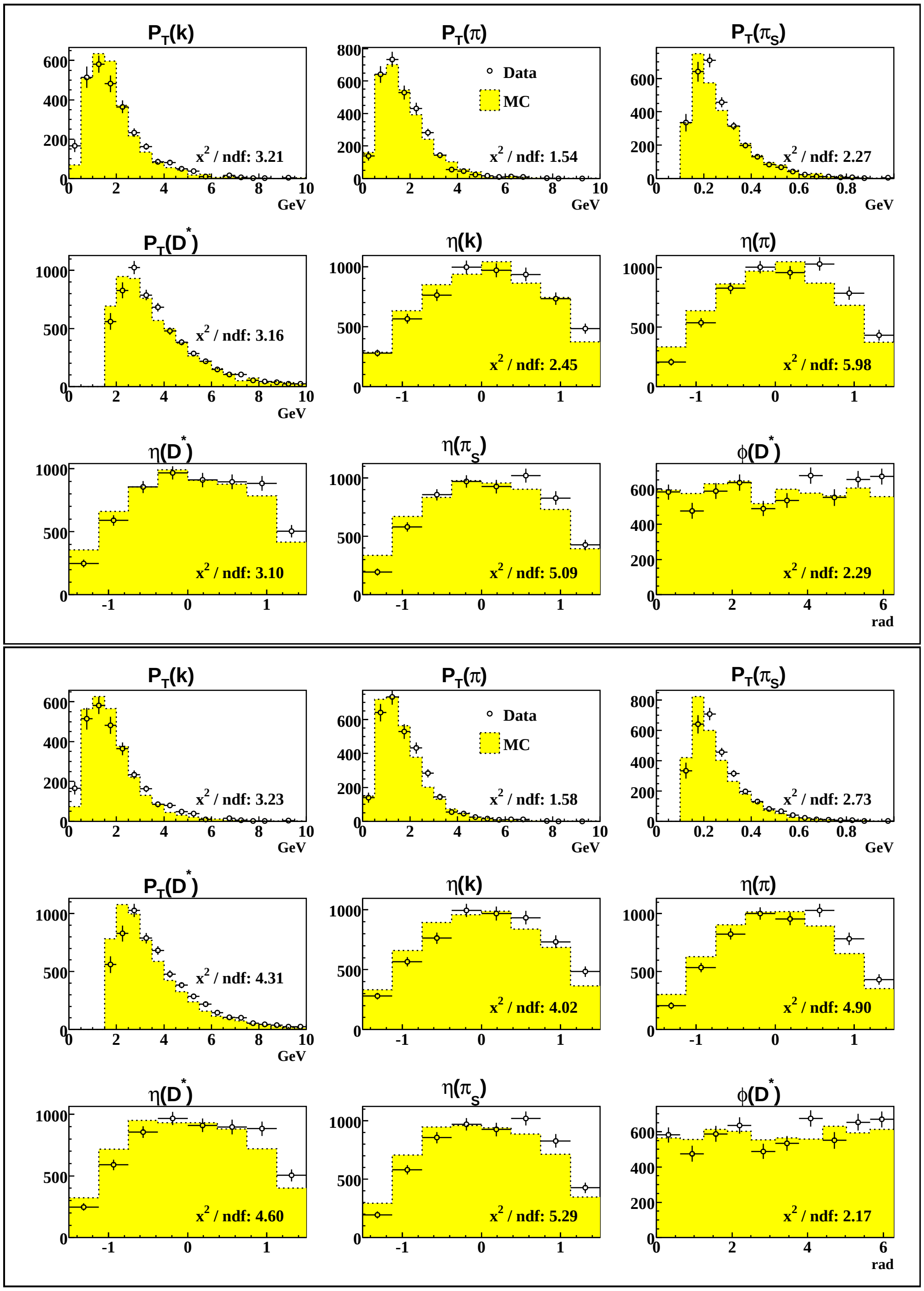

Figure 7.4: D^* kinematics control plots. Distributions of p_T and η are shown for D^* and it's decay tracks. The upper plot shows the agreement between data (points) and HERWIG (yellow) for these parameters, the lower plot shows data and RAPGAP (yellow). A measurement of χ^2 is also shown which quantifies the agreement between MC and data. Background subtraction has been performed in each bin.

to disentangle this effect from the detector and tracking factors.

7.5 Summary

In this chapter the tracking capabilities of HERA II were compared with that of HERA I and D^* reconstruction from tracks was described. Whilst HERA II tracking was found to be superior at high p_T the resolution was inferior at lower momenta. This feature was found to arise from increased multiple scattering in the MVD which was installed during the HERA I upgrade to HERA II. D^* reconstruction was then described and we learned how it's reliance on tracks makes it difficult at HERA II. The chapter then moved on to describe how D^*s are counted using ΔM distributions and a demonstration of how to calculate the associated error was given. As with the previous chapter on event reconstruction, this chapter concluded with a comparison of control plots between RAPGAP and HERWIG which showed a large discrepancy between MC and data for the $p_T(\pi_s)$ distributions, particularly at low p_T. This discrepancy is expected to be a large source of systematic error.

Chapter 8

Measurement of $\mathbf{F_2^{c\bar{c}}}$

This chapter begins with a summary of the selection cuts which define the DIS data sample from which differential cross-sections and $F_2^{c\bar{c}}$ measurements will be unfolded. The methods by which the cross-sections and $F_2^{c\bar{c}}$ are measured are then described and the principle systematic and theoretical errors are outlined. The chapter concludes with a presentation of the final cross-section and $F_2^{c\bar{c}}$ measurements with the systematic, statistical and theoretical errors included. A discussion of these results is then made, with reference to the agreement between this measurement, the HERA I measurement and the NLO predictions.

8.1 Introduction

The abundance of charm quark production in deep inelastic scattering at HERA II has made measurements of DIS charm production a fertile field of research. Indeed at very high Q^2 charm quarks contribute roughly 30% of the total cross-section[59, 60]. The predictions of Quantum Chromodynamics (in which the dominant source of charm production is BGF) are consistent with the previous measurements of D^* cross-sections[59, 60, 61, 62, 49] in the range of $1 < Q^2 < 1000$ GeV^2. The strong agreement between the two indicates strongly that BGF is indeed the dominant source of charm production and hence measurements of charm give a handle on the poorly understood gluon density in the proton.

8.2 Summary of Selection Cuts

The NC DIS events were selected using cuts that mirror those used in the HERA I measurement [49] so that if necessary the two measurements may be easily combined. These cuts were motivated by a desire to isolate and remove background events and hence select a purely DIS physics sample from which clean measurements can be made. This section combines and summaries the event selection process which is discussed in more detail in sections 5.5.1 and 6.6.

To reduce the background arising from beam gas interactions, events were required to have a reconstructed vertex less than 30 cm away from the nominal interaction point in z. As discussed in the previous chapter

$$\delta = E - p_z = \sum_i E_i(1 - \cos\theta_i),$$

was used to reject photoproduction events or DIS events with high energy Initial-State-Radiation (ISR) by demanding that $40 < \delta < 60$ GeV.

The kinematic region was defined by cuts of $5 < Q^2_{DA} < 1000$ GeV^2, $y_{JB} > 0.02$ and $y_{DA} < 0.7$, where the double angle method was used as the primary reconstruction tool for reasons given in section 6.3. This kinematic region is similar to that used in HERA I with the exception that HERA I extended to $3.5 < Q^2 < 1000$ GeV^2. This change was necessary because during the HERA upgrade the CAL was moved to accommodate the installation of the MVD, altering the smallest angle at which the scattered electron could be measured. Detector cuts of $y_{JB} > 0.02$ and $y_e < 0.95$ were placed, along with the requirement that the electron energy $E > 10$ GeV. The scattered electron was identified using the SINISTRA [63] package.

A number of FLT and TLT triggers were also required as listed explicitly in section 6.1. In general the FLT triggers require deposits of energy consistent with a DIS event and reject beam-gas background. At the third level, where it is possible to fully reconstruct the event, at least one charmed hadron candidate must be reconstructed for the event to be selected.

In summary the event selection cuts are as follows:

- Triggers:
  - $\mathrm{FLT}_{30} \cup \mathrm{FLT}_{34} \cup \mathrm{FLT}_{36} \cup \mathrm{FLT}_{44} \cup \mathrm{FLT}_{46}$.
  - $\mathrm{HFL}_{02} \cup \mathrm{SPP}_{02}$.
- Detector Cuts:
  - $5 < Q^2_{DA} < 1000$ GeV^2.
  - $y_{JB} > 0.02$.
  - $y_{DA} < 0.7$.
  - $y_e < 0.95$.
  - $40 < \delta < 60$ GeV.
  - $|Z_{vtx}| < 30$ cm.
  - $E_{\text{corrected}} > 10$ GeV.

and the following D^* selection cuts were used:

- $1.5 < p_T(D^*) < 15$ GeV.
- $-1.5 < \eta(D^*) < 1.5$.
- $p_T(K, \pi) > 0.4$ GeV.
- $p_T(\pi_s) > 0.12$ GeV.
- $-1.75 < \eta(K, \pi, \pi_s) < 1.75$.
- $1.80 < M(D^0) < 1.92$ GeV.
- $0.143 < \Delta M < 1.48$ GeV.

In total 162 pb^{-1} of HERA II data was used in the final measurement. The rate of background subtracted D^* production at HERA II was 36.4 ± 0.9 pb, much smaller than the HERA I rate of 67.7 ± 1.6 pb which extended to a lower Q^2 region.

The HERA I measurement was made using 81.9 pb^{-1} and detected a total of 5545 D^*. Whilst HERA II detected more D^*s (5898) in 162 pb^{-1} the background was much larger and fewer D^*s were reconstructed.

As a cross check the D^* production rates for both samples were compared in the range of $Q^2 > 40$ GeV^2. In this range HERA I produced D^* at a rate of 10 pb and HERA II produced D^* at a rate of 7 pb. These rates are in much better agreement and the discrepancy is caused by detector inefficiencies caused by the presence of the MVD.

To calculate the acceptance corrections 484 pb^{-1} of charm and beauty enriched RAPGAP MC was generated with $Q^2_{\text{True}} > 1.5$ GeV^2. The generated sample of events was passed through a full simulation of the detector using the GEANT [12] simulation package and selected using identical cuts to those applied to data. As a systematic check the measurements were repeated using events generated by HERWIG and passed through the same detector simulator.

8.3 Measurement Procedure

This section explains the procedure used to make differential cross-section and $F_2^{c\bar{c}}$ measurements at HERA II. The process by which the cross-sections are unfolded is first given and then associated with the extraction procedure for $F_2^{c\bar{c}}$. The systematic errors associated with these measurements are discussed in the following section.

8.3.1 Unfolding Cross-sections

The differential cross-section in an observable Y for the process $ep \to eD^*X$ can be calculated from

$$\frac{d\sigma(D^*)}{dY} = \frac{N(D^*)}{A \cdot L \cdot B \cdot \Delta Y}$$

where $N(D^*)$ is the number of reconstructed D^*s in a bin of width Δ Y. A is the acceptance correction for each bin as defined in section 6.4 and L is the integrated luminosity. The value of branching ratio $B = BR(D^{*+} \to D^0\pi^+) \times BR(D^0 \to K^-\pi^+)$ used was $(2.57 \pm 0.06)\%$ [1].

This formula is used to extract $d\sigma/dQ^2$, $d\sigma/dp_T(D^*)$, $d\sigma/d\eta(D^*)$ and $d\sigma/dx$ whose final measurement is given in section 8.5. The double differential $d^2\sigma/dQ^2dy$ is also measured and used to explicitly calculate $F_2^{c\bar{c}}$ as detailed in the following subsection.

8.3.2 Extracting $F_2^{c\bar{c}}$

The relationship of the open-charm contribution to the proton structure function and the double-differential $c\bar{c}$ cross-section in x and Q^2 is given by

$$\frac{d^2\sigma^{c\bar{c}}(x,Q^2)}{dxdQ^2} = \frac{2\pi\alpha^2}{xQ^4}\left([1+(1-y)^2]F_2^{c\bar{c}}(x,Q^2)\right).$$

The terms in this equation are as defined in section 2 where F_L is neglected. The $c\bar{c}$ cross section is obtained by measuring the D^* production cross section and employing the hadronisation fraction $f(c \to D^*)$ to extract the total charm cross-section as explained in section 8.3.1.

The ΔM plots necessary to measure this cross-section as explained in section 7.2 are shown in figure 8.1; the upper plot shows the data distributions and the lower plot the corresponding MC distributions. Due to space constraints the values on the x-axis have not been shown on these plots, although the range is precisely that used in figure 7.1. The purpose of these plots is to illustrate the size of the relative background and signal sizes and so a detailed axis is not shown. The position of these plots in the (Q^2, x) kinematic plane is as indicated in figure 6.9. These distributions indicate that it is increasingly difficult to extract a ΔM signal with increasing Q^2 because higher Q^2 events are often accompanied by high track multiplicity, increasing the background in the distribution and making reconstruction more difficult. Measurements at large Q^2 are expected therefore to be associated with a large statistical error. There is a slight degradation in resolution with increasing y although not nearly as pronounced as the degradation as a function of Q^2. Background levels also rise with increasing y. The corresponding MC distributions have a much lower background because a non-inclusive sample was used which leads in general to a clearly resolved signal in each MC bin.

The cross section measurement relies on an assessment of D^* production which can only be made in a restricted kinematic phase space. Equation 8.1 is the prescription used to extrapolate to the full kinematic region to extract an inclusive $F_2^{c\bar{c}}$ measurement. $F_2^{c\bar{c}}$ at any

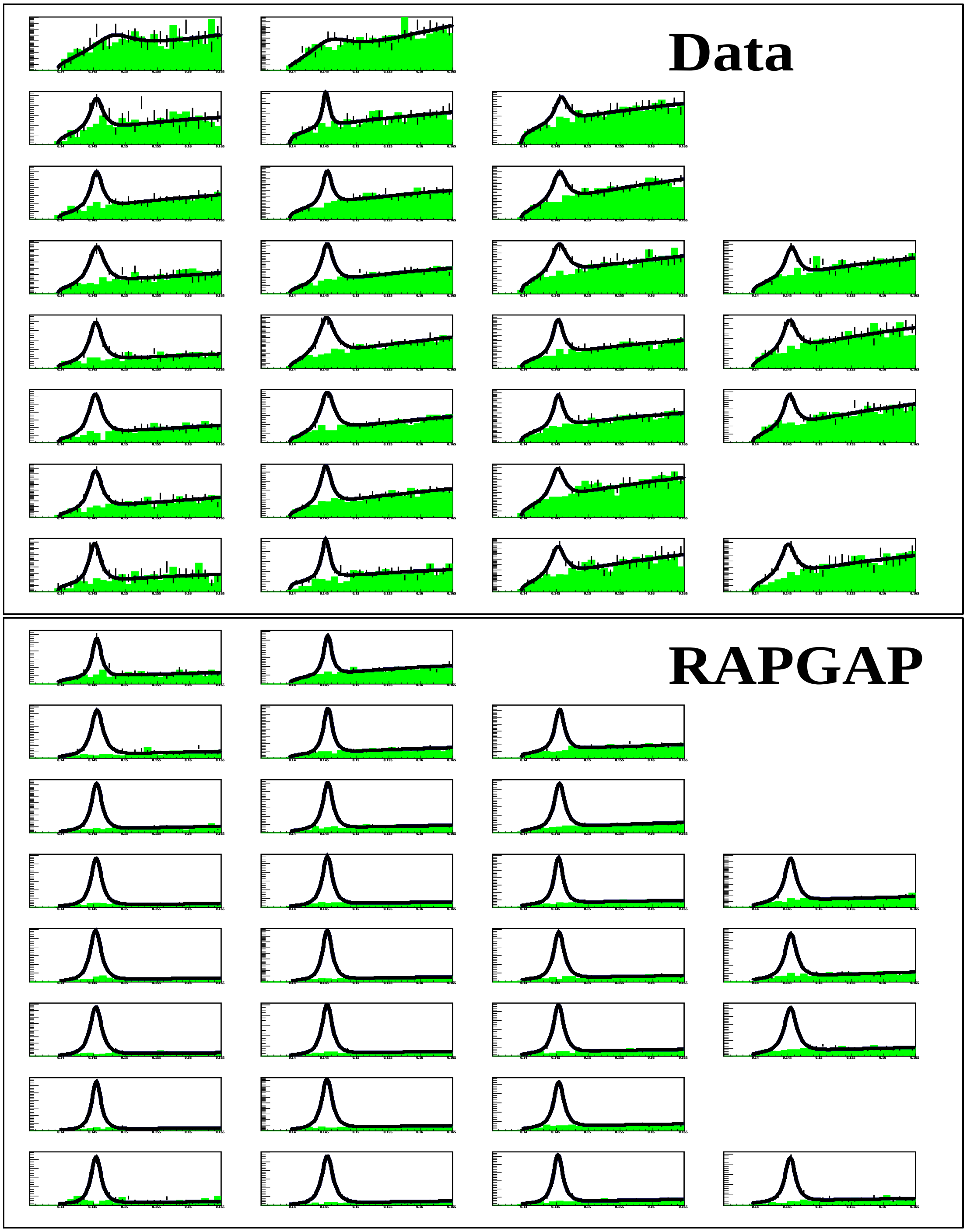

Figure 8.1: D^* ΔM plots in (Q^2, y) bins arranged as illustrated in figure 6.9. The upper plot shows the distributions for data, the lower plot for MC. On each plot the x-axis runs from 0.136 to 0.164 GeV as in figure 7.1. Wrong charge background is shown in solid green and fit to the modified gaussian is shown in black.

(x, Q^2) point is evaluated within each of the measured (y, Q^2) cross-section bins using

$$F_{2,\text{measured}}^{c\bar{c}}(x_i, Q_i^2) = \frac{F_{2,\text{theo}}^{c\bar{c}}(x_i, Q_i^2)}{\sigma_{i,\text{theo}}^{c\bar{c}}(ep \to D^* X)} \sigma_{i,\text{meas}}^{c\bar{c}}(ep \to D^* X) \tag{8.1}$$

where $F_{2,\text{theo}}^{c\bar{c}}$ is the prediction evaluated from the NLO coefficient functions [65], $\sigma_{i,\text{theo}}^{c\bar{c}}$ is the HVQDIS NLO prediction and $\sigma_{i,\text{meas}}^{c\bar{c}}$ is the cross-section measured in this analysis. $F_{2,\text{theo}}^{c\bar{c}}$ and $\sigma_{i,\text{theo}}^{c\bar{c}}$ use the same input PDFs, factorisation and normalisation scales and assume charm generation using NLO FFNS BGF predictions. The extrapolation factor by which the measured region must be extended to the full kinematic range is given in table 8.8 and ranges from around 1.5 to 3.7.

$F_2^{c\bar{c}}$ was measured at a (x, Q^2) point close the center-of-gravity of the (y, Q^2) bin. This measurement was made using the $F_{2,\text{theo}}^{c\bar{c}}$ prediction which was generated on a grid of discrete (x_i, Q_j^2) points in (x, Q^2) space. To quote a measurement of $F_2^{c\bar{c}}$ at a sensible (x, Q^2) point it was sometimes necessary to interpolate $F_{2,\text{theo}}^{c\bar{c}}$ locally by assuming the rate of change is locally constant. $F_{2,\text{theo}}^{c\bar{c}}(x, Q^2)$ is therefore evaluated from $F_{2,\text{theo}}^{c\bar{c}}(x_i, Q_j^2)$ using

$$F_{2,\text{theo}}^{c\bar{c}}(x, Q^2) = F_{2,\text{theo}}^{c\bar{c}}(x_i, Q_j^2) + m_x(x - x_i) + m_{Q^2}(Q^2 - Q_j^2)$$

where

$$m_x = \frac{F_{2,\text{theo}}^{c\bar{c}}(x_{i+1}, Q_j^2) - F_{2,\text{theo}}^{c\bar{c}}(x_{i-1}, Q_j^2)}{x_{i+1} - x_{i-1}}$$

and

$$m_{Q^2} = \frac{F_{2,\text{theo}}^{c\bar{c}}(x_i, Q_{j+1}^2) - F_{2,\text{theo}}^{c\bar{c}}(x_i, Q_{j-1}^2)}{Q_{j+1}^2 - Q_{j-1}^2}.$$

This correction was found to be typically $< 1\%$ and at most 2.5% at low Q^2 high x. $F_{2,\text{theo}}^{c\bar{c}}$ was evaluated using the same PDF, charm mass and renormalisation and factorisation scales as implemented in the HVQDIS prediction.

8.4 Systematic Errors

"Systematic errors" is the general term for all the uncertainties in the measurement that arise from the uncertainty in the assumptions made. In particular they are used to gauge the degree to which the MC simulation replicates what is seen in data and to correct for any inadequacies in this simulation. Assessment of systematic errors plays an important role in cross-section measurements which entirely use MC information to calculate the acceptance corrections. This section details the theoretical and experimental systematics relevant to the measurements in this thesis.

8.4.1 Theoretical Systematics

The NLO QCD predictions for D^* productions were calculated using the HVQDIS [11] program. This calculation carries with it a number of systematic uncertainties including

- The mass of the charm quark.
  - This value was changed consistently in the PDF fit and in HVQDIS. It was varied from the central value of 1.35 GeV by ∓ 0.15 GeV which altered the cross-section by $^{+9.7}_{-9.1}\%$ with the most significant variation at low $p_T(D^*)$.
- The factorisation and renormalisation scale μ.
  - This value was nominally set to $\sqrt{Q^2 + 4m_c^2}$ and was modified to $2\sqrt{Q^2 + 4m_c^2}$ and $\max(2m_c, \sqrt{Q^2/4 + m_c^2})$ [11] and caused a shift in the predicted cross-section by $^{+4}_{-1}\%$.

These sources of systematic error were added in quadrature and are shown in a band in figures 8.14, 8.15, 8.16 and 8.17 for the differential cross-sections in Q^2, $p_T(D^*)$, x and $\eta(D^*)$ respectively.

The extrapolation to the full kinematic region using equation 8.1 has associated with it a theoretical systematic uncertainty. This uncertainty is unchanged from the HERA I measurement [52] which was determined by consideration of the following factors:

- The AROMA fragmentation [53] was used instead of the Peterson fragmentation. The changes associated with this were typically less than 10%.
- The mass of the charm quark was changed by ± 0.15 GeV in both the HVQDIS calculation and in the calculation of $F_2^{c\bar{c}}$ which caused differences in the extrapolation of 5% at low x which rapidly shrank with increasing x.

- The upper and lower predictions from the ZEUS NLO PDF fit which arose from experimental uncertainties of the fitted data. Deviations were less than 1%.

These uncertainties are unchanged from the HERA I measurements since no theoretical advancements have been made. Therefore the calculation of these systematics are not repeated here and are instead quoted directly from the HERA I paper. In HERA I the contributions from these errors were added in quadrature and this sum is given in table 8.8.

Renormalisation and factorisation scale

The renormalisation and factorisation scale, μ, are input parameters to the HVQDIS NLO prediction. These values are not numerically well defined and therefore introduce a systematic effect into the calculation. μ is changed from $\sqrt{Q^2+4m_c^2}$ to $2\sqrt{Q^2+4m_c^2}$ and $\max(2m_c, \sqrt{Q^2/4+m_c^2})$, this range rises significantly above and below the nominal scale used. This variation was used in earlier ZEUS studies [66] and contributes only a small systematic error.

The epsilon parameter

The fragmentation uncertainty was also considered in [52] where the ϵ parameter in the Peterson fragmentation function was changed by ± 0.015. The Peterson fragmentation fraction is used to describe the fragmentation of the c quark to the D^* meson in HVQDIS and ϵ is its only free parameter. Here we recognise that this is smaller than the contribution from the other errors and so do not include it in the quadratic sum.

Choice of PDF

The HERA I measurement of $F_2^{c\bar{c}}$ [52] used the 2003 ZEUS-S NLO QCD global fit to structure function data [67] as the parameterisation of the proton PDFs. ZEUS-S is suitable for $F_2^{c\bar{c}}$ extraction because it has been constructed in the $\overline{MS}$ scheme and generates charm via the BGF process just like HVQDIS. In the ZEUS-S fit the mass of the charm quark was nominally set at 1.35 GeV although fits were also made at 1.35 ∓ 0.15 GeV for use in systematic errors. The ZEUS-S proton PDF is used to extrapolate a prediction for $F_2^{c\bar{c}}$ used in equation 8.1.

No other PDFs are implemented here since in HVQDIS the extrapolation was performed with ZEUS-S.

An assessment of the degree to which the HVQDIS extrapolation is affected by the choice of PDF was made in HERA I by using also using the CTEQQ5F3 [68] and GRV98-HO [69] PDFs in HVQDIS only. Changing the PDF will gauge the systematic contribution of the choice of parameterisation, in particular the parameterisation of the gluon density in the proton PDFs. The changes were of the order $+1.4\%$ and -16% but were not added in quadrature to the final answer since no $F_2^{c\bar{c}}$ extrapolation exists for these PDFs. $F_2^{c\bar{c}}$ is measured assuming that ZEUS-S NLO is the best choice for the extrapolation from $\sigma^{c\bar{c}}$ to $F_2^{c\bar{c}}$.

At HERA II ZEUS-S remains the latest PDF in the $\overline{MS}$ scheme that uses BGF and has been extrapolated to a prediction of $F_2^{c\bar{c}}$. It is therefore still the most suitable PDF for this measurement. Because the choice of PDF is the same as in HERA I the systematic error associated with its selection is identical to that quoted for HERA I; $+1.4\%$ and -16% for CTEQQ5F3 and GRV98-HO respectively. The systematic error associated with this quantity cannot be reduced further in this analysis.

8.4.2 Experimental Systematics

The experimental systematics used in this thesis follow those used in the HERA I measurement of charm fragmentation [70]. These systematics may be broken down into a number of categories as follows:

- Model dependence of detector acceptance corrections:
  - Varying the $\eta(D^*)$ or $p_T(D^*)$ distributions of the reference MC sample.
  - Using also HERWIG.
- The uncertainty of the tracking simulation:
  - Varying the track loss probability by 20% of its values.
  - Varying all data momenta by $\pm 0.3\%$ to account for the magnetic field uncertainty.

- The uncertainty of the beauty subtraction:
  - Varying the b-quark cross-section by a factor of 2 in the reference MC sample.
- The signal extraction process:
  - The Δ M range was changed for the D^0 signal.
  - The background normalisation was varied.
- DIS systematics:
  - Vary the electron energy scale by $\pm$ 2% and the hadronic energy by $\pm 3\%$.
- Cross checks using the electron method and fits to extract the D^* signal.

Collectively these systematics attempt to gauge the extent to which the MC model accurately describes the data. Each of these changes are made in turn and their effect on the Q^2, η and p_T cross-sections are recorded in tables 8.2, 8.4 and 8.3. The degree to which $F_2^{c\bar{c}}$ is affected is recorded numerically across tables C.1, C.2 and C.3 and graphically in figures 8.6 to 8.13 which also show the total systematic and statistical errors. These results are discussed in detail in section 8.4.6.

8.4.3 Varying the $p_T(D^*)$ and $\eta(D^*)$ distributions

To quantify the systematic associated with the poor MC description of the $p_T(D^*)$ and $\eta(D^*)$ distributions, the MC event sample was reweighted to improve the agreement and all calculations were repeated to evaluate the size of any measurement shift. The shift associated with the $p_T(D^*)$ reweighting was added in quadrature to the other systematic errors whilst the $\eta(D^*)$ reweighting was considered a cross check, with the exception of the $d\sigma/d\eta(D^*)$ measurement where the primary check is the $\eta(D^*)$ reweighting. The weights used were functions of either $p_T^{\text{rec}}(D^*)$ or $\eta^{\text{rec}}(D^*)$. Agreement between data and MC in the control plots was quantified using the χ^2 parameter as defined in equation 6.2.

The lower plots in figure 8.2 show both the $p_T(D^*)$ and $\eta(D^*)$ control plots before reweighting and the reweighting functions used to improve their agreement. These functions were obtained by taking the ratio of data to MC of each control plot and fitting to it

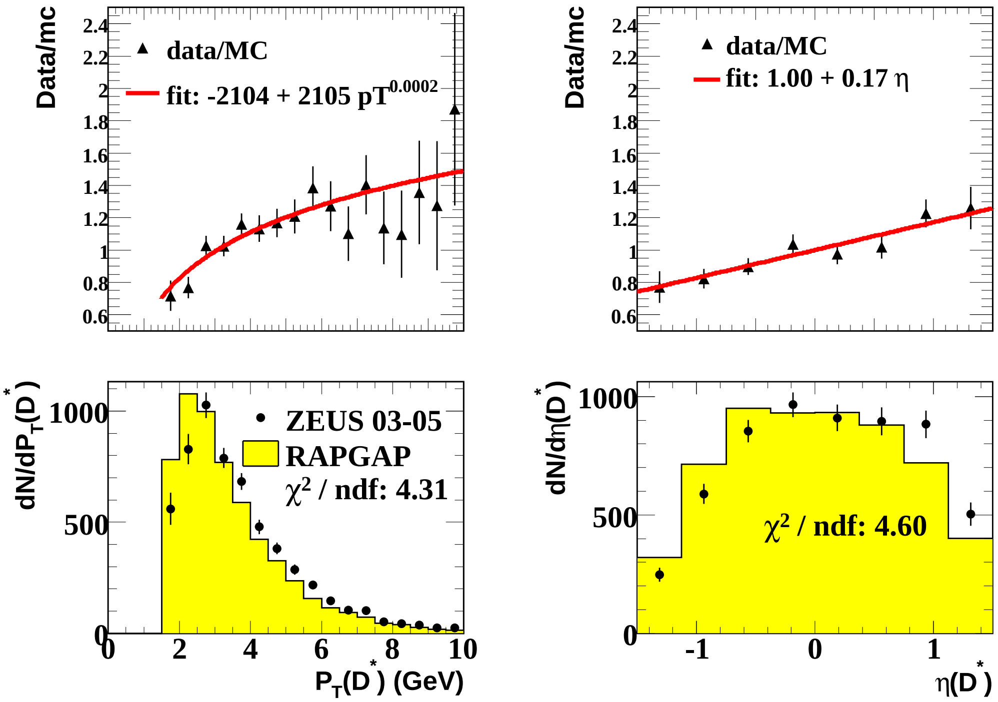

Figure 8.2: The $p_T(D^*)$ and $\eta(D^*)$ control plots (below) before the reweighting of either $p_T(D^*)$ or $\eta(D^*)$ and the ratio of data to MC in each bin and associated fit (above). In the control plots data is shown in points and RAPGAP is shown in yellow. The χ^2 parameter is defined in equation 6.2 and is used to quantify the level of agreement between MC and data. In the ratio plots (above) the fit through the points is shown by a red line. This fit is used to reweight the control plots below to improve the agreement between data and MC.

a function of the form $a + b \times p_T(D^*)^c$ for $p_T(D^*)$ and $a + b \times \eta(D^*)$ for $\eta(D^*)$. The ratio plots and fits are shown in the upper half of figure 8.2. Once the fit is performed and a, b and c are extracted the W_η and W_{p_T} reweighting functions take the explicit form

$$W_\eta = 1.00 + 0.17 \times \eta(D^*) \tag{8.2}$$

$$W_{p_T} = -2100 + 2100 p_T(D^*)^{0.00012} \tag{8.3}$$

where W_η and W_{p_T} are the weights applied to the event to improve the $\eta(D^*)$ and $p_T(D^*)$ distributions respectively.

The effect of weighting by W_η on the control plots is illustrated in figure 8.3. The χ^2/ndf

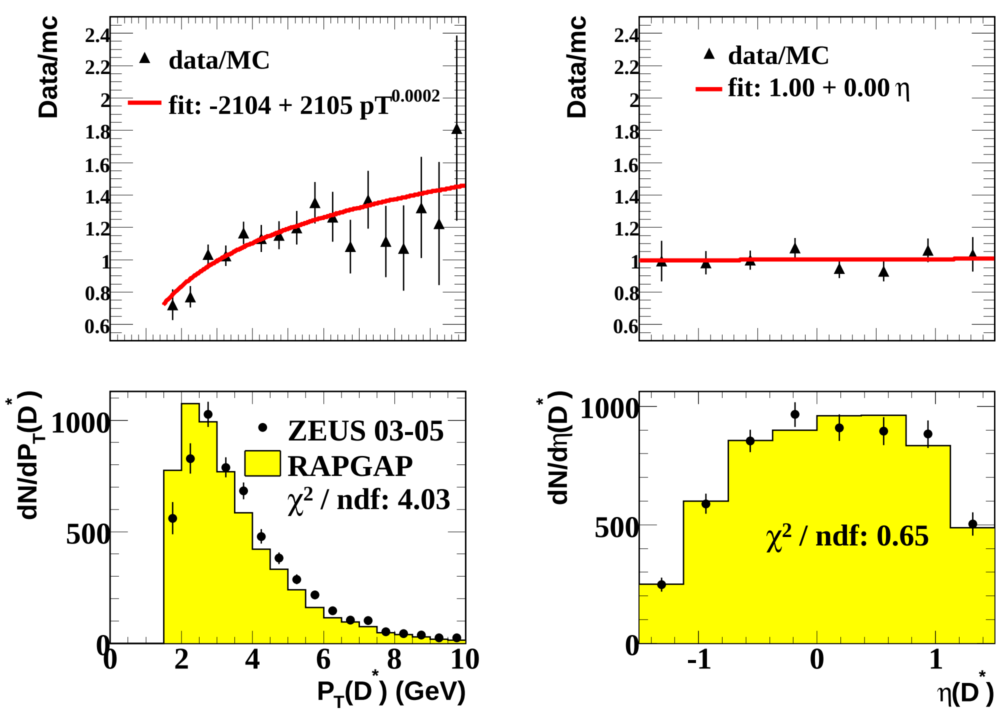

Figure 8.3: The $p_T(D^*)$ and $\eta(D^*)$ control plots (below) after the η reweighting using equation 8.2 and the ratio of data to MC in each bin and associated fit (above). Data is shown in points and RAPGAP is shown in yellow. The χ^2 parameter is defined in equation 6.2 and is used to quantify the level of agreement between MC and data. In the ratio plots (above) the fit through the points is shown by a red line.

on the $\eta(D^*)$ distribution has fallen from 4.60 to 0.65 and the fit ratio of data to MC is constant at 1 for each bin. Improvement is also recorded in the $p_T(D^*)$ distribution whose χ^2/ndf value falls from 4.31 to 4.03.

Similarly the effect of weighting by W_{p_T} on the control plots is illustrated in figure 8.4. In this case the χ^2/ndf associated with the $p_T(D^*)$ distribution has fallen from 4.31 to 0.87. A fit to the ratio of MC and data is constant at 1. Some improvement is also recorded in the $p_T(D^*)$ distribution whose χ^2/ndf value falls from 4.60 to 3.78.

The uncertainty associated with this systematic is assigned entirely to the detector, although in reality it is impossible to disentangle this from contributions from the physics simulation. The decision to assign this uncertainty to the detector is conservative, and

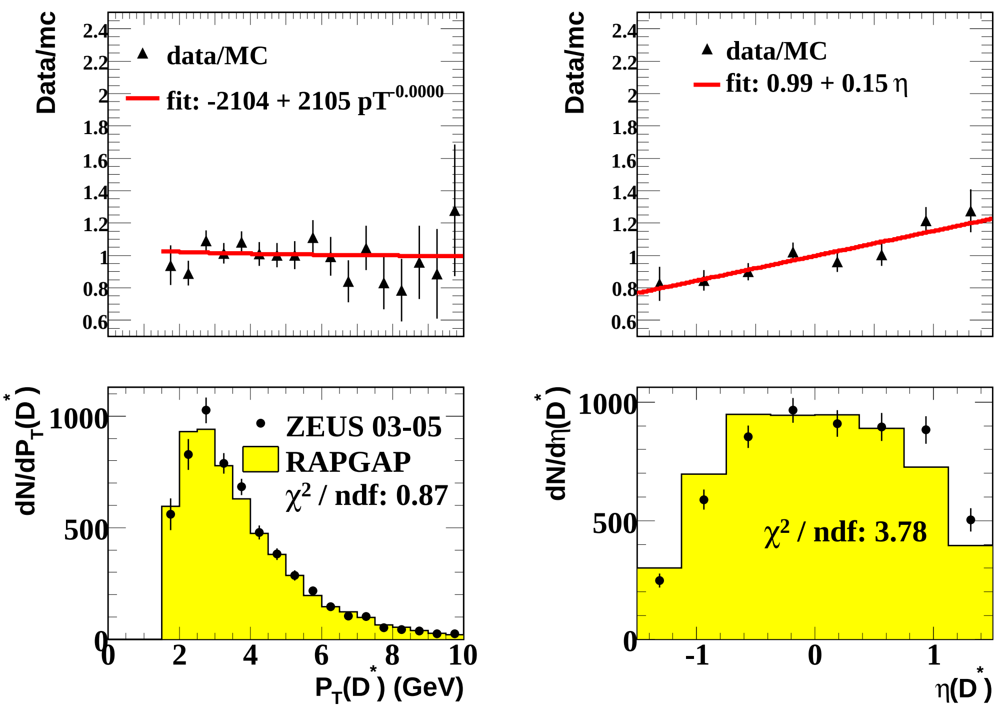

Figure 8.4: The $p_T(D^*)$ and $\eta(D^*)$ control plots (above) after the p_T reweighting using equation 8.3 and the ratio of data to MC in each bin and associated fit (above). Data is shown in points and RAPGAP is shown in yellow. The χ^2 parameter is defined in equation 6.2 and is used to quantify the level of agreement between MC and data. In the ratio plots (below) the fit through the points is shown by a red line.

given that charm production is reasonably well understood in the measured region it is not unreasonable. Along with the track loss probability this systematic error provides a significant contribution to the overall systematic error.

8.4.4 Track Loss Probability

The probability of not matching the reconstructed slow pion track to the true level track is another large source of systematic error. It was first considered in the HERA I analysis [72] and is repeated in this measurement. Because π_s is typically the hardest track to find, its contribution to this systematic is much greater than that of the K or π and so it is the only track considered. To evaluate this error a large MC sample of $D^* \rightarrow D^0\pi_s^+ \rightarrow (K^-\pi^+)\pi_s$

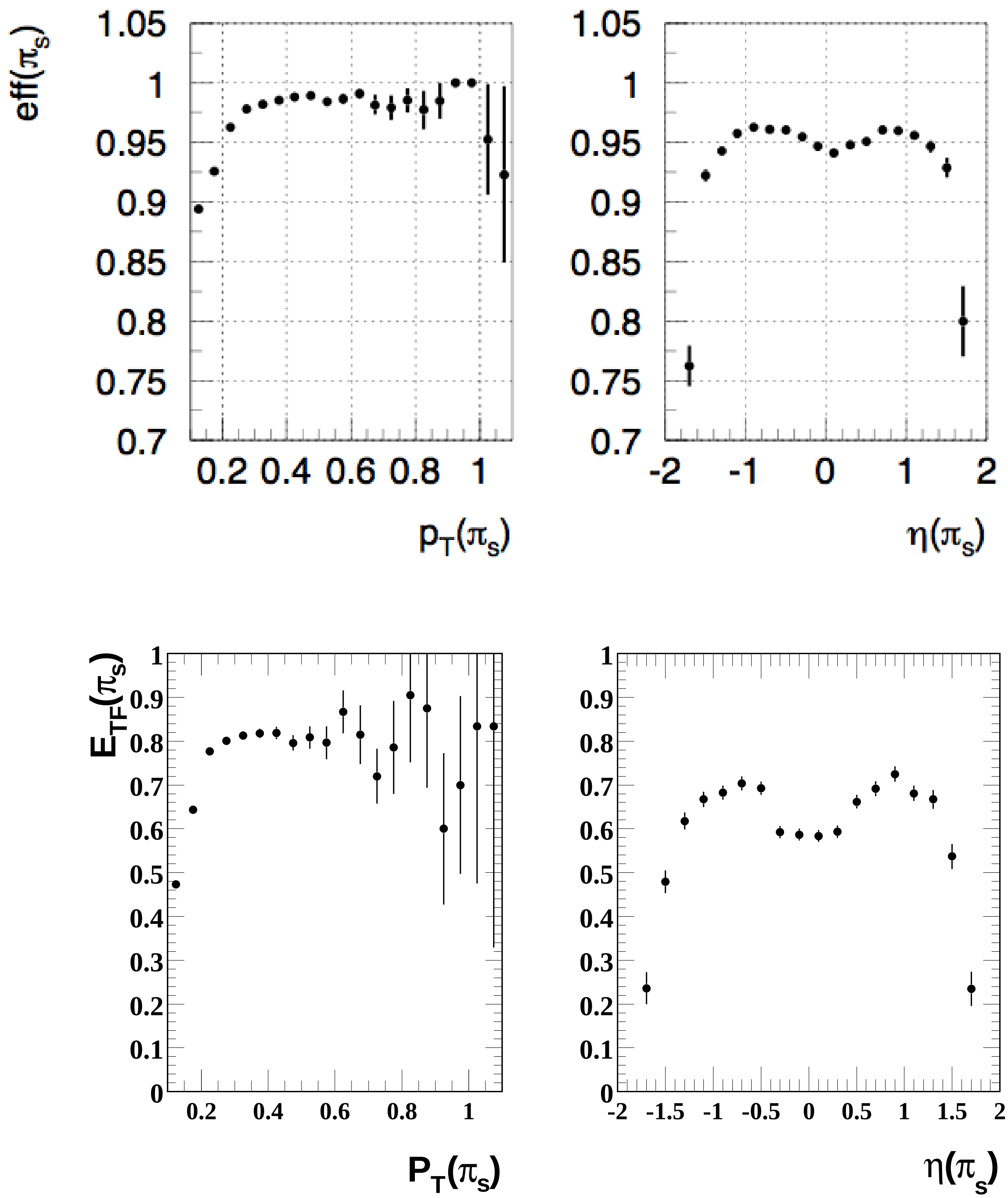

Figure 8.5: The HERA I (upper)[71] and HERA II (lower) MC efficiencies of track finding as a function of $p_T(\pi_s)$ or $\eta(\pi_s)$.

decays was used to match generator and reconstruction level $D^{*\pm}$ decay tracks. The p_T distribution of the generated π_s is made when *all* generated $D^{*\pm}$ tracks are matched to reconstructed tracks. Another $p_T(\pi_s)$ distribution is made when the generated K and π tracks are matched regardless of π_s. The ratio of the first to the second is the track finding efficiency, E_{TF}, for the π_s and was calculated in bins of $p_T(\pi_s)$ and $\eta(\pi_s)$ and is shown in figure 8.5. For the upper half of this figure is the HERA I efficiency which was was approximately 90% for $0.12 < p_T < 0.15$ GeV rising to 98% for $p_T > 0.4$ GeV. HERA II efficiencies have the same shape but are typically 20% lower in all bins.

The probability to lose a track in the dead material before the CTD or because of inefficient track reconstruction is called the track loss probability (TLP) and is defined as $1-E_{\mathrm{TF}}$. This quantity is increased by 20% [73] in the MC sample as a conservative estimate of the uncertainty and corresponds to a decrease in reconstruction efficiency. To implement this variation an event level weighting of ϵ'/ϵ is applied to all candidates where $1-\epsilon' = 1.2(1-\epsilon)$ and ϵ' is the reconstruction efficiency we wish to simulate. For SL 1 tracks this is of the order of 3% and rises with increasing SL. Because this analysis uses tracks which pass through SL 3 and above the 20% adjustment conservatively gauges the uncertainty.

When calculating the overall systematic error only the TLP for $p_T(\pi_s)$ is adjusted and the $\eta(\pi_s)$ TLP is used as a cross check. The only exception is when measuring $d\sigma/d\eta$ at which point the $\eta(\pi_s)$ TLP is the used primarily. The error associated with this procedure is one of the largest systematics and causes a variation of around 10% for either TLP adjustment.

8.4.5 Switching to HERWIG

A systematic check of the model dependence of the detector acceptance corrections is to switch the principle MC from RAPGAP to HERWIG 6.301 [10] in what is one of the largest systematic errors in this analysis. For a number of reasons HERWIG is expected to give an inferior measurement of $F_2^{c\bar{c}}$ because, amongst other things, it does not adequately simulate the mass spectrum backgrounds. To calculate the error associated with this systematic all calculations are repeated using HERWIG to measure the acceptance. The shift in the measured values is recorded and added in quadrature to the other systematics.

Control plots for HERWIG are given in figure 6.19 which suggest that the electron method is better modeled than the double angle method. The systematic contribution from HERWIG could be reduced by switching to the electron method as the principle reconstruction technique, however because the low y low Q^2 resolution of this method is very poor such a switch will significantly increase the error overall.

8.4.6 Systematic Error Analysis

To calculate the overall systematic error, each of the measurements are repeated with each systematic variation. If the measured value is shifted from the nominal position the shift is recorded and added in quadrature to all shifts in the same direction. The quadratic sum gives the overall systematic error. The size of the individual shifts is recorded in tables 8.2 8.3 8.4 and 8.5 using the key in table 8.1 to identify each systematic.

$d\sigma/d\eta$ systematic error breakdown

The effect of each systematic variation on $d\sigma/d\eta$ is given in table 8.2. The largest systematic error arises from the track loss probability and variation of the $\eta(D^*)$ MC distribution. Varying the track loss probability of $\eta(\pi_s)$ always increases the measurement by more than 10%, and the lowest increase from the corresponding $p_T(\pi_s)$ track loss systematic is a 10% increase. In principle both of these variations measure the same effect and so only one is included in the final quadratic sum. These large errors arise from the poorly understood multiple scattering effect caused by the installation of the MVD at HERA II.

The second largest systematics arise from the manipulation of the $\eta(D^*)$ distributions to improve agreement between data and MC. This reweighting increases the central value by 13% in the rear direction and decreases it by 8% in the forward direction. In the central region where there are more tracks the shift is around 2% and the trend is for the cross-section to decrease in the rear and increase in the forward direction.

Inspection of the control plots in figure 7.4 reveals a large discrepancy between MC and data, particularly at low p_T and at the forward and rear $\eta(D^*)$. This large difference manifests itself in the form of this large contribution to the systematic error and can be reduced by improving the HERA II description of ZEUS in the MC detector simulation or

Key	Description
0	The standard measurement with no systematic adjustment.
1	Varying the track loss probability of $p_T(\pi_s)$
2	Varying the track loss probability of $\eta(\pi_s)$
3	Varying the $\eta(D^*)$ distribution in MC
4	Varying the $p_T(D^*)$ distribution in MC
5	Using HERWIG instead of RAPGAP
6	Increasing the beauty cross-section by a factor 2 in MC
7	Decreasing the beauty cross-section by a factor 2 in MC
8	Increasing the track momenta in data by 0.3%
9	Decreasing the track momenta in data by 0.3%
10	Narrow the ΔM width for the D^0 signal
11	Widen the ΔM width for the D^0 signal
12	Increase the area used in background normalisation
13	Decrease the area used in background normalisation
14	Decrease the hadronic energy scale by 3%
15	Increase the hadronic energy scale by 3%
16	Decrease the electron energy scale by 2%
17	Increase the electron energy scale by 2%

Table 8.1: The key used to identify the number used to represent each systematic in the measurements.

η range	$d\sigma/d\eta$ (nb)	1	2	3	4	5	6
(-1.5, -0.8)	1.186	10.71%	11.66%	12.80%	-0.07%	3.51%	0.43%
(-0.8, -0.35)	1.446	9.79%	10.42%	4.97%	-2.84%	-2.85%	0.08%
(-0.35, 0)	1.635	10.26%	15.59%	1.46%	-3.77%	-5.72%	0.06%
(0, 0.4)	1.543	9.97%	15.73%	-1.16%	-3.49%	-4.49%	0.44%
(0.4, 0.8)	1.555	10.32%	11.03%	-3.91%	-3.30%	-2.38%	0.93%
(0.8, 1.5)	1.704	9.60%	10.77%	-8.10%	-2.64%	-1.27%	0.77%
η range	$d\sigma/d\eta$	7	8	9	10	11	12
(-1.5, -0.8)	1.186	-0.57%	-0.49%	0.00%	-3.81%	0.59%	-0.57%
(-0.8, -0.35)	1.446	0.03%	0.47%	-0.25%	-1.75%	2.87%	0.04%
(-0.35, 0)	1.635	-0.41%	0.57%	-0.67%	-2.69%	2.06%	0.02%
(0, 0.4)	1.543	-0.47%	-0.08%	-0.13%	-3.78%	3.26%	-0.23%
(0.4, 0.8)	1.555	-0.37%	-0.48%	-0.92%	1.51%	0.30%	0.23%
(0.8, 1.5)	1.704	-0.87%	-0.12%	-0.13%	-2.53%	-1.09%	-0.62%
η range	$d\sigma/d\eta$	13	14	15	16	17	
(-1.5, -0.8)	1.186	-0.57%	5.08%	-1.95%	0.35%	-0.56%	
(-0.8, -0.35)	1.446	0.04%	4.57%	-1.14%	0.37%	-0.33%	
(-0.35, 0)	1.635	0.02%	2.78%	0.01%	0.23%	-0.24%	
(0, 0.4)	1.543	-0.23%	2.06%	1.83%	0.07%	-0.10%	
(0.4, 0.8)	1.555	0.23%	1.78%	1.54%	-0.01%	-0.05%	
(0.8, 1.5)	1.704	-0.62%	1.38%	2.60%	-0.02%	0.28%	

Table 8.2: $d\sigma/d\eta$ measurement with individual systematic error contributions. A yellow box indicates a shift from the central value of between 5% and 10% once the systematic has been applied, a magenta box indicates a shift larger than 10%. The systematics checked are labeled from 1 to 17 according to the key in table 8.1. Systematics 1 and 4 are not included in the final measurement since they are cross checks of systematics 2 and 3.

by improving the underlying physics description.

The third largest systematic is caused by switching the principle MC package from RAPGAP to HERWIG. The HERWIG and RAPGAP control plots in figure 7.4 display significant differences that cause a typical shift of -5% in $d\sigma/d\eta$. All other systematic effects are much smaller than those listed above and so do not contribute significantly to the overall measurement.

$d\sigma/dQ^2$ systematic error breakdown

The systematic errors associated with $d\sigma/dQ^2$ are shown in table 8.3. The dominant sources of systematic error are similar to those which dominated $d\sigma/d\eta$. The largest contribution comes from adjusting the track loss probability of D^* in bins of $\eta(D^*)$ and $p_T(D^*)$ which cause a shift of around $+12\%$. Reweighting the $p_T(D^*)$ distribution has little effect at low Q^2 but causes a -5% drop which rises to -13% with increasing Q^2. $d\sigma/dQ^2$ is also sensitive to a switch to HERWIG which causes a variation of typically $\pm 8\%$. It would appear that $d\sigma/dQ^2$ is sensitive at very high Q^2 to adjusting the size of the ΔM width for the D^0 signal ($+70\%$) but this is likely to arise because the statistical error in this bin is large.

$d\sigma/dp_T(D^*)$ systematic error breakdown

Table 8.4 lists the $d\sigma/dp_T$ cross-section and associated systematic errors. As with the previous two measurements the systematic errors are dominated by track loss probability resulting in a shift of approximately $+10\%$ in each bin. Varying the η and p_t distributions does not affect this cross-section to the same degree as for $d\sigma/dQ^2$ and $d\sigma/d\eta$, although the effect is still large and of the order $\pm 10\%$ in the highest and lowest $p_T(D^*)$ bins when $p_T(D^*)$ is reweighted. There is no significant variation after reweighting $\eta(D^*)$. Using HERWIG instead of RAPGAP causes the second and third bins to rise by approximately 6% and a negligible amount in all other bins. All other systematics have a negligible effect.

$d\sigma/dx$ systematic error breakdown

As with all other differential cross-sections $d\sigma/dx$ is most strongly affected by adjusting the track loss probability for D^* candidates, increasing the cross-section by around 12% in each

Q^2 range (GeV^2)	$d\sigma/dQ^2$ (nb/GeV^2)	1	2	3	4	5	6
(5, 10)	0.317	11.46%	12.29%	0.75%	0.99%	-1.88%	0.00%
(10, 20)	0.134	10.89%	12.40%	-0.33%	-0.89%	-5.49%	0.33%
(20, 40)	0.044	9.19%	12.40%	-0.10%	-2.70%	6.78%	0.72%
(40, 80)	0.011	7.98%	12.16%	-0.14%	-5.01%	8.84%	1.58%
(80, 200)	2.05 $\times 10^{-3}$	7.40%	12.74%	-0.93%	-7.73%	8.77%	0.40%
(200, 1000)	3.96×10^{-5}	14.28%	13.80%	0.27%	-13.86%	3.19%	1.78%
Q^2 range	$d\sigma/dQ^2$	7	8	9	10	11	12
(5, 10)	0.317	-0.43%	0.10%	-0.22%	-4.44%	0.41%	-0.53%
(10, 20)	0.134	-0.56%	0.00%	-0.66%	-2.52%	0.40%	-0.14%
(20, 40)	0.044	-0.03%	0.24%	-0.51%	-0.95%	2.64%	0.40%
(40, 80)	0.011	-0.50%	-0.51%	-0.07%	1.44%	-3.82%	-0.55%
(80, 200)	2.05×10^{-3}	-0.73%	0.18%	0.68%	-2.24%	5.74%	-0.98%
(200, 1000)	3.96×10^{-5}	-2.05%	-5.16%	-1.70%	16.99%	67.05%	2.48%
Q^2 range	$d\sigma/dQ^2$	13	14	15	16	17	
(5, 10)	0.317	-0.53%	3.48%	-1.49%	0.30%	-0.49%	
(10, 20)	0.1341	-0.14%	1.97%	1.31%	-0.02%	0.03%	
(20, 40)	0.044	0.40%	2.75%	1.54%	0.15%	0.05%	
(40, 80)	0.011	-0.55%	2.90%	1.00%	0.24%	-0.20%	
(80, 200)	2.05×10^{-3}	-0.98%	2.91%	1.05%	0.22%	-0.11%	
(200, 1000)	3.96×10^{-5}	2.48%	10.18%	-1.09%	0.24%	-0.71%	

Table 8.3: $d\sigma/dQ^2$ measurement with individual systematic error contributions. A yellow box indicates a shift from the central value of between 5% and 10% once the systematic has been applied, a magenta box indicates a shift larger than 10%. The systematics checked are labeled from 1 to 17 according to the key in table 8.1. Systematics 2 and 3 are not included in the final measurement since they are cross checks of systematics 1 and 4.

$P_T(D^*)$ range (GeV)	$d\sigma/dp_T$ (nb/GeV)	1	2	3	4	5	6
(1.5, 2.4)	1.557	16.50%	12.40%	0.19%	11.97%	-0.39%	0.36%
(2.4, 3.1)	1.394	10.34%	12.50%	0.38%	1.25%	5.69%	0.24%
(3.1, 4.0)	0.879	6.87%	12.46%	0.12%	-2.97%	7.30%	0.11%
(4.0, 6.0)	0.358	5.22%	12.08%	-0.21%	-6.33%	0.82%	1.02%
(6.0, 15)	0.032	9.30%	12.77%	-0.16%	-9.65%	1.02%	0.43%
$P_T(D^*)$ range	$d\sigma/dp_T$	7	8	9	10	11	12
(1.5, 2.4)	1.557	-0.43%	-1.88%	0.87%	-2.44%	-1.19%	-0.72%
(2.4, 3.1)	1.394	-0.49%	0.53%	-0.04%	-4.95%	0.24%	-0.19%
(3.1, 4.0)	0.879	-0.12%	-0.46%	-1.10%	1.82%	1.73%	-0.09%
(4.0, 6.0)	0.358	-0.50%	1.07%	-0.64%	-1.19%	2.97%	0.18%
(6.0, 15)	0.032	-0.17%	1.07%	-1.26%	-3.62%	3.18%	0.24%
$P_T(D^*)$ range	$d\sigma/dp_T$	13	14	15	16	17	
(1.5, 2.4)	1.557	-0.72%	2.71%	-0.71%	0.03%	-0.11%	
(2.4, 3.1)	1.394	-0.19%	3.08%	-0.30%	0.23%	-0.07%	
(3.1, 4.0)	0.879	-0.09%	3.09%	1.31%	0.08%	-0.09%	
(4.0, 6.0)	0.358	0.18%	2.88%	1.56%	0.35%	-0.28%	
(6.0, 15)	0.032	0.24%	3.27%	2.16%	0.27%	-0.49%	

Table 8.4: $d\sigma/dp_T$ measurement with individual systematic error contributions. A yellow box indicates a shift from the central value of between 5% and 10% once the systematic has been applied, a magenta box indicates a shift larger than 10%. The systematics checked are labeled from 1 to 17 according to the key in table 8.1. Systematics 2 and 3 are not included in the final measurement since they are cross checks of systematics 1 and 4.

x range	$d\sigma/dx$ (nb)	1	2	3	4	5	6
(0.00008, 0.0004)	3719	11.32%	12.21%	3.79%	-0.32%	-11.74%	0.18%
(0.0004, 0.0016)	1661	10.45%	12.47%	1.71%	-1.06%	1.51%	0.21%
(0.0016, 0.005)	316	9.15%	12.41%	-1.43%	-3.56%	9.88%	0.83%
(0.005, 0.01)	47.5	8.34%	12.49%	-3.17%	-6.14%	8.38%	0.18%
(0.01, 0.1)	0.955	9.72%	12.08%	-4.57%	-10.23%	12.44%	0.20%
x range	$d\sigma/dx$	7	8	9	10	11	12
(0.00008, 0.0004)	3719	-0.55%	0.47%	-0.69%	-3.28%	0.32%	-1.35%
(0.0004, 0.0016)	1661	-0.23%	-0.24%	-0.23%	-2.99%	0.78%	0.15%
(0.0016, 0.005)	316	-0.25%	0.32%	-0.33%	-0.49%	2.07%	-0.28%
(0.005, 0.01)	47.5	-1.08%	-0.53%	0.48%	0.56%	2.80%	1.45%
(0.01, 0.1)	0.955	-1.03%	-2.27%	-1.28%	0.33%	5.19%	-1.48%
x range	$d\sigma/dx$	13	14	15	16	17	
(0.00008, 0.0004)	3719	-1.35%	5.09%	-2.06%	0.32%	-0.63%	
(0.0004, 0.0016)	1661	0.15%	2.95%	0.18%	0.16%	-0.18%	
(0.0016, 0.005)	316	-0.28%	1.74%	1.95%	0.09%	0.12%	
(0.005, 0.01)	47.5	1.45%	2.82%	1.70%	0.09%	-0.27%	
(0.01, 0.1)	0.955	-1.48%	1.60%	4.94%	0.03%	0.61%	

Table 8.5: $d\sigma/dx$ measurement with individual systematic error contributions. A yellow box indicates a shift from the central value of between 5% and 10% once the systematic has been applied, a magenta box indicates a shift larger than 10%. The systematics checked are labeled from 1 to 17 according to the key in table 8.1. Systematics 2 and 3 are not included in the final measurement since they are cross checks of systematics 1 and 4.

bin. Reweighting the $p_T(D^*)$ distribution causes a drop of -6% and -10% in the second last and last bins respectively. When HERWIG is used as the primary MC package the nominal value is shifted by around $\pm 10\%$.

Table 8.6 lists the final measurement for $d\sigma/dQ^2$, $d\sigma/d\eta$, $d\sigma/dp_T$ and $d\sigma/dx$ with their associated statistical and systematic errors. Generally speaking the systematic errors are larger than the statistical errors for each measurement.

$F_2^{c\bar{c}}$ systematic error

Figures 8.6 to 8.13 represent the pull on the standard measurement of $F_2^{c\bar{c}}$ for each of the systematics checked, identified on the x-axis numerically. The dotted line indicates the nominal $F_2^{c\bar{c}}$ measurement and the crosses the systematic shifted measurement. The solid red line is the result of adding each systematic shift in quadrature after separating the effects into positive and negative shifts. The yellow band represents the statistical error. The errors associated with varying the track loss probability and control plot distribution of $\eta(D^*)$ are not included in the quadratic sum since they are considered to be cross checks of the corresponding $p_T(D^*)$ variations. Typically the statistical error is smaller than the detector error except for the highest Q^2 points which are severely statistically limited. The systematics are labeled from 1 to 17 and are identified with systematics using table 8.1. This information is also recorded in tables C.1, C.2 and C.3 in appendix C.

As with the differential cross-sections for η, p_T and Q^2 the systematic error arising from track loss probability and the $\eta(D^*)$, $p_T(D^*)$ distributions is substantial. The track loss probability alone for both η and p_T causes an increase of approximately 10% in all bins. The inadequacies of the HERA II MC are also responsible for the error associated with manipulating the shape of $\eta(D^*)$ and $p_T(D^*)$ in MC. This figure can rise to as high as 25% in the highest Q^2 bins where the data is statistically limited, although this error can range from $\pm 1\%$ to $\pm 13\%$ with the η reweighting and from $\pm 1\%$ to -24% with p_T.

Switching to HERWIG also generates a large error typically between $\pm 10\%$ and can rise as high as 35% and as low as 1%. $F_2^{c\bar{c}}$ is also sensitive to altering the width of the D^0 signal since the granularity of the binning does not allow for a consistently smooth background distribution. The errors associated with this are often negligible but typically rise to around

5% and in one instance 80% but only in a statistically limited bin.

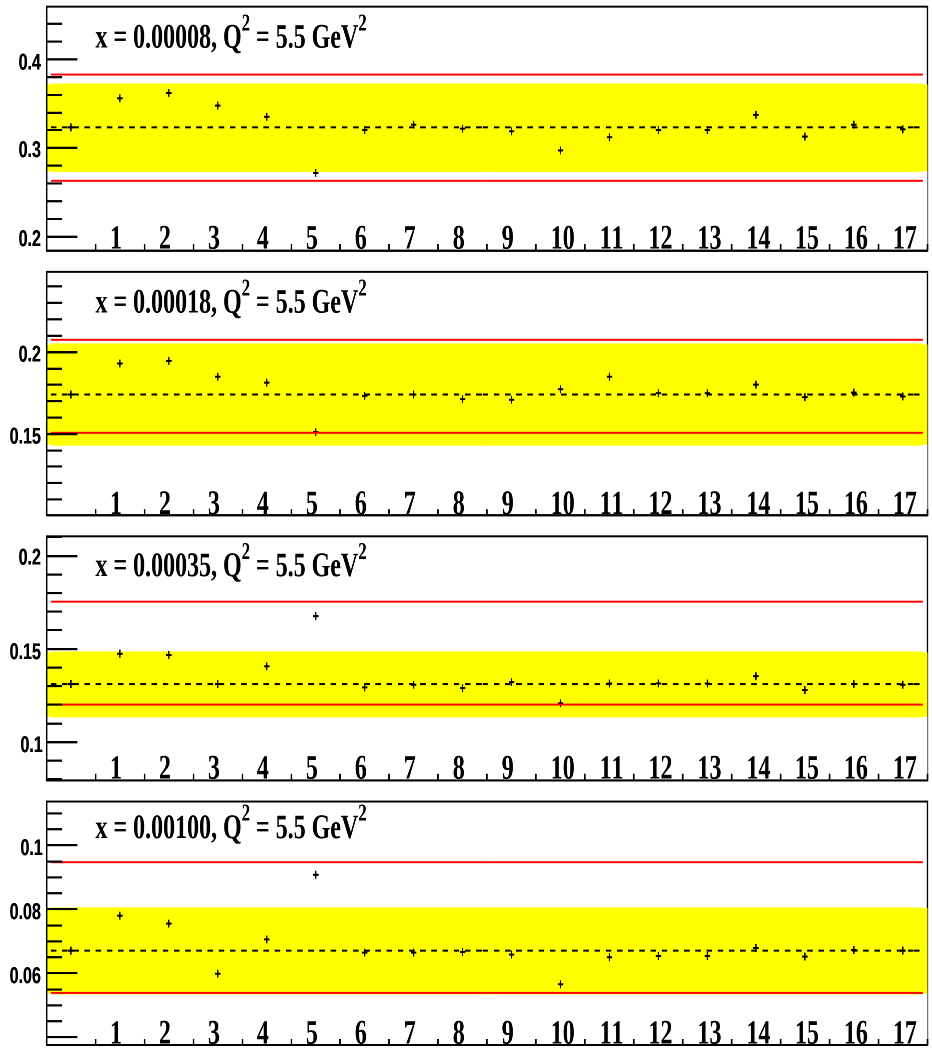

Figure 8.6: Pull on the central $F_2^{c\bar{c}}$ value by each systematic for $Q^2 = 5.5$ GeV. The dotted line indicates the nominal $F_2^{c\bar{c}}(x, Q^2)$ measurement and the yellow band the statistical error. The numbers on the x-axis correspond to systematic errors as identified in table 8.1. The crosses show the altered $F_2^{c\bar{c}}(x, Q^2)$ value. The red lines are the quadratic sum of the positive and negative shifts and correspond to the overall systematic error (Systematics 2 and 3 are not included in this quadratic sum since they are used as cross checks of systematics 1 and 4).

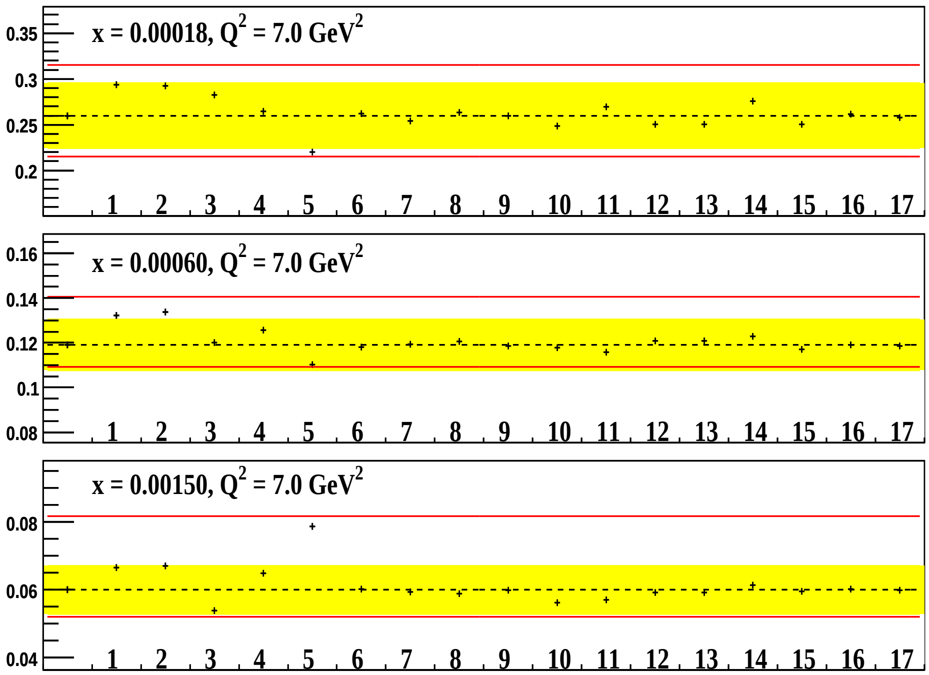

Figure 8.7: Pull on the central $F_2^{c\bar{c}}$ value by each systematic for $Q^2 = 6.7$ GeV^2. Details as for 8.6.

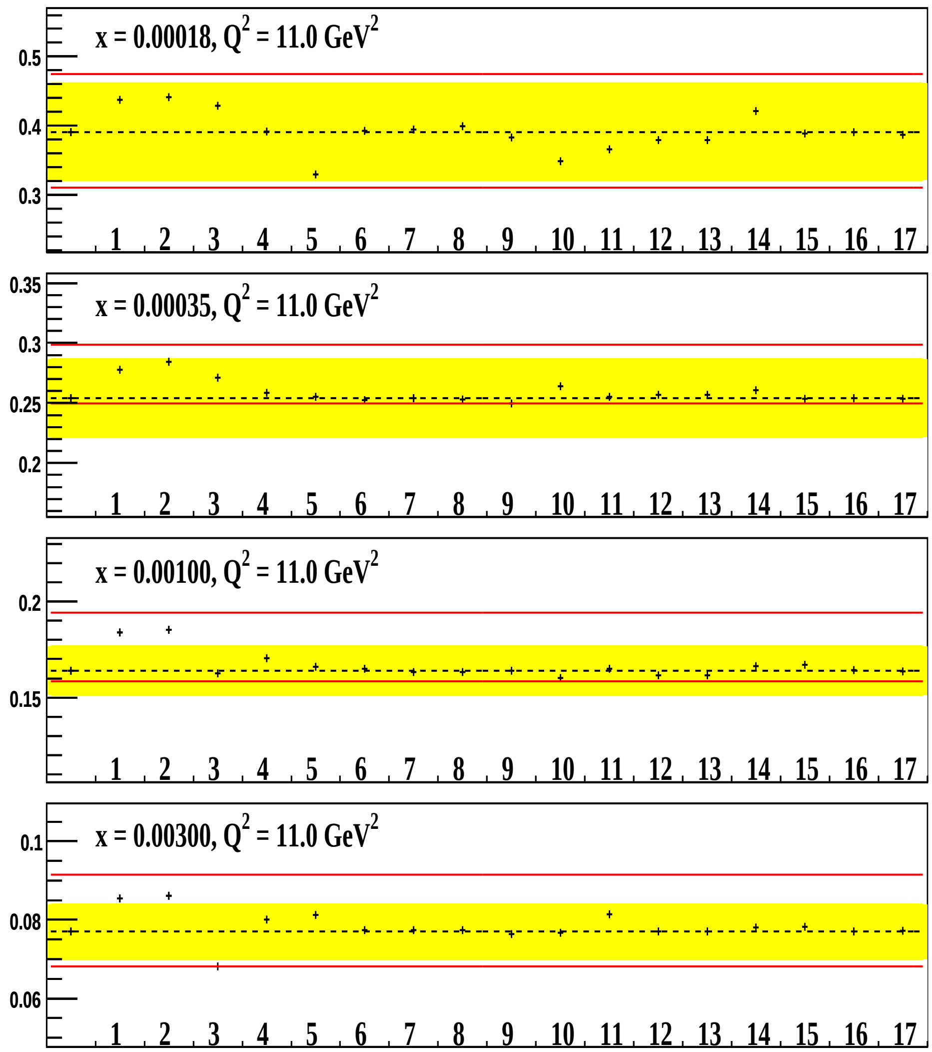

Figure 8.8: Pull on the central $F_2^{c\bar{c}}$ value by each systematic for $Q^2 = 11.5$ GeV^2. Details as for 8.6.

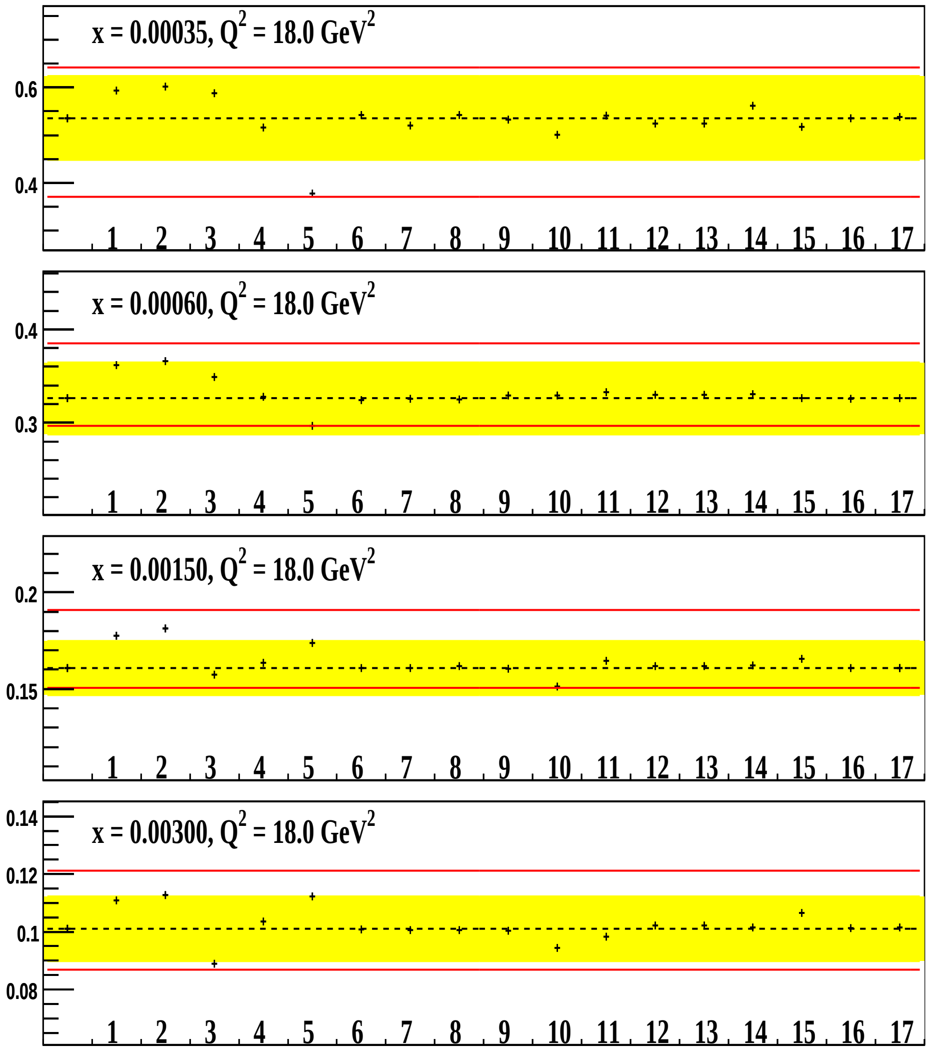

Figure 8.9: Pull on the central $F_2^{c\bar{c}}$ value by each systematic for $Q^2 = 18.8$ GeV^2. Details as for 8.6.

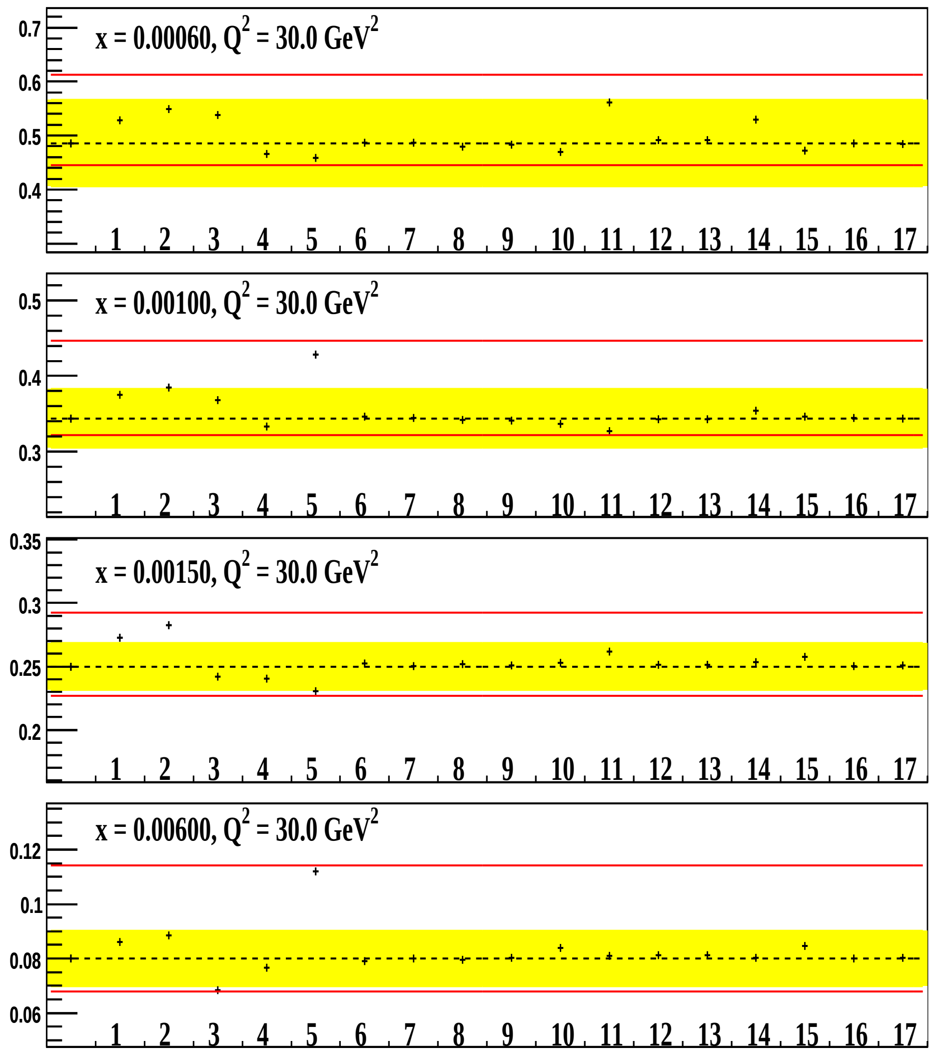

Figure 8.10: Pull on the central $F_2^{c\bar{c}}$ value by each systematic for $Q^2 = 30.9$ GeV^2. Details as for 8.6.

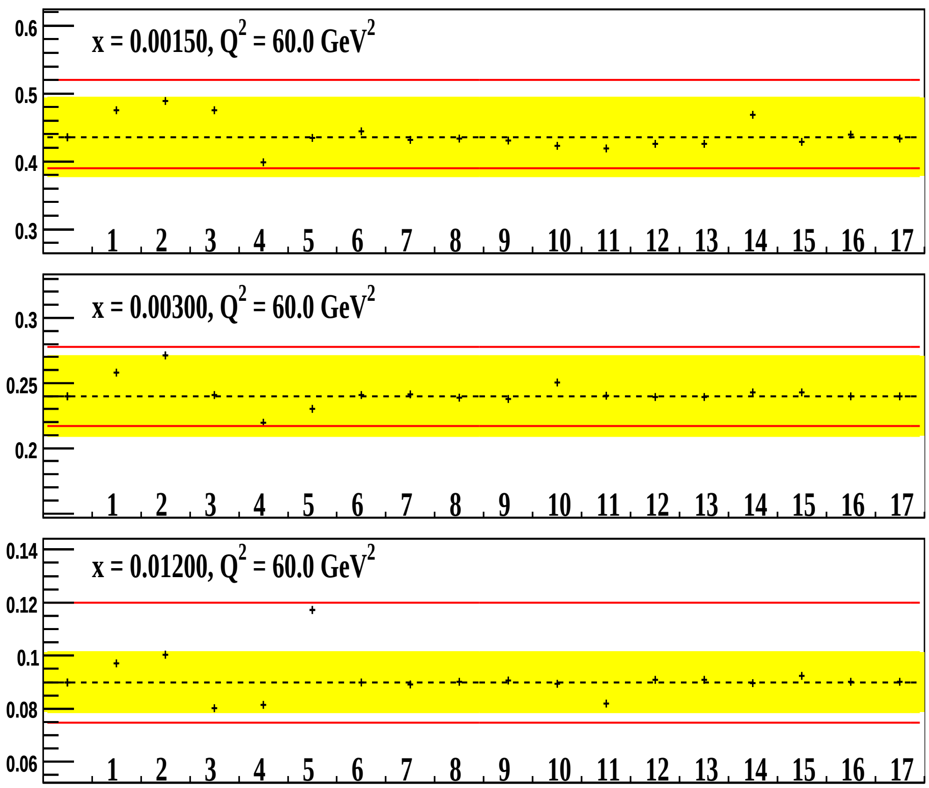

Figure 8.11: Pull on the central $F_2^{c\bar{c}}$ value by each systematic for $Q^2 = 61.1$ GeV^2. Details as for 8.6.

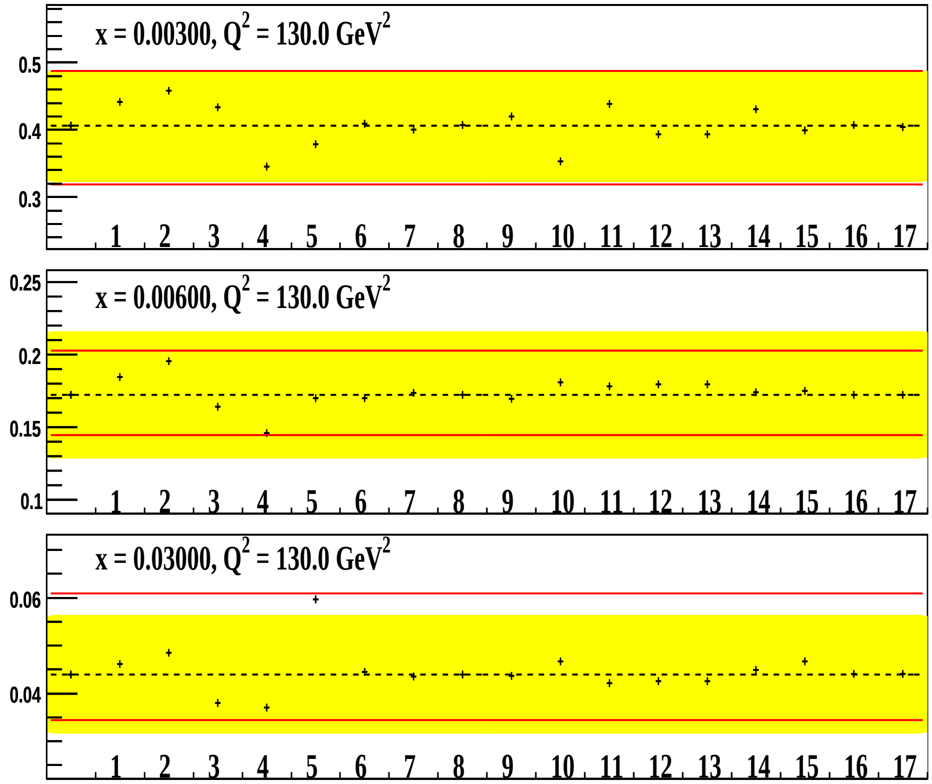

Figure 8.12: Pull on the central $F_2^{c\bar{c}}$ value by each systematic for $Q^2 = 132$ GeV^2. Details as for 8.6.

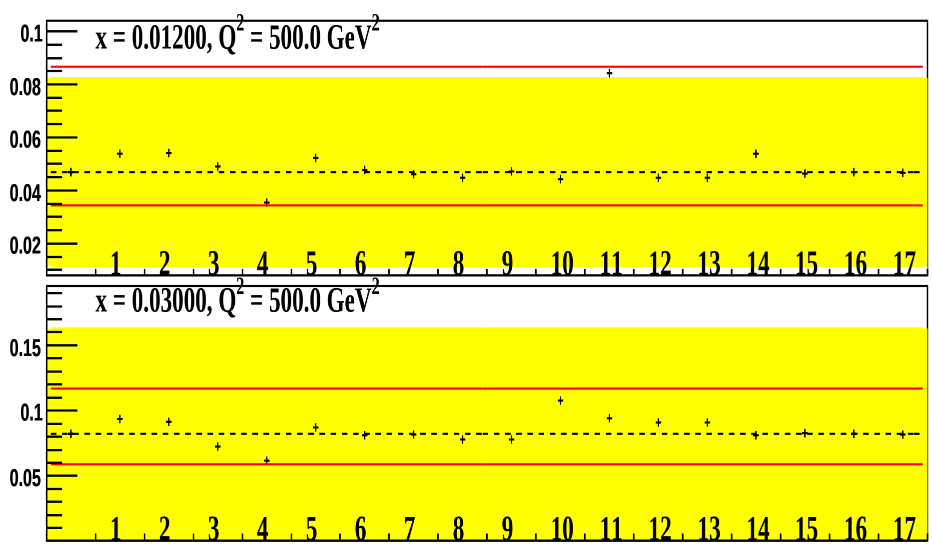

Figure 8.13: Pull on the central $F_2^{c\bar{c}}$ value by each systematic for $Q^2 = 510$ GeV^2. Details as for 8.6.

8.5 Final Results

In this section the final measurement for the differential cross sections in Q^2, $p_T(D^*)$, $\eta(D^*)$ and x, the double differential cross section $d^2\sigma/dQ^2dy$ and the final $F_2^{c\bar{c}}(x, Q^2)$ measurement are given. The measured values are presented with statistical and systematic errors given separately and where appropriate the theoretical errors are shown as well.

8.5.1 Differential Cross-section results

Table 8.6 lists the final measurement for $d\sigma/dQ^2$, $d\sigma/d\eta$, $d\sigma/dp_T$ and $d\sigma/dx$ with their associated statistical and systematic errors shown separately. Generally speaking the systematic errors are larger than the statistical errors for each measurement. These represent the first measurements of charm in DIS using HERA II data. Figure 8.14 shows the HERA I and HERA II measurements of $d\sigma/dQ^2$ with statistical and systematic errors shown. The Q^2 distribution covers 4 orders of magnitude over which there is consistency shown between HERA I, HERA II and the NLO QCD prediction. The acceptance correction is also shown in this plot which ranges from 0.25 to 0.4 and in general rises with increasing Q^2.

Figure 8.15 shows the differential cross-section in $p_T(D^*)$ which falls by 2 orders of magnitude. For the lowest bin the acceptance is approximately 0.2 but rises to 0.45 with increasing $p_T(D^*)$. In this figure the cross section is compared with the NLO prediction and agrees with reasonable consistency.

The differential cross section $d\sigma/dx$ and its acceptance is shown in figure 8.16. The acceptance ranges from 0.2 in the lowest x bin and reaches a maximum of around 0.4 in the second highest bin. The HVQDIS prediction with the ZEUS-S PDF underestimates the measured x in the small x region and overestimates it in the highest two bins. The central values are measured within experimental and theoretical errors.

Finally figure 8.17 shows the $d\sigma/d\eta$ measurement and its acceptance. The acceptance ranges from 0.2 to 0.4 and is highest in the central region. In general the central value of the measured cross-section is lower than the NLO prediction in all but the highest η bin but within experimental errors. In the highest bin the NLO prediction underestimates the measured value but as with the other bins the difference is less than the associated error.

Q^2 range (GeV^2)	$d\sigma/dQ^2$ (nb/GeV^2)	Δ_{stat}	Δ_{syst}
(5, 10)	0.317	±0.0148	$^{+0.0380}_{-0.0163}$
(10, 20)	0.134	±0.0059	$^{+0.0149}_{-0.0083}$
(20, 40)	0.044	±0.0023	$^{+0.0054}_{-0.0013}$
(40, 80)	0.011	±0.00082	$^{+0.0014}_{-0.0007}$
(80, 200)	2.05×10^{-3}	$\pm0.22\times10^{-3}$	$^{+0.27\times10^{-3}}_{-0.17\times10^{-3}}$
(200, 1000)	3.96×10^{-5}	$\pm2.61\times10^{-5}$	$^{+2.86\times10^{-5}}_{-0.60\times10^{-5}}$
$\eta(D^*)$ range	$d\sigma/d\eta$ (nb)	Δ_{stat}	Δ_{syst}
(-1.5, -0.8)	1.186	±0.08	$^{+0.15}_{-0.05}$
(-0.8, -0.35)	1.446	±0.08	$^{+0.16}_{-0.07}$
(-0.35, 0)	1.635	±0.10	$^{+0.18}_{-0.12}$
(0, 0.4)	1.543	±0.09	$^{+0.17}_{-0.11}$
(0.4, 0.8)	1.555	±0.11	$^{+0.17}_{-0.07}$
(0.8, 1.5)	1.704	±0.10	$^{+0.17}_{-0.07}$
$P_T(D^*)$ range (GeV)	$d\sigma/dP_T$ (nb/GeV)	Δ_{stat}	Δ_{syst}
(1.5, 2.4)	1.557	±0.13	$^{+0.32}_{-0.06}$
(2.4, 3.1)	1.394	±0.07	$^{+0.17}_{-0.07}$
(3.1, 4.0)	0.879	±0.039	$^{+0.096}_{-0.028}$
(4.0, 6.0)	0.358	±0.014	$^{+0.025}_{-0.023}$
(6.0, 15)	0.032	±0.002	$^{+0.0034}_{-0.0033}$
x range	$d\sigma/dx$ (nb)	Δ_{stat}	Δ_{syst}
(0.00008, 0.0004)	3719	±237	$^{+500}_{-505}$
(0.0004, 0.00016)	1661	±61	$^{+178}_{-52}$
(0.0016, 0.005)	316	±13	$^{+39.6}_{-10.4}$
(0.005, 0.01)	47.5	±4.9	$^{+5.20}_{-2.55}$
(0.01, 0.1)	0.955	±0.255	$^{+0.131}_{-0.081}$

Table 8.6: The measured values of $d\sigma/dQ^2$, $d\sigma/d\eta$, $d\sigma/dP_T$ and $d\sigma/dx$ in their respective bins. Statistical, systematic and theoretical errors are shown separately.

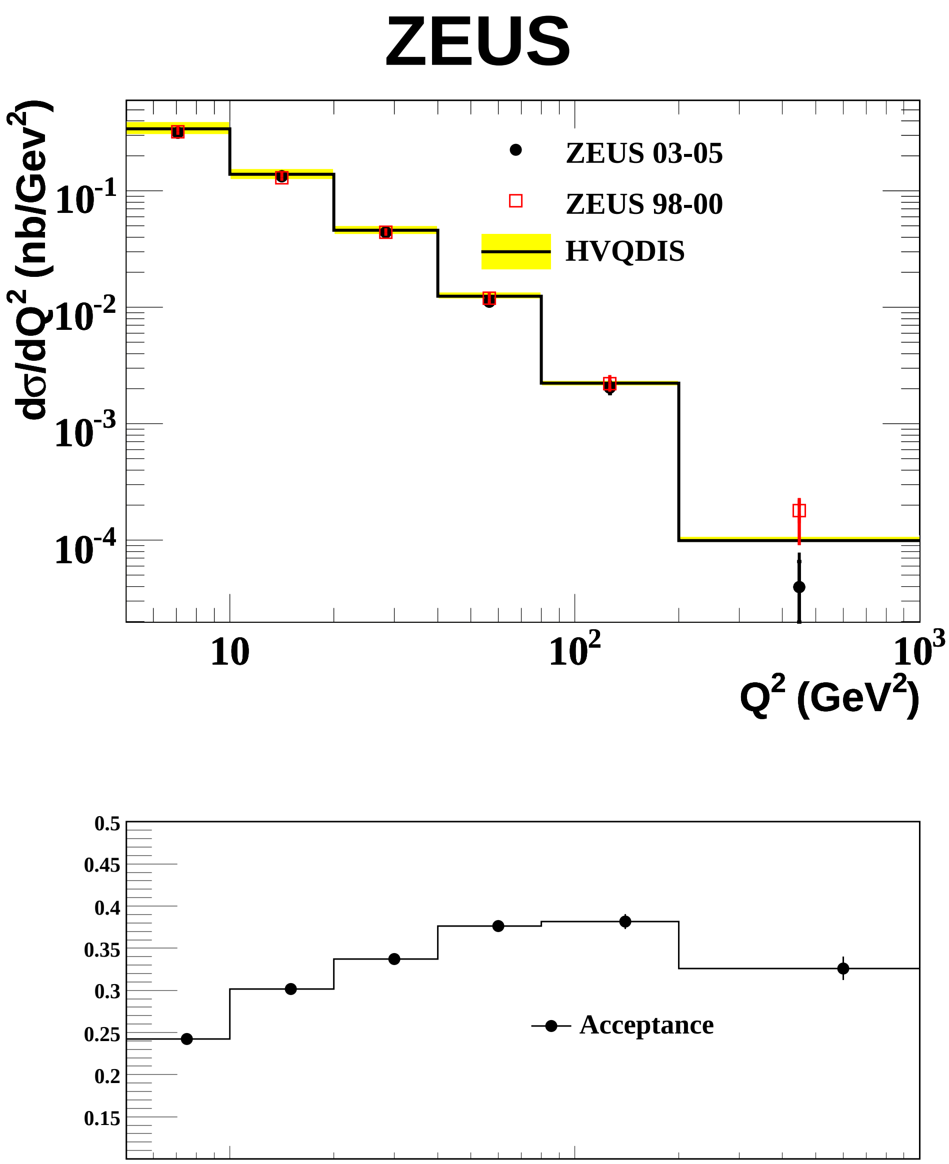

Figure 8.14: The differential D^* cross-section as a function of Q^2 is shown along with the NLO QCD prediction. The HERA II measurement (solid points) is compared to the HERA I measurement (open squares) and found to be in good agreement. Statistical errors are shown (inner error bars) and added in quadrature to the systematic error to give the total error. The solid line is the prediction from the ZEUS NLO QCD fit and the shaded yellow region indicates the theoretical uncertainty in this prediction. The acceptance is shown below.

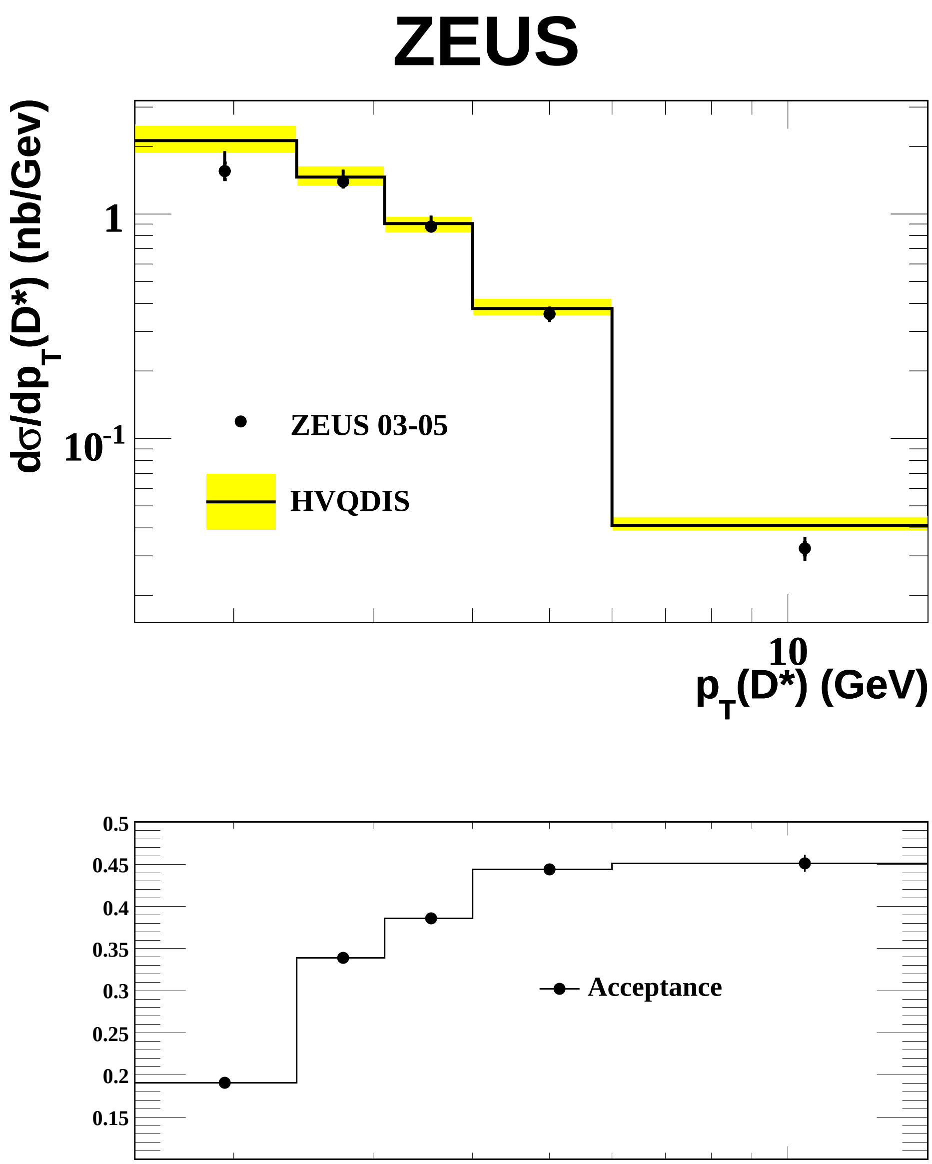

Figure 8.15: The differential D^* cross-section as a function of $p_T(D^*)$ is shown along with the NLO QCD prediction. Statistical errors are shown (inner error bars) and added in quadrature to the systematic error to give the total error. The solid line is the prediction from the ZEUS NLO QCD fit and the shaded yellow region indicates the theoretical uncertainty in this prediction. The acceptance is shown below.

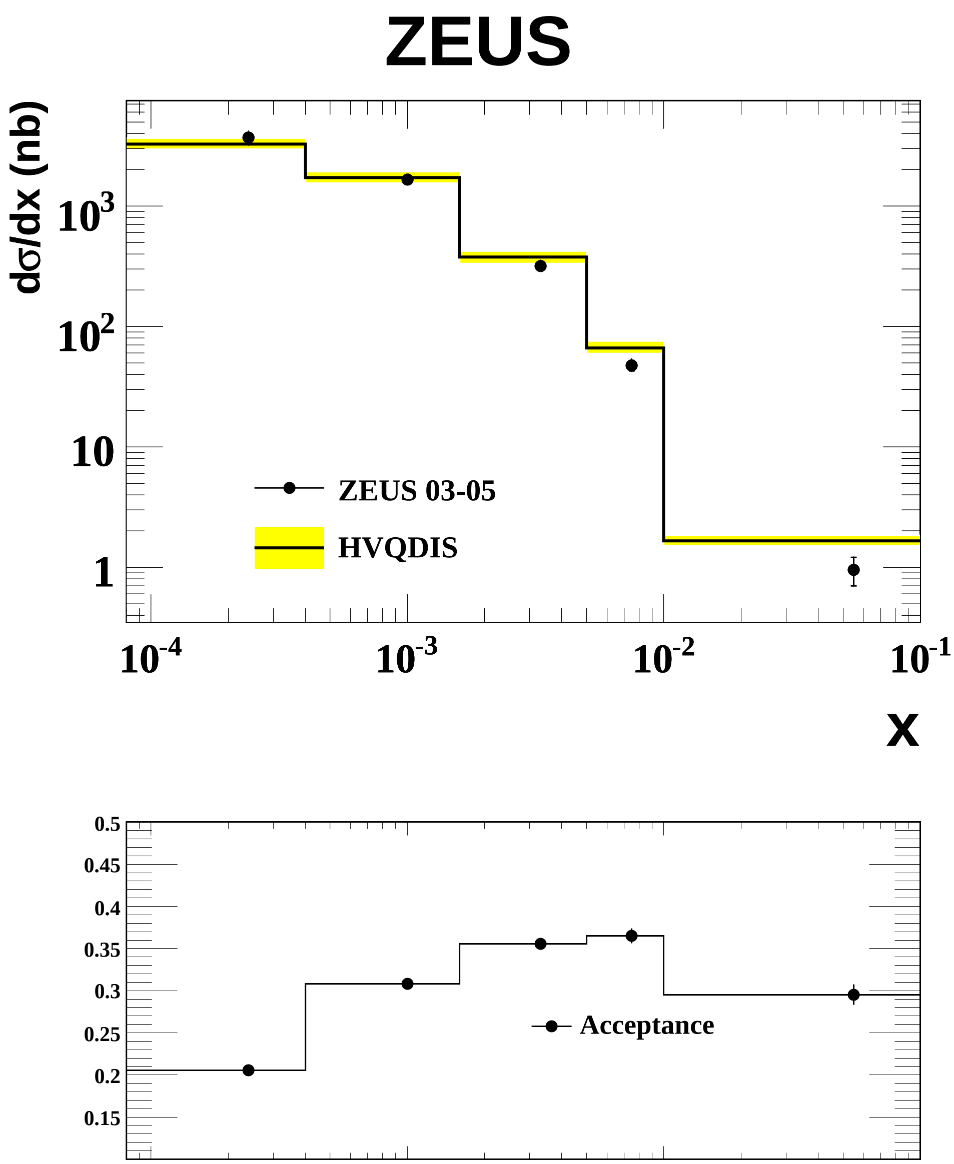

Figure 8.16: The differential D^* cross-section as a function of x is shown along with the NLO QCD prediction. Statistical errors are shown (inner error bars) and added in quadrature to the systematic error to give the total error. The solid line is the prediction from the ZEUS NLO QCD fit and the shaded yellow region indicates the theoretical uncertainty in this prediction. The acceptance is shown below.

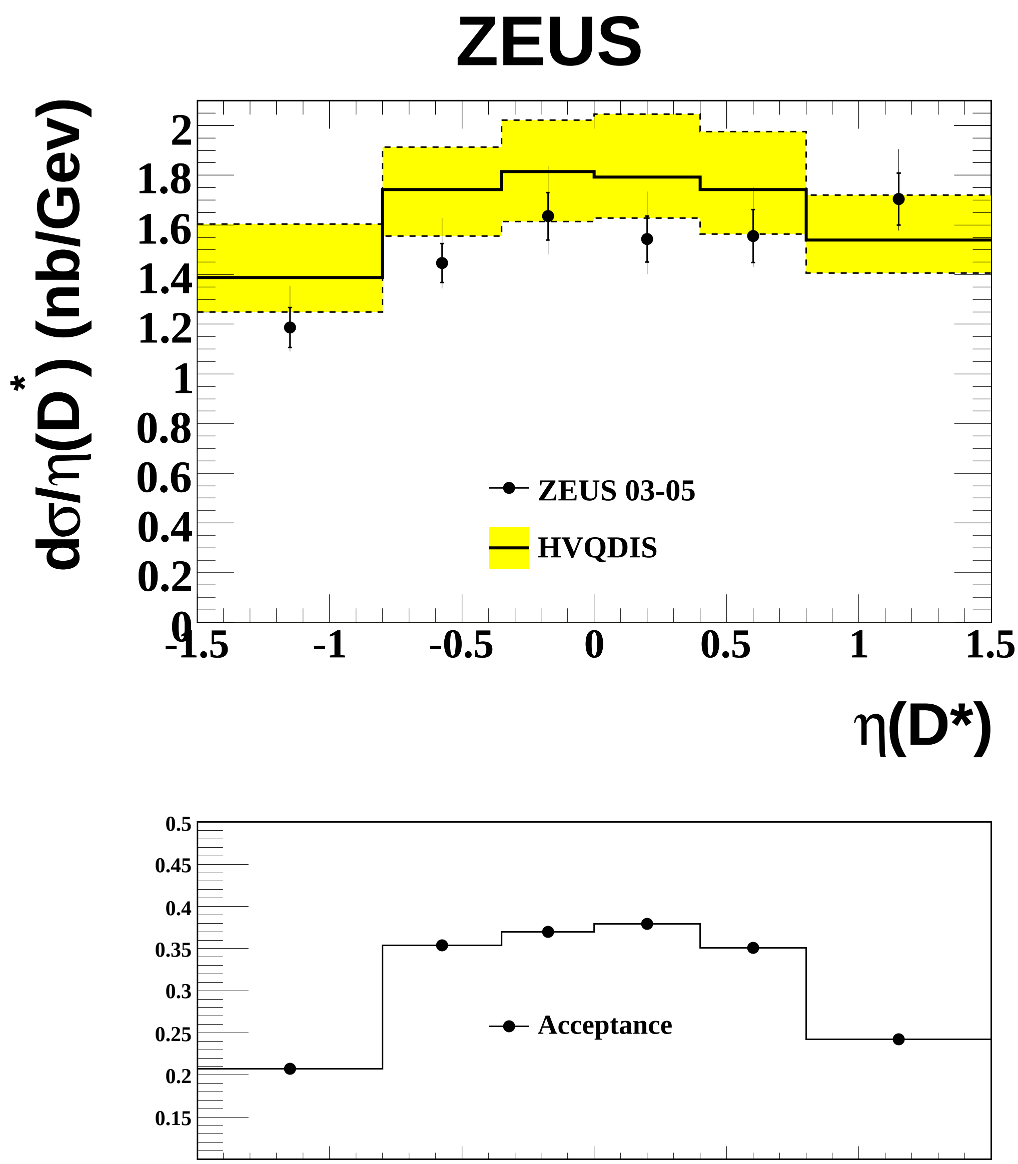

Figure 8.17: The differential D^* cross-section as a function of $\eta(D^*)$ is shown along with the NLO QCD prediction. Statistical errors are shown (inner error bars) and added in quadrature to the systematic error to give the total error. The solid line is the prediction from the ZEUS NLO QCD fit and the shaded yellow region indicates the theoretical uncertainty in this prediction. The acceptance is shown below.

8.5.2 $F_2^{c\bar{c}}$ Measurement

The acceptance corrections associated with the differential cross-section are given in figure 8.18. The acceptance never rises above 50%, although broadly speaking increases with Q^2. This modest acceptance can be understood by the limited range in $\eta(D^*)$ and $p_T(D^*)$ in which the measurements are made, leading to extrapolation factors > 2. In the $5 < Q^2 < 6.5$ region the acceptances are particularly low and are typically of the order 0.2 which implies a heavy dependence on accurate MC simulation to produce a reliable measurement. Whilst the acceptance in this bin is flat with respect to y this trend is not typical of most Q^2 bins; generally speaking the acceptance falls as a function of y from around 0.4 to 0.2 with increasing y. This behavior arises from drift between bins and resolution issues as discussed in section 6.3.

Figure 8.19 shows the differential $c\bar{c}$ cross-section in bins of Q^2 with y increasing along the x axis as open circles. In every bin the dotted line indicates the NLO HVQDIS prediction and where possible the corresponding HERA I measurement is shown in triangles. Statistical and systematic errors are shown. In the lowest Q^2 bin there could be no direct comparison between HERA I and II since the original measurement extended to below 5 GeV. There is however good agreement in the central two y bins between NLO and HERA II measurements, and agreement within errors for the outside two bins. In most Q^2 bins there is an overestimation in the lowest y bin by HVQDIS, although measurements in this bin are usually in excellent agreement with HERA I. Any discrepancy in low y measurements may arise from a correspondingly low acceptance in this bin. The lowest y bin excluded there is excellent agreement between HERA I and HERA II for all but the highest two Q^2 bins. For $90 < Q^2 < 200$ GeV^2 there is still an agreement within errors although a divergence between points begins to emerge. This divergence is slightly more pronounced for $200 < Q^2 < 1000$ GeV^2 although this may be attributed to an extremely high background in the ΔM distribution. As has been discussed earlier the background in HERA II is much worse than in HERA I for tracking and detector simulation reasons. Overall the HERA II measurements are in agreement with both HERA I values and NLO predictions, although the lowest y and highest Q^2 bins show a slight discrepancy but still agreement within errors.

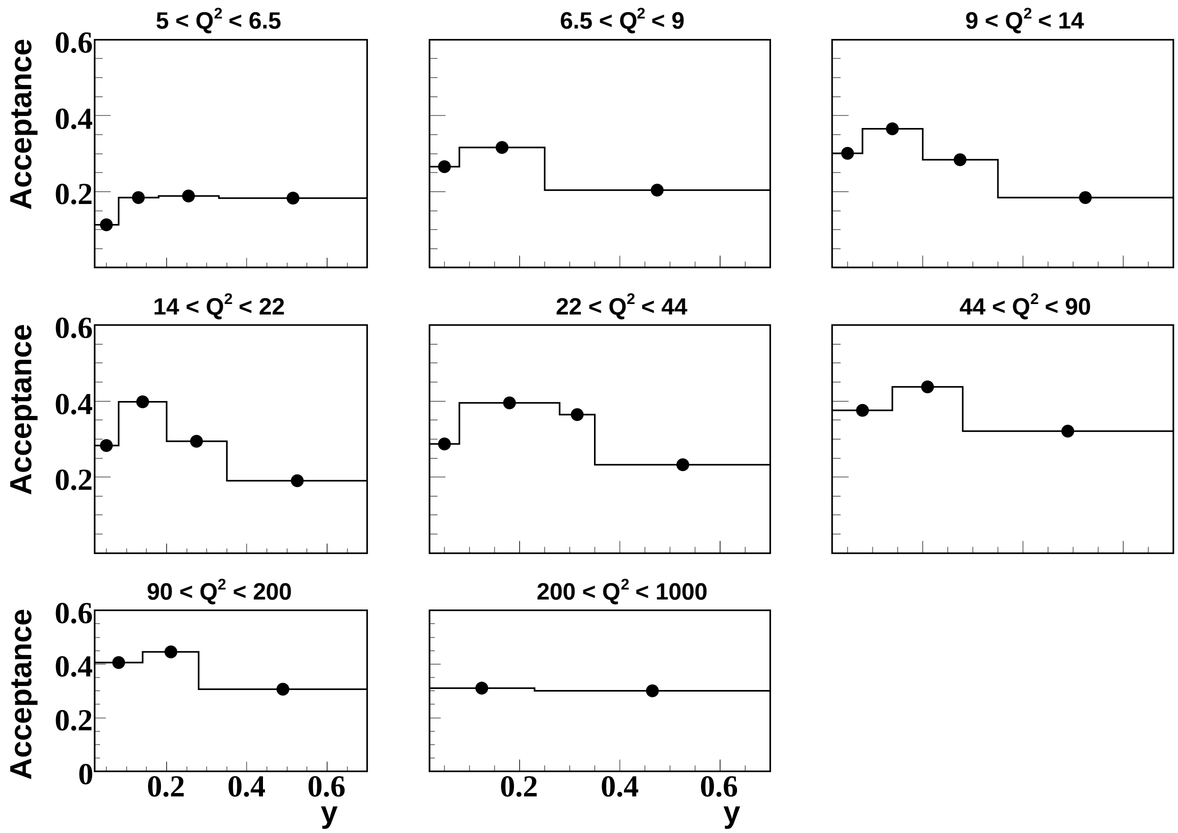

Figure 8.18: Acceptance corrections for $F_2^{c\bar{c}}$ in nine Q^2 bins. Q^2 is given in GeV^2. In each sub plot the x-axis represents the y bins in which $F_2^{c\bar{c}}$ is interpolated. The y-range covered is the same in each plot.

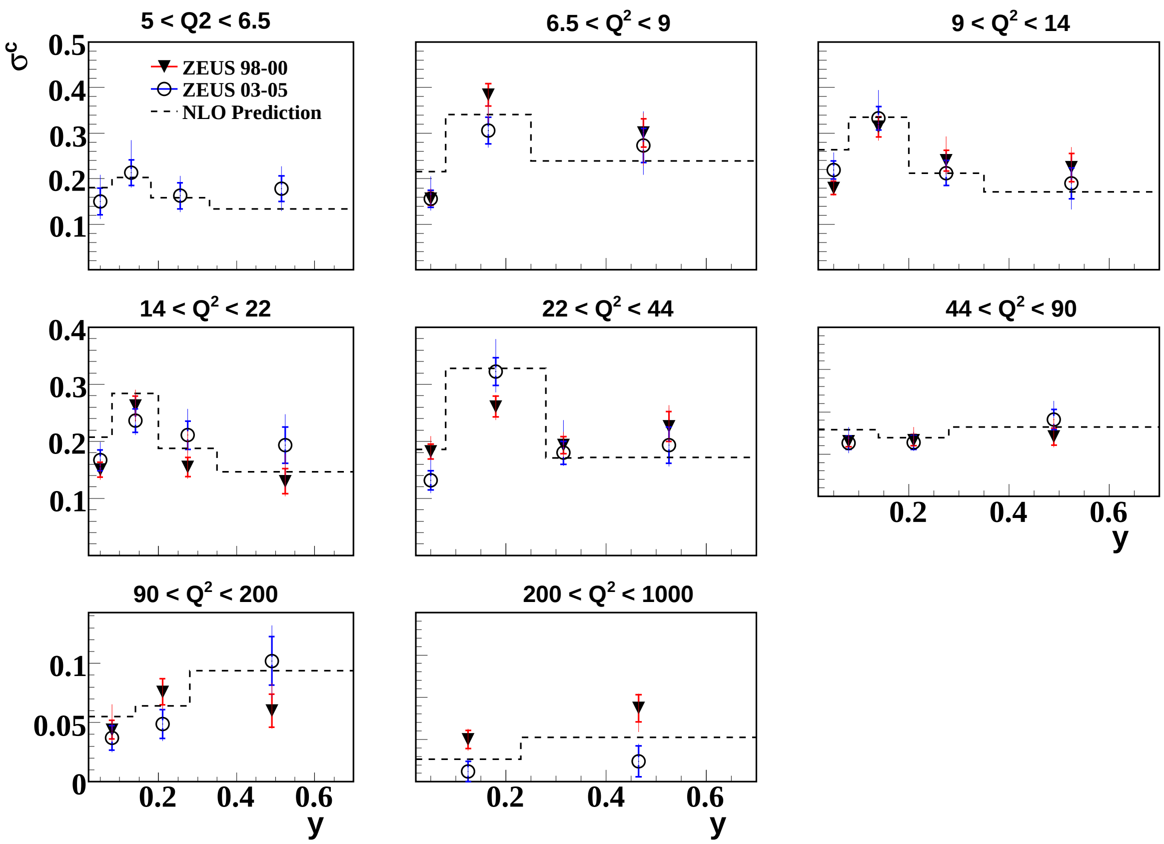

Figure 8.19: The $d^2\sigma/dydQ^2$ result used in the extrapolation of $F_2^{c\bar{c}}$ in nine Q^2 bins. In each sub plot the x-axis represents the y bins in which $F_2^{c\bar{c}}$ is interpolated. The y-range covered is the same in each plot and Q^2 is given in GeV^2. The HERA II measurement is given in open circles and blue error bars, the HERA I measurement is shown by sold triangles and red error bars. The NLO HVQDIS prediction is indicated by a dotted line. Theoretical and systematic errors are shown.

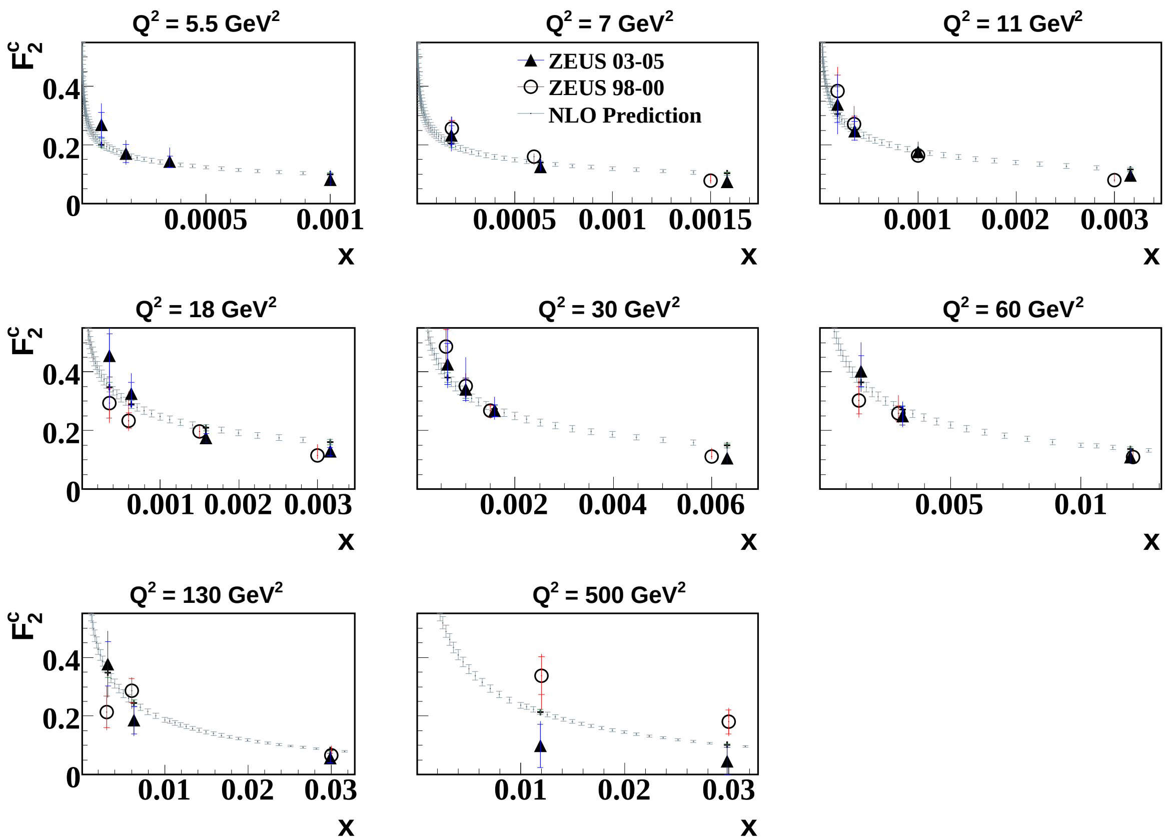

Figure 8.20: The final $F_2^{c\bar{c}}$ measurement shown in a series of plots corresponding to Q^2 points. The DIS parameter x runs along the x-axis on each sub plot. The HERA II measurement is represented by black circles, the HERA I by blue triangles . The grey band represents the prediction given by the ZEUS NLO PDF fit. Statistical and systematic errors are included.

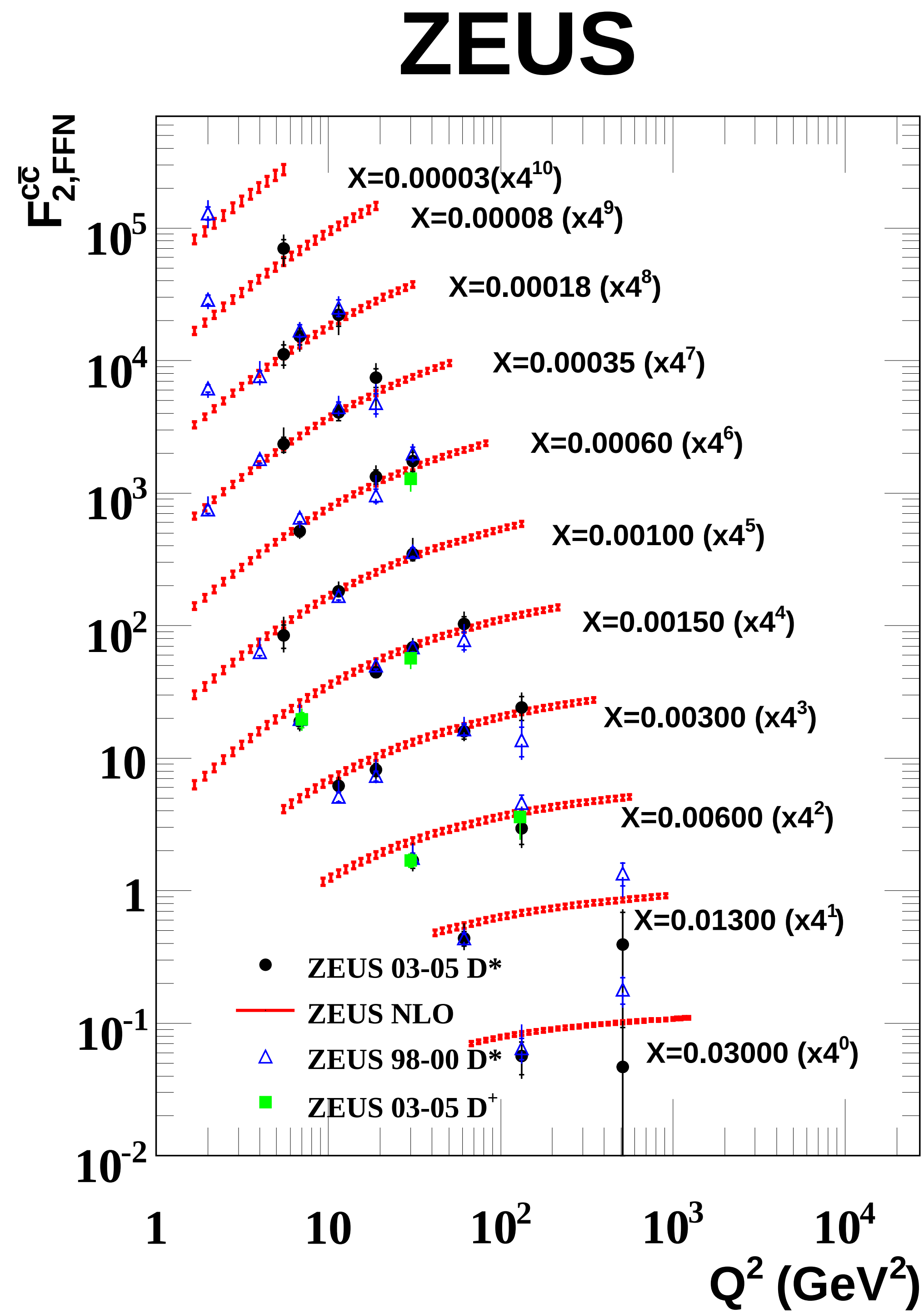

Figure 8.21: The final $F_2^{c\bar{c}}$ on a single plot as a function of Q^2 with fixed x. Measurements of $F_2^{c\bar{c}}$ are multiplied by a factor of 4^i where each x point has with it associated a corresponding i integer which increases with decreasing x. The HERA II measurement using the D^* channel is represented by black circles and the HERA I by blue triangles. A further HERA II measurement using the D^+ channel is shown in green squares. The red array represents the theory prediction given by the ZEUS-S NLO PDF fit.

Q^2 bin (GeV^2)	y bin	σ (nb)	Δ_{stat}	Δ_{sys}
5, 6.5	0.70, 0.33	0.178	$\pm$ 0.028	$^{+0.037}_{-0.037}$
	0.33, 0.18	0.162	$\pm$ 0.029	$^{+0.032}_{-0.022}$
	0.18, 0.08	0.213	$\pm$ 0.028	$^{+0.066}_{-0.016}$
	0.08, 0.02	0.150	$\pm$ 0.029	$^{+0.051}_{-0.024}$
6.5, 9	0.70, 0.25	0.272	$\pm$ 0.037	$^{+0.065}_{-0.053}$
	0.25, 0.08	0.306	$\pm$ 0.029	$^{+0.052}_{-0.024}$
	0.08, 0.02	0.155	$\pm$ 0.018	$^{+0.045}_{-0.017}$
9, 14	0.70, 0.35	0.189	$\pm$ 0.034	$^{+0.047}_{-0.045}$
	0.35, 0.20	0.212	$\pm$ 0.027	$^{+0.038}_{-0.004}$
	0.20, 0.08	0.332	$\pm$ 0.025	$^{+0.057}_{-0.011}$
	0.08, 0.02	0.219	$\pm$ 0.019	$^{+0.033}_{-0.020}$
14, 22	0.70, 0.35	0.193	$\pm$ 0.031	$^{+0.045}_{-0.070}$
	0.35, 0.20	0.210	$\pm$ 0.025	$^{+0.038}_{-0.019}$
	0.20, 0.08	0.236	$\pm$ 0.020	$^{+0.040}_{-0.014}$
	0.08, 0.02	0.166	$\pm$ 0.018	$^{+0.026}_{-0.018}$
22, 44	0.70, 0.35	0.293	$\pm$ 0.031	$^{+0.058}_{-0.019}$
	0.35, 0.22	0.179	$\pm$ 0.020	$^{+0.054}_{-0.011}$
	0.22, 0.08	0.322	$\pm$ 0.024	$^{+0.051}_{-0.028}$
	0.08, 0.02	0.131	$\pm$ 0.017	$^{+0.043}_{-0.015}$
44, 90	0.70, 0.28	0.181	$\pm$ 0.024	$^{+0.038}_{-0.021}$
	0.28, 0.14	0.127	$\pm$ 0.016	$^{+0.019}_{-0.012}$
	0.14, 0.02	0.126	$\pm$ 0.015	$^{+0.035}_{-0.018}$
90, 200	0.70, 0.28	0.101	$\pm$ 0.020	$^{+0.022}_{-0.024}$
	0.28, 0.14	0.049	$\pm$ 0.012	$^{+0.008}_{-0.007}$
	0.14, 0.02	0.037	$\pm$ 0.010	$^{+0.011}_{-0.006}$
200, 1000	0.70, 0.23	0.0243	$\pm$ 0.018	$^{+0.021}_{-0.007}$
	0.23, 0.02	0.0121	$\pm$ 0.020	$^{+0.004}_{-0.003}$

Table 8.7: Measured cross-sections and errors in each of the Q^2 and y bins for $5 < Q^2 < 1000$ GeV^2, $0.02 < y < 0.7$, $1.5 < p_T(D^*) < 15$ GeV and $|\eta(D^*)| < 1.5$.

Q^2 (GeV^2)	x	$F_2^{c\bar{c}}$	Δ_{stat}	Δ_{sys}	$\mathit{\Delta}_{\mathrm{theo}}{}^*$	$\Delta_{\mathrm{stat}}/\Delta_{\mathrm{sys}}^{\mathrm{mean}}$	extrap. factor
5.5	0.00008	0.268	$\pm$ 0.043	$^{+0.060}_{-0.060}$	$^{+0.011}_{-0.022}$	0.81	3.79
	0.00018	0.170	$\pm$ 0.030	$^{+0.034}_{-0.023}$	$^{+0.005}_{-0.011}$	1.08	2.63
	0.00035	0.142	$\pm$ 0.019	$^{+0.044}_{-0.011}$	$^{+0.003}_{-0.005}$	0.62	2.57
	0.00100	0.082	$\pm$ 0.016	$^{+0.028}_{-0.013}$	$^{+0.015}_{-0.000}$	0.65	3.75
7	0.00018	0.232	$\pm$ 0.031	$^{+0.055}_{-0.045}$	$^{+0.014}_{-0.028}$	0.70	3.18
	0.00060	0.125	$\pm$ 0.012	$^{+0.022}_{-0.010}$	$^{+0.004}_{-0.006}$	0.72	2.34
	0.00150	0.074	$\pm$ 0.009	$^{+0.022}_{-0.008}$	$^{+0.021}_{-0.000}$	0.47	3.31
11	0.00018	0.338	$\pm$ 0.061	$^{+0.0837}_{-0.0808}$	$^{+0.025}_{-0.004}$	0.85	3.29
	0.00035	0.247	$\pm$ 0.031	$^{+0.0445}_{-0.0045}$	$^{+0.009}_{-0.015}$	1.33	2.21
	0.00100	0.178	$\pm$ 0.013	$^{+0.0303}_{-0.0057}$	$^{+0.003}_{-0.004}$	0.70	2.11
	0.00300	0.096	$\pm$ 0.008	$^{+0.0144}_{-0.0089}$	$^{+0.024}_{-0.002}$	0.59	2.95
18	0.00035	0.456	$\pm$ 0.075	$^{+0.1054}_{-0.1652}$	$^{+0.019}_{-0.028}$	0.64	2.96
	0.00060	0.325	$\pm$ 0.039	$^{+0.0592}_{-0.0291}$	$^{+0.009}_{-0.012}$	0.88	1.94
	0.00150	0.174	$\pm$ 0.015	$^{+0.0299}_{-0.0104}$	$^{+0.005}_{-0.003}$	0.69	1.90
	0.00300	0.128	$\pm$ 0.014	$^{+0.0201}_{-0.0141}$	$^{+0.036}_{-0.001}$	0.66	2.69
30	0.00060	0.426	$\pm$ 0.070	$^{+0.127}_{-0.041}$	$^{+0.026}_{-0.029}$	0.95	2.47
	0.00100	0.340	$\pm$ 0.038	$^{+0.102}_{-0.022}$	$^{+0.011}_{-0.010}$	0.62	1.70
	0.00150	0.268	$\pm$ 0.020	$^{+0.043}_{-0.023}$	$^{+0.007}_{-0.005}$	0.57	1.69
	0.00600	0.105	$\pm$ 0.013	$^{+0.034}_{-0.012}$	$^{+0.024}_{-0.001}$	0.44	2.44
60	0.00150	0.402	$\pm$ 0.053	$^{+0.084}_{-0.046}$	$^{+0.012}_{-0.016}$	0.88	1.84
	0.00300	0.250	$\pm$ 0.031	$^{+0.038}_{-0.023}$	$^{+0.009}_{-0.008}$	1.00	1.54
	0.01200	0.109	$\pm$ 0.013	$^{+0.030}_{-0.015}$	$^{+0.015}_{-0.002}$	0.49	2.24
130	0.00300	0.378	$\pm$ 0.076	$^{+0.082}_{-0.087}$	$^{+0.009}_{-0.018}$	0.96	1.60
	0.00600	0.185	$\pm$ 0.046	$^{+0.031}_{-0.027}$	$^{+0.012}_{-0.010}$	1.47	1.51
	0.03000	0.056	$\pm$ 0.015	$^{+0.017}_{-0.010}$	$^{+0.008}_{-0.002}$	0.92	2.51
500	0.01200	0.047	$\pm$ 0.046	$^{+0.040}_{-0.013}$	$^{+0.021}_{-0.024}$	1.35	1.57
	0.03000	0.098	$\pm$ 0.073	$^{+0.035}_{-0.023}$	$^{+0.012}_{-0.005}$	2.78	2.24

Table 8.8: The extracted value of $F_2^{c\bar{c}}$ at each (Q^2, x) point and the associated errors errors. $\mathit{\Delta}_{\mathrm{theo}}{}^*$ indicates that the theoretical predictions are taken from an earlier analysis [52].

Figure 8.20 shows $F_2^{c\bar{c}}$ in bins of Q^2 with increasing x on the x-axis. The grey band represents the prediction given by the ZEUS NLO PDF fit, with errors propagated from experimental uncertainties associated with the fitted data. These predictions were used in the extraction of $F_2^{c\bar{c}}$ and give similar values to the central measurement. The HERA II measurements are shown in blue triangles and the nearest HERA I measurements are shown as open circles. Figure 8.21 gives this same information as a function of Q^2 with fixed x. Measurements are multiplied by a factor of 4^i where each x point has a corresponding i integer which increases with decreasing x. This information is also recorded in table 8.8 which states explicitly the statistical, systematic and theoretical errors associated with this measurement.

Because $F_{2,\mathrm{theo}}^{c\bar{c}}$ has not changed from the HERA I measurement the agreement between the central points of the HERA I and HERA II $F_2^{c\bar{c}}$ will be as good as their cross-section agreement in figure 8.19. Overall the measurements agree within errors of the NLO prediction and with their HERA I counterparts. The statistical error is of a similar order, for although the HERA II luminosity is twice that of HERA I the reconstruction efficiency is only half as good. However the HERA II systematic errors are in in some bins slightly larger than the HERA I measurement due to multiple scattering effects in the MVD and inadequate detector simulation. Figure 8.21 illustrates how scaling violations are observed at low x with increasing Q^2 in HERA II data. This figure also illustrates how for most values of x the HERA I and II measurements are almost exactly the same. Data are somewhat lower than the predictions at the lowest x and highest Q^2 points.

The cross-section results are given in table 8.7 which also includes the separate contributions of statistical and systematic errors. Table 8.8 lists the final $F_2^{c\bar{c}}$ measurement along with the statistical and systematic error contributions. The calculation of the theoretical error is not repeated since no improvements can be made over the HERA I predictions. Moreover the machinery and expertise necessary to reproduce these calculations is no longer present at ZEUS. This table also gives the ratio of statistical to mean systematic error and the extrapolation factor necessary to expand the measured kinematic region to the entire phase space. This quantity is always less than 4 and typically is between 1.5 and 2. The ratio of statistical to systematic error is typically 0.7 and is almost always < 1. In the highest Q^2 region the measurements are statistically limited in HERA I and the HERA II measurements are slightly more accurate.

8.6 Comparison with theory

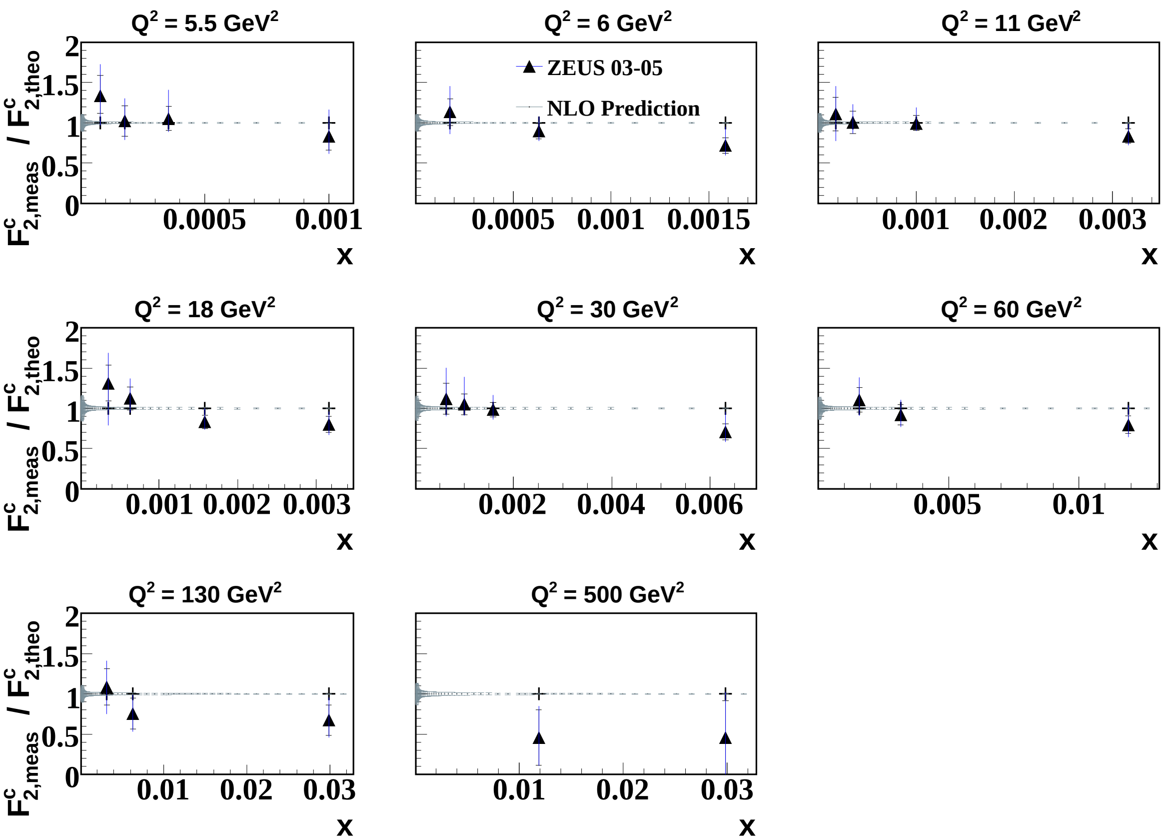

Figure 8.22: The ratio of $F_2^{c\bar{c}}$ measurement with the NLO prediction shown in a series of plots corresponding to Q^2 points. The DIS parameter x runs along the x-axis on each sub plot. The grey band represents the ratio of the prediction given by the ZEUS NLO PDF fit over itself which is 1 by definition. Statistical and systematic errors are included on the HERA II $F_2^{c\bar{c}}$ points and the error propagated from the fit to data is given on the NLO PDF fit.

Figure 8.22 shows the ratio of the measured value of $F_2^{c\bar{c}}$ to the prediction from the ZEUS NLO PDF fit. In general there is agreement within errors between the measured and predicted values although there is a tendency for the prediction to underestimate the measurement at low x and for an over estimation at higher x. This trend appears to be independent of Q^2 although the error associated with the highest Q^2 points is large. It appears therefore that the ZEUS-S PDF fit could be systematically improved by the inclusion of new charm data from the HERA II running period. Under the ZEUS-S parameterisation the gluon PDF at Q_0^2 takes the form

$$xf(x) = p_1 x^{p_2}(1-x)^{p_3}$$

where $p_1 = 1.77 \pm 0.09 \pm 0.49$, $p_2 = 0.2 \pm 0.01 \pm 0.04$ and $p_3 = 6.2 \pm 0.2 \pm 1.2$ [74]. Since the x terms are small in the region where $F_2^{c\bar{c}}$ is measured (and the trend observed) an adjustment of p_2 is unlikely to correct for this effect. A refit using HERA II charm data is likely therefore to result in a reduction of p_3 which will correct for this trend and give a better theoretical description of the data.

8.7 Future work

Improvements are being made to the regular ZEUS tracking package which will better account for multiple scattering in the MVD and will improve the vertex assignment of the D^* decay tracks. When this tracking package is complete it will be possible to re-measure $F_2^{c\bar{c}}$ using the same procedure in this thesis with reduced $\Delta M(D^*)$ background and increased statistics. At the time of writing this work is still in the development stages.

Moreover, when the HERA II ZEUS detector is fully optimised, it will be possible to simultaneously extract measurements of $F_2^{c\bar{c}}$ and $F_2^{b\bar{b}}$ using only the impact parameter (IP) of the tracks. The IP can be thought of as the distance of closest approach to the reference point in the transverse plane, and can be used to discriminate the events with heavy quarks whose lifetime is proportional to IP. This procedure has the advantage of not relying on hard selection cuts which opens up a large phase space for measurement and will increase statistics and will not require complicated kinematic reconstructions. However the MC does not yet describe the HERA II data sufficiently well and much work is required to optimize the extraction process.

If the systematic errors associated with the HERA II measurement can be reduced it will be possible to improve the measurement in statistically limited bins by combining the HERA I and II results together. It may also be possible to reduce the background on the ΔM distributions by using dE/dx tagging to identify the (K, π, π_x) D^* decay tracks, however with the present tracking technology this is likely to significantly reduce the overall statistics.

The measurement will converge with the predicted value once this charm data is included in the ZEUS-S PDF fit. Improvements to the gluon PDF will also be important to experiments at the LHC which will begin operation in the summer of 2007.

8.8 Summary

This chapter began with a summary of the selection cuts that defined the DIS data sample from which differential cross-sections and $F_2^{c\bar{c}}$ were unfolded. The method by which the cross-sections and $F_2^{c\bar{c}}$ are calculated was then described and the systematic and theoretical errors associated with these measurements presented. The chapter concluded with a discussion of the final cross-section and $F_2^{c\bar{c}}$ measurements with the systematic, statistical and theoretical errors included with reference to the agreement with HERA I and the NLO predictions. The $F_2^{c\bar{c}}$ measurement was found to be in agreement with the HERA I measurement and the NLO prediction, and the measurement was performed to new precision in the highest Q^2 region.

Chapter 9

Measurement of $\log(1/x_p)$ in the Breit frame

This chapter presents a feasibility study of the measurement of $\log(1/x_p)$ in the Breit frame. This quantity has not been measured before using a charm-only sample and will give a handle on the hadronic final state of the event. Careful measurement will also determine if the production mechanism used in the MC simulation is consistent with what is seen in nature. It opens with a definition of the Breit frame and x_p before comparing the inclusive HERA I measurement to the charm-exclusive LO MC prediction. A discussion is made of how the HERA II population of the Breit frame is statistically limited and has large errors which arise from boosting the reconstructed tracks to the Breit frame, reconstructing the D^* candidates and performing background subtraction on an extremely statistically limited sample. These effects conspire to give a large acceptance correction which can not be used for $Q^2 < 40$ GeV^2. A measurement was made for $40 < Q^2 < 80$ and $80 < Q^2 < 160$ GeV^2. The chapter concludes with an outlook of how this measurement may be improved in future analyses.

9.1 Analysis procedure

The data and MC samples used in this study are identical to those used in the extraction of $F_2^{c\bar{c}}$ in chapter 8. Events containing a D^* candidate and which pass the necessary selection cuts are boosted and rotated into the Breit frame in which the exchange boson is completely space-like. The velocity of the Breit frame with respect to the laboratory frame is given by

$$\overrightarrow{\beta} = (\overrightarrow{q} + 2x\overrightarrow{P})/(q_0 + 2xP_0) \tag{9.1}$$

where $(P_0, \overrightarrow{P})$ and $(q_0, \overrightarrow{q})$ are the 4-momenta of the proton beam and exchange photon respectively. This boost is discussed in section 2.7 and in more detail elsewhere [28]. It may be interpreted as a boost and rotation so that the photon is along the negative z axis and the plane of the scattered lepton contains the $\phi = 0$ direction. The region of $z < 0$ is defined as the current region and is where the measurement is performed. The volume for which $z > 0$ is known as the target region and contains both the scattered lepton and the proton remnant.

As discussed in section 2.7 the boson-gluon fusion (BGF) method of charm production has a tendency at low Q^2 to populate the target rather than the current region of the Breit frame. Since BGF is the dominant source of charm production the current region is sparsely populated by D^*s and measurements of the scaled momenta in this region are statistically limited.

Scaled momentum, x_p, is defined by

$$x_p = 2p^{\mathrm{Breit}}/Q \tag{9.2}$$

and was evaluated for the D^*s which populated the current region of the Breit frame which has a high measurable acceptance. $\log(1/x_p)$ was histogrammed by generating right and wrong charge distributions of $\Delta M(D^*)$ and performing the background subtraction in each $\log(1/x_p)$ bin. These quantities were used to evaluate $N(D^*)$ in the procedure explained in section 5.5.1 but now for bins in $\log(1/x_p)$ as well as Q^2. The $\Delta M(D^*)$ distributions were thus statistically limited with distributions such that the background subtraction could not be performed accurately in all bins, leading to large uncertainties in measuring $\log(1/x_p)$. Where it was possible to extract a measurement it could only be done with large statistical errors.

9.2 Measurements

Figure 9.1 shows the $\log(1/x_p)^{\text{inclusive}}$ measurement for all charged particles obtained from the ZEUS 1994-7 data [27]. The distributions have an approximately Gaussian shape with maxima which shift towards higher values as the energy increases. The growth in height reflects the increased multiplicity associated with a rise in Q. The rising edge of these distributions lie almost on top of each other with small variations. The mean and multiplicity of the distributions rise linearly with $\log Q^2$.

Figure 9.2 shows the RAPGAP true $\log(1/x_p)$ distributions for the same range of Q^2 values normalised to $N_{\text{True}}(D^*)$. Using this charm-only sample, the key features present in the inclusive sample are not reproduced; there are no obvious scaling violations in terms of multiplicity growth, mean, width or skewness unlike the inclusive sample. The tail of the distribution does not fall to zero as $\log(1/x_p) \to 0$ because the BGF charm production mechanism leads to an intrinsic p_T in the D^* and causes $x_p > 1$ for a significant fraction of events. The results of this MC truth analysis indicate that the momentum of the D^* is directly proportional to the Q of the event since the ratio of $p_{\text{Breit}}(D^*)/Q$ is approximately constant. All of these features are an indication that the underlying physics being measured is indeed different from that of the inclusive sample.

Figure 9.3 shows the number of data and MC reconstructed D^* candidates as well as the corresponding number of MC truth D^*s in a series of $\log(1/x_p)$ bins. In each Q^2 range the distributions have been normalised to the number of D^*s counted in that Q^2 bin. In most bins the evolution of the reconstructed D^*s does not match well that of the true level D^*s whose leading edge remains approximately fixed. At lower Q^2 the position of the peak occurs much later in $\log(1/x_p)$ in the reconstructed sample than in MC truth, although the peaks do appear to converge at large Q^2. In a well reconstructed, highly resolved event one would expect the MC and true distributions to fall within nearby $\log(1/x_p)$ bins. This indicates that it is difficult to resolve D^*s in the Breit frame with minimal drift between bins. However the MC reconstruction does agree with the data for $Q^2 < 160$ GeV^2 indicating that these low resolution and acceptance effects are faithfully reproduced in the simulation.

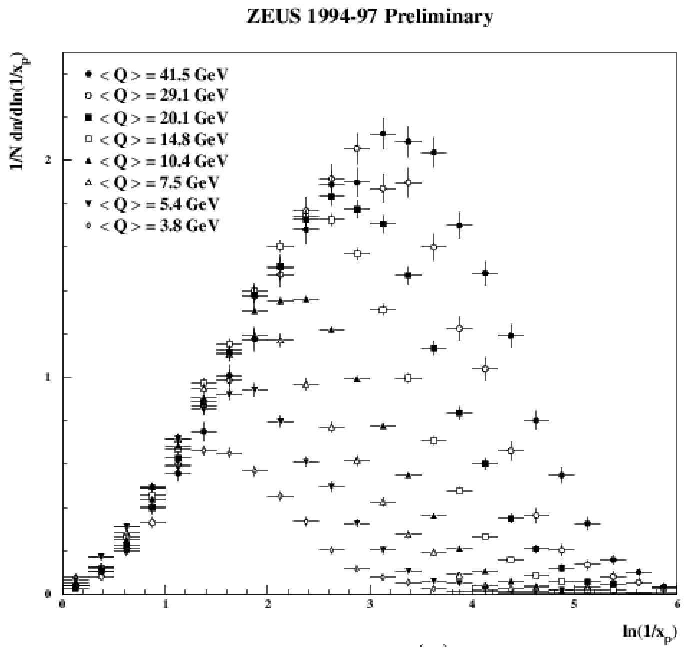

Figure 9.1: Evolution of $\log(1/x_p)^{\text{Inclusive}}$ measured at HERA I for an inclusive sample of all charged tracks [27].

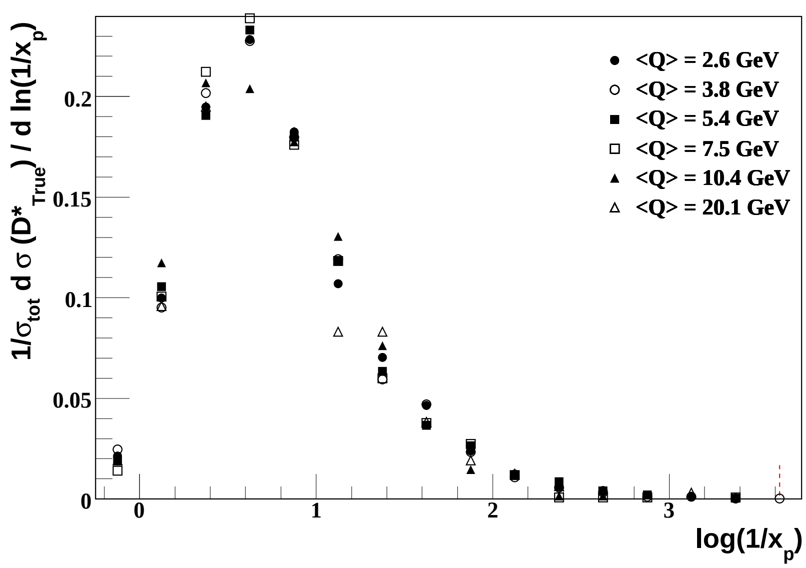

Figure 9.2: Evolution of RAPGAP MC true $\log(1/x_p)$ for D^* production.

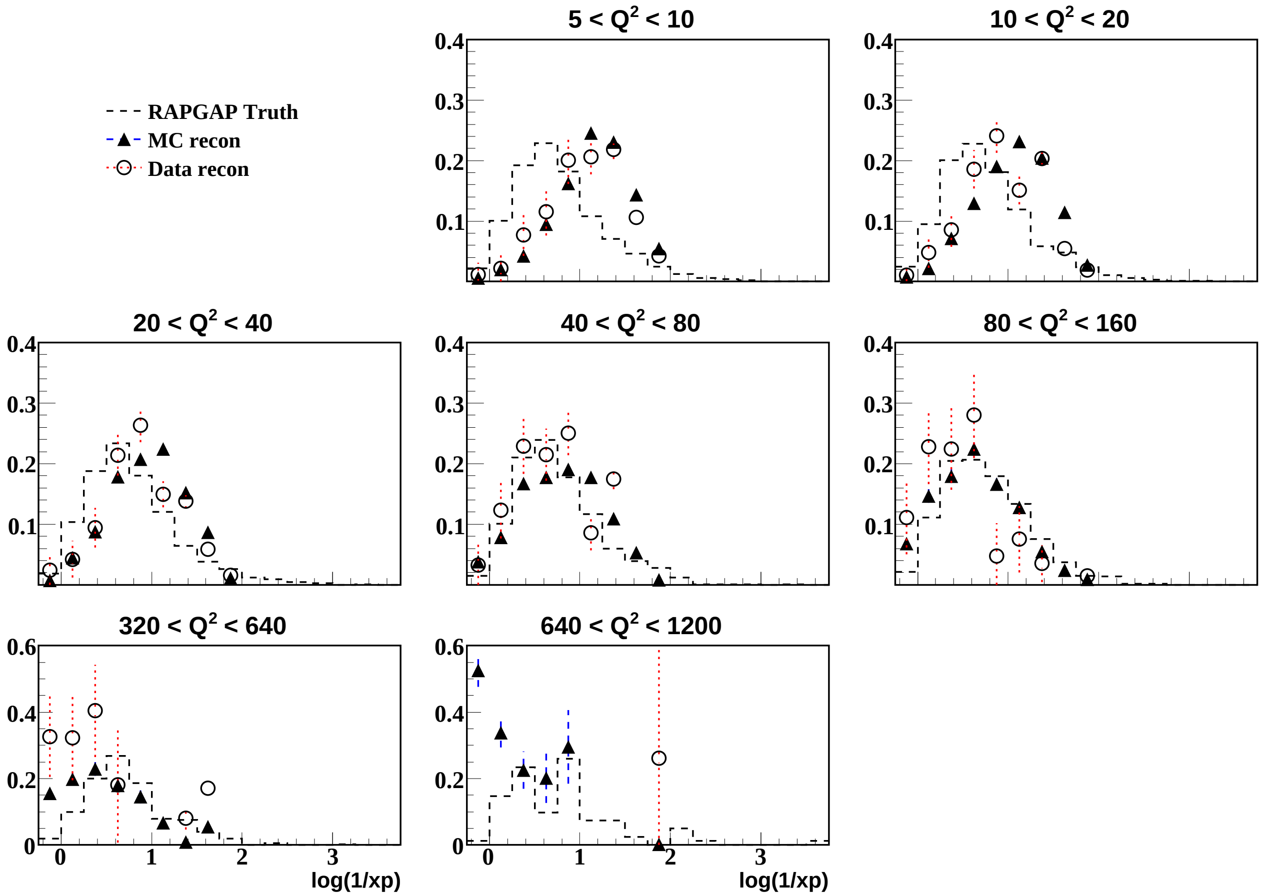

Figure 9.3: The number of reconstructed D^*s in data (open circles) and MC (solid triangles) in bins of $\log(1/x_p)$. The plots have been normalised to $N(D^*)$ in each Q^2 bin.

9.3 Discussion of measurements

The discrepancy between MC truth and the reconstructed values of x_p can be attributed to a poor reconstruction of either Q or $p^{\text{breit}}(D^*)$, both of which feature in the definition of x_p in equation 9.2. The Q^2_{DA} resolution plots in figure 6.10 illustrate how the agreement between the true and reconstructed values of Q^2 improves with rising Q^2. Figure 9.4 shows the area normalised $p^{\text{breit}}(D^*)$ distribution for MC and data reconstruction overlayed on the MC truth prediction. This figure illustrates how difficult it is to reconstruct D^*s in the Breit frame by demonstrating the extent to which $p^{\text{breit}}_{\text{true}}(D^*)$ is smeared. We can conclude that the reconstruction procedure gives an overestimation of the generated momentum which is approximately constant with rising Q^2. Therefore the high Q^2 convergence between MC

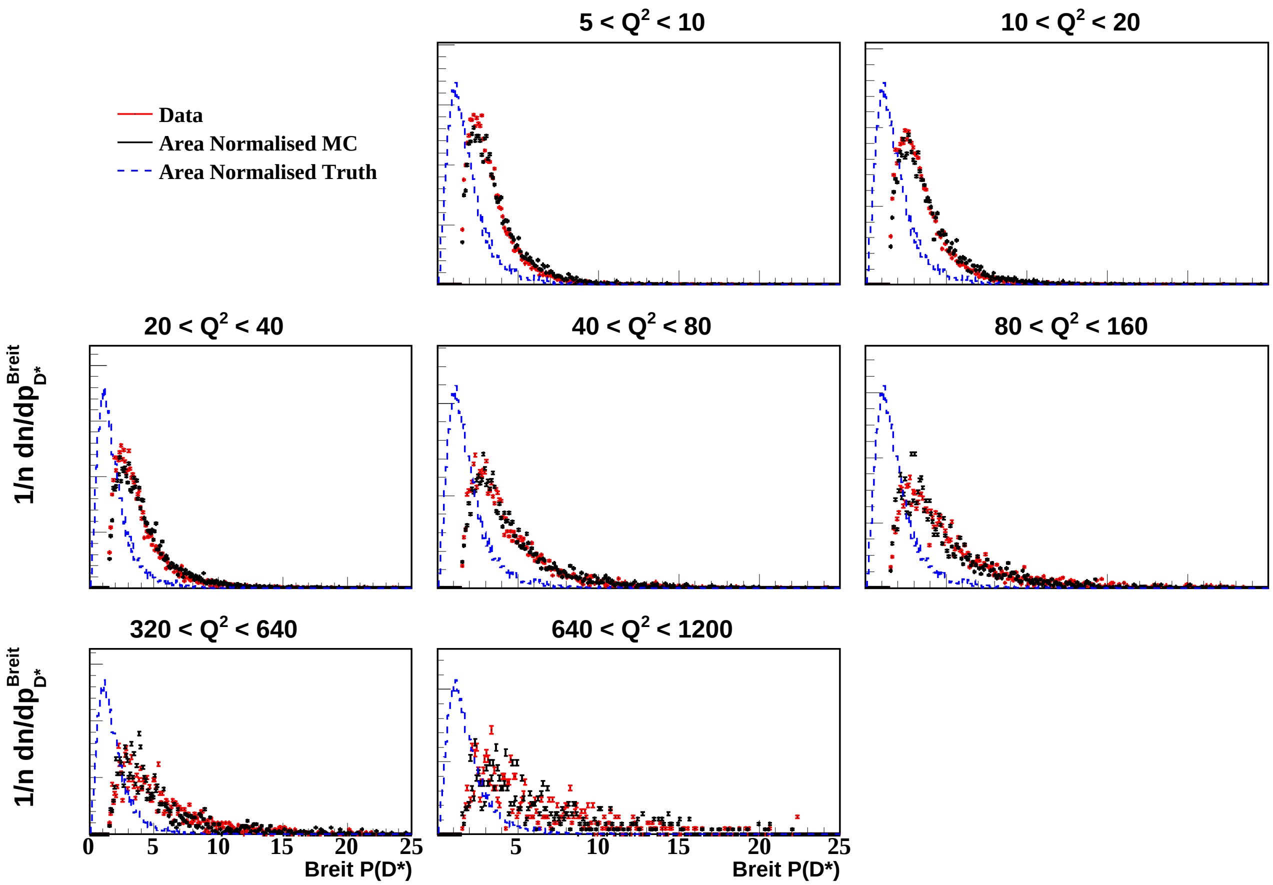

Figure 9.4: Area normalised $p^{\mathrm{breit}}(D^*)$ of for MC (black) and data (red) reconstruction and for MC truth (dashed blue).

truth and reconstructed $\log(1/x_p)$ can be attributed to the improved Q^2 resolution with increasing Q^2.

Figure 9.5 shows the correlation between the reconstructed and true values of $\log(1/x_p)$ as a profile plot in which the spread of $(\log(1/x_p)_{\mathrm{REC}} - \log(1/x_p)_{\mathrm{TRUE}})$ is given on the y-axis with true $\log(1/x_p)$ running along the x-axis. At lower Q^2 the reconstructed values are systematically higher than the truth, although as Q^2 increases the correlation becomes increasingly one-to-one; a consequence of the increasing Q^2 resolution with rising Q^2. These plots show that the $40 < Q^2 < 80$ and $80 < Q^2 < 160$ GeV^2 bins give the best correlation between true and reconstructed values, after which the statistics drop considerably and background subtraction cannot be performed meaningfully. Therefore acceptance corrections

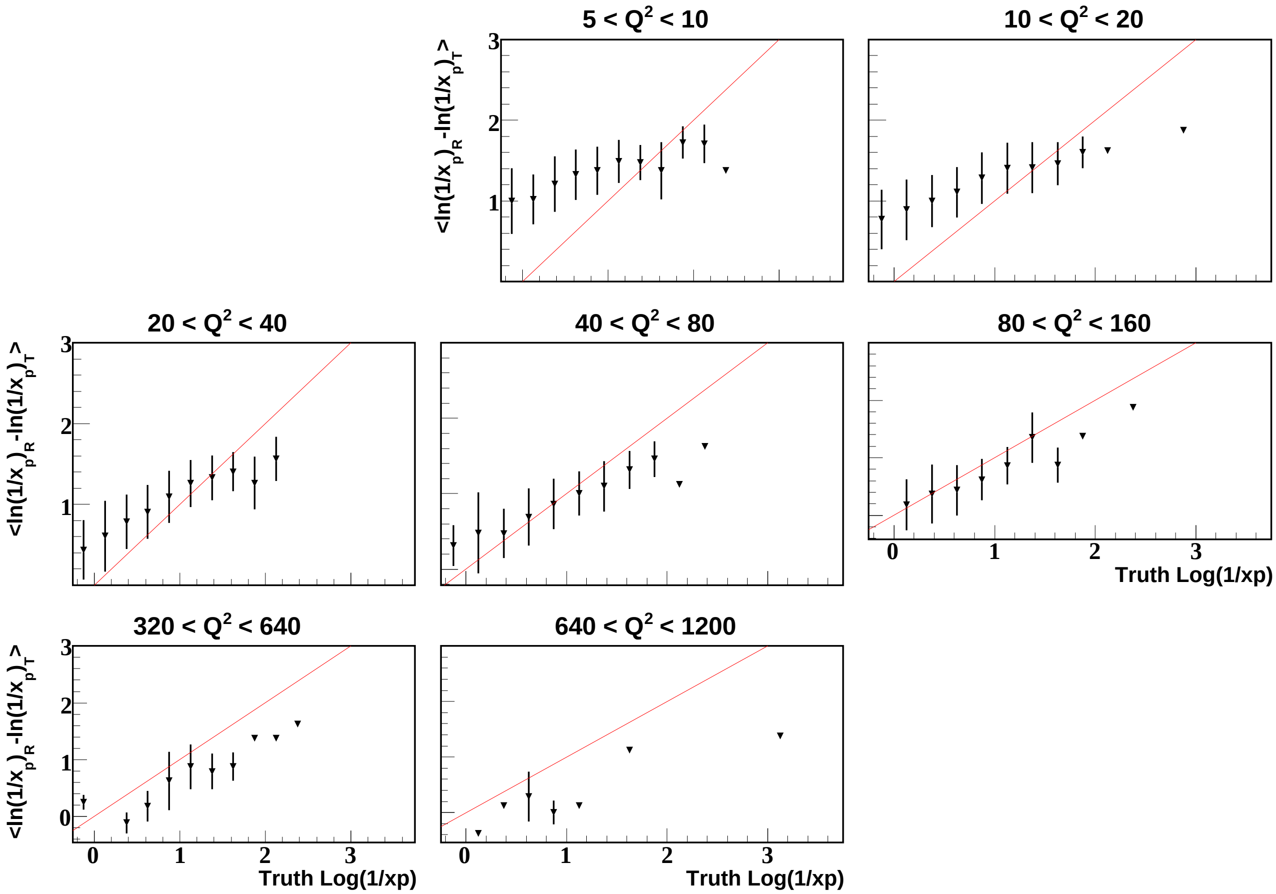

Figure 9.5: The correlation between the reconstructed and true values of $\log(1/x_p)$ shown in bins of Q^2 in a number of profile plots. The red line indicates $y = x$.

are only performed in the $40 < Q^2 < 80$ and $80 < Q^2 < 160$ GeV^2 regions in the extraction of a final measurement.

The ratio of wrong to right charge D^* candidates in the measured Q^2 and $\log(1/x_p)$ bins converge to the same value as $\log(1/x_p)$ increases. Since the background subtraction method is not statistically reliable when $N_{\rm WC}(D^*) \approx N_{\rm RC}(D^*)$ the $\log(1/x_p) > 1.25$ points are discarded. $N_{\rm WC}(D^*)$ and $N_{\rm RC}(D^*)$ are the number of wrong and right charge D^* candidates as defined in section 7.2. Because the adjustment of the background normalisation area is susceptible to statistical fluctuations it is not performed as part of the systematic error assessment of the final measurement.

In summary there are several effects at work which conspire to make a measurement of

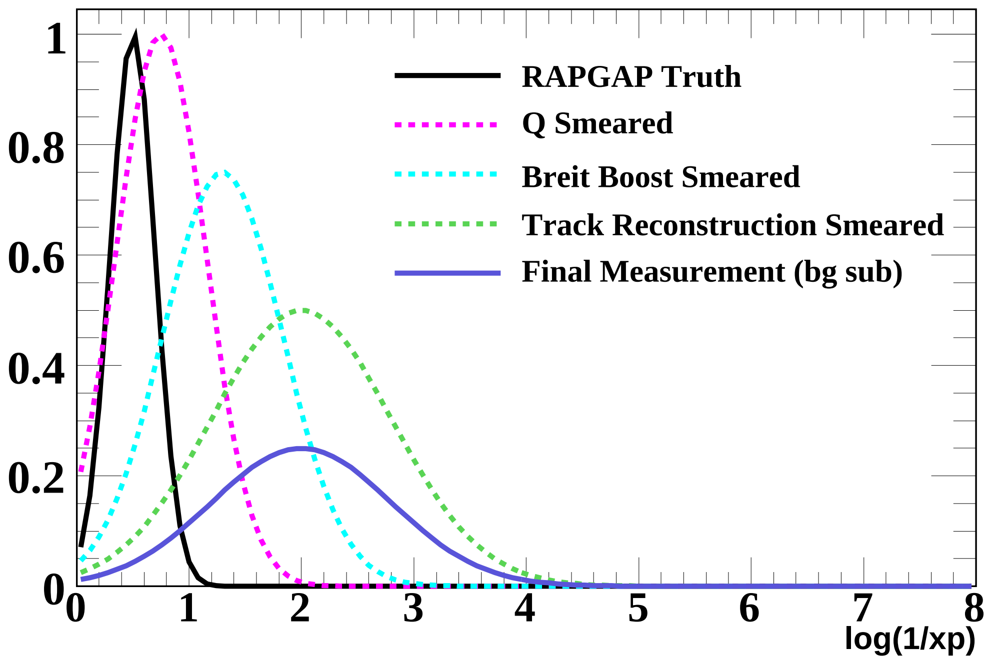

Figure 9.6: Illustration of how the truth $\log(1/x_p)$ distribution (solid black line) is smeared by the various errors associated with reconstructing x_p. This measurement involves a reconstruction of Q (dashed pink), a boost into the Breit frame (dashed cyan) and a reconstruction (dashed green) and background subtraction (solid blue) of the D^* momentum in this frame.

$\log(1/x_p)$ challenging with the current data set and reconstruction tools. These are summarised in figure 9.6 which illustrates how the truth $\log(1/x_p)$ distribution is smeared by these errors to a significant degree. A measurement of x_p requires a reconstruction of Q (dashed pink), a boost into the Breit frame (dashed cyan) and a reconstruction of the π, π_s and K (forming the D^*) momenta in this frame (dashed green). Finally in each $\log(1/x_p)$ bin the background D^* candidates must be subtracted to give the measured quantity (solid blue). The errors associated with each of these stages conspire to increase the position of the observed $\log(1/x_p)$ peak and to smear the distribution to such an extent that the acceptance correction factor is large for most Q^2 bins.

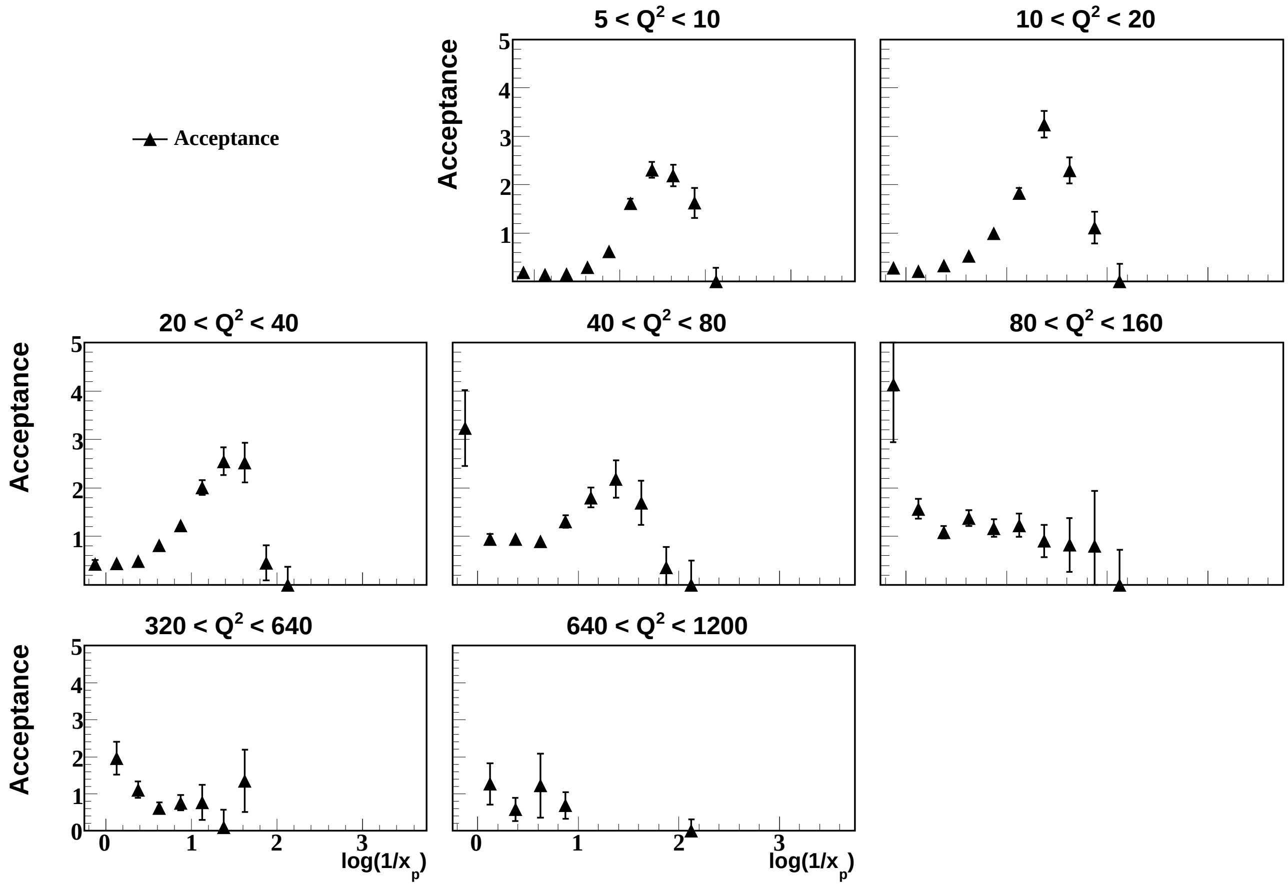

Figure 9.7: The acceptance corrections associated with the measurement of $\log(1/x_p)$ in bins of Q^2 and $\log(1/x_p)$.

9.4 Final results

The bin-by-bin acceptance correction factors as defined by equation 6.1 are given in figure 9.7. Corrections are made in the regions $40 < Q^2 < 80$ GeV^2 and $80 < Q^2 < 160$ GeV^2 where the acceptance is reasonably flat and the resolution is commensurate with the bin size. For $Q^2 > 160$ the statistics are not sufficient to perform an adequate measurement and likewise the $\log(1/x_p) > 1.25$ values are rejected due to statistical limitations.

The same systematics considered in the measurement of $F_2^{c\bar{c}}$ in chapter 8 are performed, with the exclusion of varying the background normalisation factor which is susceptible to statistical fluctuations. As with the measurement of $F_2^{c\bar{c}}$ the largest source of systematic error is the switch from RAPGAP to HERWIG ($\pm 40\%$) and adjusting the track loss probability

(±25%). However the measurement in this case is limited by statistics and not systematics.

The results of this correction with systematic and statistical errors are given in figure 9.8 and table 9.1. They are in agreement with the RAPGAP and HERWIG LO predictions within the prescribed uncertainties. A gaussian distribution is fit to the acceptance corrected data points and is shown as a blue curve whose fit parameters are given in the figure. The mean value of $\log(1/x_p)$ has been extracted using these fits for both Q^2 bins and assessed for systematic errors, concluding that

$$< \log(1/x_p) >_{Q^2=56} = 0.578 \pm 0.046^{+0.092}_{-0.010}$$

and

$$< \log(1/x_p) >_{Q^2=108} = 0.437 \pm 0.074^{+0.045}_{-0.030}$$

as seen in table 9.2. These values are consistent with each other and so $< \log(1/x_p) >$ is not observed to exhibit scaling violations. Similarly the difference between the width or amplitude in each of the Q^2 bins is not statistically significant and so these quantities are said to scale with Q^2.

9.5 Outlook and future work

A statistically limited measurement has been performed for two bins from $40 < Q^2 < 160$ GeV^2 after which the statistics fall dramatically. Using the current reconstruction tools and the current HERA II data set it is difficult to progress further in this exploratory analysis. The full HERA II data set when HERA operation stops in the summer of 2007 will double the statistics and permit a measurement in the $Q^2 > 160$ GeV^2 region.

The current ZEUS reconstruction technologies are challenging with respect to reconstructing the D^* candidates in the Breit frame. Improvements are being made to the tracking tools which will reduce the distortion arising from multiple scattering as well as providing superior vertexing capabilities. This should improve the resolution of the reconstructed D^*s so that the measurement may be performed in lower Q^2 bins. Whilst it is unlikely that the Q^2 resolution will improve, it will be possible to improve the accuracy with which the π_s (and hence D^*) is reconstructed. Improvements to the reconstruction of x will also reduce

Q^2 bin (GeV^2)	$\log(1/x_p)$ bin	$1/\sigma_{\rm tot} d\sigma/d\log(1/x_p)$	$\Delta_{\rm stat}$	$\Delta_{\rm sys}$
40, 80	-0.25, 0.0	0.013	$\pm$ 0.022	${}^{+0.008}_{-0.003}$
	0.0, 0.25	0.162	$\pm$ 0.088	${}^{+0.007}_{-0.030}$
	0.25, 0.5	0.298	$\pm$ 0.085	${}^{+0.024}_{-0.055}$
	0.5, 0.75	0.299	$\pm$ 0.085	${}^{+0.021}_{-0.109}$
	0.75, 1.0	0.241	$\pm$ 0.050	${}^{+0.060}_{-0.011}$
	1.0,1.25	0.059	$\pm$ 0.029	${}^{+0.017}_{-0.014}$
80, 160	-0.25, 0.0	0.038	$\pm$ 0.030	${}^{+0.006}_{-0.013}$
	0.0, 0.25	0.192	$\pm$ 0.074	${}^{+0.026}_{-0.046}$
	0.25, 0.5	0.285	$\pm$ 0.121	${}^{+0.021}_{-0.061}$
	0.5, 0.75	0.286	$\pm$ 0.102	${}^{+0.069}_{-0.013}$
	0.75,1.0	0.058	$\pm$ 0.091	${}^{+0.016}_{-0.063}$
	1.0, 1.25	0.087	$\pm$ 0.090	${}^{+0.041}_{-0.027}$

Table 9.1: Measurements of $1/\sigma_{\rm tot} d\sigma/d\log(1/x_p)$. The data are presented in bins of Q^2 including the associated statistical and systematic errors.

$< Q^2 >$ (GeV^2)	$< \log(1/x_p) >$	$\Delta_{\rm stat}$	$\Delta_{\rm sys}$
56	0.578	$\pm$ 0.046	${}^{+0.092}_{-0.010}$
108	0.437	$\pm$ 0.074	${}^{+0.045}_{-0.030}$

Table 9.2: Measurements of $< \log(1/x_p) >$ and associated statistical and systematic errors.

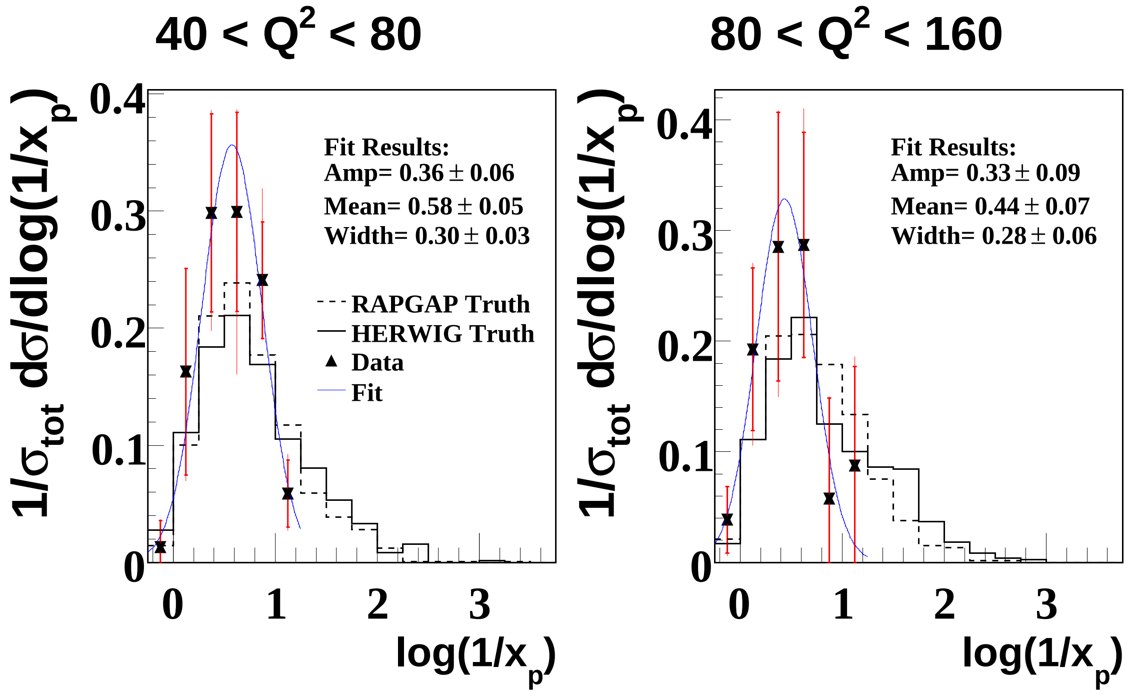

Figure 9.8: The $\log(1/x_p)$ measurement in the regions $40 < Q^2 < 80$ GeV^2 and $80 < Q^2 < 160$ GeV^2 and associated fit (blue). The fit parameters are given in the legend. Systematic and statistical errors have been added in quadrature. The data are compared to RAPGAP (dotted) and HERWIG (full).

the error associated with the boost into the Breit frame and hence the overall measurement error.

9.6 Summary

This chapter studied the feasibility of performing a measurement of x_p in the Breit frame. It opened with a definition of the Breit frame and x_p before comparing the inclusive HERA I measurement to the charm-exclusive LO MC predictions. A measurement was feasible and performed for $40 < Q^2 < 80$ and $80 < Q^2 < 160$ GeV^2 which agreed with both the LO MC prediction within the uncertainties.

Chapter 10

Summary

This thesis opened with a brief introduction to the basics of Deep Inelastic Scattering with emphasis on the Lorentz invariant variables used to characterise these events and the relationship between cross sections and structure functions. A discussion was made of the evolution of the Quark Parton Model and the impact this had on the theory of structure functions. The basic principles of DGLAP evolution, parton density functions and the nature of heavy quark production at ZEUS were presented. An outline was given of Monte Carlo event generation and the different implementations of the hadronisation and fragmentation stages of quark jet production.

The focus was then shifted to the design and operation of the ZEUS detector itself, describing the MVD, CTD, CAL, HES and SRTD components. The first three were used in the final measurements whereas the CAL, HES and SRTD were aligned in a later chapter which concluded that only a minimal adjustment of the SRTD position was required, with negligible effects on reconstructed DIS event kinematics.

Satisfied that these components were correctly aligned, a SLT J/Ψ trigger was developed using the new GTT tracking algorithm. Following an efficiency, signal-to-noise and trigger rate study a suitable trigger based on invariant mass reconstruction was developed and installed online. This trigger is capable of detecting unique J/Ψ events that are not detected by existing triggers which typically rely on detection of energy deposits in the CAL. When used in conjunction with existing triggers statistics would be improved by as much as 50%. This work was published as part of a larger GTT NIM paper [38].

The stability of the existing DIS trigger system was tested and found to be well simulated in MC. The relevant DIS kinematic variable reconstruction methods were then defined and their resolutions measured. The double angle method was found to be superior and was adopted as the principle reconstruction technique in this thesis. To improve the MC description of $E - p_Z$ it was found necessary to scale the hadronic system by 0.97 and to scale and smear the electron energy by 0.98 and 3% respectively. The event selection cuts were then given and a comparison of DIS control plots was made between the DIS Monte Carlos, HERWIG and RAPGAP, finding that RAPGAP most accurately describes the data. As a result of this RAPGAP was used to calculate the acceptance corrections.

The tracking capabilities of HERA II were then compared with those of HERA I and the method of D^* reconstruction from tracks was described. Whilst HERA II tracking was found to be superior at high p_T the resolution was inferior at lower momenta owing to multiple scattering from the MVD. The technique used to count D^*s using ΔM background subtraction was outlined and found to have greater background at HERA II. A comparison of D^* kinematics control plots between RAPGAP and HERWIG was then made showing a discrepancy between MC and data for $p_T(\pi_s)$ distributions, particularly at low p_T. This discrepancy was a large source of systematic error.

With the MC understood it was at last possible to proceed to the measurement of $F_2^{c\bar{c}}$ and associated differential cross-sections using the $D^* \rightarrow K\pi\pi_s$ decay chain. The method by which the cross-sections and $F_2^{c\bar{c}}$ are calculated was described and the systematic and theoretical errors associated with these measurements presented. The HERA II measurements were found to be in good agreement with HERA I. Good agreement was found with the NLO prediction although the results were systematically higher at low x and lower at high x. As a result it was recommended that the PDF be refit to the new charm data to correct for this. These results were made preliminary in March 2007 by the collaboration.

This thesis concluded with a feasibility study of performing a measurement of the scaled momentum quantity, x_p, in the Breit frame using only charm data. A measurement was feasible and performed for $40 < Q^2 < 80$ and $80 < Q^2 < 160$ GeV^2 which agreed with both the LO predictions within systematic and statistical uncertainties indicating that the production mechanism is well understood.

References

[1] Particle Data Group, S. Eidelman et al., Phys. Lett. B 592, 1 (2004)

[2] R.K. Ellis, W.J. Stirling and B.R. Webber, *QCD and Collider Physics*, Cambridge Monographs on Particle Physics, Nuclear Physics and Cosmology, Vol. 8. Cambridge University Press, (1996)

[3] R.P.Feynman; Phys. Rev. Lett 23 1415 (1969)

[4] R. Devenish A Cooper-Sarkar *Deep Inelastic Scattering* Oxford University Press (2003)

[5] *Measurement of the Proton Structure Function* F_2 *and* $\sigma_{tot}^{\gamma^* p}$ *at Low* Q^2 *and Very Low* x *at HERA* Physics Letters B 407 432-448 (1997)

[6] ZEUS Col., S. Chekanov et al., *ZEUS next-to-leading-order QCD analysis of data on deep inelastic scattering.* Phys. Rev. D 67, 012007, hep-ex/0208023 (2003)

[7] J. Pumplin et al., *New generation of parton distributions with uncertainties from global QCD analysis.* Preprint hep-ph/0201195, (2002)

[8] A.D. Martin et al., *MRST2001: partons and* α_s *from precise deep inelastic scattering and Tevatron jet data.* Eur. Phys. J. C, 73, hep-ph/0110215 (2002)

[9] H. Jung, Comp. Phys. Comm. 86 147 (1995)

[10] G. Marchesini et al., Comp. Phys. Comm. 67 465 (1992)

[11] B. W. Harris and J. Smith, Phys. Rev. D57, 2806 (1998)

[12] R. Brun et al., GEAN3, Technical Report CERN–DD/EE/84-1, CERN, (1987)

[13] M. Gluck, E. Reyna and A. Vogt, Z. Phys. C 67, 433 (1995)

[14] L. Lonnblad, Comp. Phys. Comm. 71, 15 (1992)

[15] B. R. Webber, Nucl. Phys. B 238, 492 (1984)

[16] B. W. Harris and J. Smith Phys. Rev. D, 2806 (1998)

[17] B. Anderson et al., Phys. Rep. 97, 31 (1983)

[18] D. R.Woood et al., Phys. Rev. D 37, 3091 - 3102 (1988)

[19] ZEUS COLL., S. Chekanov et al., Phys.Rev.D 67, 012007 (2003)

[20] C. Peterson et al., Phys.Rev.D 27, 105 (1983)

[21] *The Collins fragmentation function: a simple model calculation* A. Bacchetta, R. Kundu, A. Metz and P. J. Mulders (2001)

[22] P.D.B. Colllins, T.P. Spiller, J. Phys G11 1289 (1985)

[23] S. Catini, *Production of Heavy Flavours at High Energies* S. Proceedings of 'The Physics at HERA' workshop, Hamburg (1991) 690

[24] P. Nason and B. Webber, *Nucl. Phys* B 421 (1994) 473

[25] ALEPH Collaboration, *Phys. Lett.* B 357 487 (1995)

[26] DELPHI Collaboration, *Phys. Lett.* B 311 408 (1993)

[27] Jane Talyth Bromley *Measurement of Fragmentation Functions in DIS at HERA* PhD Thesis University of Glasgow (1998)

[28] R.P. Feynman, *Photon-Hadron Interactions*, Benjamin N.Y., (1972)

[29] J. C. Collins, D. E. Soper and G. Sterman, *Nucl. Phys.* **B 162** 104 (1985)

[30] A. Kwiakowski, H. Spiesberger and H.J. Moring, Comp. Phys. Comm 69, 155 (1992)

[31] ZEUS Col., U. Holm (ed.), *The ZEUS Detector Status report*, DESY, (1993)

[32] N. Harnew *et al.* [ZEUS Luminosity Group Collaboration], *Luminosity measurement in the ZEUS experiment* Acta Phys. Polon. B 32 2025 (2001)

[33] B. Foster *et al.* [ZEUS Collaboration], "The Design and construction of the ZEUS central tracking detector," Nucl. Instrum. Meth. A 338 254 (1994)

[34] J. Straver, *Design, Construction and Beam tests of the high resolution Uranium scintillator calorimeter for ZEUS*, Phd Thesis, University of Amsterdam, (1991)

[35] J. Ng and W. Verkerke, *An Overview of SRTD Analysis*, ZEUS Note 95-037, DESY (1995)

[36] A Pio Rinaldi, *A study of electron energy correction in DIS events with the detector ZEUS at HERA II*

[37] N. Tuning, *Proton structure functions at HERA*, (2001)

[38] ZEUS Collab *The design and performance of the ZEUS Global Tracking Trigger* (2006)

[39] C. Youngman, *The ZEUS data acquisition system* Proceedings of CHEP92 Annecy, CERN, (1992) p.222

[40] R. Hall-Wilton, M.R. Sutton, B.J. West, *The CTD-BMVD version 3.3 Global Tracking Trigger Algorithm and Performance*, DESY 01-039 (2001)

[41] M. Sutton, C. Youngman *The Global Tracking Trigger System and Architecture*, DESY 99-074 (1999)

[42] R. Klanner, G. Ingelman, A. De Roeck *Future Physics at HERA Volumes I and II* (1996)

[43] Luciano Lamberti *DIPSI: A Montecarlo Generator for Diffractive J/Ψ production*, ZEUS Note 93-113 (1993)

[44] A. Polini, M. Sutton, S. Topp-Jorgensen *The Global Tracking Trigger System and Architecture*, DESY 99-074 (1999)

[45] ZEUS Collaboration *Measurement of high-Q^2 deep inelastic scattering cross sections with a longitudinally polarised positron beam at HERA* DESY-06-015 (2006)

[46] DESY Preprint 79/48 F. Jacquet, A. Blondel, *Proceedings of the study of an eP facility for Europe* DESY-06-015 (1979)

[47] ZEUS Collaboration, J. Breitweg et al., Eur. Phys. J. C 11 427 (1999)

[48] K. Long *Presentation of the high-Q^2 NC 1999/00 paper* Presentation at the ZEUS collaboration week (2003)

[49] ZEUS Collab., S. Chekanov et al, Eur. Phys. Rev D 69, 012004 (2004)

[50] J. Loizides and Jerome Whyte *MC Tracking Resolutions* Tracking Meeting DESY Hamburg, December (2005)

[51] R. Hall-Wilton et all *The CTD Tracking Resolution* ZEUS-Note-99-024 (1999)

[52] ZEUS Coll., S. Chekanov et al., *Measurement of $D^{*\pm}$ Cross Sections and the Charm Structure Function of the Proton in DIS at HERA* DESY-03-115 (2003)

[53] G. Ingelman, J. Rathsman, G. Schules, *Comp. Phys. Comm 101* (1997) 135

[54] John Harry Loizides *Charm at HERA I and HERA II with the ZEUS experiment* PhD Thesis UCL (2004)

[55] T. Kohno, *Measurement of jet cross sections in $D^{*\pm}$ photoproduction at HERA* KEK-REPORT-2004-3 (2004)

[56] R.M.Barnett *et al*; Phys. Rev. D54 1 (1996)

[57] S. Padhi *Charm Jets in Photoproduction at HERA*. Thesis submitted to the faculty of Graduate Studies McGill University, Canada. (2003)

[58] H1 Collaboration *Determination of the Charm Fragmentation Functions in Deep-Inelastic Scattering at HERA* (2005)

[59] ZEUS Collab., J Breitweg et al, Eur. Phys. J. **C 12**, 35 (2000)

[60] H1 Collab., C. Adloff eta l., Phys. Lett. B 528, 199 (2002)

[61] ZEUS Collab., J Breitweg et al, Eur. Phys. J. B 407, 402 (1997)

[62] H1 Collab., C. Adloff eta l., Phys. Lett. B 528, 199 (1999)

[63] H. Abramowicz, A. Caldwell and R. Sinkus, *Nuclear Instruments and Methods.* A 365, 508 (1995)

[64] R. Brun et al., *GEANT3*, Technical Report CERN-DD/EE/84-1, CERN, (1987)

[65] ZEUS Collab., S Chekanov et al *A ZEUS next-to-leading-order QCD analysis of data on deep inelastic scattering DESY-02-105* (2005)

[66] B. W. Harris and J. Smith *Charm quark and $D^{*\pm}$ cross sections in deeply inelastic scattering at HERA* DESY 97-111 (1997)

[67] ZEUS Coll., S. Chekanov et al., Phys. Rev. D 68, 012007 (2003)

[68] CTEQ Coll., H.L. Lai et al., Eur. Phys. J. C 12, 375 (2000)

[69] M. Gluck, E. Reyna and A. Vogt, Eur. Phys. J. C 5, 461 (1998)

[70] ZEUS Collaboration *Measurement of charm fragmentation ratios and fractions in photoproduction at HERA* DESY-05-147 (2005)

[71] Leonid Gladilin *Measurement of charm fragmentation ratios and fractions in γp collisions at HERA. ZEUS note ZEUS-05-NNN* (2005)

[72] ZEUS Collaboration *Measurement of Charm Fragmentation Ratios and Fractions in Photoproduction at HERA* DESY-05-147 (2005)

[73] Private communication

[74] ZEUS Collab. *A ZEUS next-to-leading-order QCD analysis of data on deep inelastic scattering* DESY-02-105 (2002)

[75] H. Jung, Comp. Phys. Commun. 86, 147 (1995)

[76] G. Corcella et al., HERWIG 6.3 release note (2001)

Appendix A

Trigger

A.1 GTT Analysis Trigger Definitions

The success of any proposed trigger will depend of course on its performance against the standard trigger system already in use. This section of the appendix outlines the details of these triggers which are already in operation at the SLT.

A.1.1 SPP 04

```
If (.not.(FLTevt(58).or.FLTevt(62)) ) then
      Iflag=0
   ElseIf ( CCGefemc .gt. 5.0 .and. CCGetoth .lt. 1.0 ) Then
      CALL SBIT1(ISUBTR2(3),4)
   ElseIf ( pzovere .lt. 0.96 .and. CCGetote .gt. 1.5 .and. CCGetoth .lt. 1.0) Then
      CALL SBIT1(ISUBTR2(3),4)
   ElseIf ( pzovere .lt. 0.96 .and. CCGetote .gt. 6.0 .and. CCGetoth .lt. 4.0) Then
      CALL SBIT1(ISUBTR2(3),4)
Endif
```

FLTevt(58) is an RCAL isolated electron trigger with some additional energy cuts tuned for J/Ψ.

FLTevt(62) is an isolated electron trigger.

A.1.2 HFL 19

```
c FLT
slotset = FLTevt(8).or.FLTevt(9).or. FLTevt(10).or.FLTevt(11).or.FLTevt(14).or.FLT evt(15)
c loose = tight SLT
HFL19_PZoE = 0.96
HFL19_PT12 = 0.75
IF(slotset.and.(ep_vtx.or.no_ctd).a nd. (barrel_time_pass).and. (PzOverE.lt.HFL19_PZoE))
    THEN
    IF ( no_ctd .or. ( slu.ge.2 .and. slf.ge.2
     .and.
     ( hfl_many_tracks
     .or. (SltPt(1).gt.HFL19_PT12.and. SltPt(2).gt.HFL19_PT12 ))))
        THEN
        CALL SBIT1(ISUBTR3(3),19)
     ENDIF
ENDIF
```

FLTevt(8,9,10,11,14,15) are a number of CAL energy cuts

A.1.3 MU 02

```
IF ( (FLTevt(14).or.FLTevt(15)).and. barrel_time_pass)          Then
        CALL SBIT1(ISUBTR3(3),23)       Endif
```

FLTevt(14) is a Barrel muon Cal Energy cut. *FLTevt(15)* is an RCal muon Energy

A.1.4 GTT 05

```
IF( barrel_time_pass .and. (P zOverE.lt.0.96) .and. (FLTevt(8) .or. FLTevt(9)
      .or. FLTevt(10) .or. FLTevt(11) ) )
      then
if (rmui9s.or.rmui9n)
      then
if ( ((GTT_NVTXTRK.gt.3).and.(abs(GTT_z VTX).lt.50.)).or.
   ((GTT_NVTXTRK.le.3).and.(abs(GTT_zVTX).lt.70 .)) !.or. no_gtt )
      then
          CALL SBIT1(ISUBTR4(3),5)
endif
      else
      CALL SBIT1(ISUBTR4(3),5)      endif      endif
```

FLTevt(10) & (11) are muon CAL cuts.

MU06 is essentially MU01 with some vertex requirement.

A.2 $F_2^{c\bar{c}}$ Trigger Description

A.2.1 FLT triggers

- FLT 30 requires
  - A deposit of at least 2.08 GeV in an isolated EM tower with a deposit of at most a third of this value (or < 0.95 GeV) in the HAC tower behind it AND
  - EMC deposit > 2 GeV in the RCAL OR
  - Total RCAL EMC deposit > 3.7 GeV OR
  - A CFLT tower energy deposit > 0.5 GeV AND and SRTD hit
- FLT 34 requires

– An isolated electron in the RCAL and an RCAL energy deposit >

- FLT 36 requires

  – An isolated electron in the RCAL and an RCAL energy deposit > and a CAL energy deposit >

- FLT 44 requires

  – BCAL EMC energy > 4.8 GeV OR

  – RCAL EMC > 3.4 GeV

- FLT 46 requires

  – FLT 30 AND

  – CTD tracks originating from a vertex

A.2.2 TLT triggers

HFL 02

A heavy flavour TLT trigger. Requires a DIS electron OR one of the HFM triggers with loose cuts. HFM triggers are triggers on each of the D mesons (with loose cuts on Δ M, Pt(D*), Pt(Pi) etc.)

SPP 02

An inclusive DIS trigger.

TLT: $30 < \mathrm{E} - \mathrm{P}_z < 100$ GeV. Electron found by SIRA or EM Electron energy 4 GeV Box cut 12x12 cm

SLT = FLT DIS or FLT 36 + $30 < \mathrm{E} - \mathrm{P}_z$ GeV Remc ¿ 2.5 GeV or Bemc > 2.5 GeV or Femc $> 10GeV$ of Femc $> 10GeV$ Fhac $> 10GeV$

FLT (dis triggers) FLT28, 30, 40, 41, 36, 43, 44, 46, 47, 62

A.2.3 DST Selection

Each event was required to trigger at least one of:

- DST9
    - An offline scattered electron is found by any electron finder with an energy greater than 4 GeV.
- DST 10
    - There is a vertex found

These triggers are included for practical purposes to safely reduce the size of the sample used in the analysis. Tighter cuts are applied later in the analysis.

Appendix B

Resolution

B.1 Justification of formalism of tracking resolution

The resolution of the CTD when expressed as a function of transverse track momentum (P_T) takes the following form:

$$\sigma(P_T)/P_T = a_0 P_T \oplus a_1 \oplus a_2/P_T$$

where $\oplus$ indicates that the terms are added in quadrature so that

$$\sigma(P_T)/P_T = \sqrt{((a_0 P_T)^2 + (a_1)^2 + (a_2/P_T)^2)}$$

This form arises from consideration of both scattering effects and inaccuracies in measuring the position of hits along the fitted track as outlined elsewhere [51]. This appendix briefly outlines how these effects lead to the resolution formalism given above.

Contribution from errors in hit measurement

The $a_0 P_T$ term arises from an error in the measurement (σ_{HIT}) on each hit assigned to the reconstructed track where, for a CTD track, $\sigma_{\mathrm{HIT}} \approx 200\mu$. The error on a curved track of radius R obeys the relation $\sigma(R) \approx \sigma_{\mathrm{HIT}} R^2$ and since a measurement of curvature is in essence a measurement of momentum it follows that $\sigma(P_T) \approx P_T^2$ is also true. We therefore quickly arrive at:

$$\sigma(P_T)/P_T = a_0 P_T.$$

Contribution from multiple scattering

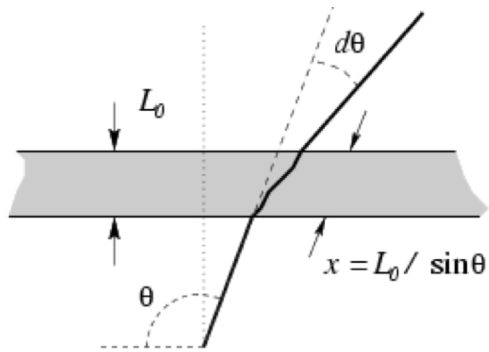

Figure B.1: The effect of multiple scattering of a particle traveling at angle θ through a medium of thickness L_0.

Another important contribution to track smearing is the multiple scatter effect arising from the presence of dead material in the path of the decay particle. Multiple scattering can occur inside the CTD, distorting the hits in a process which depends (amongst other things) on $1/p$. This leads to an error contribution of the form $\sigma(P_T) \approx P_T$ and an additional error term

$$\sigma(P_T)/P_T = a_1.$$

These first two terms would be entirely sufficient to describe the overall error if there was no scatter prior to arrival in the CTD. However at ZEUS there exists dead material in between the vertex and the CTD in the form of the beampipe, MVD and CTD inner wall. The presence of this material causes smearing of the transverse momentum at the production vertex (P_T) into the transverse momentum measured inside the CTD (P_T^{CTD}). This leads to the additional a_2 term which also appears in the parameterisation above. To understand this term we consider the production of a particle produced at the primary vertex with momentum p and polar angle θ as illustrated in figure B.1. Since low momentum tracks are more susceptible to multiple scattering the amount of smearing to θ caused by multiple scattering depends on $1/p$ and is given by

$$\sigma(\theta) = \frac{0.014}{P}\sqrt{L_0/\sin\theta}$$

where $L_0/\sin\theta$ is the distance in radiation lengths traveled by a particle (before it reaches the CTD) at angle θ through a particle of thickness L_0 [56]. P here is measured in GeV. It is interesting to observe that during multiple scattering the magnitude of the track momentum is unaffected by multiple scattering, only the direction is altered.

Given that $\sigma(P_T) = \sigma(\theta)p\cos\theta$ it follows immediately from substitution that $\sigma(P_T) = p\cos\theta\sqrt{L_0/\sin\theta} \times 0.014/p$ which leads inexorably by cancellation to

$$\frac{\sigma(P_T)}{P_T} = \frac{0.014\sqrt{L_0}}{P_T}\cos\theta/\sqrt{\sin\theta}$$

At this stage it is possible to assign approximate values to coefficients here and gauge any detrimental effect that the installation of the MVD may have had on the tracking resolution at ZEUS. To some extent the detrimental effects of increased multiple scattering will be offset by reduced errors on assigning hits to tracks once the MVD has been properly aligned. For tracks that are fully contained within the CDT $\cos\theta/\sin\theta \approx 0.5$ both before and after the ZEUS upgrade. Taking this approximation the a_2 error term takes the general form

$$\sigma(P_T)/P_T = a_2/P_T$$

as required.

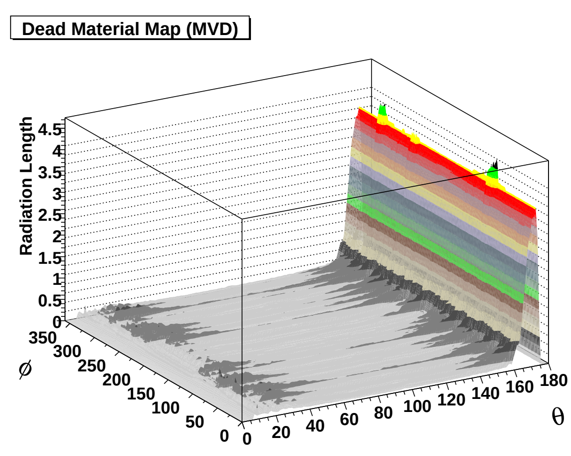

Figure B.2: The Dead Material Map of the MVD as a function of θ and ϕ as implemented in the 2002 MC.

Prior to the installation of the MVD a particle will have to traverse only the CTD and beampipe, a distance corresponding to 3% of a radiation length allowing for an approximation of $\sigma(P_T)/P_T \approx 0.0012/P_T$. The inclusion of the MVD contributes 3.75% of a radiation length (figure B.2), increasing the total to 6.75% which modifies the error approximation to $\sigma(P_T)/P_T \approx 0.0019/P_T$.

This represents the last significant contribution to the error assigned to the CTD tracks. When all of these contributions are combined we obtain the final form of the error

$$\sigma(P_T)/P_T = a_0 P_T \oplus a_1 \oplus a_2/P_t$$

whose coefficients are extracted by fits to data as outlined in section 7.3.2. Such fits yield the following results:

$$\text{CTD Tracking} : \sigma(P_T)/P_T = 0.0063P_T \oplus 0.0083 \oplus 0.0032/P_T$$

$$\text{REG Tracking} : \sigma(P_T)/P_T = 0.0038P_T \oplus 0.0134 \oplus 0.0033/P_T$$

$$\text{ZTT Tracking} : \sigma(P_T)/P_T = 0.0034P_T \oplus 0.0150 \oplus 0.0034/P_T$$

The corresponding HERA I result is

$$\text{HERA I} : \sigma(P_T)/P_T = 0.0063P_T \oplus 0.0070 \oplus 0.0016/P_T.$$

The ratio $a_{2,fit}^{\text{HERA I}} : a_{2,fit}^{\text{HERA II,}} = 1 : 2$ when a_2 is extracted from the fit and $a_2^{\text{HERA I}} : a_{2,prediction}^{\text{HERA II}} = 2 : 3$ from prediction. From first inspection is appears that HERA II tracking resolution is under performing compared to our naive calculation. However in the calculation the modal value of radiation length was selected, in reality the detector map is not uniform in ϕ so there are a number of regions where there is more dead material than has been accounted for in our approximation.

Appendix C

$F_2^{c\bar{c}}$ Results

(Q^2 (GeV^2), x)	F_2^{cc}	1	2	3	4	5	6
(5.5, 0.00008)	0.268	10.18%	12.01%	7.67%	3.71%	-15.90%	-0.91%
(5.5, 0.00018)	0.170	10.92%	11.83%	6.22%	4.19%	-13.05%	-0.30%
(5.5, 0.00035)	0.142	12.60%	12.10%	0.11%	7.33%	27.81%	-1.12%
(5.5, 0.001)	0.098	16.50%	12.76%	-10.55%	5.36%	35.47%	-0.94%
(7, 0.00018)	0.232	12.99%	12.45%	8.72%	1.89%	-15.22%	0.86%
(7, 0.0006)	0.125	11.18%	12.35%	0.83%	5.69%	-7.45%	-0.78%
(7, 0.0015)	0.074	10.91%	11.67%	-10.17%	8.24%	31.27%	0.35%
(11, 0.00018)	0.338	11.83%	12.73%	9.69%	0.10%	-15.66%	0.28%
(11, 0.00035)	0.247	9.41%	12.03%	6.73%	1.77%	0.43%	-0.56%
(11, 0.001)	0.178	12.09%	13.06%	-0.90%	3.96%	1.26%	0.52%
(11, 0.003)	0.096	11.08%	11.94%	-11.54%	4.08%	5.59%	0.41%
(18, 0.00035)	0.456	10.76%	12.35%	9.67%	-3.80%	-29.39%	1.15%
(18, 0.0006)	0.325	10.89%	12.20%	7.08%	0.45%	-8.92%	-0.50%
(18, 0.0015)	0.174	10.27%	12.60%	-2.31%	1.60%	8.01%	-0.01%
(18, 0.003)	0.128	9.87%	11.62%	-12.05%	2.57%	11.09%	-0.10%
(30, 0.0006)	0.426	8.79%	12.96%	10.70%	-4.23%	-5.57%	0.05%
(30, 0.001)	0.340	9.15%	11.87%	6.92%	-3.07%	24.57%	0.75%
(30, 0.0015)	0.268	9.12%	13.05%	-3.18%	-3.83%	-7.74%	0.87%
(30, 0.006)	0.105	7.54%	10.77%	-14.37%	-4.14%	39.91%	-1.20%
(60, 0.0015)	0.402	8.98%	12.09%	9.09%	-8.48%	-0.37%	1.95%
(60, 0.003)	0.250	7.54%	13.02%	0.44%	-8.46%	-4.17%	0.30%
(60, 0.012)	0.109	7.81%	11.38%	-10.85%	-9.49%	30.19%	-0.22%
(130, 0.003)	0.378	8.67%	12.98%	6.77%	-15.00%	-6.82%	0.84%
(130, 0.006)	0.185	7.20%	13.59%	-4.60%	-15.26%	-1.22%	-1.17%
(130, 0.03)	0.056	4.74%	10.35%	-13.71%	-15.73%	35.68%	1.04%
(500, 0.012)	0.047	14.79%	15.08%	4.15%	-24.57%	11.20%	1.72%
(500, 0.03)	0.098	14.04%	11.19%	-11.74%	-24.89%	5.90%	-0.74%

Table C.1: Part B of the individual systematic errors associated with the measurement of $F_2^{c\bar{c}}$. A yellow box indicates a shift from the central value of between 5% and 10% once the systematic has been applied, a magenta box indicates a shift larger than 10%. The systematics checked are labeled from 1 to 17 according to the key in table 8.1.

$(Q^2$ (GeV^2), x)	F_2^{cc}	7	8	9	10	11	12
(5.5, 0.00008)	0.268	0.97%	-0.39%	-1.37%	-7.96%	-3.39%	-0.94%
(5.5, 0.00018)	0.170	0.03%	-1.59%	-1.88%	1.98%	6.32%	0.60%
(5.5, 0.00035)	0.142	-0.26%	-1.42%	0.95%	-7.70%	0.35%	0.41%
(5.5, 0.001)	0.098	-0.85%	-0.36%	-1.64%	-15.53%	-2.85%	-2.38%
(7, 0.00018)	0.232	-2.31%	1.32%	-0.10%	-4.49%	3.76%	-3.71%
(7, 0.0006)	0.125	0.27%	1.41%	-0.36%	-1.06%	-2.67%	1.59%
(7, 0.0015)	0.074	-0.90%	-1.73%	-0.10%	-6.32%	-4.78%	-1.32%
(11, 0.00018)	0.338	0.88%	2.00%	-2.11%	-10.74%	-6.56%	-2.93%
(11, 0.00035)	0.247	0.00%	-0.37%	-1.63%	3.88%	0.42%	1.18%
(11, 0.001)	0.178	-0.41%	-0.54%	0.08%	-2.38%	0.62%	-1.59%
(11, 0.003)	0.096	0.61%	0.52%	-0.75%	-0.28%	5.68%	0.04%
(18, 0.00035)	0.456	-2.89%	1.13%	-0.62%	-6.46%	0.84%	-2.26%
(18, 0.0006)	0.325	-0.15%	-0.25%	1.06%	1.04%	2.13%	1.23%
(18, 0.0015)	0.174	-0.11%	0.55%	-0.38%	-6.04%	2.29%	0.62%
(18, 0.003)	0.128	-0.30%	-0.29%	-0.65%	-6.58%	-2.58%	1.13%
(30, 0.0006)	0.426	0.04%	-1.34%	-0.60%	-3.44%	15.54%	1.27%
(30, 0.001)	0.340	0.16%	-0.58%	-0.76%	-2.03%	-5.00%	-0.34%
(30, 0.0015)	0.268	0.01%	0.66%	0.26%	1.19%	4.79%	0.42%
(30, 0.006)	0.105	0.14%	-0.70%	0.49%	4.75%	1.27%	1.67%
(60, 0.0015)	0.402	-1.02%	-0.65%	-1.23%	-2.91%	-3.97%	-2.24%
(60, 0.003)	0.250	0.58%	-0.42%	-0.90%	4.41%	0.11%	-0.33%
(60, 0.012)	0.109	-0.90%	0.06%	0.75%	-0.75%	-9.04%	0.94%
(130, 0.003)	0.378	-1.34%	0.20%	3.55%	-12.96%	8.06%	-3.15%
(130, 0.006)	0.185	0.90%	0.15%	-1.43%	5.10%	3.47%	4.28%
(130, 0.03)	0.056	-0.94%	-0.25%	-0.86%	6.11%	-4.13%	-3.21%
(500, 0.012)	0.047	-2.02%	-4.80%	0.36%	-5.91%	79.57%	-4.85%
(500, 0.03)	0.098	-0.27%	-4.70%	-5.26%	31.40%	15.06%	10.83%

Table C.2: Part B of the individual systematic errors associated with the measurement of $F_2^{c\bar{c}}$. A yellow box indicates a shift from the central value of between 5% and 10% once the systematic has been applied, a magenta box indicates a shift larger than 10%. The systematics checked are labeled from 1 to 17 according to the key in table 8.1.

(Q^2 (GeV^2), x)	F_2^{cc}	13	14	15	16	17
(5.5, 0.00008)	0.268	-0.94%	4.41%	-3.03%	1.00%	-0.61%
(5.5, 0.00018)	0.170	0.60%	3.54%	-0.82%	0.76%	-0.71%
(5.5, 0.00035)	0.142	0.41%	3.25%	-2.22%	-0.03%	-0.21%
(5.5, 0.001)	0.098	-2.38%	1.41%	-2.51%	0.37%	0.00%
(7, 0.00018)	0.232	-3.71%	6.02%	-3.62%	0.52%	-0.75%
(7, 0.0006)	0.125	1.59%	3.21%	-1.65%	-0.04%	-0.34%
(7, 0.0015)	0.074	-1.32%	2.25%	-0.75%	0.26%	-0.29%
(11, 0.00018)	0.338	-2.93%	7.60%	-0.59%	-0.13%	-1.18%
(11, 0.00035)	0.247	1.18%	2.54%	-0.17%	0.01%	-0.14%
(11, 0.001)	0.178	-1.59%	1.53%	1.87%	0.19%	-0.25%
(11, 0.003)	0.096	0.04%	1.41%	1.64%	0.00%	0.39%
(18, 0.00035)	0.456	-2.26%	4.67%	-3.37%	-0.23%	0.49%
(18, 0.0006)	0.325	1.23%	1.36%	0.19%	-0.04%	0.11%
(18, 0.0015)	0.174	0.62%	0.78%	2.83%	-0.06%	0.00%
(18, 0.003)	0.128	1.13%	0.44%	5.44%	0.17%	0.50%
(30, 0.0006)	0.426	1.27%	8.87%	-2.99%	-0.07%	-0.40%
(30, 0.001)	0.340	-0.34%	3.07%	0.73%	0.25%	0.03%
(30, 0.0015)	0.268	0.42%	1.26%	3.06%	0.08%	0.29%
(30, 0.006)	0.105	1.67%	0.22%	5.66%	0.12%	0.36%
(60, 0.0015)	0.402	-2.24%	7.42%	-1.55%	0.74%	-0.59%
(60, 0.003)	0.250	-0.33%	1.16%	1.22%	-0.10%	-0.07%
(60, 0.012)	0.109	0.94%	-0.42%	2.66%	0.10%	0.09%
(130, 0.003)	0.378	-3.15%	5.98%	-1.54%	0.39%	-0.39%
(130, 0.006)	0.185	4.28%	1.22%	1.76%	0.03%	0.03%
(130, 0.03)	0.056	-3.21%	1.97%	6.17%	0.08%	0.26%
(500, 0.012)	0.047	-4.85%	14.54%	-1.19%	0.01%	-0.72%
(500, 0.03)	0.098	10.83%	-1.19%	0.77%	0.00%	-0.10%

Table C.3: Part C of the individual systematic errors associated with the measurement of $F_2^{c\bar{c}}$. A yellow box indicates a shift from the central value of between 5% and 10% once the systematic has been applied, a magenta box indicates a shift larger than 10%. The systematics checked are labeled from 1 to 17 according to the key in table 8.1.

Don't be afraid
What your mind conceives
You should make a stand
Stand up for what you believe
And tonight
We can truly say
Together we're invincible

Muse, *Invincible*